THE USE OF PASSIVE TELEMETRY IN ROTOR FAULT DIAGNOSIS

LUTFI ALI AREBI

A thesis submitted to the University of Huddersfield in partial fulfilment of the requirements for the degree of Doctor of Philosophy

29 Aug. 2014

Table of Content

List of Figures

List of Tables

List of Abbreviations

ADC	Analogue-to-Digital Converter
ASK	Amplitude shift keying (digital modulation technique)
BNC	Bayonet Neill Concelman: type of connector
CBM	Condition Based Maintenance
CM	Condition Monitoring
DAC	Digital to Analogue Conversion
DAS	Data Acquisition System
DAS	Data Acquisition System
DCM	Duty Cycle Modulator
DCS	Duty Cycle Signal
Enc	Encoder
FFT	Fast Fourier Transformation
FTF	Frequency Transfer Function
g	Gravity =9.81 m/s^2
HRC	Hard Rubber Coupling
IAS	Instantaneous Angular Speed
ICP	Integrated Circuit Piezoelectric Accelerometers
ICs	Integrated Circuits
IEPE	Integral Electronic Piezoelectric Accelerometers
ISO	International Standard Organization
MEMS	Micro – Electro Mechanical Systems
OOK	On-Off Keying (digital modulation technique)
Opto	Opto-Interrupter
PCB	Printed Circuit Board
PPR	Pulse Per Revolution
PSK	Phase Shift Keying
PWM	Pulse Width Modulation signal
RF	Radio Frequency
RMS	Root Mean Square
RPM	Revolution Per Minute
SNR	Signal To Noise Ratio
TNC	Threaded Neill–Concelman: type of connector
TSA	Time Synchronous Averaging
VSWR	Voltage Standing Wave Ratio: This is the ratio of maximum voltage to minimum voltage in standing wave pattern. It varies from +1 to infinite.
WL	Wireless Sensor

List of Nomenclature

A(ω)	Acceleration in frequency domain
a(t)	Acceleration in time domain
θ	Angular displacement
α_j	Angular position of pin j on first shaft
φ_j	Angular position of pin j on second shaft
ω	Angular speed
j	Bolt reference index
a_c	Centripetal acceleration
C_{r1} , C_{r2}, C_{r3}	Coupling critical damping
C_1, C_2, C_3, C_4	Damping coefficients of rotor1, 2, 3 and 4 respectively
a_{tx} ,a_{ty}	Decomposing a_x and a_y in tangential direction
T_m	Driving torque
K_b	Effective coupling stiffness
Δn	error in rotating speed
Fx_{12}, Fx_{23}, Fx_{34}	Force excitations due to misalignment in the x-direction
Fy_{12}, Fy_{23}, Fy_{34}	Force excitations due to misalignment in the y-direction
$dmforcex1$, $dmforcex2$, $dmforcex3$, $dmforcex4$	Forces generated by eccentric mass due to misalignment in the x-direction (shafts 1, 2, 3 and 4)
$dmforcey1$, $dmforcey2$, $dmforcey3$, $dmforcey4$	Forces generated by eccentric mass due to misalignment in the y-direction (shafts 1, 2, 3 and 4)
e_c	Geometric mass centre from rotational centre
a_x ,a_y	Lateral accelerations
m_1 m_2 m_3 m_4	Mass of the rotors and loader
e_{12} , e_{23} , e_{34} (δ)	Misalignment between shafts
N	Number of equivalent jaws in each flange
J_1, J_2, J_3, J_L	Polar moments of inertia of rotor1, 2, 3 and loader respectively
r	Radius of the centre of coupling pin position on reference shaft
R_j	Radius position of bolt j on second shaft
Ω	Reference rotor speed
a_w	Rotational (angular) acceleration
f_s	Sampling frequency
n	shaft speed at which the resolution is calculated (RPM);
V(ω)	Speed in frequency domain
v(t)	Speed in time domain

K_1, K_2, K_3, K_4	Stiffness coefficients of rotor1, 2, 3 and 4 respectively
a_{txy}	Sum of tangential lateral accelerations a_{tx} and a_{ty}
a_t	Tangential acceleration
a_{tw}	Tangential acceleration due to angular acceleration
N_c	The number of base unit counted at the specified clock frequency
M	The resolution of shaft encoder, i.e. the number of pulses per revolution
Mg_{12}, Mg_{23}, Mg_{34}	Torque excitation of coupling due to misalignment
M_{x12}, M_{x23},M_{x34}	Torque generated by coupling due to misalignment
$dmtorque1$	Torque generated by eccentric mass due to unbalance (shaft1)
$dmtorque2$	Torque generated by eccentric mass due to unbalance (shaft2)
$dmtorque3$	Torque generated by eccentric mass due to unbalance (shaft3)
$dmtorque4$	Torque generated by eccentric mass due to unbalance (shaft4)
ε	Torsional displacement
T_L	Torsional load
φ (θ_1)	Total rotation displacement of shaft 1
θ (θ_2)	Total rotation displacement of shaft 2
E_T	Total sensor output
U	Total stored potential energy
X,Y	Vibration differentials
X1,Y1	Vibration displacement levels of shaft 1
X2,Y2	Vibration displacement levels of shaft 2
a_s	Wireless output due to relative change in direction of the earth's gravity

Abstract

The sensors most commonly used for monitoring machine health are wired accelerometers because of their high performances and good stability. However, these transducers are usually large in size; require an external power source. Hence, there is a need for cheaper and reliable alternative for the conventional accelerometers. This thesis reports the development of a wireless accelerometer based on Micro-Electro-Mechanical System (MEMS) inertial sensor and off-the-shelf digital RF communication modules. It is small enough to be installed on the rotating shaft of a machine. In addition, it has a high enough resolution to be used to analyse the dynamic behaviour of rotating shaft.

The wireless sensor is mounted with its sensitive axis in the tangential direction with respect to the centre of the rotor. This position allows the sensor to perform high resolution tangential acceleration measurements and nullifies the centripetal acceleration..

To assist in the validation of the wireless sensor, a mathematical model was derived to simulate the vibration signals from the test rig. Experimental and simulated results both confirmed the effectiveness of the wireless sensor in detecting different degrees of misalignments and unbalance of a flexible rotor system.

The wireless sensor has been confirmed to possess the capability of detecting small degrees of misalignment using the spectral amplitude of the peak at 2X running speed compared to other conventional sensors (wired accelerometers, laser vibrometers).

In addition, the results of the experiment and simulation have also confirmed the capacity of the wireless sensor to detect different shaft unbalance grades at 1X running speed using spectral and order magnitudes. However, the wired sensors used for comparison failed to show any clear separation of the different grades of shaft unbalance.

Moreover, it has been observed that the instantaneous angular speed (IAS) derived directly from the wireless sensor correlates well with that obtained from a shaft encoder and showed the capacity to detect the main features of rotor dynamics. An advanced algorithm has been developed to remove the gravity effect. The application of the algorithm has made the IAS computed from the wireless sensor more indicative to that obtained by a shaft encoder.

Declaration

No portion of this work referred to in this thesis has been submitted in support of an application for another degree or qualification of this or any other university or other institute of learning.

Copyright

Acknowledgements

First of all I want to thank my supervisor, Prof. Andrew Ball. He made this thesis possible by offering me a collaborator position at the school of computing and engineering. From our frequent discussions at the beginning of my Thesis I learned step by step how to do scientific work. In all phases this work has benefited much from his comments, suggestions and cooperation. Last but not least, I want to thank him for the opportunity to participate in international conferences.

I am grateful to my second supervisor, Dr Fengshou Gu, for our many fruitful discussions, in which I learned to see my thesis in a broader scientific context.

I want collectively to thank all CMGROUP members for the constantly good working atmosphere over the years.

Last and always, special thanks extended to my family: my wife and my children: Ahmed, Fatma, Arwa and Yusuf. Special and grateful thanks to my father, sole of my mother and all my brothers and sisters for their high expectations.

The Author

Lutfi Arebi graduated from the Libya, Tripoli University, with a B.Sc. in computer and electronic engineering in 1992 and has got a M.Sc. degree in embedded systems from the University of Manchester. In Jan 2009 he commences the research on condition monitoring that is presented in this thesis in the Maintenance Engineering research Group at the University of Huddersfield.

Publications

1. Arebi, Lutfi, Gu, Fengshou and Ball, Andrew (2012) A comparative study of misalignment detection using a novel Wireless Sensor with conventional Wired Sensors. Journal of Physics: Conference Series, 364. 012049. ISSN 1742-6596.

2. Arebi, Lutfi, Gu, Fengshou, Hu, Niaoqin and Ball, Andrew (2011) Misalignment Detection using a Wireless Sensor Mounted on a Rotating Shaft. In: Proceedings of the 24th International Congress on Condition Monitoring and Diagnostics Engineering Management. COMADEM, Stavanger, Norway, pp. 1289-1299. ISBN 0954130723

3. Arebi, Lutfi, Gu, Fengshou and Ball, Andrew (2010) Rotor Misalignment Detection using a Wireless Sensor and a Shaft Encoder. In: Future Technologies in Computing and Engineering: Proceedings of Computing and Engineering Annual Researchers' Conference 2010: CEARC'10. University of Huddersfield, Huddersfield, pp. 6-13. ISBN 9781862180932.

4. Arebi, Lutfi, Fan, Yibo, Gu, Fengshou and Ball, Andrew (2010) Investigation of Wireless Sensor Deployed on a Rotating Shaft and It's Potential for Machinery Condition Monitoring. In: 23rd International Congress on Condition Monitoring and diagnostic Engineering Management, June 28-July 2, 2010, Japan.

5. Arebi, Lutfi, Gu, J., Ball, Andrew and GU, Fengshou (2010) Investigation of a Rotating Shaft with a Novel Integrated Wireless Accelerometer. In: The Seventh International Conference on Condition Monitoring and Machinery Failure Prevention Technologies, 22-24 June 2010, Ettington Chase, Stratford-upon-Avon, England, UK.

CHAPTER ONE

Introduction

This chapter begins with an overview of the more common conventional techniques used for machinery condition monitoring. This is followed by a detailed description of the motivation, aims and objectives of the research. Finally, the structure of the thesis is described and the content of the remaining chapters is given.

1.1 Introduction

Health monitoring is the process of studying and assessing the condition of machinery, and is crucial for preventing failure. Machine health monitoring can be achieved by its dynamic analysis which requires determining the dynamic characteristics of the machinery, including natural frequencies, mode shapes and damping factors via modal analysis.

The development of reliable monitoring systems to prevent machine performance degradation proceeding as far as malfunction, or even catastrophic failures has been the focus of research Thesis in a wide array of industries which use rotary machinery (Jardine, A. K., Lin, & Banjevic, 2006)

It is obvious that industrial machinery is expensive, and the financial success of an enterprise can depend on achieving low operating and maintenance costs. To achieve these requirements, condition monitoring has become essential. The benefit of condition monitoring is to minimise unplanned interruption of production, reduce maintenance of machinery and improve reliability and safety.

Although condition monitoring was well established in the 1960's, it is still developing in parallel with the advances in transducers and computer technology (Barron, 1996). In the mid-1980's developments accelerated due to the advent of desktop computers. The availability of computers made the collection of data from the machine easier and developments in data analysis allowed the user to make a more informed decision on maintenance strategies.

Rotary machines such as turbines, generators and electrical motors are one of the most important areas of industrial research, particularly rotating shafts. The role of rotary shaft is power transmission. These shafts can carry different parts such as bearings, disks, gears, etc.

There have been many techniques developed to monitor rotating machinery based on conventional wired transducers. This chapter presents conventional condition monitoring techniques including different transducers used to monitor rotary machinery vibration and angular speed.

1.2 Conventional Condition Monitoring Techniques

The monitoring technique or method is determined by the mechanical process being monitored, maintenance goals and added cost. In addition, the physical nature of the process, temperature, vibration, sound, debris, etc. can play a vital role in choosing the right technique. However, for complicated machine plants, a complex condition monitoring techniques may be required.

There are hundreds of papers, covering both theory and practice, on condition monitoring methods and techniques published every year in academic journals, conference proceedings and technical reports (Jardine, A. K., et al., 2006). Some of them are illustrated in (Kelly,

1997; Lees, A., Sinha, & Friswell, 2009; Lees, A. W., 2007 (b); Mathew & Davis, 1998; Mobley & Davies, 1998; Sasi, A. Y. B., Gu, Li, & Ball, 2006; Yesilyhurt, 1997)

Condition Based Maintenance (CBM) is a maintenance program that recommends maintenance actions based on the information collected through condition monitoring (Jardine, A. K. S., Lin, & Banjevic, October 2006). The main purpose of CBM is to avoid unnecessary maintenance tasks by acting only when there are signs of sufficient abnormality of the machine part(s). This approach is based on the acquisition, processing and analysis of data collected from different machine parameters. These parameters include: vibration amplitude, noise level and spectrum, drive speed and motor current, and provide valuable information which can be used to assess the condition of the machine and help in planning the schedule of maintenance work. CBM can substantially reduce maintenance costs and unnecessary downtime if properly implemented.

Figure 1.1 presents the main three steps of CBM (Jardine, A. K. S., et al., October 2006):
1. Data acquisition step (information collecting), to obtain data relevant to system health.
2. Data processing step (information handling), to handle and analyse the data or signals collected in step 1 for better understanding and interpretation of the data.
3. Maintenance decision-making step (decision-making), to recommend efficient maintenance policies.

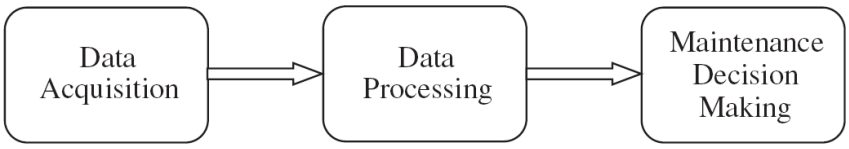

Figure 1.1 Condition based Maintenance main steps (Jardine, A. K., et al., 2006)

1.3 Monitoring Methods for Rotor Dynamics

The condition monitoring of machinery has led to development of a number of new methods for monitoring the machinery processes, see (Liang, 2000), (Collacott, 1997), (Matthew, 1987), (Jardine, A. K., et al., 2006), (Huer & Zhaojian, 2010; Sasi, Y. A., 2005) and (Jardine, A. K., et al., 2006). These methods can be summarized as following:

1.3.1 Machine Parameters

This type of monitoring is concerned with the change of machine performance parameters to identify machine abnormality. Speed, current, performance and power consumption are good examples of parameters that can be monitored to detect changes of machine characteristics. The trend change, for instance, of pressure, temperature and current are good indication to detect the change in machine characteristics.

In practice current or speed fluctuation can be analysed using spectral analysis for monitoring purposes (Liang, 2000), (Pereira & Da Silva Gazzana, 2004), (Tsoumas, Mitronikas, Georgoulas, & Safacas, 2005), (Sasi, A. Y. B., et al., 2006), (Li, Y., Gu, Harris, & Ball, 2005) and (Trevor & Hunt, 1996). Current trend change is a sign of a defective component of the machine. This monitoring method suggests systematic measurement of a monitored parameter and plotting the data recorded against time or frequency.

1.3.2 Vibration Analysis

Vibration is naturally generated by rotary machines. Each part of such a machine has its distinctive vibration patterns. These patterns contain valuable information about the machine condition. The ability to measure and record the vibration signature of rotating machinery without interrupting normal operation is a powerful technique for monitoring its condition.

Transducers can measure acceleration, velocity and displacement. Vibration is usually measured by accelerometers. The selection and mounting position of the accelerometers are important decisions in vibration analysis (Crawford & Crawford, 1992). Vibration analysis is one of the most usable methods in machinery condition monitoring techniques. It depends on the vibration signal's frequencies(De Silva, 2005). The following are the useful frequency ranges of different signals (Barron, 1996):
Acceleration: from zero up to and beyond 20 kHz.
Velocity: from 2 Hz to 2 kHz.
Displacement: from zero up to 200 Hz.

These waveforms are analysed and processed in a variety of ways such as determining the root mean square (RMS) and variance of the waveforms in the time domain, and waveform power spectrum analysis in the frequency domain. Time-frequency, wavelet and higher order spectral analyses are recent signal analysis procedures used to examine vibration waveforms for machine condition(Jardine, A. K., et al., 2006).

The potential use of vibration analysis methods for condition monitoring in time, frequency and time-frequency domains, has enabled condition analysis of a wide range of machine components. That includes(De Silva, 2005): gears, bearing, couplings, rotors/ shafts, fan/ pump assemblies. The failures causes can be classified by: unbalance, looseness, misalignment, wear, poor lubrication, damage/perishing, aero/hydrodynamic forces, cavitation.

Vibration based condition monitoring is the most cost-effective approach but may suffer difficulties due to noise sources such as vibration from other machinery(Dalpiaz & Rivola, 1997). However, it is not a general purpose condition monitoring technique since it provides vibration related information only and some defects such as wear may not generate vibration signals worth monitoring.

1.3.3 Acoustic Analysis

This approach focuses on the analysis of acoustic or noise waveforms produced by machinery processes. Microphones are often used to record acoustic signals which are then compared with vibration waveforms. Microphones have wide frequency range, can give comprehensive information due to their sensitivity and are easy to install (Sasi, Y. A., 2005). Therefore, microphones are used in many applications such as gear boxes and bearings (Sasi, Y. A., 2005). The acoustic monitoring technique can be on-line and non-intrusive which make it an attractive option. However, the major limitation of acoustic monitoring is that background noise contaminates the acoustic waveforms (Kelly, 1997).

1.4 Fault Diagnosis of Rotating Machinery

Over the last century, rotating machinery has been studied in more and more detail. Rotor dynamics is essential for engineers and scientist involved in the transportation and power-generation industries. The analysis and design of rotating machinery is crucial in terms of the cost of both production and maintenance. Therefore, fault diagnosis of rotating machinery becomes critical. The design of rotating machinery becomes increasingly complex due to technological advancement, and condition monitoring strategies become more advanced in order to cope with the burdens being placed on individual components of a machine (Edwards, Lees, & Friswell, 1998).

Vibration in rotating machinery usually is due to some externally applied load, such as misalignment, cracked or bent shafts, or mass unbalance. Vibration condition monitoring as a method of fault diagnosis has been examined by Smith (Smith, 1980) and Taylor (Taylor, 1995). Smith covered the types of general faults listed above and described qualitatively how they may be recognised from their vibration characteristics. He also discussed effects caused by nonlinearities. Taylor included information on how measured data should be processed in order for a diagnosis to be performed. Earlier studies have carried out these researches using conventional wired accelerometers to measure the vibration and perform the diagnosis process. The challenge is to measure the rotor vibration directly using a novel wireless accelerometer for diagnosing various rotor problems.

1.4.1 Misalignment

Rotor misalignment is one of the most common causes of vibration in the operation of rotating machinery, yet it remains incompletely understood. Despite the rapid increase in understanding of rotor dynamics, no satisfactory analysis explains the range of observed phenomena. Sekhar and Prabhu (Sekhar, A. S. & Prabhu, 1995) discussed the effect of coupling misalignment on the vibration of rotating machinery. Shaft misalignment can be a major cause of vibration, due to reaction forces generated in the shaft couplings. It is generally accepted that a significant 2X of rotor speed vibration response is a major feature of rotor

misalignment(De Silva, 2005; Prabhakar, Sekhar, & Mohanty, 2001). A model based method is usually used for fault prediction, where the 2X component is more significantly affected than the 1X. By using this model based method it is possible to predict the vibration response due to misalignment at the various harmonics. It is valuable in terms of both fault diagnosis and machinery design.

1.4.2 Mass Unbalance

Mass unbalance is one of the most frequently occurring causes of rotor vibration in industrial rotor bearing systems (Edwards, et al., 1998). Presence of unbalance changes the dynamic behaviour of the system. This change is equivalent to additional loads acting on the healthy system. The fault model for unbalance developed by Platz and Markert describes the effect of static and kinetic unbalances of the rotor system (Platz & Markert, 2001).

Jalan and Mohanty demonstrated a model based fault detection system for a simple rotor bearing system (Jalan & Mohanty, 2009). By simple measurement of the radial vibration alone and applying the proposed model based technique, faults in a rotor bearing system were easily identified. Lees and Friswell presented a method to estimate the unbalance configuration in a flexibly-mounted rotor-bearing system from vibration measurements at the bearing pedestals (Lees, A. & Friswell, 1997). With the vibration measured by wired accelerometers and using an accurate model, mass unbalance can be identified where the 1X of rotor speed response is significantly affected (De Silva, 2005; Xu & Marangoni, 1994 a).

1.4.3 Bent Shafts

A bent shaft is one of the causes of the vibration in rotary machinery. It may be caused in several ways, for example due to creep thermal distortion or a previous large unbalance force (Edwards, et al., 1998). The unbalance force generated by a bent shaft is slightly different to that caused by conventional mass unbalance. However, bent shafts have great effect on 1X of rotor speed when the geared system mounted on stiff viscoelastic supports(De Silva, 2005; Kang, Hsu, Lee, & Shiau, 2011). More details about bowed shafts and their effects can be found in (Braut, Zigulic, & Butkovic, 2008; Kang, et al., 2011; Nicholas, Gunter, & Allaire, 1976; Yang, T. & Hsu, 2009).

1.5 Conventional Wired Sensors Used for Rotor Fault Diagnosis

The above mentioned common rotor faults are usually investigated using wired transducers. Since the most common cause of rotor faults is vibration, accelerometers are frequently used to detect and diagnose these faults. Several types of accelerometers manufactured by many well-known manufacturers are available all over the world. The selection of accelerometers is

based on their technical specifications and measurement requirements such as frequency range to be measured, amplitude of vibration, etc.

The conventional wired transducers used for rotor fault detection are:

1. Accelerometers (Vibration)
    a. Piezoelectric Accelerometers
    b. Charge mode or capacitive type accelerometers
    c. Integral Electronic Piezoelectric (IEPE).
2. Encoders (Instantaneous angular speed)
3. Laser vibrometers (Displacement, velocity)
4. Magnetic pickups (Displacement)
5. Current and voltage eddy transducers (Power, Displacement)

The frequently used transducers for rotor fault detection will be discussed in more details in the next chapter.

1.6 Wireless MEMS Accelerometer

From the above review, in dynamic health monitoring, the utilization of appropriate transducers is required to provide accurate measurement of machinery responses in both frequency and time domains. Conventional devices utilised for health monitoring are based on wired transducers. These transducers are usually large in size, require high actuation power and have narrow frequency bandwidths compared to MEMS ones, which reduce their accuracy, versatility and applicability to smaller machinery.

To monitor the rotary shaft, the accelerometers are mounted on the bearing housing according to the measuring standard ISO 10816-3,2009 (De Silva, 2005; Iso10816-3, 2009). The recorded vibration signal will be different according to which moving part is generating the signal. This contaminated vibration signal could be used to record the vibration of the rotary shaft directly. The advances in developments of IC micro fabrication and micro electro mechanical systems (MEMS) have led to the design of progressively smaller footprint, low dynamic mass and actuation power sensors. In addition, MEMS sensors provide wide frequency bandwidths, high measuring accuracies and a digital output. With such advantages, MEMS sensors can potentially replace conventional piezoelectric transducers.

To transfer data from MEMS sensors to signal analysers, traditional wiring methods can be used. Such methods provide reliable data transfer and are simple to integrate. However, in order to study rotating machinery, MEMS sensors attached to conventional positions (static) can be either wired or transmit their signal wirelessly. In the case of direct mounting on a rotor, wireless transmission is essential. With the rapid developments of microelectronic and wireless technologies, designers and researchers now have the capabilities to develop and implement wireless health monitoring systems. With wireless transmission it may be possible

to achieve long distance monitoring. In addition, the measuring accuracy might increase due to the direct measurement of rotor vibration as well as angular velocity. Consequently, there is a need to implement and test wireless communications capabilities using MEMS sensors (Elwenspoek & Wiegerink, 2001; Lynch, J., 2004; Lynch, J. P., Law, Straser, Kiremidjian, & Kenny, 2000).

Most of the recent research efforts have been concentrated on the development of wireless systems for health monitoring of civil engineering structures, such as building and bridges (Chung, Enomoto, & Shinozuka, 2003) (Lynch, J., 2004): (Lynch, J. P., et al., 2000). Such structures are usually characterized by large masses and low resonance frequencies. Thus, health monitoring systems designed for civil engineering structures might not be applicable to mechanical structures.

The advances in microelectronic systems means off-the-shelf wireless transmitters and receivers are available at low cost. Using these modules, MEMS accelerometers are integrated into wireless communication systems designed to transmit acceleration signals digitally. The digital wireless system is used to perform high resolution tilt and rotation measurements of the angular and linear acceleration of rotors. In addition, the developed digital system can be used to measure angular rates. Results from developed wireless MEMS accelerometers are presented in this thesis to confirm their potential for accurate and effective health monitoring of rotating machinery.

In this research, an in-depth study of the application of MEMS wireless accelerometers to health monitoring of rotating machinery is presented. Commercially available MEMS sensors have been used. Characteristics of the selected MEMS sensors have been studied using analytical, computation and experimental techniques. In addition, development of instrumentation and methodologies for wireless health monitoring of rotor dynamics are presented.

1.7 Research Motivation

A rotating shaft is always the key component of mechanical systems such as motors, pumps, engines and turbines. Due to the heavy use of shafts, defects such as unbalance, cross-sectional cracks and misalignment will develop. There are many techniques used to monitor such defects; by analysing the vibration of the shaft as well as the instantaneous angular speed (IAS) of the rotating shaft. The vibration is usually measured by placing accelerometers on the bearing housing whereas IAS is measured using a laser-based, direct general-purpose analogue-to-digital converter ADC based method for a shaft (encoder) and a magnetic pickup for gears. The development of a wireless sensor which can be mounted tangentially on the shaft could help to measure rotor vibrations and IAS simultaneously. Developing new techniques based on a wireless MEMS accelerometer is presently the most challenging problem

in condition monitoring. Using advanced analysis of the information extracted from a wireless accelerometer the faults can be detected.

The vibration response measured using wired accelerometers mounted on non-rotating structural components such as bearing housings according to the measuring standard ISO 10816 Part 1 (De Silva, 2005; Iso-10816-1, 1995) is usually contaminated by the vibration from other parts of the machinery. For instance, the magnitude of the signal from a faulty bearing could be so large as to hide a rotor related fault and vice versa. In addition, the signals are attenuated by the body of the bearing housing.

The rotor related faults also can be monitored using the encoder mounted at the end of the rotor using an IAS technique. Ben Sasi showed that IAS techniques can be used to diagnose mechanical faults of a diesel engine and an induction motor using both time-intervals and FFT (Sasi, Y. A., 2005). Sweeney and Randall showed that a gear based power transmission system exhibits speed fluctuations due to a combination of effects, including geometric errors and transmission errors (Sweeney & Randall, 1996).

Research efforts have identified wireless communication technology, MEMS accelerometers and digital signal processing, as key areas of innovation that can be used to develop a novel wireless monitoring system for rotating machinery. The maximum speed of the machine subjected to the test is 1420 RPM which is equivalent to 25 Hz. The challenge of replacing wired sensors by wireless ones motivates this research for further investigation to rotor dynamics.

1.8 Research Aims and Objectives

The aim of this research is to develop and test an accurate and sensitive MEMS wireless accelerometer suitable for condition monitoring application for rotating shaft fault diagnosis.

The objectives of this research are focused on three main areas:

Sensor improvement:

- **Objective 1:** To develop a MEMS based wireless sensor unit and deploy it on a rotating shaft by mounting it in tangential direction.
- **Objective 2**: To improve a wireless sensor unit for rotor dynamics measurements.
- **Objective 3:** To benchmark the new sensing system by comparing its measured data by wired sensor measured data.
- **Objective 4:** To investigate the characteristics of the rotor dynamics including IAS extraction methods, and parameters that might influence the IAS evaluation from a wireless sensor.
- **Objective 5:** To measure the IAS and vibration of the system using conventional methods.

Rotor Modelling:

- **Objective 6:** To develop an accurate model that takes into account the dynamics of bearings and couplings.
- **Objective 7:** To improve the model to be a more accurate by taking into accounts the dynamics including misalignment, eccentricity and unbalance.
- **Objective 8:** To study the characteristics of the rotor dynamics based on the model and measurements made under normal and misaligned conditions.
- **Objective 9:** To study the characteristics of the rotor dynamics based on the model and measurement under normal and unbalanced conditions.

Rotor Diagnosis

- **Objective 10:** To develop more advanced analysis techniques for rotor dynamics based fault diagnosis, i.e. to differentiate between unbalance and misalignment.
- **Objective 11:** To benchmark the wireless sensor diagnostic performance with conventional vibration measurements such as contact accelerometers and non-contact laser displacement systems.
- **Objective 12:** To study the characteristics of the rotor dynamics based on the model and measurement.
- **Objective 13:** To develop more advanced analysis techniques for rotor dynamics based fault detection using Time synchronous Averaging (TSA).
- **Objective 14:** To develop more advanced techniques for IAS based diagnosis.

1.9 Thesis Outline

The thesis consists of ten chapters, the contents of which are briefly described below:

• ***Chapter Two***: This chapter introduces conventional commercial accelerometer types with the basic principle of their operation. In addition, it gives a detailed description of the structure and theory of operation of MEMS accelerometers. An overview of wireless technology and a literature review of wireless sensors for condition monitoring are presented. Finally, the internal structure and theory of operation of the MEMS accelerometer used in this Thesis is presented.

• ***Chapter Three***: This chapter begins with design considerations. Then it defines duty cycle signal and its frequency analysis. It then describes duo-binary carrier suppressed filtering using a Sallen-key active low pass filter, and design of a wireless accelerometer node circuit. Sensitivity and calibration are discussed. In addition, wireless accelerometer power consumption is presented. Finally, the uncertainty of the wireless sensor measurements is examined.

• ***Chapter Four***: This chapter begins by introducing IAS; it then briefly demonstrates conventional angular speed transducers used for obtaining IAS. The speed measurement error equation for encoders is derived and discussed. The resolution of all sensors for IAS

measurement is determined. Methods for IAS extraction from encoder are briefly presented. Also, IAS extraction from a wireless sensor is discussed. Then, a comparison is made between the IAS obtained from the wireless sensor and other sensors. Finally, the TSA is applied to the signals and a new approach of IAS extraction is discussed. Moreover, the IAS resulted from the last method is compared to IAS from other sensors after applying TSA.

• ***Chapter Five***: This chapter begins with an overview of the bearing test rig used to carry out the investigations. The data acquisition system and the transducers used to perform the various experiments are described.

• ***Chapter Six***: To verify the measured results, this chapter presents a mathematical model that simulates various vibration signals of the test rig. It begins with a literature review of rotor system misalignment modelling. It then describes the lumped mass method for modelling the test rig for a two rotor system. The derived equations are solved using state space approach. The results of the model are presented. Then, a more advanced analysis method is used to model the four rotor system taking into account the bearings. In both models, the wireless sensor output is derived and explained.

• ***Chapter Seven***: This chapter introduces a literature review for parallel misalignment. Then it investigates a novel approach for monitoring shaft parallel misalignment using a wireless vibration sensor which can be mounted on the surface of the rotating shaft. This measurement system can more effectively diagnose faults of rotating shafts because the signal to noise ratio is higher due to direct sensor installation and combined response measurements. Both theoretical analysis and experimental results show that the scheme outperforms IAS measurement when detecting shaft misalignments.

• ***Chapter Eight***: In this chapter a systematic comparison is made using the bearing test rig for detection of shaft misalignment between wireless sensor and other three common sensors: a laser vibrometer, an accelerometer and a shaft encoder. These four sensors are used to measure simultaneously the dynamic responses: IAS from the encoder, bearing house acceleration from the accelerometer, shaft displacements from the laser vibrometer and angular acceleration from the wireless sensor. These responses are then compared in both the time and frequency domains for detecting and diagnosing different levels of shaft misalignment. Results show the effectiveness of wireless accelerometer in detecting the faults.

• ***Chapter Nine***: In this chapter the bearing test rig is used to conduct a systematic comparison of detection of shaft unbalance between the wireless sensor and two other common sensors: an accelerometer and a shaft encoder. These three sensors are used to measure simultaneously the dynamic responses: IAS from the encoder, bearing housing acceleration from the accelerometers and angular acceleration from the wireless sensor. These

responses are then compared in both the time and frequency domains for detecting and diagnosing different levels of shaft unbalance. Results show the effectiveness of wireless accelerometer in detecting the two different unbalance cases.

Chapter Ten: This chapter summarises the achievements of the research work and explains how the aim and objectives stated in Chapter One were achieved. A summary of the author's contributions to knowledge and the novel aspects of the research are also included. Finally, recommendations for future work for the wireless accelerometer development and usage are provided and conclusions made.

CHAPTER TWO

Wireless Sensing Technology

This chapter introduces conventional accelerometers commercially available. It also, presents the basic principle of their operation and then provides a detailed description of MEMS accelerometers, their structure and theory of operation. An overview of wireless technology and a literature review of wireless sensors used for condition monitoring are presented. Finally, the chapter presents the internal structure and theory of operation of the MEMS accelerometer to be used in this research Thesis.

2.1 Introduction

Conventional wired accelerometers are commonly used in dynamic rotor vibration monitoring and with shaft encoders and laser vibrometers, are used to determine the condition of a rotating shaft. Conventional sensors are mounted on static parts of the machinery. The cables for such sensing systems contain wires which carry the signal and are vulnerable to corruption by ambient noise. Deploying a sensor directly on the shaft cannot be achieved using conventional wired sensors. In such cases, wireless accelerometers are necessary.

Advances in low cost and low power MEMS accelerometers have led to the development of a wireless sensor which can be mounted on the surface of the rotating shaft. Moreover, such an arrangement will improve detection sensitivity and hence enable the detection of faults in their incipient stage.

The earlier the rotating shaft defect is diagnosed the lower the cost of maintaining the machine (Kelly, 1997). The conventional accelerometers most used will be discussed and basic principle operation presented. Since the novel wireless accelerometer utilised is based on MEMS accelerometers, a detailed description of their structure and theory of operation is presented. An overview of wireless technology and a literature review of wireless sensors are given. Finally, the internal structure and theory of operation of MEMS accelerometers are discussed.

2.2 Accelerometers

An accelerometer is a sensing element that measures acceleration; acceleration is the rate of change of velocity with respect to time. It is a vector that has magnitude and direction. Accelerometers measure in units of "g" (the standard value of gravitational acceleration at the earth's surface = 9.81m/s²). Modern accelerometers can measure: vibration, shock, tilt, impact and motion of an object. The relationships between velocity and displacement for translational and rotational system can be expressed as:

$$a = \frac{dv}{dt} = \frac{d^2x}{dt^2} = \ddot{x} \qquad \textbf{2.1}$$

$$\alpha = \frac{d\omega}{dt} = \frac{d^2\theta}{dt^2} = \ddot{\theta} \qquad \textbf{2.2}$$

Where:

Transitional system:	Rotational system:
$a = \ddot{x}$: acceleration	α : acceleration
$v = \dot{x}$: speed	ω : speed
x : displacement	θ : displacement

Although it is possible to compute the acceleration of an object from displacement or velocity, most accelerometers use a sensing method in which the movement of an inertial or seismic mass relative to the accelerometer housing is detected (Fraden, 2010).

Basically, an accelerometer is a solid frame with an inertia element (*m*) whose movement may be transformed into an electric signal. The mechanism of conversion can be, for instance, piezoelectric (Fraden, 2010). Figure 2.1 shows a general mechanical structure of such an accelerometer. Mass, *m*, is supported by a spring having stiffness *k* and the mass movement is damped by a damping element with a coefficient *d*. The mass is constrained to move only in the vertical direction relative to the accelerometer housing. During operation, the accelerometer case is subjected to acceleration $\ddot{x}_i$, and the output signal is proportional to the deflection x_o of the mass *m*. Since the accelerometer mass m is constrained to linear motion, the system has one degree of freedom.

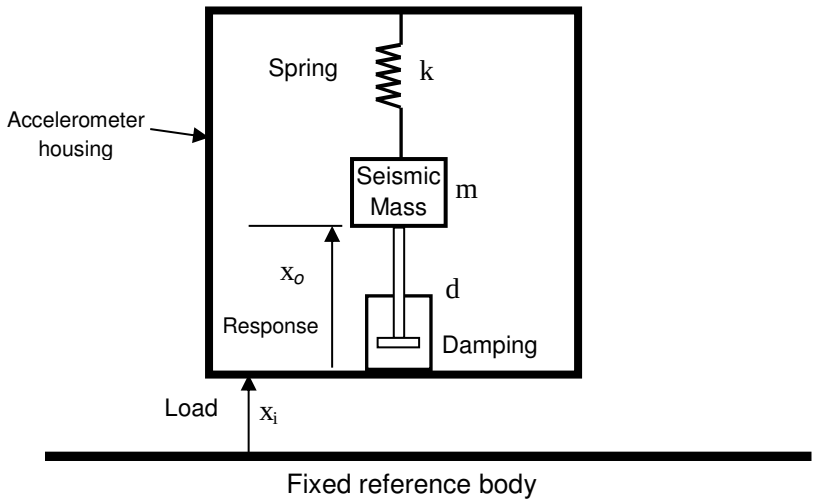

Figure 2.1General layout of an accelerometer (Gardner, 1994)

The accelerometer is essentially a mass-spring damper system in which the loading force $-m\ddot{x}_i$ drives a second order damped harmonic oscillator. The equation of motion of this system can be expressed as:

$$m\ddot{x}_o + d\,\dot{x}_o + k\,x_o = -m\ddot{x}_i \qquad \textbf{2.3}$$

Where, x_o is the displacement of the inertial mass (*m*) relative to the rigid frame. Under conditions of a sinusoidal acceleration of constant amplitude, the displacement amplitude, x_o, is directly proportional to the magnitude of the input acceleration, x_i, where (Fraden, 2010):

$$x_o = \left(\frac{m}{k}\right)\ddot{x}_i \qquad \textbf{2.4}$$

The behaviour of this dynamic system is determined by four parameters; the frequency and magnitude of the driving force, the natural frequency of the system ω_o and the damping factor of the system ξ where;

$$\omega_o = \sqrt{\frac{k}{m}} \quad \textbf{2.5}$$

$$\xi = \frac{d}{2\sqrt{mk}} \quad \textbf{2.6}$$

There are different types of accelerometers and each has its own unique characteristics, advantages and disadvantages. Accelerometers can be classified according to the physical effect used as the sensing mechanism: piezoelectric, capacitive and Integrated Electronic Piezoelectric (IEPE) accelerometers. A brief review of these accelerometers is given below.

2.2.1 Piezoelectric Accelerometers

Piezoelectric accelerometers use crystalline materials such as barium titanate, lead-zirconate, lead-titanate and lead metaniobate, which generate an electric potential when subject to an applied stress. This is known as the piezoelectric effect. A crystal is sandwiched between the case and the seismic mass which exerts a force proportional to the acceleration. These sensors operate from frequencies as low as 2 Hz and up to about 5 kHz, they have good off-axis noise rejection, high linearity, and a wide operating temperature range (up to 120° C)(Fraden, 2010).

2.2.2 Capacitive Accelerometers

Capacitive accelerometers produce a change in electrical capacitance, when subjected to acceleration. A capacitive acceleration sensor basically contains two components, the first is a fixed plate and the other is a plate attached to the seismic mass, which is free to move inside the housing. These plates form a capacitor whose value is function of the distance between the plates. It is supposed that the capacitor value is modulated by the acceleration (Fraden, 2010). The accelerometer senses the capacitance change between a static condition and the dynamic condition.

2.2.3 IEPE Accelerometers

IEPE refers to a type of accelerometer transducer that is packaged with a built-in charge amplifier or voltage amplifier. IEPE accelerometers are widely used nowadays because of their capability of measuring vibrations with low noise at low frequency (<< 1 Hz) (Levinzon, 2008). Moreover, IEPE accelerometers have the advantages of high sensitivity, large dynamic range,

wide frequency and temperature ranges, low-output impedance and can be extremely compact (Levinzon, 2008).

2.3 MEMS Accelerometers

The main factors that determine sensor success are its performance, cost and reliability. However, sensor performance characteristics are severely limited by its size in some applications (Reilly, Leach, Cuenat, Awan, & Lowe, 2006). The reduction of sensor size usually leads to an increase in usage due to its lighter weight. The mass of an accelerometer will often determine where it can be employed and so reduction in mass will increase its marketability. The cost of a sensor is another important factor. Clearly, less material is needed to manufacture a smaller sensor but the cost of material processing is often a more significant factor. Silicon technology has facilitated the production of small, reliable processors in the form of Integrated Circuits (ICs) using microelectronic technology (Reilly, et al., 2006).

Sensors are the interface between our world and electronic systems. They provide information on the system being monitored through signal conditioning circuits to computers. By processing that information a decision can be taken. Initially sensors were large and posed great challenges in terms of the packaging of the total measurement system. In the past few years sensors have decreased in size due to the introduction of solid-state devices and the advancement in micron size devices.

Micro Electro Mechanical Systems (MEMS) are devices (with micron size tolerances) that are fabricated using techniques similar to those used to manufacture integrated circuits, and are able to monitor many tasks and functions that include mechanical, electrical, optical, fluidic, and other types of processes (Michael, 2005). MEMS are increasingly finding applications in many areas including condition monitoring (industrial processes), health care, etc. MEMS accelerometers are low cost, low power with a mass that varies between 1 and 4 g, they are capable of measuring both static acceleration (e.g., gravity) and dynamic acceleration (e.g., vibration)(Analog Devices, 2009).

The output of this type of device is a signal whose duty cycle (ratio of pulse width to period) is proportional to the acceleration in each direction as shown in Figure 2.2. These outputs are treated as digital output which can be read directly with a microprocessor counter (Analog Devices, 2009). The integration of MEMS systems with neighbouring circuitry allows for electrical actuation and signal detection with better performance, programmability and adaptability along with miniaturisation and simplicity of the total system at a lower production cost (Chen & Kuan, 2000). More information about the MEMS Generative accelerometer type ADXL202AE can be found later in this chapter.

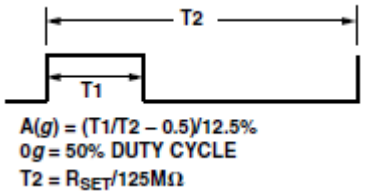

Figure 2.2 ADXL202 Duty Cycle output (Analog Devices, 2009).

2.3.1 Sensing Mechanisms in MEMS Accelerometers

Typical sensing mechanisms used in MEMS sensors include piezoresistive, piezoelectric, capacitive, resonant membranes and thermal sensing technology (Elwenspoek & Wiegerink, 2001; Fraden, 2010). Each of these signal transducers require different fabrication techniques and operate using different signal conditioning circuitry.

In this thesis, capacitive MEMS accelerometers are used because such accelerometers provide high measurement accuracy and are sensitive to gravitational acceleration, which enable high-resolution measurements of tilt and rotation (Elwenspoek & Wiegerink, 2001; Fraden, 2010).

2.3.2 Comparison between Capacitive and Piezoresistive MEMS Accelerometers

The main advantages of piezoresistive accelerometers are the simplicity of their construction and fabrication processes, and the relative ease with which signal can be read. However, piezoresistive devices have some critical drawbacks such as low sensitivity and high temperature dependence. Complex temperature compensation circuits are often needed and a very large seismic mass is essential for an acceptable sensitivity.

Capacitive sensing is dominant in MEMS accelerometers for several reasons. Both surface and bulk micromachining can be used to fabricate a variety of capacitive accelerometers with performance ranging from the low-end automotive application to high-precision inertial navigation. Compared to piezoresistive accelerometers, capacitive accelerometers have high sensitivity, low power consumption, low noise level, stable DC characteristics and lower temperature dependence (Elwenspoek & Wiegerink, 2001; Fraden, 2010).

2.4 Wireless Technology

Wireless technology is widely used in such common devices as mobile phones and internet access. The main question in the use of wireless is "How far can it go?". In the context of condition monitoring the important point is that the range of a wireless link could vary from a few feet to a few miles. The transmission range is determined by many factors including the power of transmission, type and gain of the antenna used, the receiver performance and the

required radio frequency link. The advances in wireless electronics have led to cheaper and lower power wireless transmitter and receiver modules. These modules are fabricated in such way that no external RF components except antennas are needed.

2.5 Why Wireless in Condition Monitor?

Cost and flexibility are the two main factors that make a wireless sensor valuable and appealing. In cases such as a rotating shaft, where use of a wired sensor is impossible unless indirect contact or laser sensors were used or a wireless sensor must to be deployed. Wireless condition monitoring can make monitoring much easier.

2.6 Overview of MEMS Wireless Sensing (Literature Review)

The deployment of a novel wireless accelerometer directly on the drive shaft has not been the subject of much investigation. (Bejarano, Jia, & Just, 2009) used a wireless sensor to identify a crack on a rotating shaft. From (Bejarano, et al., 2009) it can be seen that the presence of a crack in a rotating shaft changes its vibration characteristics. (Cabanas et al., 2011) used a wireless device for the early detection of broken rotor bars in induction motors. ZigBee™ transceiver modules were used to transfer the data. The instrument used was statically deployed near the induction motor(Zigbee Alliance, 2007).

(Korkua, Jain, Lee, & Kwan, 2010) used a MEMS tri-axis accelerometer to monitor the vibration and study the unbalance of an induction motor. The vibrations in the three directions were conditioned and transmitted through a Zigbee wireless network. The MEMS accelerometer was positioned on the top of the motor casing. Under different operating conditions, the wireless health monitoring is found to work satisfactorily (i.e, detects the motor specific fault).

(Sarkimaki, Tiainen, Ahola, & Lindh, 2005) explored the applicability of wireless technologies to transfer and collect condition monitoring and maintenance data, and found that wireless technology offers cost reduction. (Chung, Enomoto, Loh, & Shinozuka, 2004; Shinozuka, Feng, Chou, Chen, & Park, 2004) used a MEMS accelerometer wireless network to monitor the behaviour of a real bridge structure. Chung et al have compared the results from wireless with that from traditional cabled sensor. They found that MEMS-based wireless sensors are cost-effective for carrying out real-time monitoring missions. Shinozuka et al have shown the feasibility of using MEMS-based accelerometers and wireless communication in monitoring the health condition of bridge structure.

Most of the researches listed above used a static accelerometer. The challenge of this work is to deploy the wireless sensor on rotating shaft. In order to use a MEMS accelerometer effectively and develop a useful wireless sensor, a better understanding of their structure and theory of operation is necessary. The rest of this chapter concentrates on these issues.

2.7 Analogue Devices ADXL202 Dual-axis Accelerometer

In this thesis, the Analogue Devices ADXL202 dual-axis accelerometer has been used. This MEMS accelerometer is used in a wide range of consumer, industrial, military, and automotive applications (Analog Devices, 2009) (Hsu, 2008; Kovacs, 1998). The ADXL202 accelerometer has a measuring range of ±2 g (g = 9.81 m/s^2). It provides both analogue and digital output signals, with sensitivities of 312 mV/g and 12.5 %/g, respectively. It requires a DC voltage supply between 3 and 5.25 VDC for operation and is capable of operating in a wide range of temperatures. Table 2.1 summarizes the characteristics of the ADXL202 accelerometer (Analog Devices, 2009).

Table 2.1 characteristics of the MEMS accelerometer used in this research (Analog Devices, 2009).

Measuring range	± 2 g
Resonance frequency	10 kHz
Sensitivity (Digital output)	12.5 %/g
Operating voltage supply	3.0 to 5.25 VDC
0 g duty cycle	50%
Operational Weight	160 mg
Sensitivity (Analogue outputs)	312 mV/g
Temperature	-40 to 85 °C

2.7.1 Sensor Structure

The ADXL202 sensor element is a differential capacitor whose output is proportional to acceleration. The performance of the sensor is dependent on sensor beam design, see Figure 2.3 (Weinberg, 1999). The beam is made up of many fingers. Each set of fingers is as shown in Figure 2.3. The differential capacitance of each finger is proportional to the overlapping area between the fixed outer plates and the moving finger, and the displacement of the moving finger. In order to reduce noise and increase resolution, a large differential capacitance is needed (Weinberg, 1999).

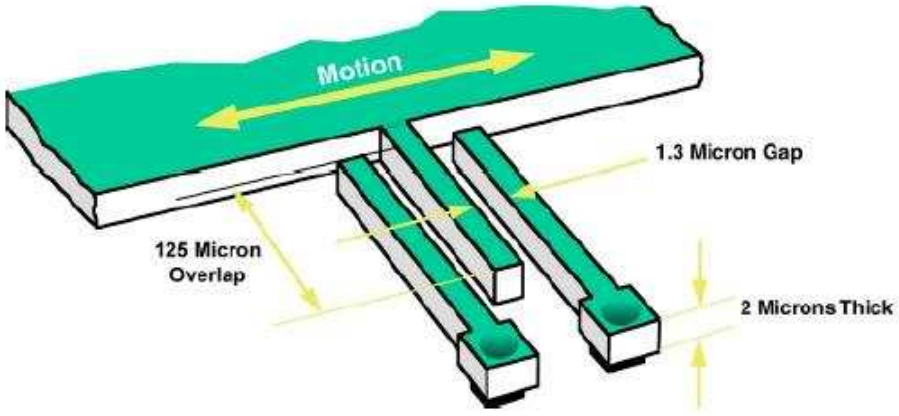

Figure 2.3 Beam Dimensions for a Single Finger (Weinberg, 1999).

The height of the capacitor finger is fixed at 2 micron by the process technology, while the length of beam overlap (125 micron) is adjustable to certain extent. However, longer fingers are harder to manufacture and increase the beam size which increases the cost (Weinberg, 1999).

The movement of the beam is controlled by the polysilicon springs holding the beam as shown in Figure 2.4. These springs and the beam's mass obey Newton's Second Law, F = *m a* (Where, F is force, m is mass, and a is acceleration), and the deflection (*x*) of a restraining spring obeys Hooke's Law and is proportional to the applied force, F = *k x*. Where k is stiffness and x is the displacement caused by the force.
Thus:

$$x = \left(\frac{m}{k}\right) a \qquad \textbf{2.7}$$

According to the manufacturing process, the only two parameters that can be controlled are the spring stiffness (*k*), and mass (*m*). Reducing the spring constant is an easy way to improve beam sensitivity. The resonant frequency of the beam is proportional to the spring constant, and the accelerometer must operate at frequencies below the resonant frequency (Harris, Cyril M & Piersol, 2010) (i.e. in the flat region of the response). However, higher spring constants make for more rugged beams (higher shock survivability). If the spring constant is kept as high as possible, the only parameter left to change is mass (Weinberg, 1999).

For the ADXL202 a novel beam structure was developed, see Figure 2.4. The fingers that constitute the X and Y axis variable capacitors are integrated along the sides of a single square beam. This result is a reduction of the overall sensor area, yet the larger common beam mass enhances the resolution. A spring suspension system, shown in Figure 2.5, situated in the corners of the beam, was designed to minimize cross-axis sensitivity (i.e., with acceleration along one axis, any tendency toward motion or outputs in the orthogonal direction is suppressed) (Weinberg, 1999).

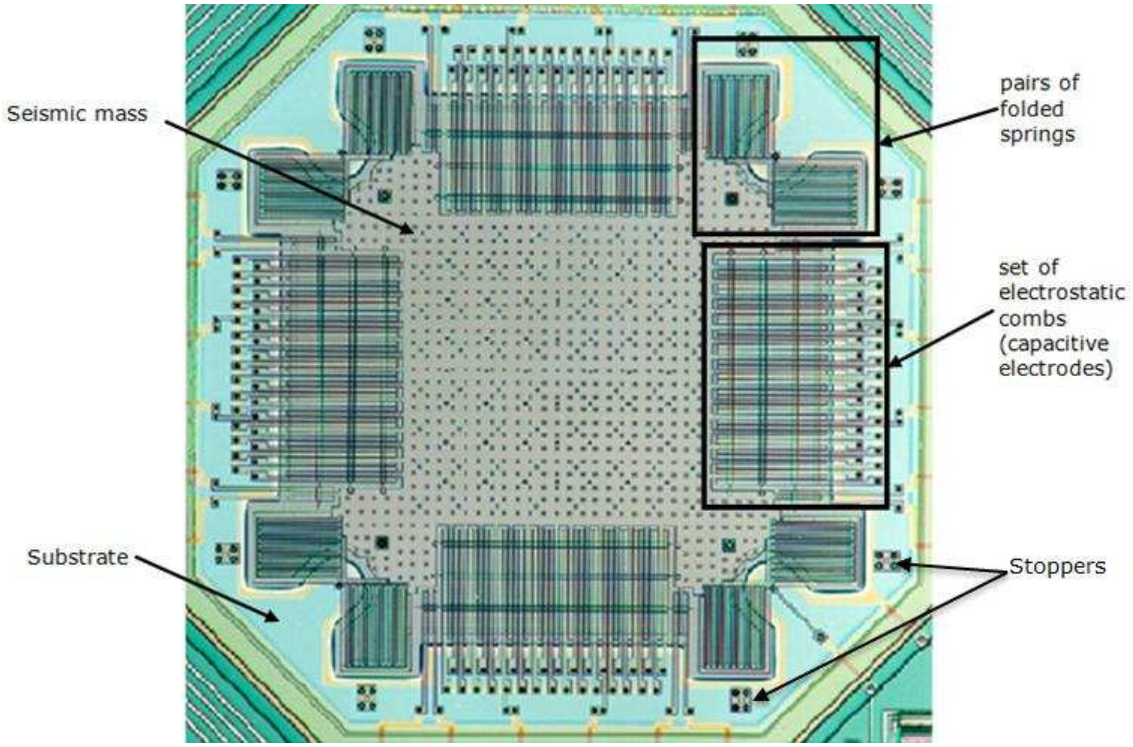

Figure 2.4 ADXL202 Beam Structure (Weinberg, 1999).

Figure 2.4 shows the stopper that connects the spring elements and the seismic mass. Its unique design prevents over travel in any one direction and helps to prevent contact of the capacitive plates.

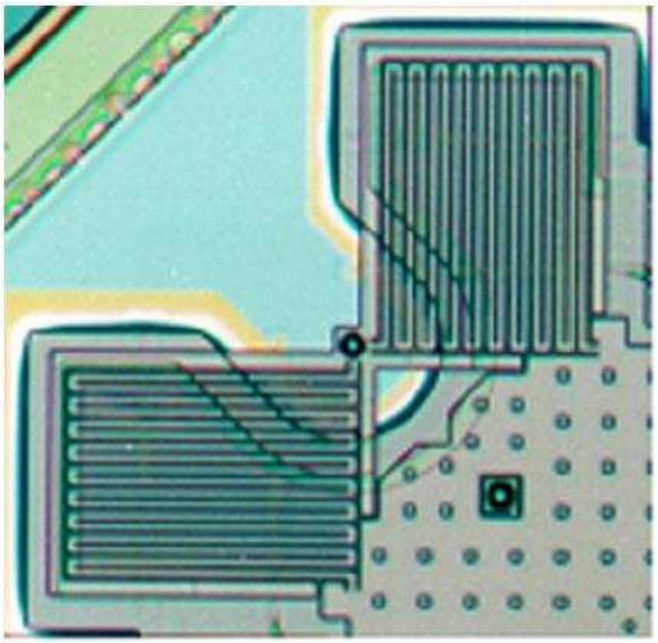

Figure 2.5 One set of folded springs of the ADXL202 accelerometer (Weinberg, 1999).

2.7.2 Theory of Operation

Figure 2.6 shows a schematic of the MEMS sensor, which illustrates the principle of operation of the dual-axis accelerometer. The tethers, or spring elements, are utilised to constrain movements of the seismic mass. According to Figure 2.6, the vertical capacitive electrodes are used to sense motions in the x-axis, and the horizontal capacitive electrodes are used to sense motions in the y-axis (Analog Devices, 2009).

The seismic mass is attached to a reference frame by four sets of spring elements, located at the four corners of the seismic mass. Each set of spring elements consists of two multi-folded springs. The folded springs are orientated in such a way that they are perpendicular to each other in order to allow motions of the seismic mass in the horizontal and vertical directions, respectively, providing dual-axis sensitivity.

The fixed outer plates are driven with square waves that are 180 degrees out of phase. When the movable fingers (and hence the beam) are centred between the fixed outer plates, both sides of the differential capacitor have equal capacitance and the AC voltage on the beam is zero. However, if the beam is displaced due to an applied acceleration, the differential capacitance will be unbalanced and an AC voltage of amplitude proportional to the displacement of the beam will result as illustrated in Figure 2.6.

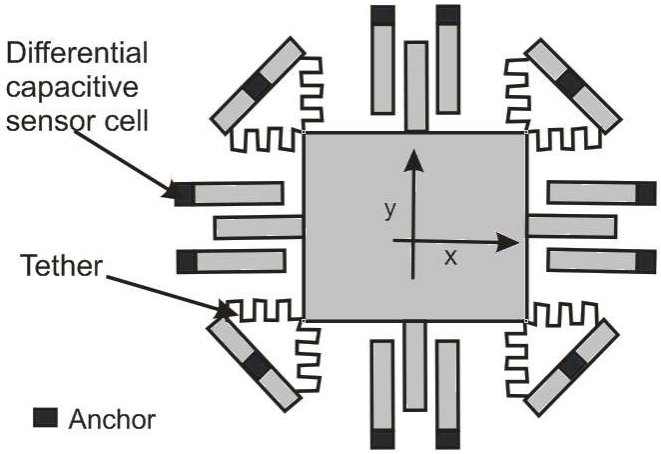

Figure 2.6 Schematic showing the principle of operation of a dual-axis accelerometer (Hsu, 2008)

The AC voltage is amplified and then demodulated by a synchronous demodulator. The output of the demodulator drives the duty cycle modulator (DCM) through a 32-kΩ resistor which incorporates external capacitors to set the bandwidth of each axis, creating a simple first-order RC low pass filter (Richey, 1999). The analogue signal is filtered and converted to a Pulse Width Modulated (PWM) signal output by the DCM. The period of the PWM output may be set from 0.5 to 10 ms, using a single resistor (R_{SET}) (Analog Devices, 2009). A 0g acceleration

produces a 50% duty cycle output. Refer to Figure 2.7 for interactions and connections between the various circuits inside the device as described above.

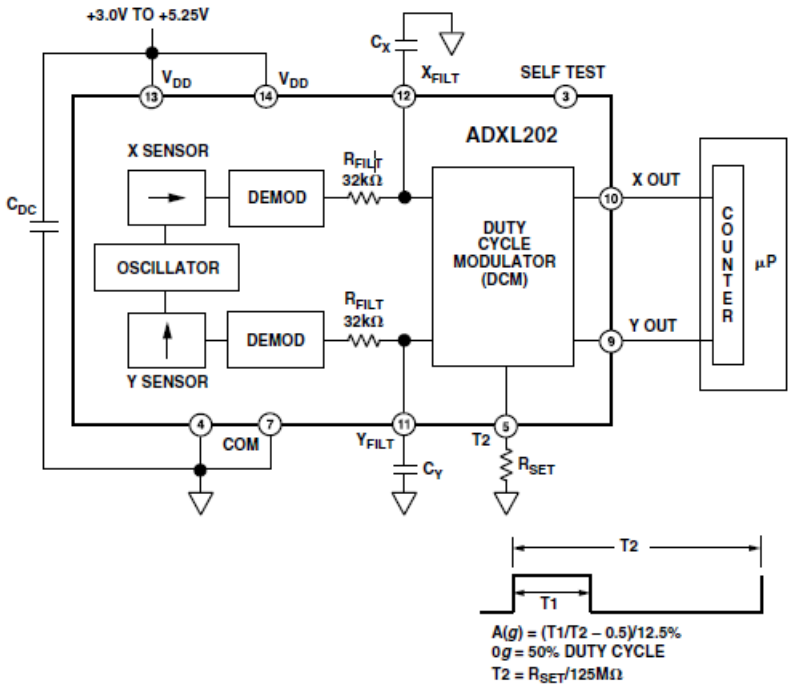

Figure 2.7 ADXL202 Circuit Architecture (Analog Devices, 2009).

2.8 Summary

The most common accelerometers for detecting rotor dynamics have been briefly presented. The principle mode of operation of accelerometers using piezoelectric crystals is based on displacement of a seismic mass with respect to the housing. The motion complies with Newton's second law.

Accelerometers based on piezoelectric, capacitive and IEPE follow the same principle as does the wireless accelerometer based on MEMS accelerometer but on a micro scale. The MEMS based on capacitive effects are characterized by low power consumption, high sensitivity, large temperature range and low noise level compared to piezoresistive accelerometers.

More effective health monitoring of dynamic components of machinery such as rotors raises the need for wireless technology. The internal structure of the ADXL202 accelerometer shows that the manufacturer can alter the spring stiffness and mass to improve beam sensitivity and hence obtain a higher resonant frequency and wider frequency bandwidth. The internal circuitry translates the structural behaviour of the accelerometer into an electrical signal that directly corresponds to the acceleration.

The design and implementation of the ADXL202-based wireless sensor are elaborated in Chapter 3.

CHAPTER THREE

Wireless Accelerometer Node Design

This chapter begins with design considerations for a low cost, low power wireless MEMS based accelerometer including circuit design of the wireless node. Then setting sensor bandwidth and centre frequency are presented. Since the output of the MEMS accelerometer is a duty cycle signal (DCS), the analysis and filtering of this type of signal is discussed. After the new wireless sensor was constructed, it was calibrated using a wired MEMS accelerometer of the same type and different one. Also, the power consumption was measured. In addition, the sensitivity of the new sensor was determined, and the frequency response is presented. In order to estimate the performance of the wireless sensor, the static and dynamic sensor characteristics were examined and the communication link was analysed. Finally, sensor noise analysis, resolution and signal to noise ratio were evaluated.

3.1 Design Consideration

Condition monitoring systems need to be reliable and miniaturised in order to increase their versatility and widen their range of application to new and different environments. MEMS inertial sensors could be used because they are low cost, lightweight, require low power, have high resolution digital output and have reliable long distance wireless data transfer (Hsu, 2008). An additional requirement is simple driving electronics. The purpose of this research is to design such a wireless MEMS inertial system to perform effective and accurate health monitoring of rotating shafts.

Accuracy of the wireless accelerometer is a function of the accuracy of both the sensor and the wireless system. The accuracy of a MEMS inertial sensor is a function of its frequency range which is a function of resonance frequency, the higher the natural frequency the greater the frequency range of the sensor (Hsu, 2008). The reliability of a wireless communication link is a function of the quality of the electronics and the transceiver Radio Frequency (RF) link.

Since the selected MEMS sensor provides a digital output, a wireless system was developed and characterised to ensure reliable long (max 900 m) distance data transfer. Digital wireless transmitter and receiver modules available are used to send and receive the acceleration data. These modules determine the transmission range of the wireless MEMS accelerometer.

3.2 Wireless Accelerometer Node Design

The wireless accelerometer used in this research was developed using MEMS accelerometer ADXL202AE (described in Section 2.7) with duty cycle output (digital output).

The off-shelf RF transmitter and receiver modules with carrier frequency of 418 MHz were used to construct a wireless data communications link. The transmitter and receiver were manufactured by LINX (Linx, 2009 R, 2009 T). These RF modules transmit and receive digital signals. The modules use a Phase Shift Keying (PSK) algorithm of digital modulation. Figure 3.1 shows the RF modules used photo, and

Table 3.1 summarizes important characteristics of the modules (Linx, 2009 R, 2009 T). The LR Series transmitter module used is ideal for the cost-effective wireless transfer of serial data, control, or command information in the range of 418 MHz band. When paired with a compatible Linx receiver, a reliable wireless link is formed, capable of transferring serial data at rates of up to 10,000 bps at distances of up to 900 m. The minimum operating DC voltage is 2.1 VDC whereas the typical is 3.0 Volt. In addition, the temperature that the module can be operated lies in the range between -40^{o} C to 70^{o} C.

Figure 3.1 RF transmitter and receiver modules(Linx, 2009 R, 2009 T).

Table 3.1 Important characteristics of the RF transmitter (Linx, 2009 T)

Carrier frequency	Data rate	Supply voltage 3V			Data range	Temperature range
		min	typical	max		
418 MHz	10,000 bps	2.1	3.0	3.6	900 m	-40°C to 70 °C

Figure 3.2 shows the block diagram of the wireless accelerometer system. The wireless sensor unit comprises the MEMS accelerometer and RF transmitter module. The received digital signal (DCS) is passed through a low pass filter to reconstruct the analogue form of the acceleration and then recorded. The digital form of the received signal is also recorded for further analysis. The recorded signal is subjected to advanced data processing algorithms for analysis, i.e. time and frequency domain analysis. In order to get a better understanding of the wireless sensor output signal, the time and frequency analysis of the DCS is presented in the following section.

Figure 3.2 Wireless sensing system block diagram.

3.3 Duty Cycle Signal (DCS)

The one DCS in one period is shown in Figure 3.3. It has a period of T and duty cycle D (50%). The value of D defines ON time as a percentage of total period of the signal, T. 100% being continuously ON. A low duty cycle is associated with low power because the power is OFF for most of its period (Bhargavi, 2011).

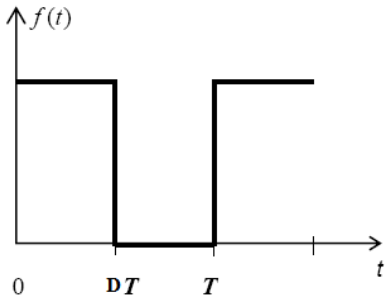

Figure 3.3 Duty cycle signal with period T and duty cycle (Bhargavi, 2011).

These signals can each be decomposed into a DC component plus a square-wave identical to the duty-cycle but with time-average amplitude of zero, see Figure 3.4.

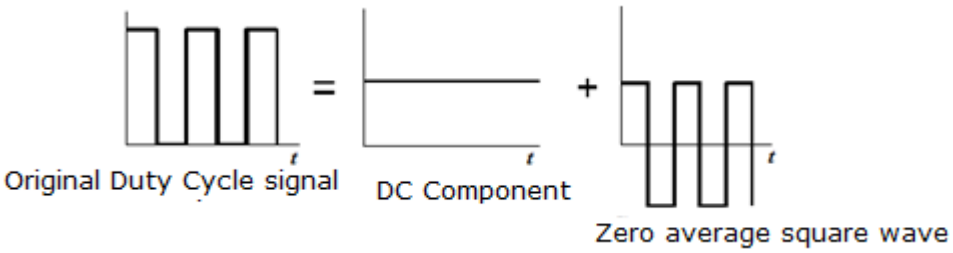

Figure 3.4 Decomposition of a Duty Cycle Signal (Bhargavi, 2011).

The DCS resolution is defined as the maximum number of pulses that can fit into a DCS period. The DCS period is defined as an arbitrarily time period in which DCS take place. It is chosen to suit specific application (Bhargavi, 2011).

3.3.1 Frequency Analysis of the DCS

The DCS is periodic signal so it can be expressed in terms of its harmonics using Fourier analysis. Figure 3.5 shows the one DCS signal time shifted to be a symmetrical function. D in Figure 3.5 denotes the duty cycle (0≤D≤100%), and T denotes the DCS period in seconds.

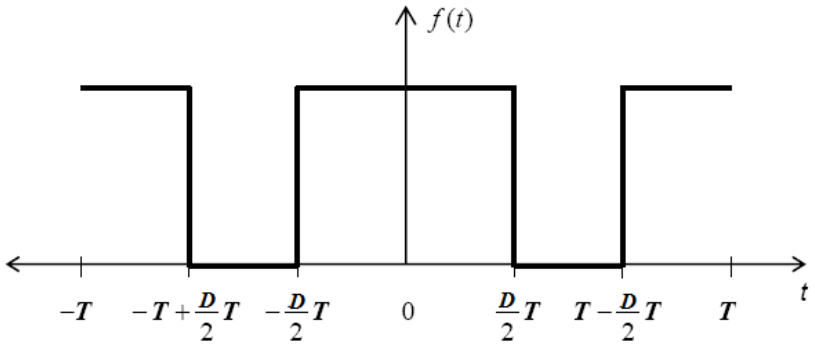

Figure 3.5 DCS time-shifted for even symmetry (Bhargavi, 2011).

The Fourier series representation of an even periodic function *f*(t) shown in Figure 3.5 can be computed as (Bhargavi, 2011):

$$f(t) = a_0 + \sum_{n=1}^{\infty} \left(a_n \cos(\frac{2n\pi t}{T}) + b_n \sin(\frac{2n\pi t}{T}) \right) \quad \textbf{3.1}$$

Where:

$$a_0 = \frac{1}{2T} \int_{-T}^{T} f(t)dt$$

$$\mathrm{a_n} = \frac{1}{\mathrm{T}} \int_{-T}^{T} f(t) \cos\left(\frac{2n\pi t}{T}\right) dt \quad \textbf{3.2}$$

$$b_n = \frac{1}{\mathrm{T}} \int_{-T}^{T} f(t) \sin\left(\frac{2n\pi t}{T}\right) dt \quad \textbf{3.3}$$

It immediately follows from Equation (3.1) that for an even function b_n has a zero value. Let K denote the amplitude of the signal *f(t)* in Figure 3.5. One obtains the following results after performing the necessary integrals in Equations (3.2):

$$a_0 = K.D$$
$$a_n = K \,.\frac{1}{n\pi}\left[sin(n\pi D) - \sin\left(2n\pi\left(1 - \frac{D}{2}\right)\right)\right] \quad b_n = 0 \quad \textbf{3.4}$$

The DC value a_0 is equal to the duty cycle signal amplitude K multiplied by the duty cycle D, i.e. the average value over the cycle. This is the value of the DC component required to reconstruct the analogue signal from the duty cycle signal. The analogue voltage is within the range of the level change in DC voltage. The values of a_n represents the amplitude of harmonic components of the duty cycle signal which exist at integer multiples of the DCS carrier frequency 1/T (Hz).

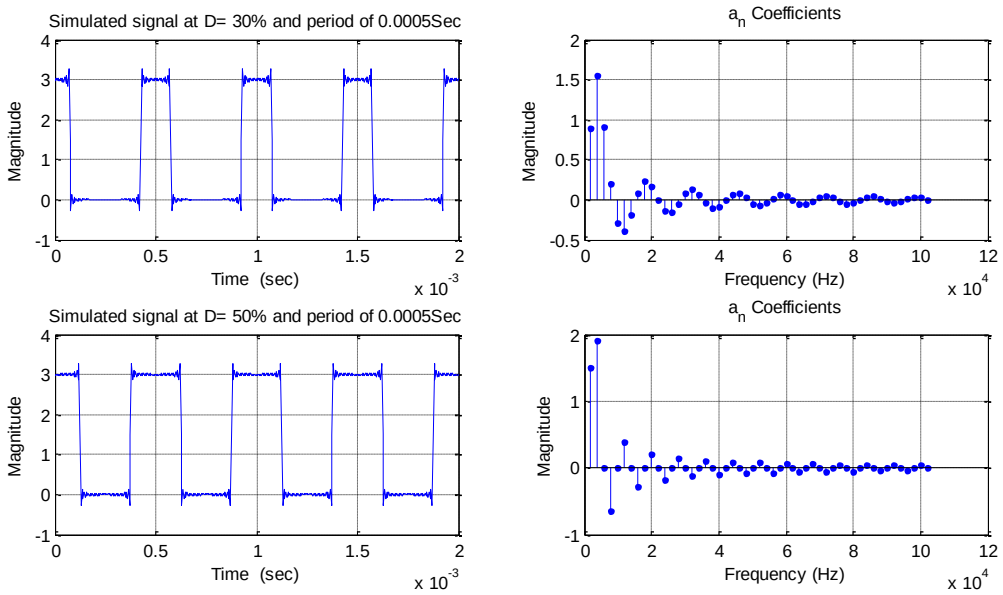

Figure 3.6 Simulation two DCS-time signals and corresponding amplitudes of harmonic components (an).

Figure 3.6 shows, in the first column, DCSs of amplitude 3 V in time domain with 30% and 50% ON time. The DCS period is 0.5 ms and is sampled every 0.005 ms, giving 100 samples over the period. A MATLAB simulation program was used to generate these signals using Equation (3.4). The second column shows 50 components of the (a_n) coefficients of the signals, i.e. amplitudes of the harmonics. The ON time has noticeable effect on the harmonics amplitudes. As the D value of the duty cycle increases so do the amplitudes of the lower harmonics. In addition, the DC shift of the analogue form of DCS signal is directly proportional to duty cycle as illustrated in Figure 3.7. By low pass filtering the DCS, the analogue form and the DC shift of the DCS signal can be obtained. This is usually known as Digital to Analogue Conversion (DAC).

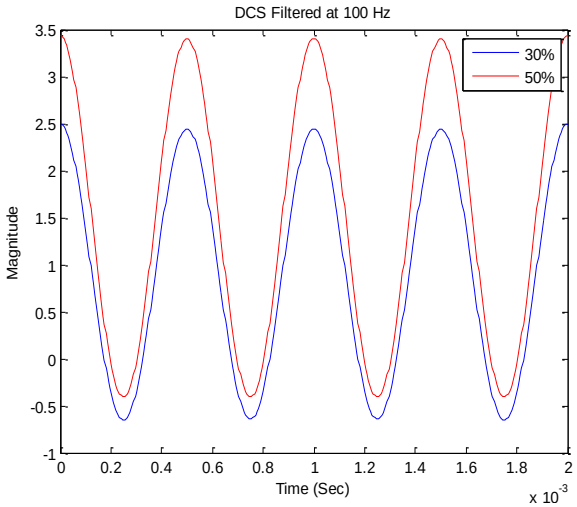

Figure 3.7 Simulation DCS-filtered with low pass at 100 Hz (DAC) for D = 30% and D= 50%.

3.3.2 Filtering Duty Cycle Signal

The easiest and cheapest way to reconstruct the analogue signal from the duty cycle is to use a low-pass filter with cut-off frequency below the carrier frequency. This filter will remove the high frequency harmonics, leaving only the DC component. In addition, the filter will allow the duty cycle to be varied at frequencies up to the cut-off frequency and reflect this variation with a corresponding voltage level change in the DC output. However, the ideal filter cannot be built, and a real filter will always allow some portion of the harmonics to pass through. This produces ripples in the desired output, as illustrated in Figure 3.8 below.

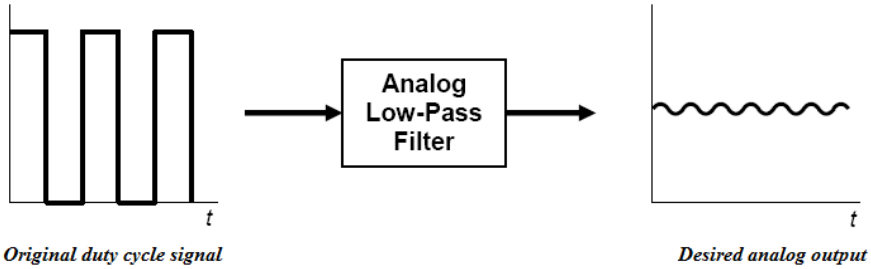

Figure 3.8 Analogue filtering of DCS signal (Bhargavi, 2011) showing ripples on the "Desired analogue output".

There are two methods to reduce these ripples. The first is to modify the analogue low-pass filter by decreasing the pass-band cut-off frequency. The second is to increase the stop-band roll-off (i.e., a higher order filter). However, these two methods have drawbacks. Increasing the stop-band roll-off generally means a more complex analogue filter circuit, and correspondingly a higher cost. Alternatively, decreasing the pass-band cut-off frequency also decreases the bandwidth. In other words, the reconstruction of the analogue signal is limited in bandwidth by the bandwidth of the analogue low-pass filter. It is clear that a trade-off between harmonic ripple and duty cycle carrier frequency is the only way to design a practical analogue low-pass filter.

3.3.3 Analogue Low-Pass Filter Design Consideration

The DCS is converted to an analogue signal using a low-pass filter. The performance of this filter heavily depends on the type of filter used. Active filters (built using op-amps) are preferred because of their no loading impedance, from which passive filters (built using resistors, inductors and capacitors) suffer. The input and output impedance can change the properties of the filter.

Two important filter properties in DCS applications are: bandwidth and the stop-band roll-off rate. The filter bandwidth is defined as the frequency at which the filter frequency response magnitude is -3 dB (Analog Devices, 2009). The effective filter bandwidth is directly related to the maximum frequency of the DCS signal. The stop-band roll-off rate is the slope of the

frequency response magnitude at high frequency. Combined with the bandwidth, the roll-off rate determines the amount of harmonic ripple that will be in the output of the filter.

3.4 Circuit Design Process

The first step in the design is to select the period of duty cycle (T_2) so that the analogue output can be reconstructed. This can be achieved by setting T_2 to <1 ms, as the accelerometer is designed to operate at duty cycle periods of between 0.5 ms and 10 ms (Analog Devices, 2009). Hence, the range over which the analogue signal can be reconstructed is between 0.5 ms and 0.9 ms.

The duty cycle period was adjusted to 0.544 ms by selecting the value of resistor R_{SET} (see Figure 2-7) to be 68 kΩ. The bandwidth of the accelerometer is set to 500 Hz by setting capacitors C_x and C_y to 0.01 µF (see Figure 2.7). According to the accelerometer data sheet provided by (Analog Devices, 2009) the calculations of duty cycle period, frequency of DCS, and the bandwidth of the accelerometer are:

$$T_2 = \frac{R_{set}}{125\ M\Omega}$$

$$T_2 = \frac{68.0\ K\Omega}{125000\ K\Omega} = 0.000544\ \text{sec} = 0.544\ \text{ms}$$

$$f = \frac{1.0}{T_2} = \frac{1.000}{0.544\ \text{ms}} = 1.838\ \text{kHz}$$

$$\text{Bandwidth} = \frac{5.0\ \mu F}{C_{(x,y)}} = \frac{5.0\ \mu F}{0.010\ \mu F} = 500\ \text{Hz}$$

The printed circuit boards (PCBs) of the wireless accelerometer and the receiver were produced using Protel from Altium Designer software. This software was chosen because the footprint of the accelerometer (ADXL202AE), the transmitter (TXM-418-LR) and the receiver (RMX-418-LR) are available from their manufacturers only in the format of this software. All these components were surface mounted.

Figure 3.9 shows the circuit diagram of the wireless accelerometer and the receiver. All the values accorded with the requirements and the specifications of the components in the data sheet. The rate at which the data is transmitted is 10 kbps.

3.4.1 Construction of the Circuit

The circuit was constructed on a PCB and evaluated in accordance with the requirements. The dimension of the final sensor shown in Figure 3.11 is 42 mm width and 45 mm length with 10 mm depth. The wireless sensor is powered by a 3.0 V Lithium coin battery embedded underneath the PCB to minimise the size of the device and possible vibration. Power analysis will be discussed in Section 3.7. Since the wireless accelerometer on the rotating rotor is

subjected to high levels of vibration, precautions were also taken to minimise possible vibration of components such as the splatch antenna. Its unique design makes it suitable for this application as well as its low cost.

3.4.2 Wireless Accelerometer Operation

The DCS signal of the accelerometer shown in Figure 3.11 is transmitted at a radio frequency of 418 MHz. This radio frequency signal is detected by the receiver module shown in Figure 3.10 and passed to the low pass filter to reconstruct the analogue signal from the DCS. Both DCS and the analogue signal from the low pass filter are fed to the data acquisition system (DAS). The signal is sampled at 96000 Hz by the DAS and the recorded data is then processed using MATLAB to obtain the acceleration signal.

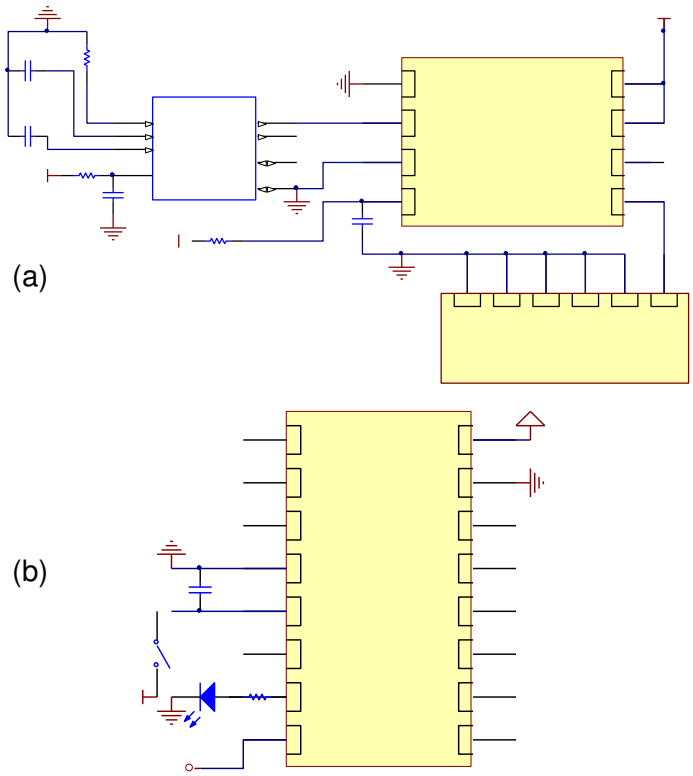

Figure 3.9 Circuit schematic designs for wireless accelerometer and receiver and their PCBs (a) Wireless accelerometer node, and (b) Receiver

Figure 3.10 Receiver module circuit

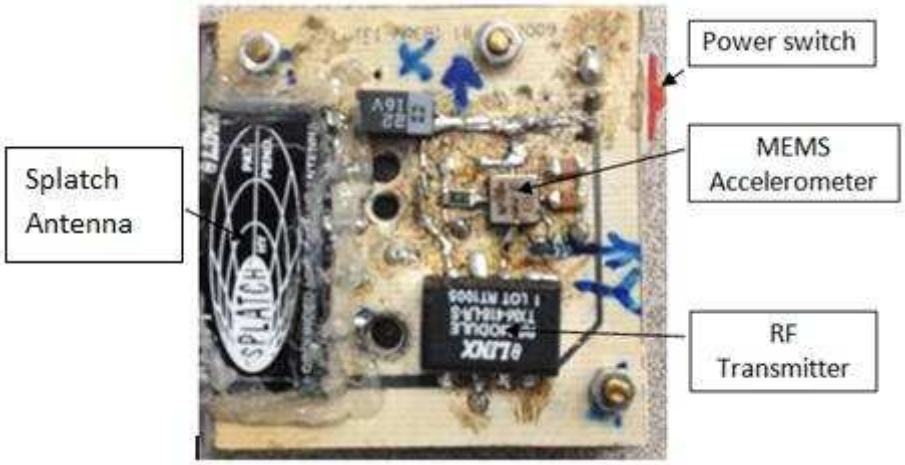

Figure 3.11 Wireless accelerometer.

3.4.3 Analogue Low-Pass Filter Design

A Sallen-Key active low pass filter was chosen to reconstruct the analogue signal from the DCS see Figure 3.12. The components were selected to match the frequency of the duty cycle (1.838 kHz calculated in Section 3.4) using equations and information from the data sheet of the accelerometer. The LM358 Dual Operational Amplifier was used. It works with dual or single range supply voltage (±1.5 V to ±16 V, 3 V to 32 V)(Texas & Instruments, 2000). The transfer function of the Sallen-Key active low pass filter is given below in Equation (3.5)(Texas Instruments, 1999):

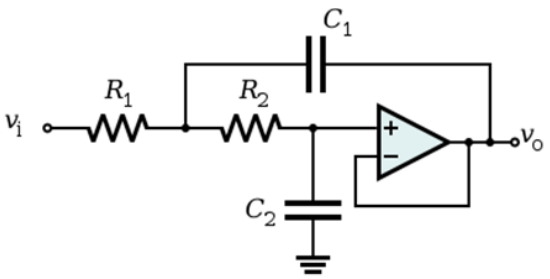

Figure 3.12 Low pass Sallen-Key circuit (Texas Instruments, 1999)

$$\mathrm{H(s)} = \frac{V_o}{V_i} = \frac{\mathrm{K}}{\mathrm{s^2(R_1R_2C_1C_2) + s\big(R_1C_1 + R_2C_1 + R_1C_2(1-K)\big) + 1}} \quad \textbf{3.5}$$

Let R_1=R_2=R and C_1=C_2=C with gain K=1

$$\Longrightarrow \qquad \mathrm{H(s)} = \frac{1}{\mathrm{s^2(R^2C^2)+s(2RC)+1}} \quad \textbf{3.6}$$

$$f_c = \frac{1}{2\pi \mathrm{RC}}$$

Using the passive components R=120 kΩ, C=10 nF, the cut-off frequency of the filter is 133 Hz. However, the value of the resistor actually used was 121 KΩ, therefore, the cut-off frequency was f_c=132 Hz.

$$\Rightarrow \qquad H(s) = \frac{1}{s^2(1.4641E-6)+s(0.00242)+1} \qquad \textbf{3.7}$$

Figure 3.13 shows the bode plot of the transfer function given in Equation (3.7) of low pass filter.

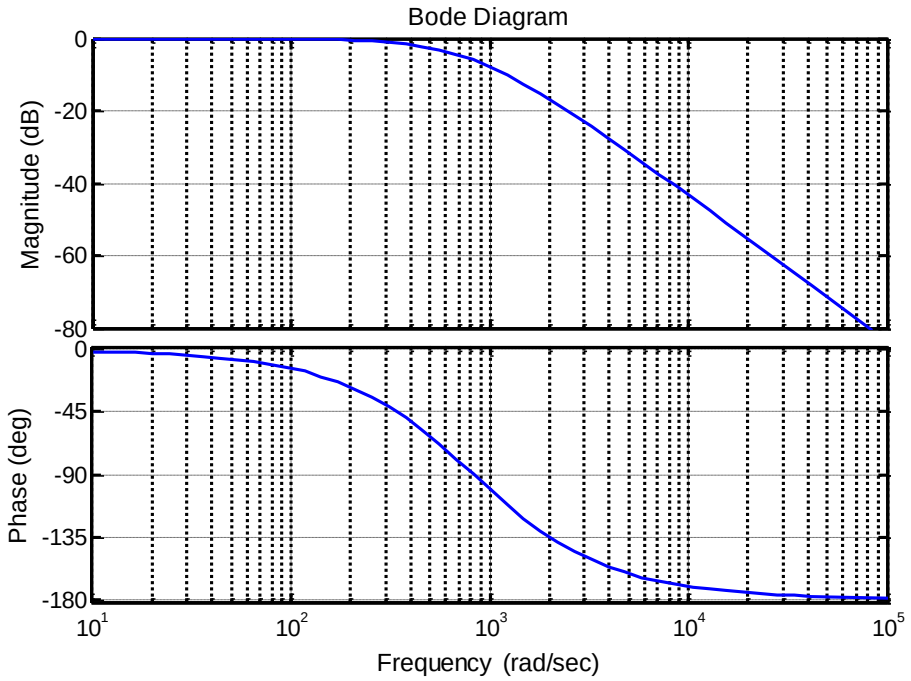

Figure 3.13 Bode diagram of transfer function (3.7)

3.5 Sensitivity of the Wireless Sensor

The static sensitivity of the wireless sensor was derived by pointing the x-axis vertically. The +1 g accelerometer output was measured (A) and then the sensor was turned 180° to measure -1 g (B). Using values of the two readings, in voltage and duty cycle, from the oscilloscope as shown in

Table 3.2 the sensitivity was determined according to Equation (3.8) (Analog Devices, 2009):

$$Sensitivity\ (S_a) = \frac{A-B}{2g} \qquad \textbf{3.8}$$

Table 3.2 Experimental static sensitivity calculation.

Characteristics	Wireless sensor (1.838 kHz)	
	Duty cycle	Analogue
At 0 g	57.2%	1.714 V
At +1g	72.8%	2.183 V
At -1g	54.5%	1.634 V

1- Using duty cycle percentage:

$$Sensitivity(S_a) = \frac{72.8\% - 54.5\%}{2g} = 9.15\%/g$$

Since the voltage supply V_{DD} =3.0 Volts

$$S_a = \frac{9.15\%}{g} \times\ 3.0\,V\ =\ 274.50\frac{mV}{g} = 27.45\frac{mV}{ms^{-2}}$$

2- Using corresponding analogue voltage;

The value of the sensitivity given in

Table **3.2** is calculated using Equation (3.9):

$$\text{Sensitivity}\ (S_a) = \frac{\Delta \text{V}}{\Delta \text{g}} \qquad \textbf{3.9}$$

$$\Delta \text{V} =\ \text{V}_{+1\text{g}}\ - \text{V}_{-1\text{g}}$$

$$S_a = \frac{\Delta \text{V}}{\Delta \text{g}} = \frac{2.183\ \text{V} - 1.634\ \text{V}}{2 \times g} = 274.50\frac{\text{mV}}{g} = 27.45\frac{mV}{ms^{-2}}$$

The sensitivity determined by Equations (3.8) and (3.9) gives the same results. the measurements resolution will be discussed in Section (4.3.1).

3.6 Wireless Sensor Power Consumption Analysis

The wireless sensor relies on the power supplied from a 3.0 V battery. The power consumption of the main components of the sensor was analysed to determine how much power is needed to keep the sensor functioning. Table 3.3 lists the power consumption of the main components of the wireless accelerometer taken from their datasheets (Analog Devices, 2009; Linx, 2009 T).

Table 3.3 Power consumption of main components of the wireless accelerometer.

Component	Power supply	Power consumption
MEMS Accelerometer	3.0 Volt 0.6 mA (Typical) 1.0 mA (Max.)	1.8 mW (nominal) 3.0 mW (Max.)
Transmitter TXM-418-LR	3.0 Volt 3.4 mA Power down current= 5.0 nA	Operational power=10.2 mW Power down power= 15.0 nW
Total	~0.6mA (Typical) ~4.4 mA (Max)	~12.0 mW (Nominal) ~13.0 mW (Max.)
Battery	3.0 volt 190 mA (Max.)	570 mW (Max.)

To maintain satisfactory operation of the wireless accelerometer node, it is necessary to establish the minimum power required (2.7 Volt). Without the drop-off resistors of the MEMS accelerometer and the transmitter module, the 3.0 V battery will provide the required power supply, but over time the battery will degrade and the voltage will drop below the minimum voltage required to keep the accelerometer functioning. Therefore, an ON/Off-switch is used to save the power when the accelerometer not in use. Table 3.4 shows the minimum limits for major components of the wireless accelerometer.

Table 3.4 Operating power of wireless accelerometer node.

Component	Operating power (VDC)		
	Min	Typical	maximum
ADXL202	2.7	3	5.25
RF Transmitter	2.1	3	3.6

The power supply of the receiver determines the amplitude of DCS signal. Thus, the receiver is connected to a constant 5 VDC power supply.

3.7 Wireless Accelerometer Operation Considerations

There are many factors that might contribute to the performance of the sensor, not least the vibration the sensor will experience during its operation when mounted directly on a rotating shaft. To reduce the effect of vibration some measures were considered. All soldered components were checked to eliminate loose or weak contacts. Special attention was paid to the antenna as it is prone to vibrate. Thus, the antenna was soldered and glued on all sides to ensure it could not vibrate during the dynamic tests. Also, the power switch was tested carefully to avoid it becoming loose during the experiments. As stated earlier, the battery was placed underneath the PCB to ensure tightness of fit and to prevent any loss of contact during the dynamic tests.

3.8 Calibration Procedures

Generally the manufacturers follow the International code ISO/16063-21 (Iso/16063-21, 2003) which gives the guidelines for the calibration of vibration by comparison to a reference transducer. The calibration procedure adopted generally uses a sinusoidal vibration generator (shaker) with varying frequency and amplitude. A well-calibrated comparison accelerometer is usually used to characterise the measured responses of the accelerometer to be calibrated.

In general, accelerometer calibration procedures use the following types of signal measurements (Sinha, Jyoti K., 2005):

(a) Periodic signal-sinusoidal or/and swept-sine,

(b) Random,

(c) Impulsive.

The random and impulsive vibrations are not suitable for our purpose because the acceleration intended to measure has no impulsive and random vibrations. Hence, the shaker will be used in its periodic mode. Measurement of the relative accuracy of the sinusoidal response accuracy satisfies the specified calibration procedure. This calibration procedure is important for wireless sensor accuracy evaluation and also to reduce the degree of uncertainty of measurements.

3.8.1 Test Setup

Figure 3.14 shows the main apparatus of the test configuration used to carry out the comparison between the MEMS wireless accelerometer and a calibrated conventional accelerometer (reference accelerometer). The test setup consists of the following:

1. Electro-dynamic shaker (JZK-51-SHAKER),
2. Power amplifier for the shaker,
3. Signal generator,
4. SINOCERA data acquisition system,
5. A computer with Data acquisition control software (YE7600), see Section 5.4.
6. DC power supply for the reference accelerometer.
7. Reference accelerometer (wired MEMS)

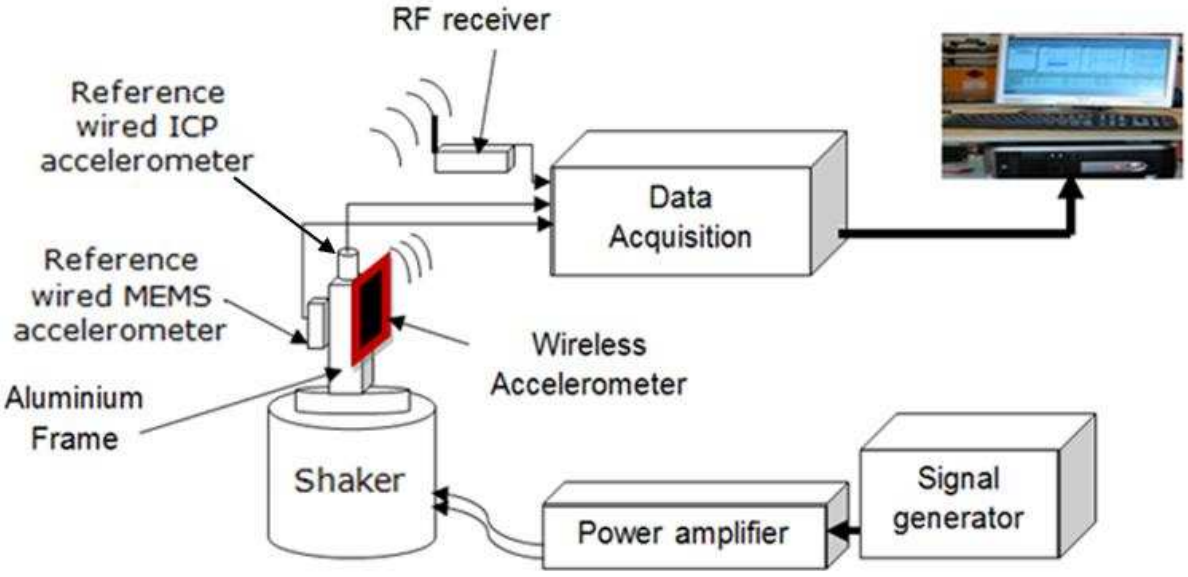

Figure 3.14 Test rig configuration

The Electro-dynamic shaker, model JZK-51-SHAKER, has a wide frequency range from 10 Hz-2 KHz, Maximum force output is 500 N, and maximum acceleration in the sinusoidal mode is 410 m/s^2. Its maximum peak to peak displacement is -7.5 mm to +7.5 mm. The Power amplifier (LDS PAE shaker power Amplifier PA25E) is a linear amplifier used to drive the

electro-dynamic shaker. It accepts any type of input wave shape over a frequency range of 10 Hz-10 kHz. It exhibits low distortion over its frequency range and operates with a wide variety of load impedances. A FeedBack function generator was been used as the sweep function generator.

The data acquisition module (SINOCERA YE6232B) is a high-performance USB device. It has 24-bit A/D parallel data acquisition system. It also has a Voltage/IEPE input; 16 channel, built-in programmable gain amplifier and real-time digital filters.

3.8.2 Test Rig Configuration

The test setup configuration is shown in Figure 3.14; which shows how the apparatus was connected. The excitation generated by the signal generator is fed into the power amplifier where it is amplified and applied to the shaker. A sinusoidal excitation signal of different frequencies with fixed amplitude was used. The amplitude was set to 1g, since the wireless sensor range is ±2g. The range of frequency was selected between 10 Hz to 120 Hz which cover the dynamic of the test.

The accelerometers were mounted back to back on the aluminium frame. The output from the reference accelerometer was connected directly to the data acquisition system while the output from the wireless accelerometer was connected through the low pass filter where the accelerometer DCS output was filtered. The output waveforms from both accelerometers were displayed on a computer screen before recording. Finally, the voltage signals from the accelerometers were recorded using the data acquisition system. Then the generation of the time domain and the frequency domain of the signals were processed using MATLAB.

3.8.3 Test Methodology

The methodology was based on applying the same excitation to both the wireless accelerometer and the reference accelerometer so that they experienced identical motion on the shaker. The input to the shaker was driven by a sinusoidal excitation signal of different frequencies and fixed amplitude. These signals were amplified before being fed to the shaker. The responses from both of the accelerometers were recorded. The signal from the wired accelerometer was used as a reference for frequency and amplitude levels. The analogue voltage output of the accelerometers was converted into digital signals by the data acquisition which was connected into the PC where the acquired signals were displayed using a data acquisition program created in SINOCERA software. The program also converted the vibration signals from time domain to frequency domain using a Fast Fourier Transformation (FFT) technique, and the acquired signals were then displayed on the front panel in time and frequency domains.

3.8.4 Frequency Response

The frequency response of the wireless accelerometer was compared with the reference accelerometer with known frequency response. The accelerometers outputs acquired were:

1- Wireless accelerometer DCS filtered at 100 Hz has sensitivity 40 mV/ms^{-2} (under the test).
2- Wired ICP Accelerometer (Integrated Circuit Piezoelectric Serial Number 00016) has sensitivity 5.106 mV/ms^{-2} (Reference 1).
3- MEMS wired accelerometer has sensitivity 34.8 mV/ms^{-2} (Reference 2).
4- Wireless DCS (unfiltered version of wireless accelerometer output).
   Both wired sensors were used as reference to the wireless sensor

All the three sensors are mounted on the aluminium rectangular frame. The wireless accelerometer is mounted on one side and wired MEMS accelerometer on the other side of the frame while the ICP accelerometer is mounted on the top of the same frame as shown in Figure 3.14. The sensitivity difference is taken into account in the analysis.

The outputs of the three accelerometers were then recorded using data acquisition with sampling rate of 96000 Hz. The accelerometers' bandwidth was determined and the signal outputs with respect to different vibration frequencies were recorded. The maximum signal frequency response was plotted using MATLAB code as shown in Figure 3.15. It is clear from Figure 3.15 the amplitude response of the wireless accelerometer is less than the other two accelerometers. The wireless signal is filtered at 40 Hz and it is clear that the amplitude output decreases above 100 Hz. The other accelerometers have higher bandwidth (500 Hz) which is reflected on their higher amplitude response. For all three accelerometers at low frequencies, below 10 Hz, the amplitude response is much lower than in the range 10-40 Hz.

Figure 3.16 (top) shows the first harmonic 1X of each sensor. The curves show much the same trends as the maximum signal response.

Figure 3.16 (bottom) shows the difference between the wireless accelerometer and the MEMS wired accelerometer relative to the ICP wired accelerometer. The wired MEMS accelerometer has a closer response to the reference accelerometer whereas the wireless accelerometer has significant differences.

To compensate for difference between wired and wireless accelerometers, a modified wireless response was generated as shown in Figure 3.17. This modified response was found using MATLAB functions as follows:

1- The difference between the wireless and reference accelerometer was determined at each frequency.
2- The coefficients of the polynomial p of the difference determined in step 1 were obtained using MATLAB function *Polyfit*.

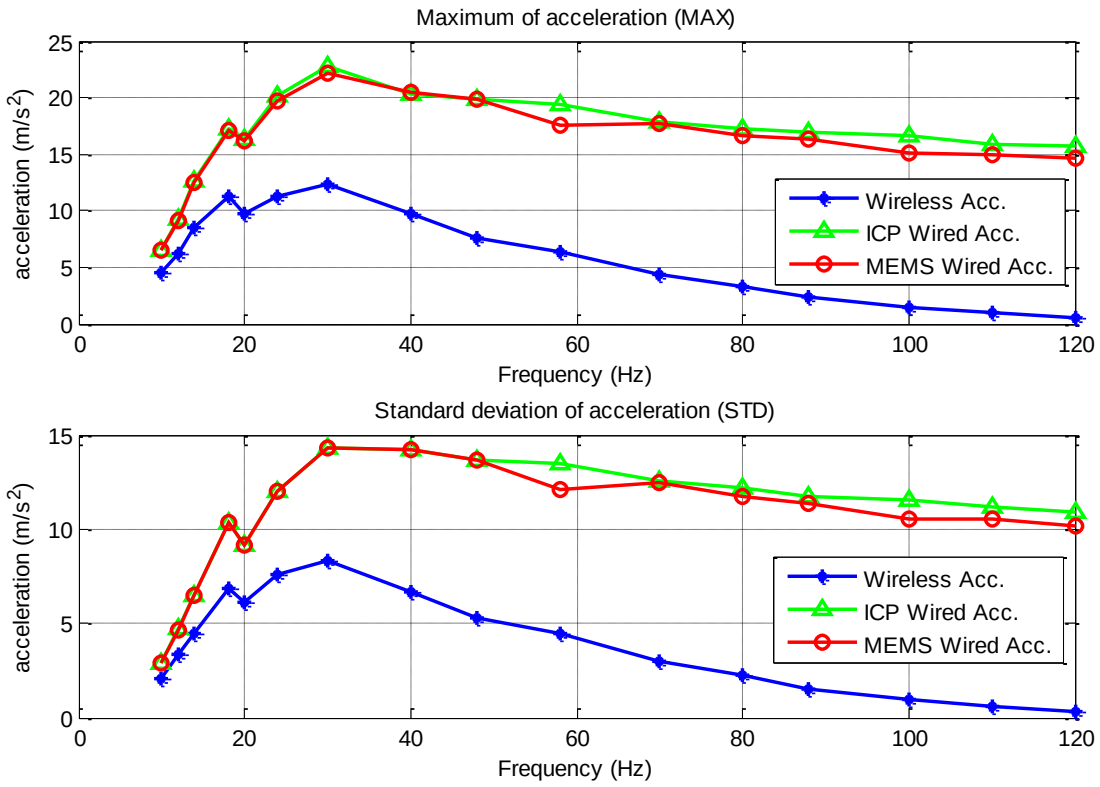

Figure 3.15 Accelerometers amplitude frequency response and its standard deviations

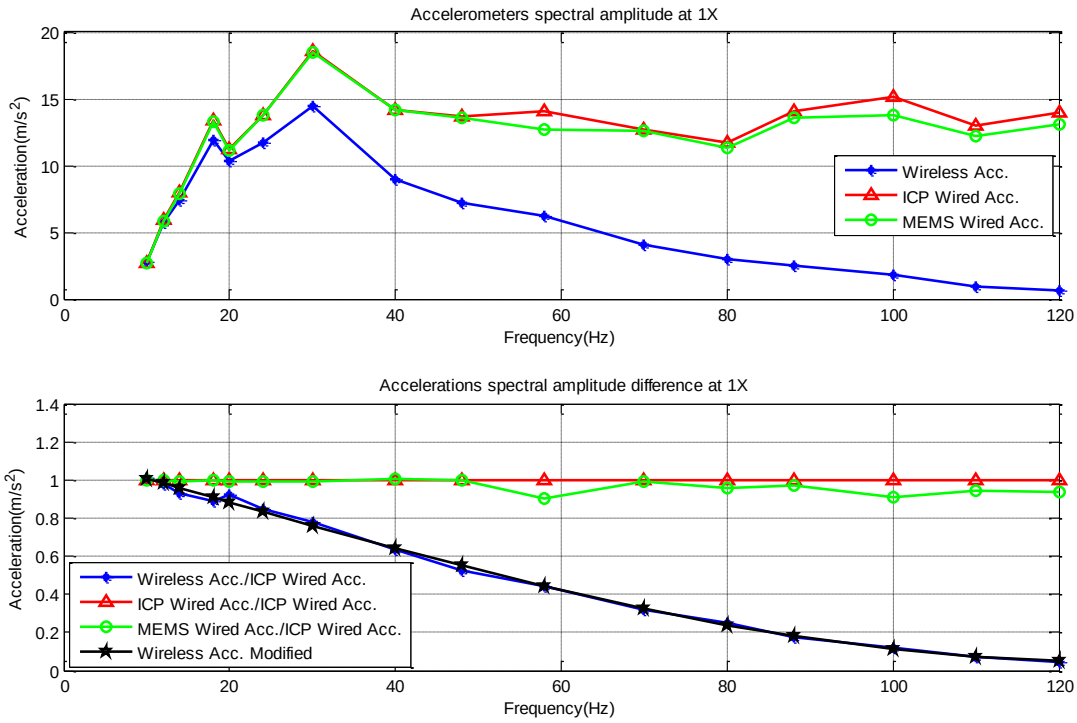

Figure 3.16 Accelerometers amplitude frequency response

$$p(x) = p_1 x^n + p_2 x^{n-1} + p_3 x^{n-2} \ldots . p_n x + p_{n+1} \quad \textbf{3.10}$$

The elements of p obtained were the polynomial coefficients for descending powers of x: $p_1, p_2, \ldots, p_{n+1}$

3- By evaluating the coefficients obtained in step 2, the values of a polynomial of degree 3 were evaluated at frequency of interest (x) using MatLab function Polyvalue.

$$y = p_1 x^n + p_2 x^{n-1} + p_3 x^{n-2} \ldots . p_n x + p_{n+1} \quad \textbf{3.11}$$

The y value represents the acceleration for each frequency x. Figure 3.16 shows the modified wireless values determined by using Equation 3.11 at various frequencies using the following P values vector:

$$P = [0.0000 \quad -0.0000 \quad -0.0122 \quad 1.1310]$$

4- The values of the polynomial obtained in step 3 were used to modify the response of the wireless sensor to approximate more closely to the reference accelerometer reading as shown in Figure 3.17. The values were then saved to a file to be used in the later rotor dynamics investigations. The modified frequency response was used in the experiments and investigations throughout this research.

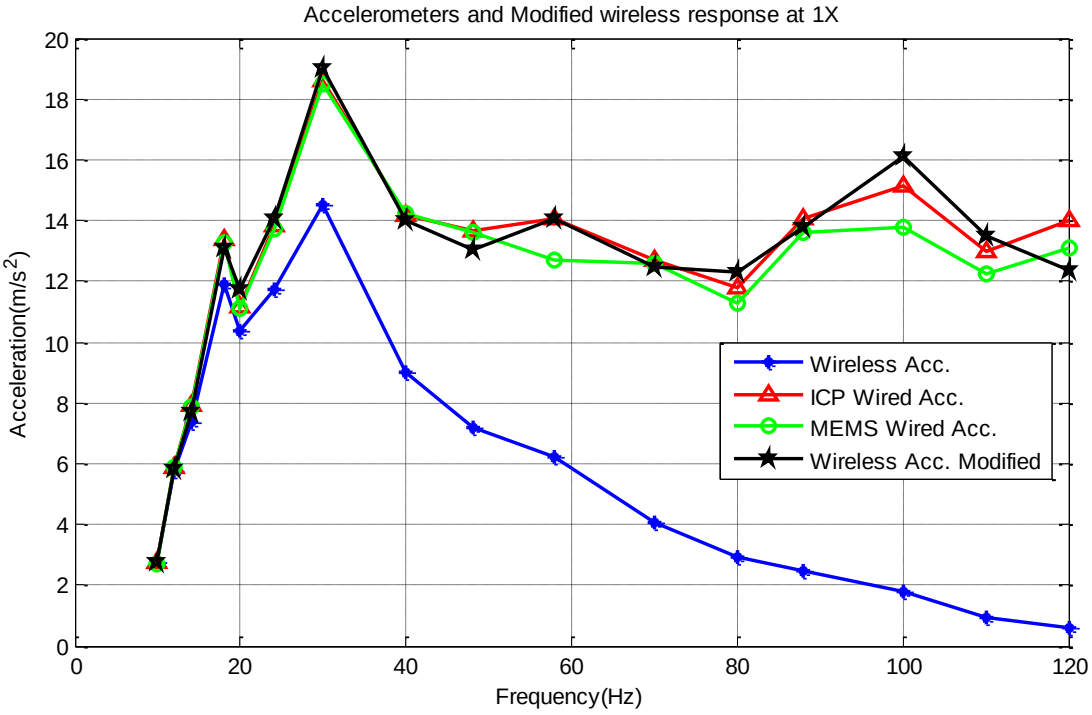

Figure 3.17 Acceleration amplitude modified response of wireless accelerometer at 1X

3.9 Frequency Transfer Function (FTF)

To better understand the frequency response of the wireless sensor, the frequency transfer function needed to be obtained. To determine the frequency transfer function, LMS analysis system was used. This system used a well-known transfer function accelerometer as reference. Both the reference and the wireless sensors were mounted on the aluminium frame on the JZK-51 model shaker.

The frequency of the driving signal was swept from zero to 512 Hz with resolution 0.5 Hz, and the two responses were recorded. The vibration signal was amplified using the LDS power amplifier. Three consecutive measurements were taken. The acquisition parameters were: bandwidth: 512 Hz, spectral line: 1024 (FFT), resolution: 0.5 Hz, average time (the duration of each reading): 10 s.

Figure 3.18 shows the output FTF of the wireless sensor (+ve direction of sensitivity) obtained from the LMS system. The cut-off frequency used in this experiment was 512 Hz. The figure shows that the wireless sensor at frequencies below 10 Hz, had a very poor response. Moreover, the response of the wireless sensor obtained from the LMS system demonstrated a very similar trend to that shown Figure 3.17. The measurements from the wireless sensor according to the FTF could be used for effectively measuring tangential vibration, over the range of interest. In addition, the repeatability of the wireless sensor measurements indicated that the responses were reproducible, see Figure 3.18. In addition, the response shows an overshoot at 75 Hz which is caused by the system resonance.

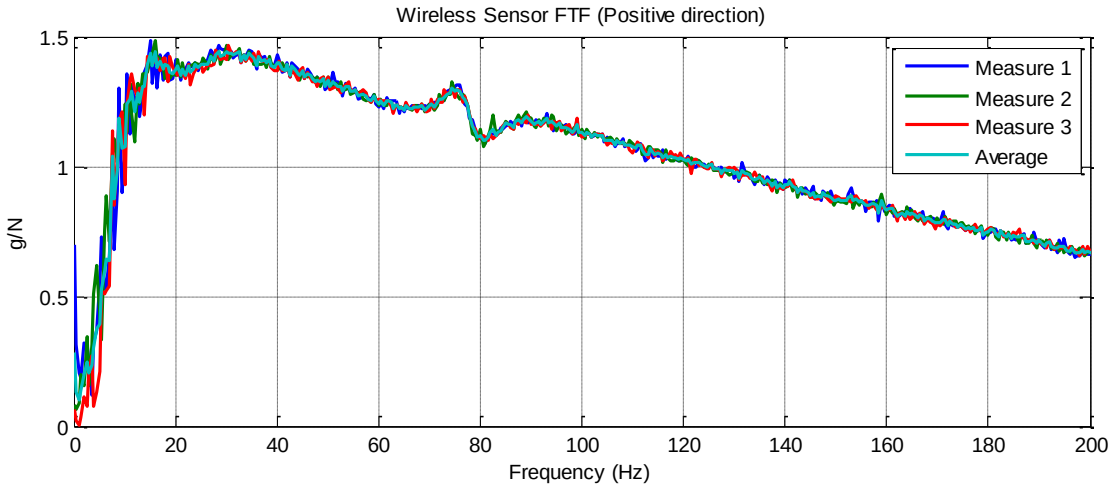

Figure 3.18 FTF of wireless accelerometer (+ve sensitivity direction)

Figure 3.19 shows the output FTF of the wireless sensor (-ve direction of sensitivity) obtained from the LMS system. Compared with that of positive direction, it is clear that the magnitude of the ripple on the plot is lower for sensor sensitivity in the –ve direction. Below about 10 Hz, the magnitude of the ripples is substantial. On the other hand for the sensor in the -ve

direction the trend is smoother with no disturbance in the range 20-65 Hz. However, repeatability in the +ve direction for wireless sensor measurements are not as clear as in the -ve direction. Moreover, the response in the negative direction also has overshooting but shifted to approximately 73 Hz. From both FTF, both directions can be used within the range of interest (10-60 Hz).

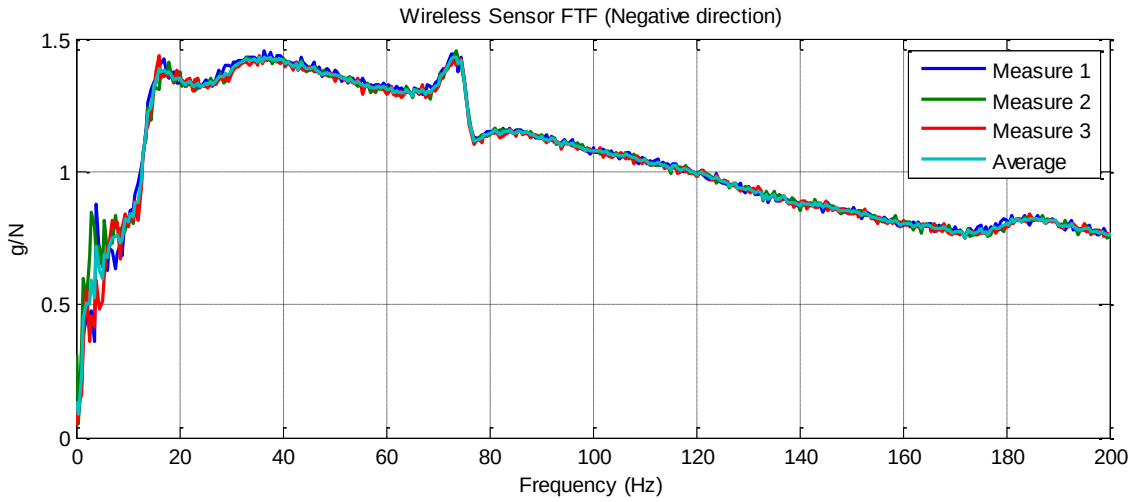

Figure 3.19 FTF of wireless accelerometer (-ve sensitivity direction)

3.10 Wireless Accelerometer on Rotor Analytical Analysis

The conventional wired accelerometers are usually mounted on the housing of bearings to measure vibration(Iso10816-3, 2009). The scheme proposed in this research was to mount the wireless accelerometer directly on the rotating shaft and a metallic holder was designed to mount and hold the accelerometer on the shaft. The wireless sensor was mounted tangentially with respect to the rotor, see Figure 3.20. The axis of maximum sensitivity of the sensor is also supposed to be tangential. The sensor is placed in such a position (Tangentially) to minimise the effects of centripetal acceleration ($a_c=r\omega^2$) which could adversely affect sensor operation. Errors possible due to misalignment of the mounting of the wireless accelerometer are now considered.

Figure 3.20 shows one possible error that affects the output of the wireless sensor. It shows the sensor axis is misaligned by an angle β and is not normal to the centripetal force. To understand the consequent effect, an analytical representation is carried out.

Any change in angular speed of the shaft will produce a tangential acceleration, thus the tangential acceleration is a function in the IAS and at constant angular speed will be zero. Even though this acceleration will be very small compared to the centripetal acceleration the IAS can, theoretically, be derived from the measured tangential acceleration and confirmed by measuring the actual IAS. From Figure 3.20 the acceleration acting in the axis of sensitivity of the mis-aligned wireless accelerometer can be derived as:

$$a_s = -gcos(\omega t)cos(\beta) + a_t\cos(\beta) - a_c\sin(\beta) \quad \textbf{3.12}$$

Where;

a_s : Wireless sensor effective output acceleration

a_t : Tangential acceleration

a_c : Centripetal acceleration

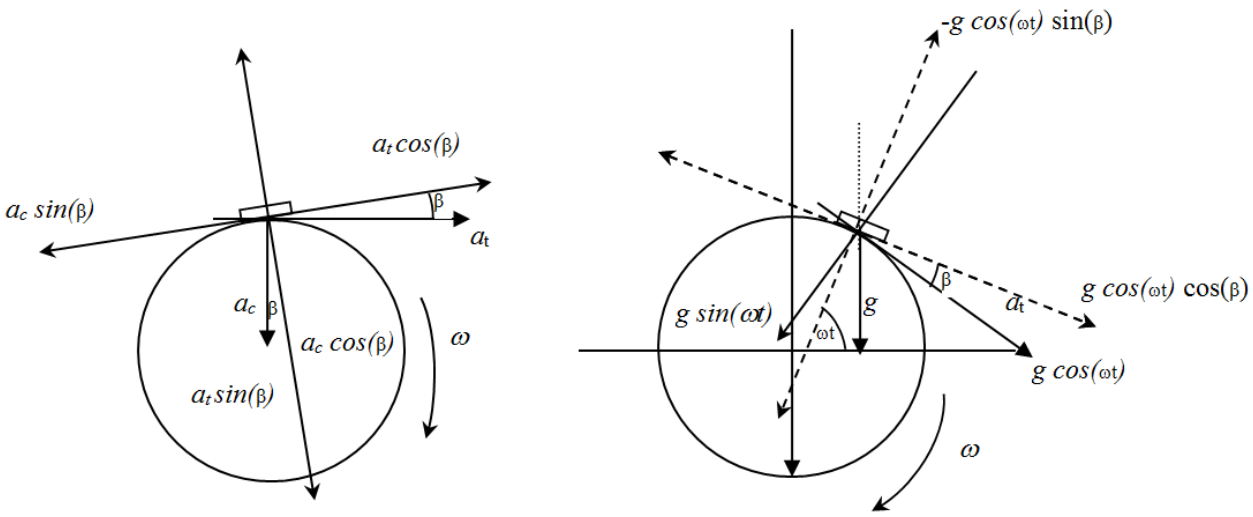

Figure 3.20 Mis-aligned sensor on the rotor

Assuming that the instantaneous angular speed fluctuations ($\bar{\omega}$) of the rotor can be written as sinusoidal waveform with amplitude A rad/sec and initial constant phase of α:

$$\bar{\omega} = Asin(\omega t + \alpha) \quad \textbf{3.13}$$

Where, ω is the average angular speed of the rotor; Thus, the tangential acceleration due to change in the IAS can be given by:

$$a_t = r\frac{d\bar{\omega}}{dt} = rA\omega cos(\omega t + \alpha) \quad \textbf{3.14}$$

Where, $\frac{d\bar{\omega}}{dt}$ is the Instantaneous Angular Acceleration (IAA); The centripetal acceleration can be derived as:

$$a_c = r(\omega + \bar{\omega})^2 = r\big(\omega + Asin(\omega t + \alpha)\big)^2 \quad \textbf{3.15}$$

By substituting Equations (3.14) and (3.15) in Equation (3.12), the accelerations acting on the axis of sensitivity equation is derived below.

$$a_s = -gcos(\omega t)cos(\beta) + [rA\omega cos(\omega t + \alpha)]\cos(\beta) - \Big[r\big(\omega + Asin(\omega t + \alpha)\big)^2\Big]\sin(\beta)$$

$$a_s = \big[\big(rA\omega cos(\omega t + \alpha)\big) - gcos(\omega t)\big]cos(\beta) - \Big[r\big(\omega + Asin(\omega t + \alpha)\big)^2\Big]\sin(\beta) \quad \textbf{3.16}$$

Using the derived accelerations acting in sensitivity axis Equation (3.17) a simulation program was implemented. The results show that any change in the value of angle of inclination β will affect the sensor output. The above analysis is based on the sensor positive axis of sensitivity. Figure 3.21 show the tangential and centripetal accelerations, and acceleration predicted by the wireless sensor at β=0°. It shows that in such a position the wireless sensor will read tangential acceleration modified by the gravity component from the sensor. Despite high value of the centripetal acceleration, having the sensor axis accurately tangential eliminates its effect.

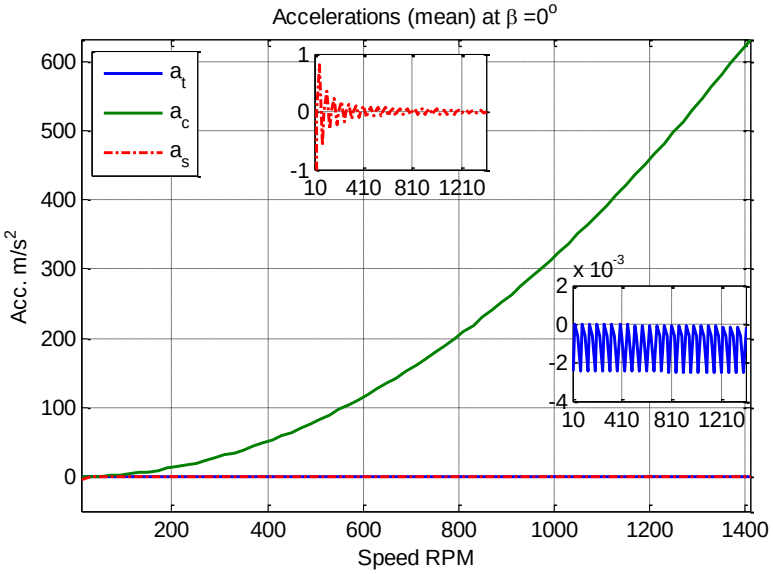

Figure 3.21 Mean of estimated accelerations (tangential, centripetal, wireless sensor) at β=0°

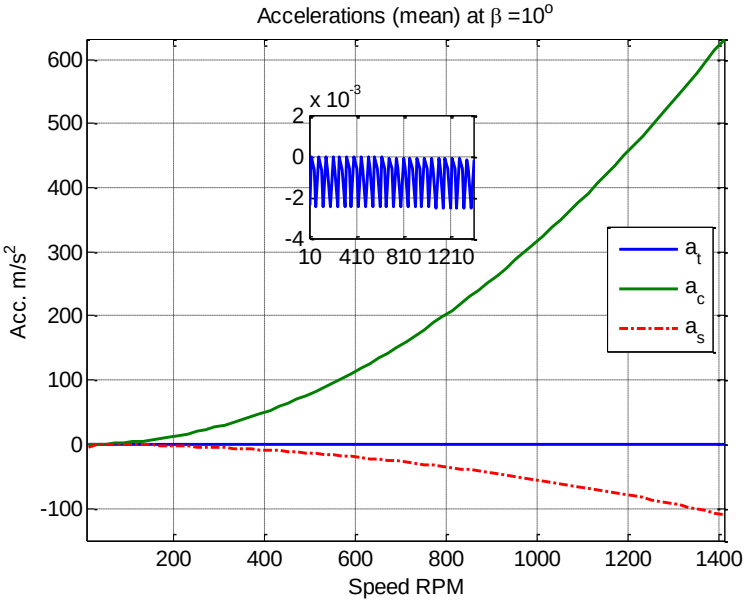

Figure 3.22 Mean of estimated accelerations (tangential, centripetal, wireless sensor) at β=10°

Figure 3.22 and Figure 3.23 show the accelerations where β is set to 10° and -10° respectively. It can be seen that the mean DC value is decreased at β=10° and increased at β=-10°. Thus it is seen that both angles affect the sensitivity of the sensor output. From this simulation, increase and decrease in the DC value of the sensor output can be achieved, and will be confirmed experimentally in Section 3.12.

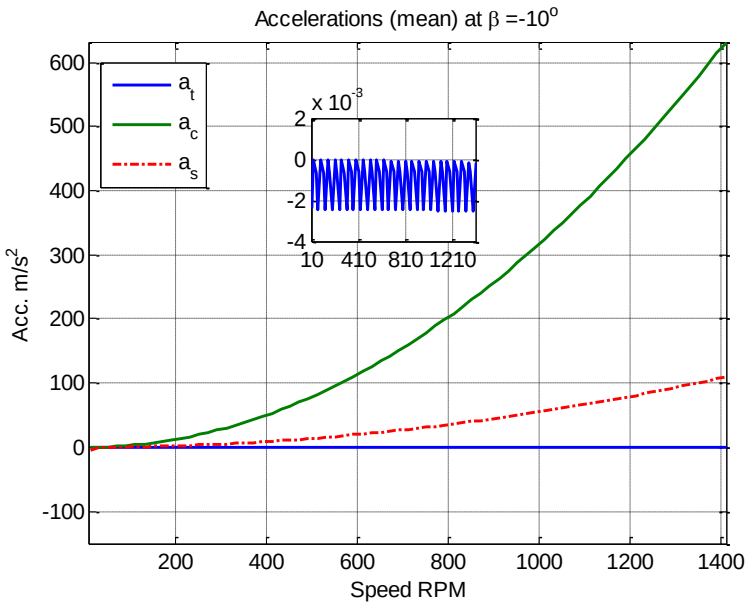

Figure 3.23 Mean of estimated accelerations (tangential, centripetal, wireless sensor) at β=-10°

The other possible error in mounting the sensor on the rotor is where the centre of the sensor is moved tangentially as shown in Figure 3.24. In such a position the accelerometer is not perpendicular to the centripetal acceleration. Analytically, Equation (3.17) was derived from Figure 3.24 and shows the effect of centripetal acceleration on the sensor reading.

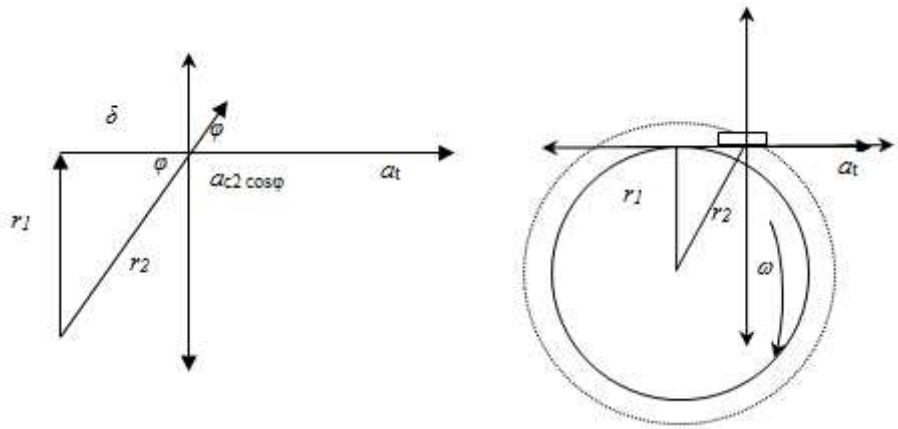

Figure 3.24 Wireless accelerometer not perpendicular to the centripetal acceleration

According to Figure 3.24, the accelerations acting on the sensitivity axis of the sensor excluding gravitational acceleration can be derived as follows:

The centripetal acceleration $a_c = r\bar{\omega}^2$

$$a_{c1} = r_1\bar{\omega}^2, \qquad a_{c2} = r_2\bar{\omega}^2$$
$$a_{c1} = \frac{a_{c1}\, r_2}{r_1}, \quad cos\varphi = \frac{\delta}{r_2}$$

$$a_s = a_{c2}cos\varphi + a_t\ ,\ a_s = a_{c2}\frac{\delta}{r_2} + a_t \qquad \textbf{3.17}$$

Obviously, if $\delta = 0$ → r1=r2, $a_s \approx a_t$ and hence the sensor will read the tangential acceleration. However, if $\delta \neq 0$ then the wireless sensor will not read the tangential acceleration due to the effect of the centripetal acceleration. Thus, measures should be taken to confirm that the sensor is installed in the tangential position. The accuracy of the installation is found by running the test rig at full speed with crystal clear perception of the acceleration signal from the wireless sensor. This operation guarantees that the wireless sensor in the tangential direction and the centripetal acceleration nullified.

3.11 Dynamic Characteristics of Wireless Sensor on the Rotor

The dynamics of a rotating shaft is very complex. The different effects which play major roles in machinery vibration include residual unbalance, misalignment, bent rotor, etc., and are being studied by, amongst others, (Hariharan, V., Srinivasan, & Engg, 2009; Huer & Zhaojian, 2010; Jalan & Mohanty, 2009; Lees, A. W., 2007 (a); Qi, He, Li, Zi, & Chen, 2008; Redmond, I., 2010; Tejas, H. Patel & Ashish, K. Darpe, 2009; Tejas, H. Patel & Ashish, K. Darpe, 2009). These effects will affect sensor readings. Thus, the wireless sensor was subjected to dynamic tests to determine how different effects affected the readings.

Figure 3.25 shows the different angular positions that the wireless sensor was mounted to check its response. The reference angle is 0^o at which the highest DC value was achieved. The direction of angular shift with respect to 0^o is opposite to the shaft rotation. At each angular position, the wireless sensor DC response is determined. The aim of this experiment is to find the wireless response at different angular position around the monitored rotor. The next section will explain the experimental procedure and the results.

3.11.1 Test Procedure

The wireless sensor is fixed on metal holder (Hose Clip) shown in Figure 3.26. The weight of the sensor and holder was 58 g. The wireless accelerometer was mounted directly on the shaft in the tangential direction using metal holder. Also the angle of inclination β is adjusted in positive direction ($+5^o$) according to theory presented in Section 3.11. The position of the

sensor at which high DC achieved was marked as a reference. The test rig was run at different speeds and the sensor readings taken. Then the angular position (see Figure 3.25) of the sensor was changed and same procedure followed. This experiment was repeated by sequentially placing the sensor at different angular positions. The results showed that each angular position of the sensor on the rotor had different characteristics see Figure 3.27. It shows decreasing trend of the DC.

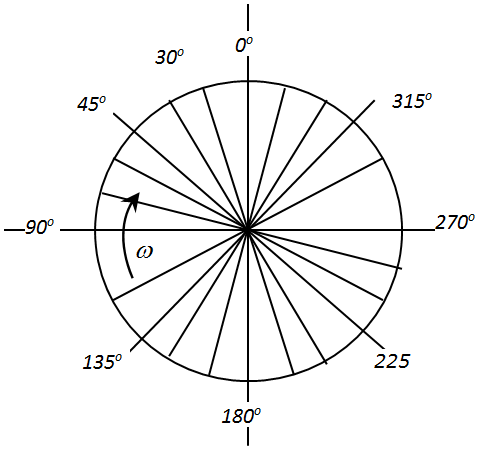

Figure 3.25 Wireless accelerometer suggested angular positions on the shaft.

By changing the inclination angle β in negative direction (-5°), the experiment results show an increase trend of DC as illustrated in Figure 3.28. The discussion of the results obtained will be presented in the following section.

$$U_{58g} = 58 \times 10^{-3} kg \times 15 \times 10^{-3} m = 870 \times 10^{-6} kg.m$$

$$U_{58g} = 870 \times 10^{-6} kg.m \times (148.7)^2 = 19.24\ N$$

Where: (148.7 rad/s) is the maximum rotor speed

Figure 3.26 Wireless accelerometer (a) Fixed on metal holder (b) Mounted on shaft.

3.11.2 Results and Discussion

According to the analytical analysis discussed earlier, the two possible sensor inclinations: increasing DC and decreasing DC were tested. Firstly, with decreasing DC, the different angular placements were tested. Figure 3.27 shows the DC values of the wireless sensor with respect to different angular placements at different speeds. It is clear that at an angle of 0^{o} the highest DC value is observed whereas at 250^{o} showed the lowest values. Figure 3.25 shows how angles were determined. In addition, the sensor angular position on the rotor determines the characteristics of that position of the rotor. Furthermore, the unbalance force imposed by the sensor and holder mass will contribute to the change in the measured acceleration (refer to Figure 3.26). Consequently, the correct angular position can be found from this chart which is the position that gives the signal of greatest DC value.

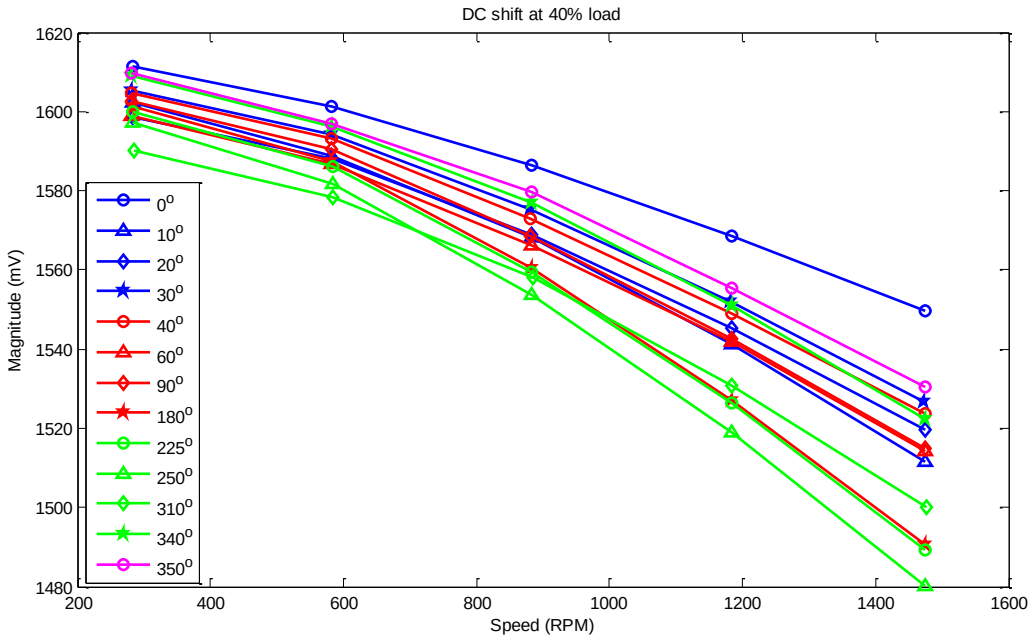

Figure 3.27 Wireless sensor with inclination angle (β=5°) with different angular placement and speed, DC case.

Secondly, with increasing DC, the different angular placements were tested. Figure 3.28 shows the DC values of the wireless sensor with respect to different angular placement at different speeds. The angular placement of 120^{0} has the highest DC values whereas at 30^{0} showed the lowest values. In addition, it is clear that the sensor angular position on the rotor significantly affects the measured dynamic characteristics of the rotor due to the unbalance added by the wireless sensor and holder mass as explained earlier. Consequently, the proper angular position can be found from this chart. In this case, the angular placement at 120^{o} the right position since wireless sensor can read the highest DC values at high speed. The possible factor that affects the measurement is the geometric centre of rotor mass (residual rotor unbalance and sensor holder mass contribution) which can cause this phenomenon. Depending

on the position of the sensor relative to that point the measurement will change accordingly. The wireless sensor and its holder mass (58g) add to the residual rotor unbalance at different positions made such observation of the sensor output.

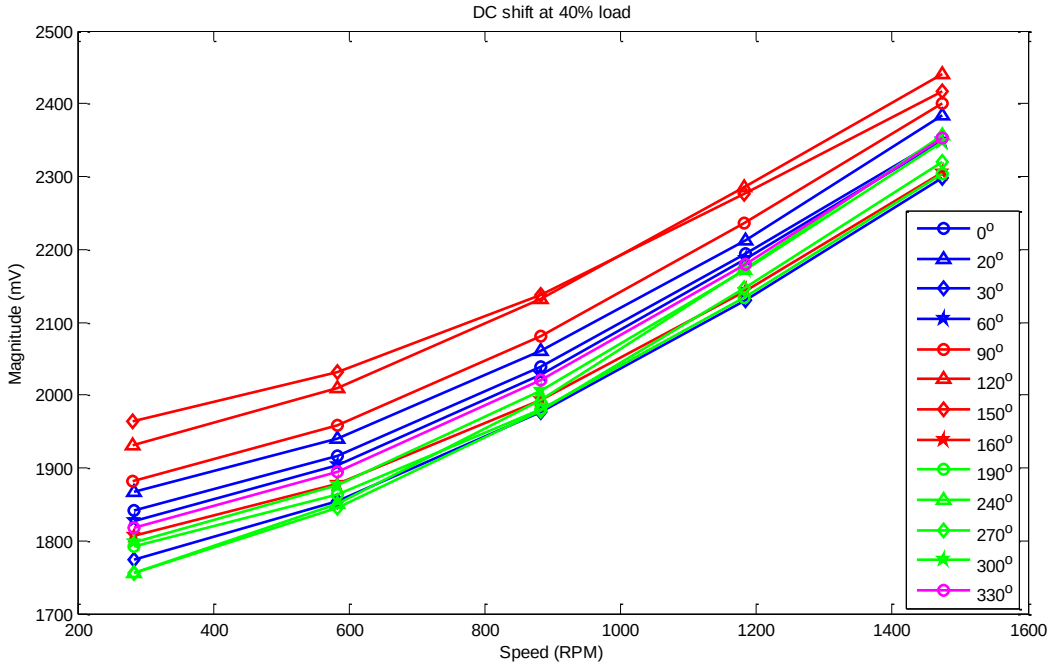

Figure 3.28 Wireless sensor decreasing with different angular placement, DC case.

3.12 Transmission Link Analysis

3.12.1 Module Description

The TXM-418-LR transmitter is a low-cost, high-performance synthesised ASK / OOK (Amplitude shift keying / On-off keying) transmitter, capable of sending serial data at up to 10,000 bps. The transmitter is completely self-contained, requiring only an antenna as additional RF component. When combined with an LR Series receiver, a reliable serial link is formed capable of transferring data over line-of-sight distances of up to 1,000 m (Linx, 2009 T). The module's low power consumption makes it ideal for battery-powered applications. Where range is critical, the LR receiver is a good choice due to its outstanding sensitivity (Linx, 2009 R). Modulation delay is 30 nsec.

3.12.2 Antenna Type and Performance

The Splatch planner type compact antenna from Linx Technologies was chosen as suitable for this application (Linx, 2009 A). Its centre frequency is 418 MHz, and has a low voltage standing wave ratio (VSWR) of less than 1.9 at centre frequency (Linx, 2009 A). It is also

suitable for the wireless accelerometer node. Its input impedance matches the transmitter and the receiver units, and hence the communication link. The specifications given in the Linx Technologies design data sheet were followed to obtain best performance (Linx, 2009 A). As described in Section (3.4.1) the antenna was glued to the PCB to avoid any vibration that might affect the signal transmission link.

Possible errors due to transmission are negligible since the modulation delay is very small (30 nSec). Also the transmission speed is much higher than the acceleration signal bandwidth. In addition the reflection signal will not affect signal reception.

3.13 Noise Analysis

An analogue signal in terms of voltage duty cycle signal proportional to acceleration was successfully obtained from the wireless accelerometer as shown in the Figure 3.29 (a). This signal was conditioned and converted to digital using a MATLAB 7.1 code to obtain the acceleration signal in the time domain. Figure 3.29 (b) shows a noisy sample in order to demonstrate the performance of the filters used for signal conditioning.

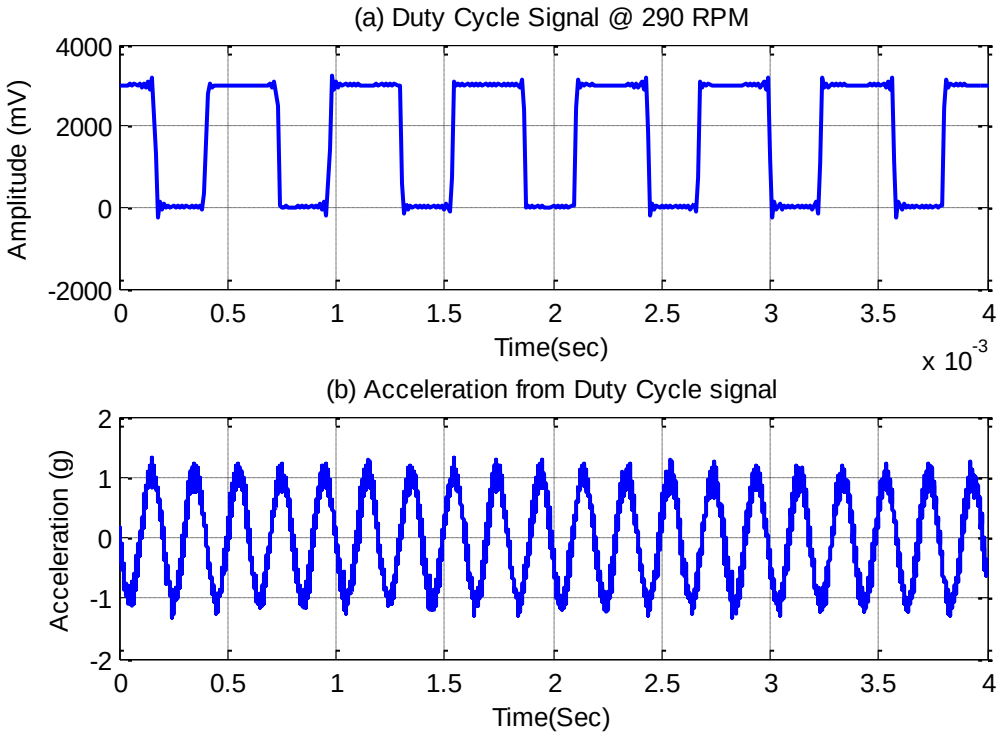

Figure 3.29 Measured acceleration in (a) Duty Cycle Signal form (b) Analogue signal form

A capacitor of 0.05 µF at the output of the accelerometer filters the signal at 100 Hz as explained in Section 3.4.3. This limits the bandwidth to 100 Hz, reducing noise. Digital filters and a Hanning window were applied to the acceleration signal in the time domain to reduce noise and spectrum leakage in the frequency domain, see Figure 3.30 (a) and (b). Then the

filtered signal was transferred to the frequency domain by means of the spectrum of the acceleration, as shown in the Figure 3.30 (b). The wireless accelerometer captures the rotor speed as shown by the large spike in Figure 3-39 (b) at 5 Hz (=290 RPM).

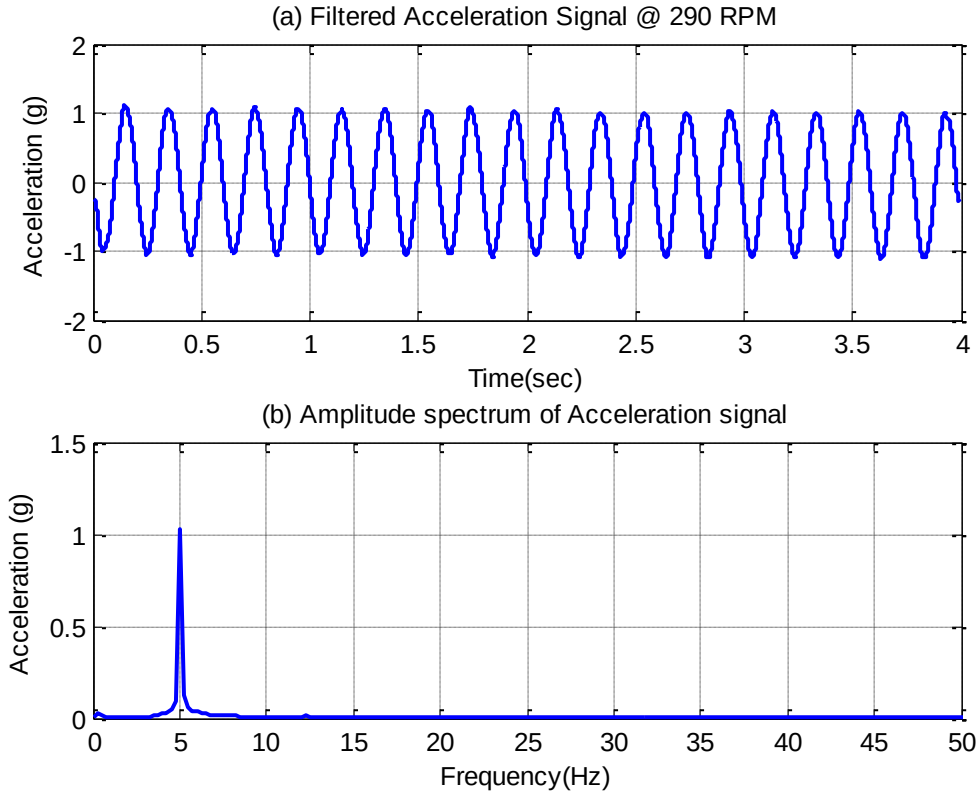

Figure 3.30 (a)Filtered Acceleration signal (b) Amplitude spectrum

3.13.1 MEMS ADXL202E Noise

With the single filtered by a filter bandwidth (*BW*) with pole roll-off characteristics, the typical noise of the ADXL202E is determined by the following equation (Analog Devices, 2009):

$$\text{Noise(RMS)} = \left(\frac{200\mu g}{\sqrt{Hz}}\right) \times \sqrt{BW \times 1.6} \qquad \textbf{3.18}$$

From Equation (3.18), noise is proportional to the square root of the bandwidth of the accelerometer. For instance, at 100 Hz the noise will be equivalent to an acceleration of 2.53 mg. Figure 3.31 show the relationship of ADXL202E noise with respect to the its bandwidth. As the bandwidth increases the noise increases.

Typical noise sources in MEMS accelerometer measurements stem from the mechanical vibration of the polysilicon springs, from the signal conditioning circuitry and from the measurement system itself (Andrejašic, 2008). The mechanical noise source is the vibration of the springs while the electrical noise source is the signal conditioning circuitry (Mohd-Yasin,

Korman, & Nagel, 2003). Spectral peaks emerge, originating from the oscillators inside the accelerometers signal conditioning circuitry (Mohd-Yasin, et al., 2003). In today's accelerometers, due to high seismic mass, the mechanical noise floor is nearly negligible compared to electrical noise, but with a proper electrical circuitry design, electrical noise floor can be reduced significantly (Mohd-Yasin, et al., 2003).

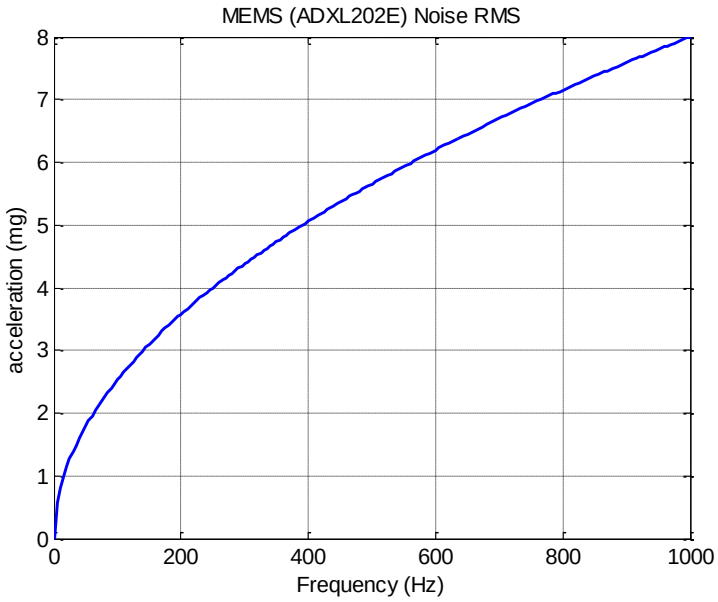

Figure 3.31 Characteristics of Wireless ADXL202E Noise RMS.

3.13.2 Wireless Accelerometer Resolution

The resolution is defined as the smallest signal change that can be detected; and it is governed by the sensitivity, i.e. the magnitude of the response for a given input and noise. It can be improved by either increasing sensitivity, or by lowering the noise (Mohd-Yasin, et al., 2003). Lowering the noise floor can be achieved by low-pass filtering the sensor output. The accelerometer bandwidth will determine the measurement resolution. Therefore, for a bandwidth of 500 Hz, the resolution of the sensor was calculated using Equation (3.19) and found to be equal to 5.7 mg/$Hz^{1/2}$.

3.13.3 Wireless Accelerometer Signal-to-Noise Ratio (SNR)

The signal to noise ratio compares the level of a desired signal to the level of noise. Equation (3.18) gives the noise (RMS) of the MEMS ADXL202 used in this research. The maximum acceleration that the sensor can measure is ±2g. Therefore, the SNR of the wireless sensor then can be computed as:

At 500 Hz bandwidth the

$$\text{Noise(RMS)} = \left(\frac{200\mu g}{\sqrt{Hz}}\right) * \sqrt{500 \times 1.6} = 5.6569\, mg \approx 5.7mg \quad \textbf{3.19}$$

$$\text{Signal to Noise ratio } (SNR) = \frac{\pm 2\text{g}}{5.7 \times 10^{-3}} = \pm 3633 \quad \textbf{3.20}$$

Which means the magnitude of the signal compared to the noise floor is very high (3633). Figure 3.32 shows the sensor signal to noise ratio in dB at different bandwidths. The red curve represents negative sensitivity axis direction while the blue one represents the positive sensitivity axis direction. It shows that the sensor has high SNR and this implies the sensor can detect small accelerations.

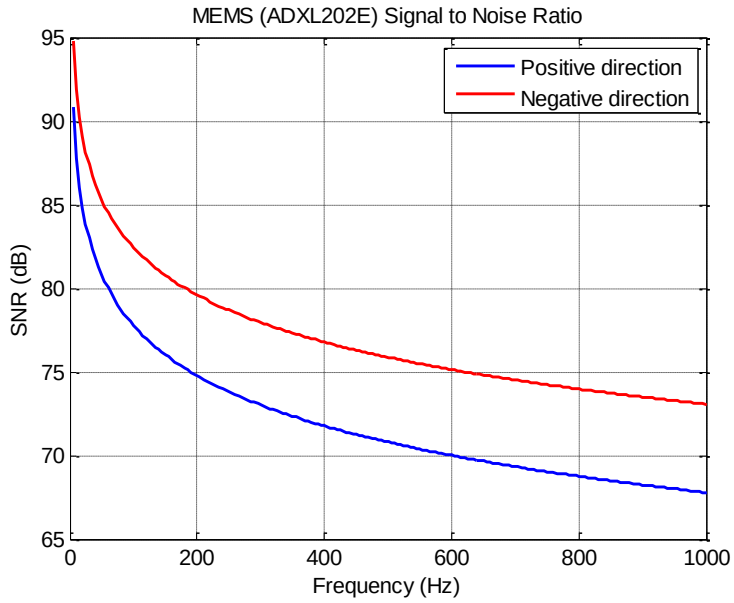

Figure 3.32 Wireless ADXL202 signal to noise ratio

3.14 Summary

In this chapter, an improved MEMS wireless accelerometer has been proposed. The improvement consists of integrating the MEMS accelerometer (ADXL202) with a wireless transmitter and receiver. The design and implementation considerations have been found that the components prone to vibration such as antenna and battery should be installed carefully. The digital output waveform of the wireless sensor (DCS) has been described. The analogue form of the acceleration is obtained through low pass filtering of the DCS signal.

The sensitivity of the wireless sensor has been obtained ($274.50\,\text{mV}/g$) and the new wireless accelerometer has been calibrated with reference to a known MEMS wired sensor. The response of wireless sensor magnitude has been found less than that of the wired sensors. Therefore, to improve the performance of the wireless sensor, its frequency response was

modified using wired sensors frequency response. This modified response will be used in next rotor dynamics investigations.

Power consumption of the wireless sensor unit has been found that the minimum voltage to keep the sensor working is 2.7 VDC. Moreover, the receiver unit should be connected to stable power supply to maintain the magnitude of the received DCS not affected by any small drop in the power of transmitter unit.

To obtain the best response from the wireless sensor, careful attention should be paid when installing the sensor on the rotating shaft. The experimental and analytical analyses show that if the sensor is not placed accurately tangential to the centre of the rotor, the centripetal acceleration will significantly affect the output reading of the sensor.

It has been shown that there are two ways that installation of the sensor can increase or decrease the DC shift of the measured acceleration. Both are achieved by changing the inclination of the sensor. When the inclination angle β is negative, the DC shift will increase with speed whereas at positive inclination angle decrease. Furthermore, the angular placement of the wireless sensor should not change once it is installed. Finally, the sensor has high signal to noise ratio (3633) for a bandwidth of 500 Hz and a resolution of 5.7 mg. All these procedures confirm the capability of the new wireless sensor to usefully detect vibration signals originating from the rotor dynamics.

CHAPTER FOUR

Instantaneous Angular speed (IAS)

This chapter begins by introducing IAS, it then briefly describes conventional angular speed transducers used for obtaining IAS. The speed measurement error equation for encoders is derived and discussed. The resolution of all sensors for IAS measurement is determined. Methods for IAS extraction from an encoder are briefly presented. Also, IAS extraction from a wireless sensor is discussed. Next, a comparison is made between the IAS obtained from the wireless sensor and other sensors. Finally, the time synchronous averaging (TSA) is applied to the signals and a new approach to IAS extraction is discussed. The IAS obtained from the wireless accelerometer after applying TSA and correction of gravitational effects is compared to IAS from other sensors.

4.1 Introduction

In practice mechanical rotating systems often rotate with varying speed. Sweeney and Randall (Sweeney & Randall, 1996) showed that a gear-based power transmission system exhibits speed fluctuations due to a combination of effects, including both geometric and transmission errors. Li, et al., (Li, Yuhua et al., 2005) have reviewed some representative angular speed measurement methods. Charles et al., (Charles, Sinha, Gu, Lidstone, & Ball, 2009) used the IAS from the main drive shaft to represent the torsional vibration of a diesel engine and introduced polar representation method for the IAS rather than an FFT-based method to discriminate between healthy and faulty cases. Ben Sasi et al., (Sasi, A. B., Payne, Gu, & Ball, 2001) used the variation in IAS to monitor electric motors. Feldman and Seibold (Feldman & Seibold, 1999) investigated the magnitude and location of damage in a rotor system using IAS (torsional vibration). These investigations have shown that IAS is useful for the condition monitoring of a wide variety of machines (Sasi, A. B., et al., 2001; Sasi , Gu, Payne , & Ball, 2004; Yang, J., Pu, Wang, Zhou, & Yan, 2001).

Rotary encoders are often used to measure the IAS. There are a variety of rotary encoders available for a wide range of applications (Resor, Trethewey, & Maynard, 2005). Many of the available encoders operate on the principle that the encoder provides an output when a tooth passes through the sensing location. The output is a pulse signal characterized by voltage level and is detected and collected by a data acquisition system. The pulses are often recorded together with time information so that the IAS of the rotary component can be determined by data processing.

Different data processing schemes may be used to obtain IAS from the pulse signals. These schemes fall into two categories: finite difference (Belanger, 1992) and inverse time (Remond, 1998). The finite difference method is used to find the average angular speed in a given time interval, which requires a large number of pulses per revolution (PPR) for accurate determination of velocities. The inverse time scheme is used to obtain the average speed between two adjacent pulses, for which a high frequency clock should be used to sample the pulse signal.

Laser-based techniques are commonly used for IAS measurement in laboratory investigations. However, because of the high cost of laser-based instrumentation, it is unlikely to be widely accepted for on-site IAS measurement for condition monitoring. Instead, much cheaper devices such as shaft encoders, magnetic pick-up sensors, etc., provide alternative means for IAS measurement. These devices produce signals in the form of an electrical pulse train. The time interval between successive pulses is inversely proportional to the speed of the rotor.

For early fault detection and diagnosis, it is necessary to measure the IAS as accurately as possible (high number of pulse per revolution encoder). Recently, Li, et al. (Li, Yuhua, et al., 2005) have addressed the influences of different sensor configurations on IAS measurement and proposed a number of basic rules for accurate IAS measurement. Usually, a higher clock counter (or a higher sampling rate) produces a higher accuracy of IAS measurement.

In contrast to previously published works, this study investigates a novel scheme for the measurement of IAS. Specifically, a wireless accelerometer mounted directly on the rotor. This technique aims to provide good measurement accuracy over a wide IAS range so that it can be applied to a wide range of condition monitoring and fault diagnosis applications.

4.2 IAS Concept

Most rotor machine components rotate at variable angular speed. This results from force variation inherent in their operation (Sweeney & Randall, 1996). Over the last few years, IAS-based condition monitoring has made a significant progress. This section focuses on the concept of IAS and the different transducers used to measure it. The average angular speed over time Δt may be defined as:

$$\omega = \frac{\Delta\theta}{\Delta t}\ (rad/sec) \qquad \textbf{4.1}$$

Where, $\Delta\theta$ is the angular displacement, and Δt is the time taken to complete the displacement.

In the limit as Δt tends to zero, the average speed approaches the instantaneous value of $\omega = d\theta/dt$. In other words, by reducing the time between consecutive measurements the measured angular speed tends to the IAS. Thus, the resolution of IAS is limited by the number of discrete points on the rotor used for the measurement. Hence, the number of pulses per revolution (PPR) determines the resolution of the IAS transducer (Sweeney & Randall, 1996).

The angular speed of the rotor is measured by several types of transducers (Kenjo & Nagamt, 1985; Staebler, 2000; Zimmerman, 2002):

1. Potentiometers,
2. Hall-effect Sensing Devices,
3. Photo Pick up Encoders, (Opto-interrupter),
4. Absolute Encoders,
5. Incremental encoder,
6. Resolvers, and
7. Laser encoders.

The ones used in this study were incremental encoder and Opto-inturrupter as reference to the new wireless sensor. The other transducers are out of scope of this thesis.

4.3 Speed Measurement Error or Resolution Analysis

Rotational speed calculation based on pulse counting is (Li, Y., et al., 2005):

$$n = \frac{60\, f_s}{M\, N_c} \tag{4.2}$$

Where

n: Shaft speed to be determined (RPM);

M: The resolution of shaft encoder, i.e. the number of pulses per revolution (PPR);

N_c: The number of base units counted at the specified clock frequency (RPM);

f_s: The clock frequency or sampling frequency (Hz).

To estimate the error due to the uncertainty of pulse counting, Equation (4.3) is a first-order Taylor expansion of Equation 4.2 with respective to N_c (Li, Y., et al., 2005);

$$\Delta n = \frac{60\, f_s}{M\, {N_c}^2}\Delta N_c = \frac{n}{N_c}\Delta N_c \tag{4.3}$$

The counting uncertainty is between N_c and $(N_c + 1)$, i.e. the maximum counting error is no more than 1, so the absolute error for the worst case occurs at $\Delta N_c = 1$;

$$\Delta n = \frac{n}{N_c}\Delta N_c = \frac{n}{N_c} \tag{4.4}$$

Considering the error at a specific rotating speed n_0, the number of base units counted can be calculated using Equation (4.2) as;

$$N_{c0} = \frac{60\, f_s}{M\ n_0} \tag{4.5}$$

The maximum error at speed n_0 is;

$$\Delta n_0 = \frac{60\, f_s}{M\, {N_{c0}}^2} = \frac{n_0}{N_{c0}} \tag{4.6}$$

Substituting Equation (4.5) into Equation (4.6) gives;

$$\Delta n_0 = \frac{60\, f_s}{M\, {N_{c0}}^2} = \frac{{n_0}^2 M}{60\, f_s} \tag{4.7}$$

Equation (4.7) shows the relationship between the maximum error and the measurement parameters.

The error calculation can be based on the estimate of the speed measurement resolution, which is defined as the possible speed difference that can be achieved by pulse counting method using a shaft encoder.

To obtain high accuracy measurement, the resolution values should be configured based on measurement system as low as possible. For condition monitoring applications, a sensor with dozens or hundreds of pulses per revolution is sufficient for most machinery monitoring and diagnosis. The determination of resolution is based on the machine operation specifications(Li, Y., et al., 2005).

In implementing speed measurement, the parameters M and f_s usually remain unchanged. However, machines may operate at different speeds, and the measurement accuracy will vary with the speed. Table 4.1 below shows how the resolution is different with operating speeds when *M* =360 PPR at f_s=100 kHz, f_s=20 MHz and when M=100 PPR at f_s =96 kHz.

Table 4.1 RPM resolution with different speeds and different sample rates

n_0 – shaft speed (RPM)	Δn_0 (RPM)- at f_s=100 kHz M=360 PPR	Δn_0 (RPM) - at f_s=20 MHz M=360 PPR	Δn_0 (RPM)- at f_s=96 kHz M=100 PPR
500	15	0.075	4.340
1000	60	0.300	17.36
1500	135	0.675	39.06
2000	240	1.200	69.44
10000	6000	30.00	1736.11

The resolution may be too poor to resolve the speed variation at a sampling rate (base clock unit) of 100 kHz whereas at low M (100 PPR) at 96 kHz, the resolution is improved than that at 360 PPR. However, a 20 MHz clock rate would be acceptable as the resolution is significantly higher (i.e. Δn is inversely proportional to the sampling rate).

4.3.1 Determination of Sensor Resolution

To better understand the capability of sensors (wireless, encoder, opto-interrupter) in capturing the IAS, the resolution of each sensor is calculated. The resolution of the encoder and opto-interrupter can be calculated assuming that they generate ideal trains of pulses and instability of the clock frequency is negligible. Thus, Equation (4.8) can be used to calculate the relative speed error ε(Li, Y., et al., 2005);

$$\varepsilon \approx \frac{\Delta n}{n} \approx \frac{1}{N_c}\Delta N_c$$

As the maximum counting error is ±1, the maximum measurement error can be rewritten as(Li, Y., et al., 2005);

$$\varepsilon = \pm \frac{n\,M}{60\,f_s} \tag{4.8}$$

Where n is the measured speed of the rotor, f_s is sampling frequency, and M the number of pulses per revolution from the sensor. Using Equation (4.8), the resolution of encoder and opto-interrupter can be calculated as (rated speed driving shaft 1420 RPM, sampling frequency 96 kHz)

- Encoder resolution;

$$\varepsilon = \frac{1420 * 100}{60 * 96000} \times \frac{2 * \pi}{60} = 0.0026\, rad/sec \tag{4.9}$$

- Opto-interrupter resolution;

$$\varepsilon = \frac{1420 * 60}{60 * 96000} \times \frac{2 * \pi}{60} = 0.0015\, rad/sec \tag{4.10}$$

- Wireless accelerometer resolution;

The RMS of accelerometer noise is determined by the following equation (Analog Devices, 2009):

$$\text{Noise(RMS)} = \left(\frac{200\mu g}{\sqrt{Hz}}\right) \times \sqrt{BW \times 1.6} \tag{4.11}$$

Since the bandwidth of the accelerometer is 500 Hz, then the noise (RMS) can be calculated as:

$$\text{Noise(RMS)} = \left(\frac{200\mu g}{\sqrt{Hz}}\right) \times \sqrt{500 \times 1.6} = 5.6569\ \text{mg} \approx 5.7\text{mg}$$

For circular motion the amplitude of tangential acceleration can be computed using;

$$a_t = r\left|\frac{d\omega}{dt}\right|$$

Assuming a_t behaves in sinusoidal form;

$$d\omega = \frac{a_t}{r}dt$$

$$\Delta\omega = \int \frac{a_t}{r}dt$$

$$\Delta\omega = \frac{a_t}{r \times 2 \times \pi \times f} \tag{4.12}$$

Hence, the wireless sensor IAS resolution at full speed can be determined using Equation (4.12)

$$\Delta\omega = \frac{5.7 \times 10^{-3} \times 9.8}{15.35 \times 10^{-3} \times 2 \times \pi \times 25} = 0.023 \text{ rad/sec}$$

The relationship between frequency and the resolution of each sensor is depicted in Figure 4.1 below:

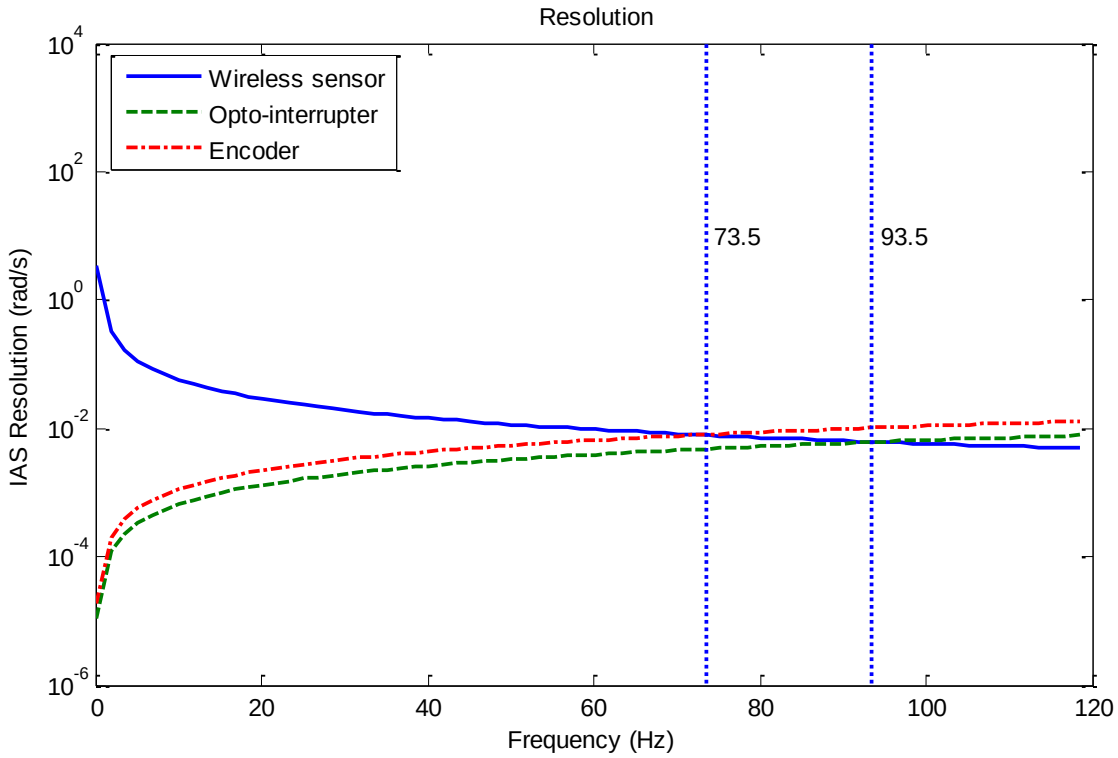

Figure 4.1 Resolution with angular speed for 96 kHz clock frequency for encoder, opto and wireless accelerometer

Figure 4.1 shows that the resolutions of sensors come close between about 75 Hz (4500 RPM) and about 95 Hz (5700 RPM). These values are well above the maximum speed of the test rig (1420 RPM). The expected results showed clear difference between the wireless sensor and the other two sensors.

4.3.2 Experimental Investigation of Resolution

The resolution of the sensor limits its accuracy. To verify the resolution of the wireless sensor for the different conditions of the shaft, the test rig was subjected to different conditions of horizontal misalignment (see Section 5.2.3). The purpose of this experiment was to test the capability of each sensor in determining the IAS for four test cases: aligned and three different degrees of shaft misalignment. Table 4.2 shows the spectral amplitudes for 2X, 3X and 4X of running speed harmonics for each of the three sensors (wireless, encoder, opto-interrupter) at different conditions.

Table 4.2 IAS spectral amplitudes for first three harmonics at different degrees of shaft parallel misalignment

Alignment case	Sensor	2X *(rad/s)*	3X *(rad/s)*	4X *(rad/s)*
High level of misalignment 1.60 mm	Encoder	1.60	0.30	0.30
	Opto	1.44	0.23	0.20
	Wireless	2.16	0.38	0.40
Medium level of misalignment 0.35 mm	Encoder	0.13	0.08	0.20
	Opto	0.24	0.09	0.07
	Wireless	0.45	0.20	0.11
Small level of misalignment 0.25 mm	Encoder	0.10	0.06	0.15
	Opto	0.08	0.06	0.04
	Wireless	0.40	0.22	0.10
Aligned (0.03 mm)	Encoder	0.20	0.09	0.10
	Opto	0.05	0.05	0.02
	Wireless	0.10	0.05	0.02

From the amplitudes of the spectral harmonics (2X, 3X and 4X) for all three sensors and referring to their resolution (see Figure 4.1, and Equations (4.9 -4.11)), it is clear that:

- At the highest level of misalignment all three sensors clearly indicate the presence of vibration fluctuations. At the medium level of misalignment the encoder appears the least reliable and the wireless sensor the most reliable for indicating vibration fluctuations. At the smallest level of misalignment the wireless sensor appears the most sensitive of the three devices. However, in the aligned case the wireless sensor, at 3X and 4X running speed, hardly captures the IAS because of the closeness of resolution of the sensor and the signal amplitude.
- The second harmonic (2X) of running speed appears the most reliable harmonic for identifying shaft speed fluctuations.
- Also, it's clear from the resolution plot (Figure 4.1) that the resolution of both encoder and opto-interrupter increases with rotational frequency nonlinearly whereas the wireless sensor resolution decreases as rotational frequency increases.

Resolution change with respect to the alignment condition is demonstrating the sensors capability for fault detection with different degrees. However, the wireless sensor results show more capability for small fault detection.

4.4 IAS Extraction

IAS extraction from the encoder (train pulse signal) is important for IAS based condition monitoring. Elapsed time uses the time interval between successive pulses (Li, Y., et al., 2005). However, an alternative is frequency domain analysis based on an FFT-based approach and using the Hilbert transform. For the wireless sensor, the extraction is achieved by integrating the acceleration signal in the frequency domain.

Extraction methods will be discussed in more detail in the following sections. A comparison between both IAS from encoder and wireless accelerometer has been developed.

4.4.1 Time-Interval Technique

To compute the variation in the speed of the shaft, the train of pulse per revolution generated by an encoder can be used.

In this approach, time intervals between pulses were measured and then the approximate IAS is calculated for a portion of the shaft revolution. In rotary incremental encoders the speed of the rotor is inversely proportional to the time interval, Δt, between successive pulses (Li, Y., et al., 2005), but the values of Δt in the train are not uniform because of the variation of the rotor speed. Thus with the time interval technique one measures the pulse duration, Δt_i, between successive pulses, (i.e. elapsed time or time span for pulse i), as shown in Figure 4.2. Computing the inverse of these time intervals gives the IAS variation waveform.

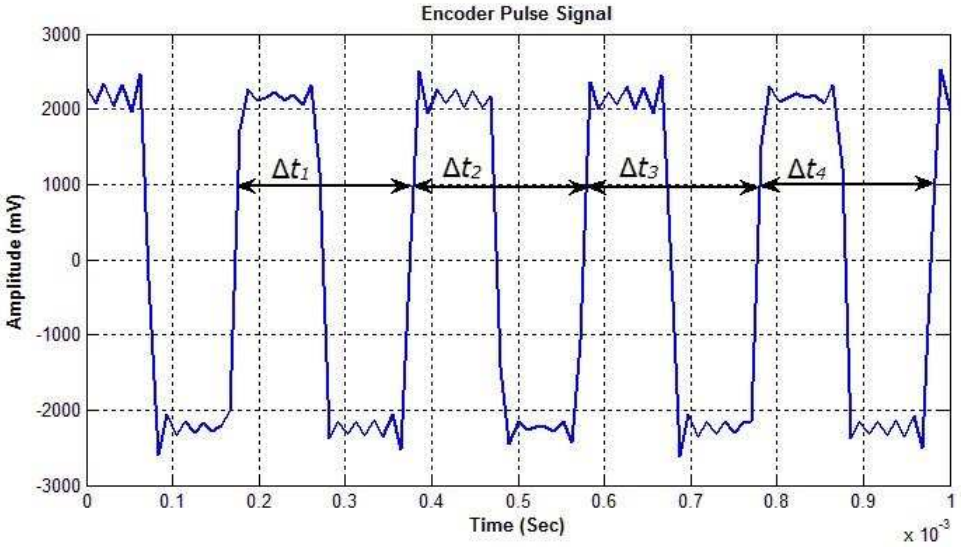

Figure 4.2 Typical signal pulses in time interval technique

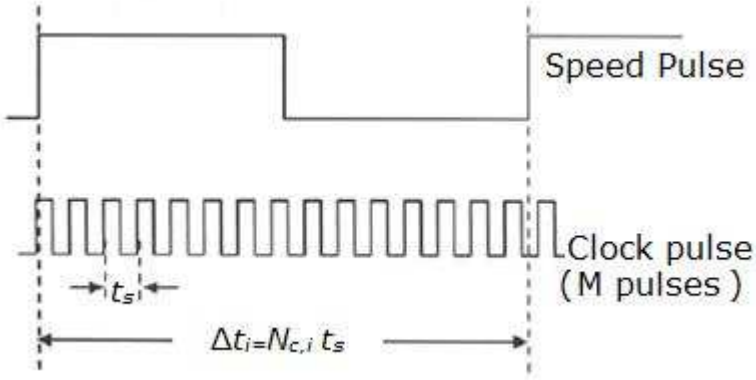

Figure 4.3 IAS Time interval principle

Consider *M* evenly spaced encoder pulses in one revolution, assume the duration of the clock cycle is t_s seconds and the number of clock cycles in a pulse is N_c, then the IAS in *rad/sec* can be calculated as; see Figure 4.3

$$\omega = \frac{2\pi}{\Delta t_i M} \tag{4.13}$$

The time interval of the given speed pulse is given by (Li, Y., 2003b);

$$\Delta t_i = N_{c,i} t_s \tag{4.14}$$

The IAS can be calculated by substituting Equation (4.14) into Equation (4.13). For the IAS software-based time-interval approach, the calculation of pulse intervals Δt_i is based on the measurement of the zero-crossing points between successive pulses of the encoder signal, as shown in Figure 4.2. These zero-crossing points are calculated by differentiating the encoder output signal to determine the beginning and the end of the pulse time intervals, Δt_i. Hence, the IAS signal can be calculated by substituting the resulting Δt_i into Equation (4.13). In this research, the IAS software-based time interval method was used for the encoder pulse train whereas the FFT-based approach was used for the wireless acceleration signal. For further details of IAS techniques see (Li, Y., 2003b).

4.4.2 Extraction of IAS using FFT

The IAS can be extracted using the FFT by constructing the analytic representation of the signal s(t) using Hilbert transform as (Gu, Yesilyurt, Li, Harris, & Ball, 2006);

$$\begin{gathered} w(t) = s(t) + iH[s(t)] = A(t)e^{i\emptyset_s(t)} \\ s(t) = Acos\left(\omega_c t + \emptyset(t)\right) \end{gathered} \tag{4.15}$$

Where, H represents the Hilbert transform (HT) which is defined by;

$$H[s(t)] = \frac{1}{\pi}\int_{-\infty}^{\infty} \frac{s(\tau)}{\tau - t} d\tau \tag{4.16}$$

Where, the $H[s(t)]$ value of the integral is used. Using Equation (4.15), IAS is then calculated by;

$$\omega(t) = \frac{d\emptyset_s}{dt} = \frac{d}{dt} Im\{\ln[w(t)]\} = Im\left[\frac{\dot{w}(t)}{w(t)}\right] \tag{4.17}$$

The principle of the frequency domain method is that band-pass filtering can be used. This not only reduces computational effort but also allows the filter types and filter bandwidth to be adjusted automatically based on the characteristics of the s(t) spectrum and hence achieve best noise suppression (Vakman, D, 1994; Vakman, David, 2000). A Gaussian window proved

to be best for the estimation of linear signals (Vakman, D, 1994; Vakman, David, 2000). In this study, a Hanning window was used and its width was adjusted based on the spectral width of interest to produce minimum distortion to the experimental signals by noise. Besides, as both the differentiation of W(t) and the Hilbert transform (Equation 4.17) can be calculated through a frequency domain approach, this method has a high efficiency in implementation. The implementation can be found in detail in (Gu, et al., 2006).

4.4.3 IAS Extraction from Wireless Accelerometer

To determine the variation in the angular speed using the wireless accelerometer signal, the FFT was used. The sensor was mounted directly, tangentially on the shaft, and so provided useful information, which could be used to find the variation in IAS of the shaft. This can be achieved using FFT property given by:

$$\mathcal{F}\left\{\frac{\mathrm{d}}{\mathrm{dt}}\mathcal{X}(\mathrm{t})\right\} = \mathcal{J}\omega\mathrm{X}(\omega) \qquad \textbf{4.18}$$

Since the acceleration *a*(t) can be defined in terms of velocity *v*(t) as;

$$a(\mathrm{t}) = \frac{\mathrm{d}}{\mathrm{dt}}\upsilon(\mathrm{t}) \qquad \textbf{4.19}$$

Using the FFT property in Equation (4.18), the relation between acceleration and velocity can be rewritten as;

$$\mathcal{F}\left\{\frac{\mathrm{d}}{\mathrm{dt}}\upsilon(\mathrm{t})\right\} = \mathcal{J}\omega\mathrm{V}(\omega) \qquad \textbf{4.20}$$

Where; V(ω) is the speed (v(t)) FFT;

The relationship between acceleration and velocity from Equations (4.19) and (4.20) can be written as;

$$\mathcal{F}\{a(\mathrm{t})\} = \mathcal{J}\omega\mathrm{V}(\omega) \qquad \textbf{4.21}$$

Consequently;

$$\mathrm{V}(\omega) = \frac{1}{\mathcal{J}\omega}\mathrm{A}(\omega) \qquad \textbf{4.22}$$

Where; A(ω) is the acceleration (a(t)) FFT;

From Equation (4.22) the velocity can be obtained by computing the inverse FFT of the acceleration and divided by its angular speed. This means that the integration can be done efficiently using the FFT to determine the velocity (IAS) from the tangential acceleration (a_t).

4.5 Comparison Study of IAS from Encoder and Wireless

The signals attained from both wireless accelerometer and encoder were subjected to signal processing techniques, explained in Sections 4.4.1-4.4.3, to extract IAS in the time domain. The block diagram in Figure 4.4 depicts the comparison procedures for IAS extraction. This comparison study benchmarked and validated the wireless accelerometer for future fault diagnosis.

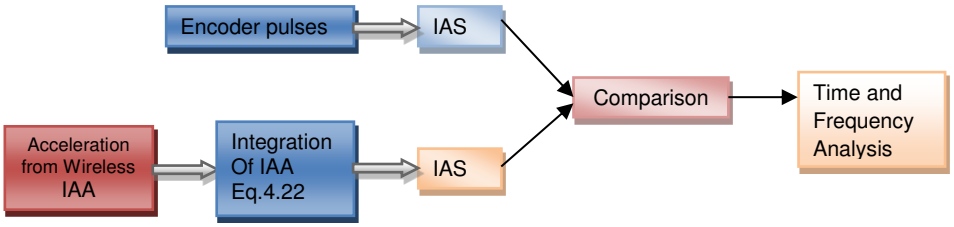

Figure 4.4 IAS extraction block diagram

4.5.1 Experiment Setup

The test rig consisted of a 3-phase electrical induction motor as prime power source and a DC generator to apply a load to the motor, as shown in Figure 4.5. The motor is connected to the generator through a single shaft, which is connected by two pairs of flexible couplings and supported by single bearing housing. The test rig had a variable speed controller and could run at a speed ranging from 60 RPM to 1420 RPM.

The construction allowed the study of different types of shaft misalignments such as angular and parallel misalignments in different parts of the shaft system. A MEMS wireless accelerometer sensor was mounted directly on the section of shaft connected to the motor shaft by a flexible coupling see Figure 4-5. The axis of principal sensitivity of the sensor was positioned tangentially to the shaft rotation. To benchmark the results from the wireless sensor, a shaft encoder (RI32) was mounted at the end of the induction motor. Outputs from both the wireless accelerometer and encoder pulses were measured simultaneously at a sampling rate of 96 kHz.

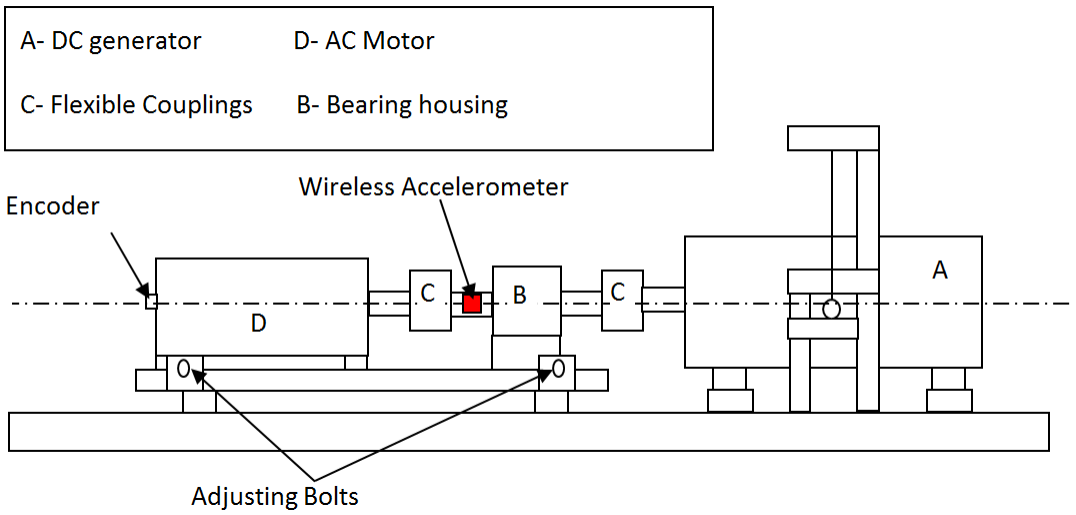

Figure 4.5 Schematic presentation of the test rig

4.5.2 Experimental Procedure Steps

After the various devices were connected to the DAS, the test rig was run at 20, 30, 40 and 50% of rated speed (284, 426, 568 and 710 RPM) while the load was fixed at 50% (2 Kw) of rated load (4 Kw). Then the following steps were followed:

- The test rig was run sequentially at 284, 426, 568 and 710 RPM.
- Wireless and encoder data was collected simultaneously.
- To avoid any unwanted variation in the measurements, and to carry out a better investigation, both signals were measured at the same load condition, speed and sensor location.
- Each speed test was repeated six times to demonstrate repeatability and avoid uncertainty.
- The collected data was then subjected to advance data analysis procedures and techniques to extract the IAS from both sensors using MATLAB codes.

During post-processing, the DCS signal is low pass filtered to obtain the acceleration signal in the tangential direction in analogue form. The pulse train signal used a time interval technique (Gu, et al., 2006) to obtain the IAS signal. The measured acceleration from the wireless sensor was integrated to obtain the IAS signal in the frequency domain.

4.6 Results and Discussion

4.6.1 Validation of the Proposed Scheme

The output of the encoder is 1000 pulses per revolution and the wireless accelerometer produces a duty cycle that varies according to the orientation of the accelerometer with respect of the vertical axis due to the change in the angle between its axis and the downward

gravitational force. The duty cycle signal is filtered using an active low pass filter to reconstruct the analogue form of the acceleration. In the case of the rotating shaft, the amplitude of the analogue form of the duty cycle signal changes slightly in magnitude as shaft speed increases. Figure 4.6 shows the output waveforms from wireless (acceleration) and encoder (IAS).

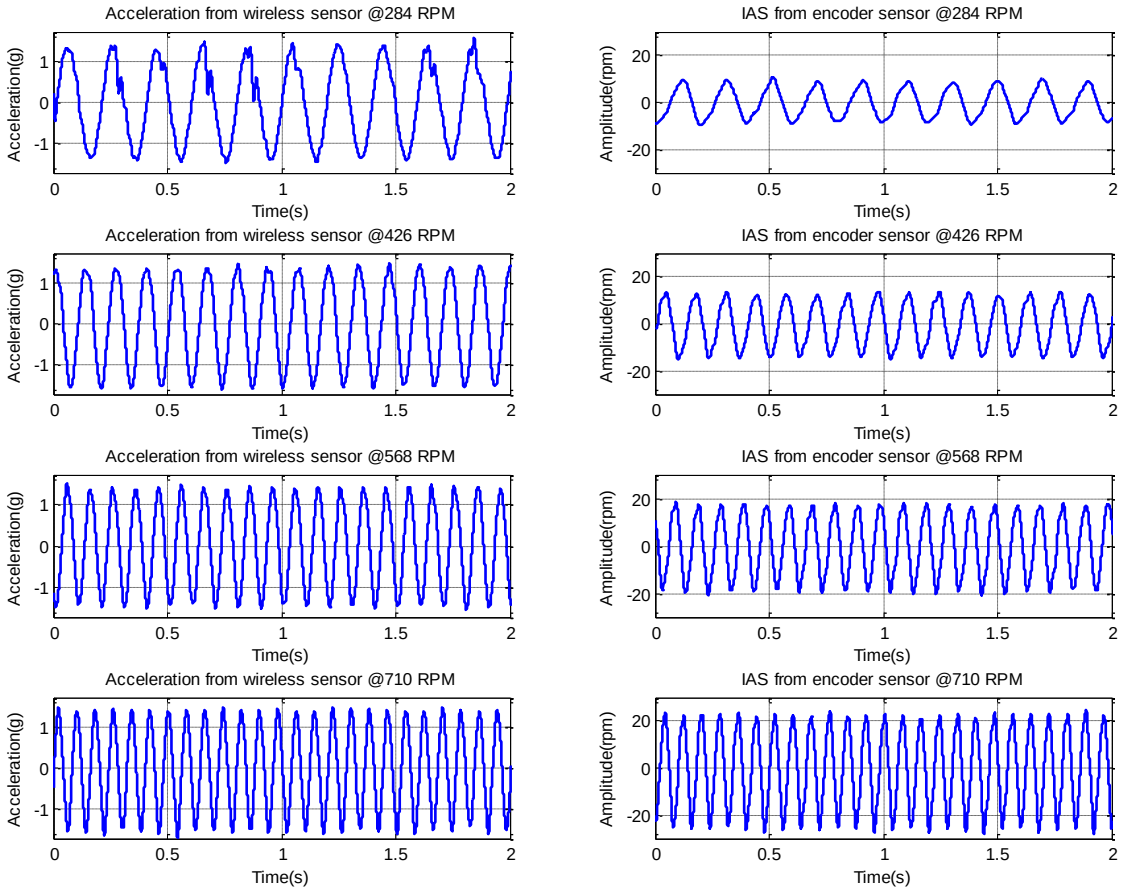

Figure 4.6 Output waveforms from wireless (Acceleration) and encoder (IAS).

Figure 4.7 shows the IAS from both the encoder and wireless accelerometer extracted from them at 284, 426, 568 and 710 RPM. The integration of tangential acceleration measured by wireless sensor according to equation (4.22) produces the IAS in the frequency domain. Then the inverse of FFT is computed to bring the IAS waveforms in the time domain.

The acceleration measured by wireless accelerometer represents the tangential acceleration of the shaft. From Figure 4.7 it is clear that the IAS waveform from the wireless accelerometer has the different amplitude at different speeds. However, the IAS from wireless is well correlated to that from encoder.

The encoder pulse time-intervals are proportional to the speed of the shaft. The algorithm used to extract the IAS from the encoder waveform is based on these time-intervals of consecutive pulses. Consequently, as the speed increases, the widths of these pulses (time-intervals) get smaller as shown in Figure 4.8 and hence the amplitude will increase.

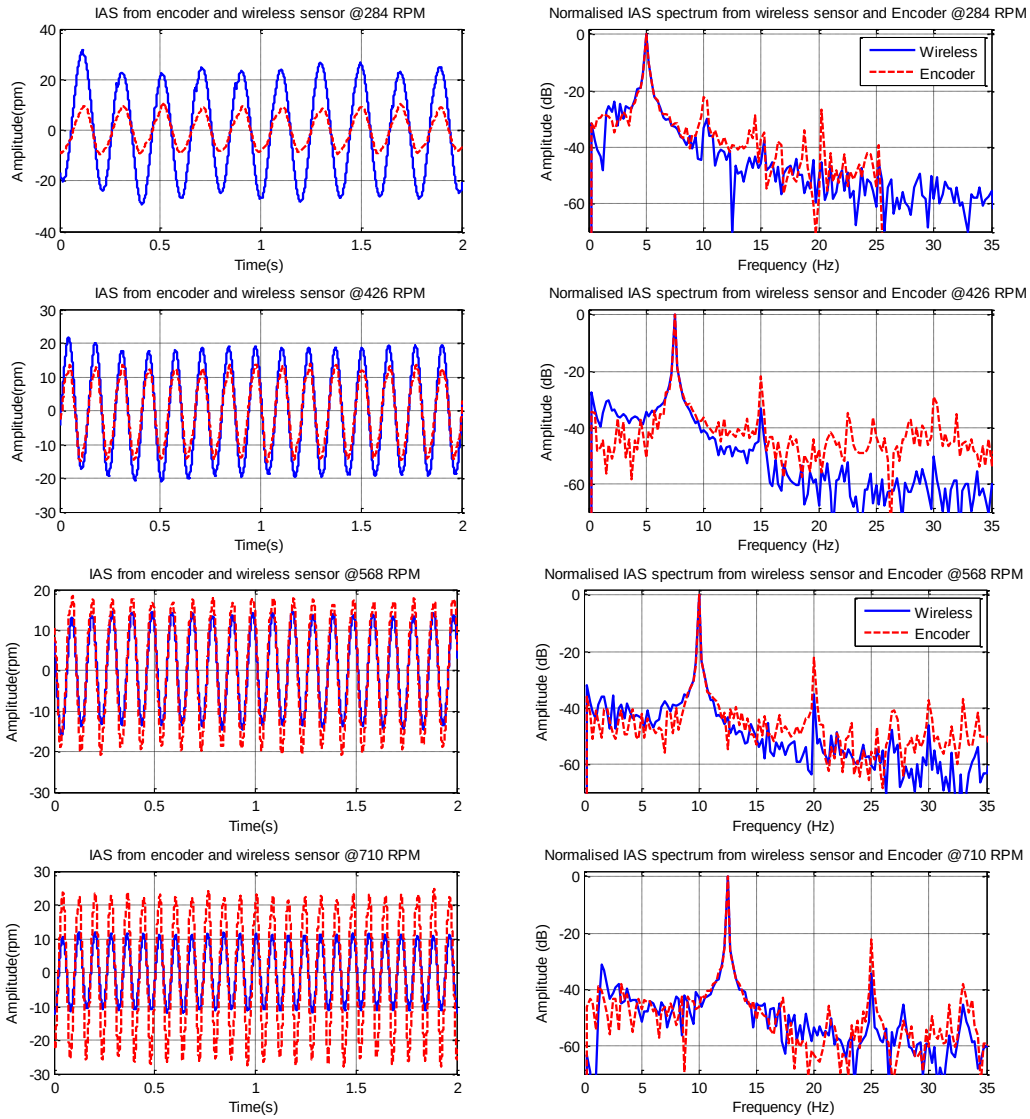

Figure 4.7 IAS measured by wireless accelerometer and encoder in time and frequency domains.

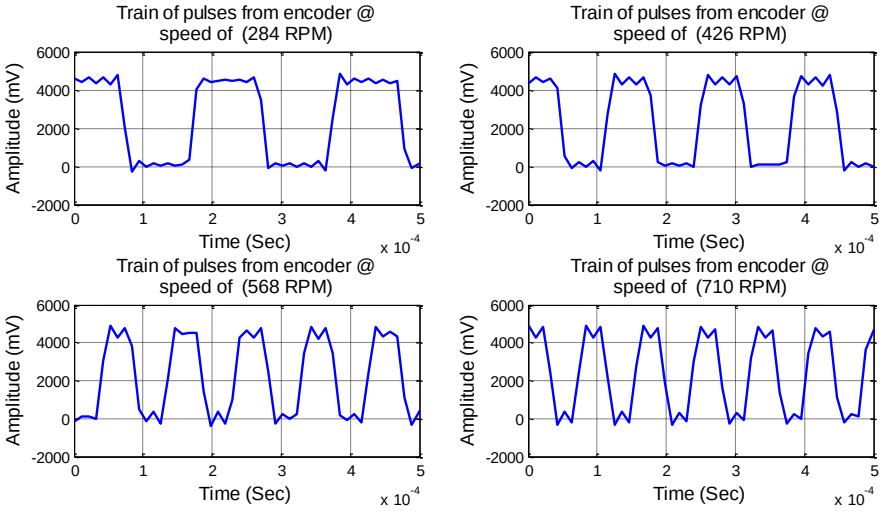

Figure 4.8 Typical encoder signals at different shaft speeds

Figure 4.9 presents the IAS signals extracted from encoder and wireless accelerometer when the test rig was run at 568 RPM. It can be observed that the profiles of the two waveforms are very similar and this confirms that the wireless sensor can capture the dynamic behaviour of the rotor. However, the amplitude of the wireless sensor is lower than that of encoder. This is due to the effect of gravity which is the bases of MEMS accelerometer used. The wireless accelerometer gravitational effect removal algorithm after applying TSA to the measured signal will be elaborated later in this chapter.

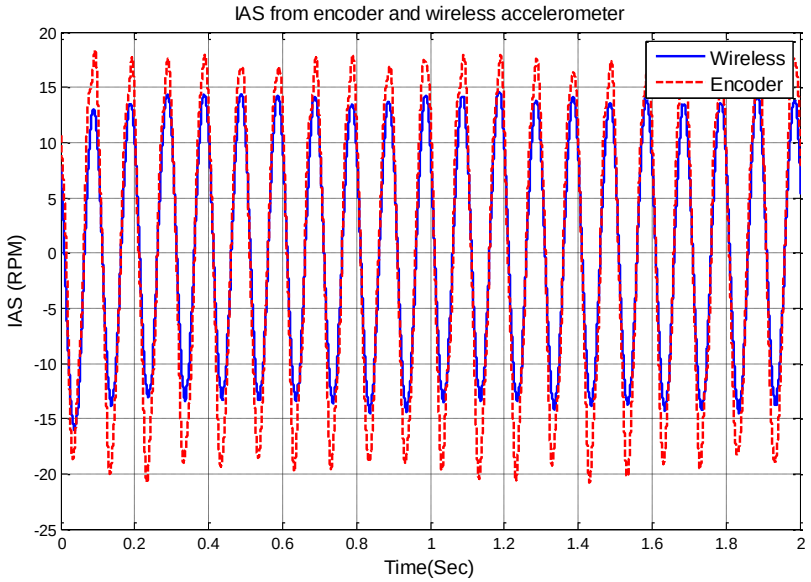

Figure 4.9 IAS waveforms of wireless accelerometer and encoder at 568 RPM

To allow a more detailed comparison, Figure 4.10 shows the normalised IAS and accelerations spectra from both encoder and wireless accelerometer. From Figure 4.10 (a), it can be seen that the IAS and its higher order harmonics (2X, 3X and 4X) can be resolved by both signals. The wireless sensor shows a lower noise level in the high frequency range but shows much higher amplitudes in the low frequency range. Moreover, the wireless IAS high amplitude noise at low frequency is largely due to the numerical integration used to calculate IAS.

Figure 4.10 (b) shows that the normalized amplitudes of the acceleration signal for both sensors. It shows also wireless noisier amplitude than IAA from encoder in the low frequency range. The figure also shows that the encoder has the greater noise level at high frequencies. This confirms that the signal from wireless sensor has a higher signal-to-noise ratio.

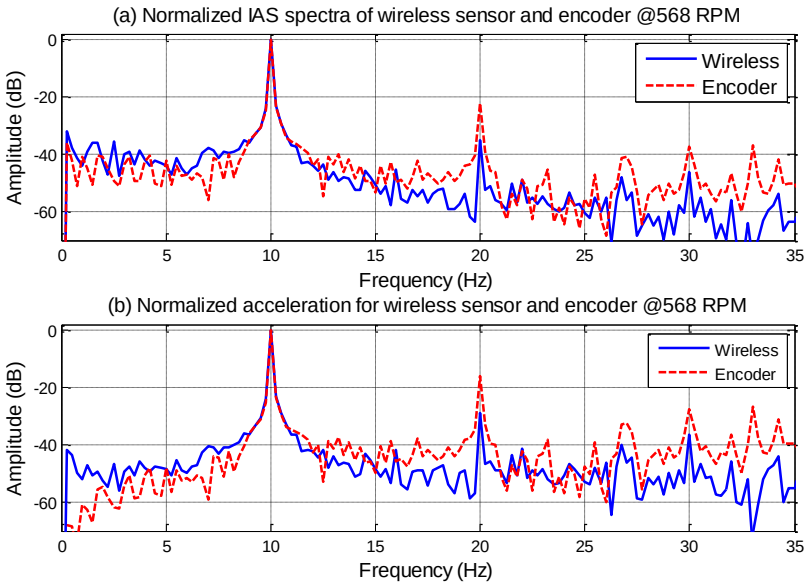

Figure 4.10 IAS and acceleration spectra from wireless accelerometer and encoder for drive speed set at 568 RPM.

4.6.2 Summary

This research has shown that it is possible to develop a wireless sensing system to measure the dynamics of a rotary shaft. The IAS results obtained from the wireless sensor are comparable to those obtained from a contact encoder.

The signal from the wireless accelerometer has high signal-to-noise ratio which will increase the possibility of small fault detection. From the IAS shown in Figure 4.10 (a), it can be seen that the rotational frequency and its higher order harmonics can be resolved by both signals but the signal from the wireless sensor shows lower noise levels in the high frequency range but much higher amplitudes in low frequency range. Although the wireless accelerometer used is bandwidth limited by the active low pass filter (133 Hz), the information used in the extraction of IAS shows acceptable features for fault diagnosis.

The acceleration signal acquired from the wireless sensor has almost constant amplitude and does not vary with the speed of the shaft, see Figure 4.6. This confirms the operation of the accelerometer which is based on the gravity (duty cycle) change around the rotor movement. However, the vibrations generated by the motion in the direction of sensor sensitivity axis are still can be captured. Due to the gravitational effect on the reading of the wireless sensor, it is possible to subtract this acceleration after removing noise from the signal using Time Synchronous Averaging (TSA) algorithm. The steps of this procedure will be presented in the following sections.

The algorithm used to extract IAS from the encoder is based on the time-interval between successive pulses. As the speed of the shaft increases, this interval becomes smaller and the

amplitude of the IAS will increase accordingly. This explains the increase in the amplitude of IAS extracted from encoder signal.

The IAS from the wireless accelerometer is extracted from the accelerations acting in tangential direction. The amplitude of the IAS signal extracted from wireless accelerometer decreases as the speed of the rotor increases as shown in Figure 4.7. This occurs as result of the numerical integration and division by angular speed of the acceleration signal from the wireless sensor. This problem is investigated using TSA algorithm by subtracting the gravitational effect in the rest of this chapter.

4.7 Time Synchronous Averaging (TSA)

The TSA reduces the random noise element and cancels out vibration components which are not synchronised with the rotation of the rotor of interest. This improves the signal to noise ratio (SNR) of the collected signals for more accurate feature calculation.

In addition, TSA aligns signals according to the angular position of a particular rotating shaft, which allows phase information to be taken into account and to eliminate the influences of random speed variations. TSA has been found to be very efficient in cleaning signals subject to time varying processes by suppressing random noise and noise from uncorrelated sources such as vibrations from nearby components.

To study the effectiveness of TSA, the IAS results obtained in conventional time and frequency domain are compared with those obtained in angular and order domain (TSA). Moreover, the gravitational correction to the IAS from TSA wireless is compared with those obtained before the application of those corrections under different operating speeds.

There are many TSA methods. For computational efficiency and reliable implementation, a shaft encoder based method has been adopted in this research. The shaft encoder, mounted on the input shaft, produces 100 pulses per turn as the angular position reference signal. The wireless vibration and reference signals were measured simultaneously and sampled at a rate of 96 kHz for 20 seconds at each of the operating settings.

The equation used to derive the synchronous average y(t) of time signal x(t) using trigger signal c(t) having a frequency f_t is equivalent to the convolution of x(t) and c(t) (Braun, 2011; Mcfadden & Toozhy, 2000);

$$y(t) = c(t) * x(t) \quad \textbf{4.23}$$

Where c(t) is a train of N impulses of amplitude 1/N, spaced at intervals $T_t = 1/f_t$ given by;

$$c(t) = \frac{1}{N}\sum_{n=0}^{N-1}\delta(t + nT_t) \quad \textbf{4.24}$$

This equivalent to multiplication of Fourier transform X(f) of the signal by C(f) in the frequency domain and can be represented by;

$$Y(f) = C(f).X(f) \quad \textbf{4.25}$$

Where C(*f*) is a comb filter function of the form;

$$C(f) = \frac{1}{N}\frac{\sin(\pi N T_t f)}{\sin(\pi T_t f)} \quad \textbf{4.26}$$

Increasing the number of averages N narrows the peak of the comb and reduces the amplitude of the side lobes between the peaks. Thus, in the frequency domain, synchronous averaging for large values of N can be seen as the complete removal of all components except those that occur at integer multiples of frequency f_t (Mcfadden & Toozhy, 2000).

This technique is applied to the wireless acceleration waveforms as well as the IAS of encoder and opto-interrupter. TSA not only removes unwanted noise from wireless waveform, but also brings the signal to the angular domain which helps to remove the effects of gravitational effect on wireless sensor waveforms.

4.7.1 Gravity effect removal from wireless acceleration algorithm

The wireless sensor output is a function of the angle the accelerometer's axis makes with the vertical axis. The angular rotation of the sensor will produce a sinusoidal signal with amplitude greater than or equal to g (g = 9.81 ms^{-2}). The wireless accelerations acquired at different speeds are measuring almost same magnitude. As mentioned earlier, it has been caused by the gravitation effects on the sensor reading. To find out the accelerations that the wireless sensor measures apart from the gravitation, TSA has to be applied to transfer the signals from the time domain to the angular domain. Using the average signal from TSA, the tangential acceleration of the rotor can be extracted. The following are the algorithm steps used to extract the acceleration without gravitation effects after TSA was applied to the wireless signal (in the angular domain):

1- Collect a reference signal $X_{ref}(\theta)$ at low speed.
2- Calculate the order spectrum using FFT of $X_{ref}(\theta)$ and find the 1st order (O_1).
3- Compute the magnitude and phase of X_{ref} at rotor first order as:

$$A_1 = |X_{ref}(O_1)|$$
$$\emptyset_1 = Angle\left(X_{ref}(O_1)\right)$$

4- Generate equivalent gravitational acceleration signal using the magnitude and phase derived in step 2 for (n) revolutions as:

$$\alpha(\theta) = (0: N-1)/N2\pi n$$
$$X_a(\theta) = g/A_1 cos(\alpha(\theta) + \emptyset_1) \quad \textbf{4.27}$$

5- Rescale new measured signal after application of TSA (X) by multiplying it by g and divide it by A_1

$$X(\theta) = X(\theta) \times g/A_1 \quad \textbf{4.28}$$

6- Subtract the signal generated in step 5 (equation 4.28) from the signal generated in step 4 (equation 4.27) to get the new acceleration signal without the effect of gravitation as:

$$X_{-g}(\theta) = X(\theta) - X_a(\theta) \quad \textbf{4.29}$$

The resulting signal in step 6 is used to compute the IAS from wireless signal. The IAS results obtained by application of this algorithm are then compared with the corresponding IAS from encoder and Opto-interrupter.

4.7.2 Experiment Setup and Results Investigation

The same test rig was used. The opto-interrupter system was used on the flexible coupling between motor shaft and wireless sensor, see Figure 4-5. This position was chosen to determine any change in the IAS as close as possible to the wireless sensor. 60 PPR were generated by the opto, and 100 PPR from the encoder. The rotating disk (see Figure 5.11 and Figure 5.12) was mounted on the side of the wireless sensor. The load was set to 50% of rated load. The speed was set in 6 steps of 40, 50, 60, 80, 90 and 100% of rated speed.

The experiment procedure was the same as explained above in Section 4.5.2 except for the introduction of the opto-interrupter. The techniques used to attain the IAS from all sensors were the same as for the previous experiment. The wireless sensor was adjusted in such a way that the DC shift was an increasing trend (-ve β).

By applying this technique, the IAS from wireless and the other devices can be compared with the normal analysis of these signals. In addition, an advanced technique (TSA) was applied to the wireless signal. It removes gravitational effects from the wireless accelerometer signal and allows direct comparison with the IAS signals from other sensors.

4.7.3 Results and Discussion

4.7.3.1 Waveform Characteristics

Figure 4.11 shows the IAS waveforms from wireless, encoder and opt-interrupter before application of TSA to the raw data. The amplitude of wireless is decreasing with increase speed whereas the other sensors increasing. All IAS signals are in phase as found earlier. Since the wireless sensor measurement is driven by the gravity, an advanced technique has been introduced to eliminate this effect. Using TSA procedure to reduce any un-periodic noise in predefined period, the gravitational effect can be corrected.

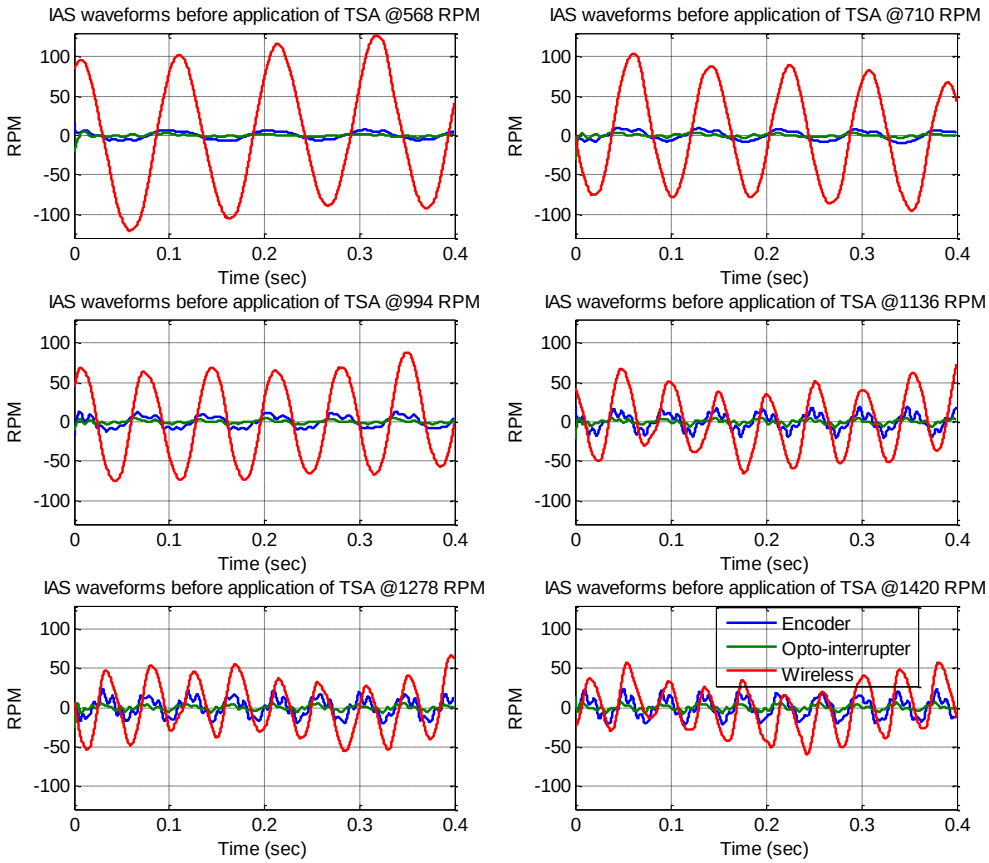

Figure 4.11 IAS waveforms from wireless accelerometer, encoder and opto-interrupter at six shaft speeds before applying TSA

Figure 4.12 illustrates the wireless acceleration and the corresponding IAS before and after eliminating the gravitational effects after application of TSA. The magnitude of the acceleration and hence the IAS after correction are increasing with respect of shaft speed. The yield acceleration is the accelerations acting in tangential direction of the shaft.

Figure 4.13 shows the IAS waveforms acquired from sensors at different speeds after applying TSA. The IAS from the wireless sensor was derived applying the TSA. The IAS from the other sensors was computed using the FFT procedure described earlier. It is clear that the IAS from the wireless accelerometer has the highest amplitude.

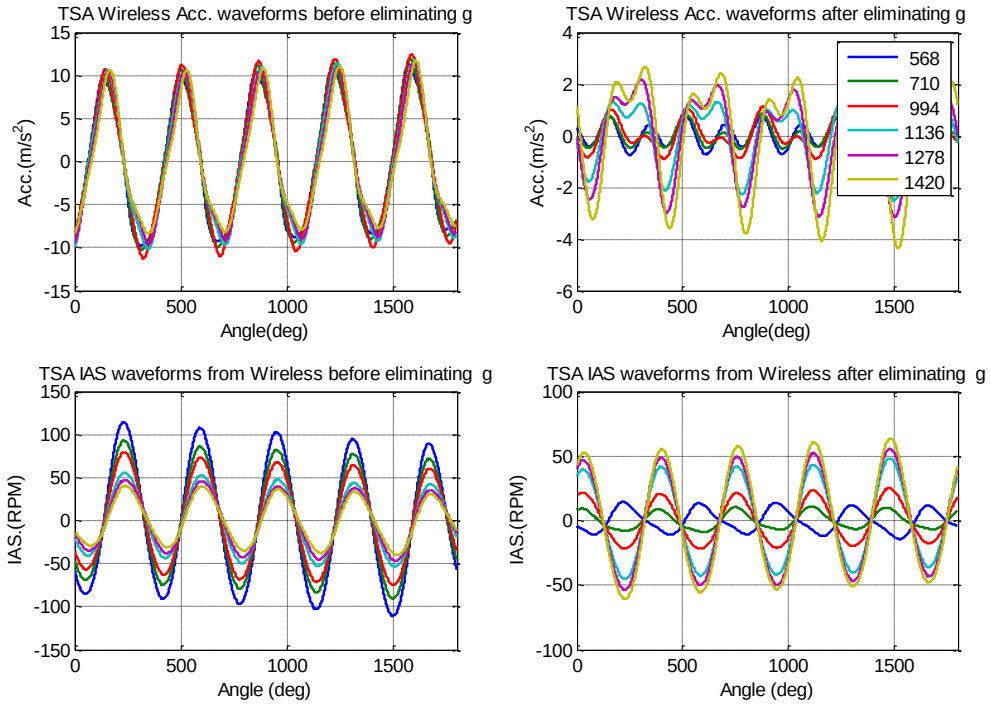

Figure 4.12 TSA of IAS and Acceleration waveforms from wireless accelerometer before and after gravitation correction at different shaft speeds

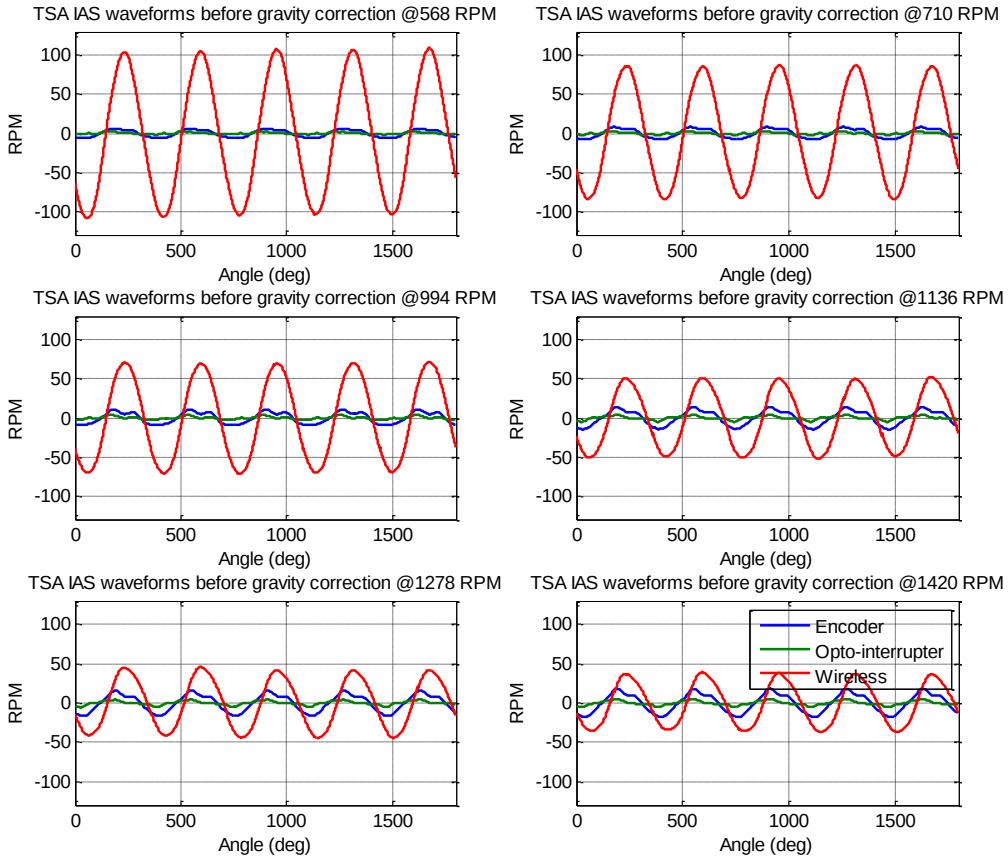

Figure 4.13 IAS waveforms from wireless accelerometer, encoder and opto-interrupter at six shaft speeds after applying TSA

Figure 4.14 shows the IAS waveforms acquired from sensors at different speeds after applying TSA. The IAS from the wireless sensor was derived by eliminating gravitational effects from the raw signal after applying the TSA. The IAS from the other sensors was computed using the FFT procedure described earlier. It is clear that the IAS from the wireless accelerometer has the highest amplitude. The out-of-phase characteristic exhibited by the wireless sensor is due gravitational correction computational process.

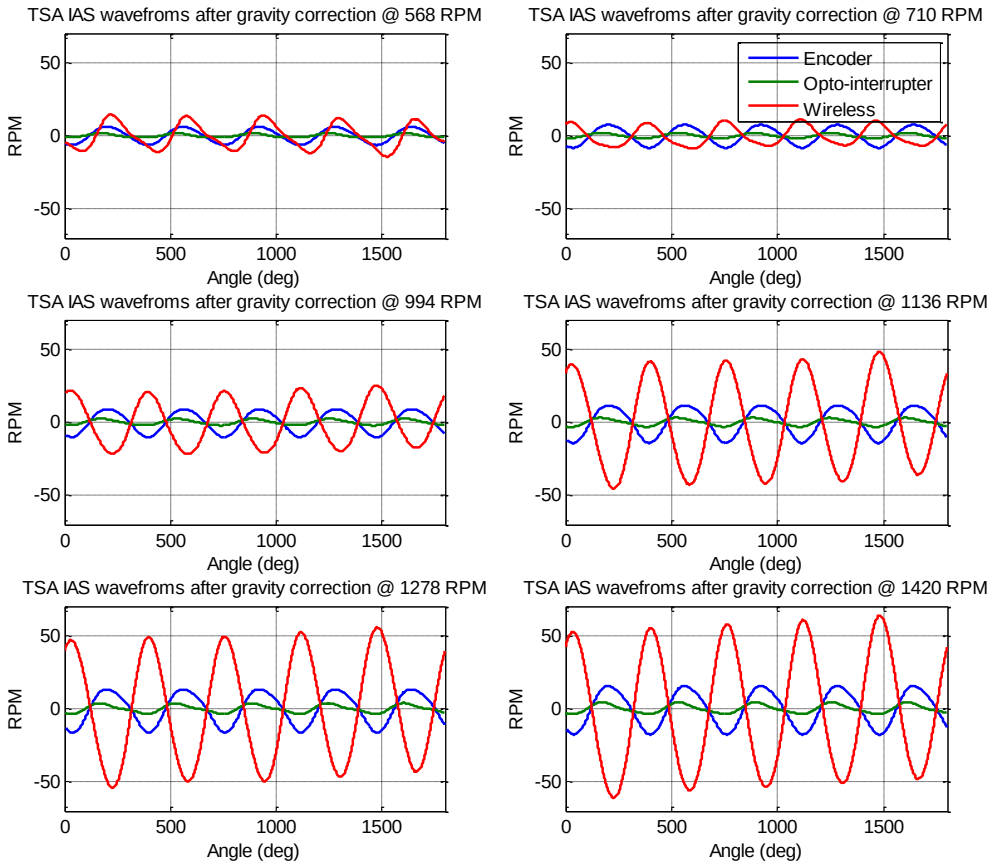

Figure 4.14 IAS waveforms from wireless accelerometer, encoder and opto-interrupter at six shaft speeds after applying TSA and gravitational correction

To better understand the behaviour of the waveforms, the order spectral amplitudes are derived from the FFT of time domain signals. The following section discusses these results before and after application of TSA and gravitational correction.

4.7.3.2 Order Spectra of TSA Signals

Figure 4.15 shows the amplitudes of the spectral harmonics 1X, 2X, 3X and 4X extracted from the IAS signals before application of TSA shown in Figure 4.11. Each column in Figure 4.15 corresponds to the output from a different device. The first column is the acceleration measured by the wireless accelerometer, the second, third and fourth columns are the IAS derived from the wireless accelerometer, the encoder and the opto-interrupter, respectively.

The amplitudes of the spectral harmonics from the signals of both encoder and opto-interrupter exhibit very similar characteristics. On the other hand, the signal from the wireless accelerometer exhibits very different characteristics.

The first harmonic, 1X of IAS from the wireless accelerometer (without TSA correction) shows amplitudes that decrease with increase of angular speed, whereas the first harmonic for the encoder and opto-interrupter increases with speed.

For the second harmonic, 2X, the wireless IAS increases at higher speeds. On the other hand, the other sensors show increase amplitudes with increase of speed. Since the wireless sensor was mounted close to the coupling, the third harmonic 3X was directly influenced by the forces acting on the coupling jaws and shows a similar trend for the second harmonic, 2X, of the other sensors with significant difference in values. These values affected by the gravitational effect on the wireless sensor measurements and the un-periodic noise effect. In addition, the sensitivity and resolution difference between various sensors play vital role in these values refer to Section 4.3.

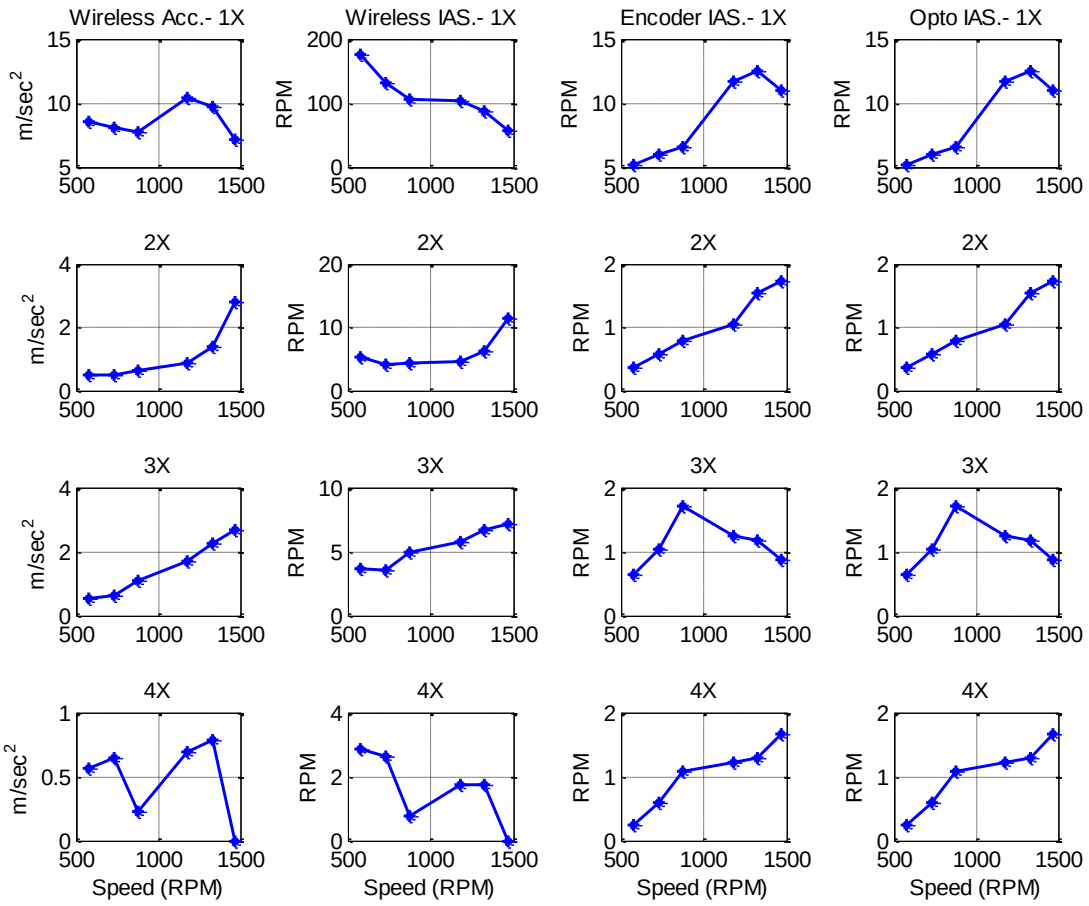

Figure 4.15 Magnitude of the spectral harmonics (1X, 2X, 3X and 4X) of the IAS obtained from wireless accelerometer, encoder and opto-interrupter before application of TSA and gravitational correction

Figure 4.16 shows the amplitudes of the order spectral harmonics 1X, 2X, 3X and 4X corresponds to waveforms (see Figure 4.13) shown in Figure 4.15 after the application of TSA to the waveforms of all sensor signals.

The first harmonic, 1X of IAS from the wireless accelerometer shows amplitudes smoothen previous trend as well as the first harmonic for the encoder and opto-interrupter.

For the second harmonic, 2X, the wireless IAS initially decreases and then increases at higher speeds whereas the other sensors show increase amplitudes with increase of speed except at high speed decreases. The harmonics amplitudes 3X and 4X was influenced by the nonlinear forces acting on the rotor.

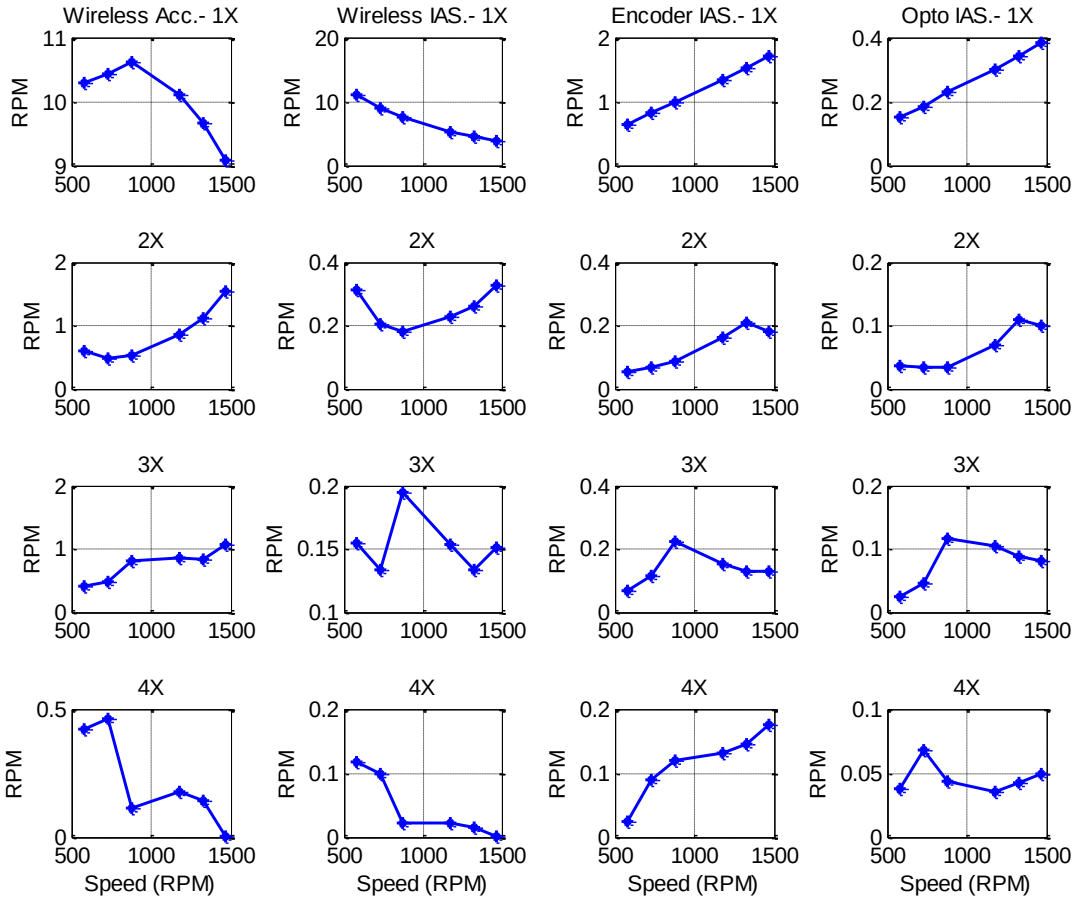

Figure 4.16 Magnitude of the spectral harmonics (1X, 2X, 3X and 4X) of the IAS obtained from wireless accelerometer, encoder and opto-interrupter after application of TSA and before application gravitational correction

After application of gravitational correction, Figure 4.17 shows that the first harmonic, amplitudes 1X, of IAS measured with the wireless accelerometer a linear increase with shaft drive speed. The other sensors show the same trend. The shapes of the 2X, 3X and 4X harmonics for all the sensors change only slightly but the magnitudes are closer.

The amplitude difference between the IAS values measured by the different sensors is due to the position of the sensors resolution and sensitivity of each sensor see Section 4.3.

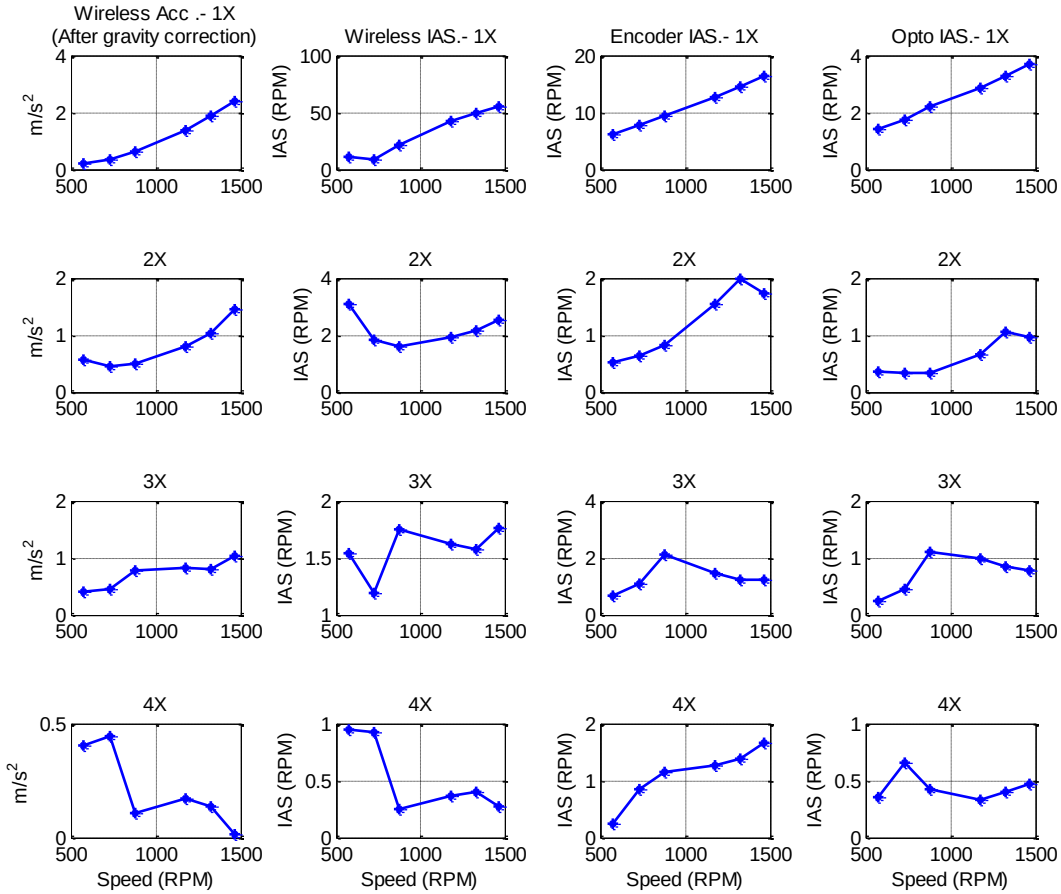

Figure 4.17 Magnitude of the spectral harmonics (1X, 2X, 3X and 4X) of the IAS obtained from wireless accelerometer, encoder and opto-interrupter after application of TSA and gravitational correction

4.8 Summary

The investigation of IAS from wireless sensing system has indicated direct correlation to the dynamics of a rotary shaft. The derived IAS results obtained from the wireless sensor acceleration have been compared to those obtained from a contact encoder and opto-interrupter and good agreement obtained.

Application of TSA to the IAS data from the wireless sensor and encoder and opto-interrupter significantly improved. The TSA removes random noise and cancelling out vibration components which were not synchronised with the rotation of the rotor. In addition, the removal of gravitational effects from the wireless signal provided dramatic change in its computed IAS. Together the TSA and the corrections brought values of the IAS from all three sensors into close proximity.

The gravitational correction of IAS has noticeable effect on the phase. This effect may be caused by numerical estimation of the gravitational signal. However, it still presenting acceptable way of detecting the IAS by the new wireless sensor.

In addition, comparing the IAS signal amplitudes from encoder (1000 PPR) in Section 4.6 and (100, 60 PPR) in Section 4.7.3, the magnitude of IAS is varies with that respect. This complies with resolution graph in Figure 4.1 which is derived from equation 4.8. As the number of pulses increases the amplitude increases.

The algorithm used to extract IAS from the encoder and opto-interrupter was based on a FFT (Hilbert Transform) and the results obtained provide solid evidence the agreement with IAS from wireless sensor. The amplitude of IAS from encoder and opto-interrupter using elapsed time algorithm can be as obtained by FFT. This can be shown in Section 4.6 and 4.7.3.

In general, the waveform comparison between the two types of signals reveals the following main observations:

- The amplitude of the IAS increased with shaft operating speed. Whereas, in the time domain the amplitude of the signal from the wireless sensor exhibited the opposite behaviour see Figure 4.11.
- Variations in the wireless signal are more visible in the frequency domain because the TSA technique tends to reduce the noise and cancel out the components that are not synchronised with the rotation of the rotor see Figure 4.15, Figure 4.16, Figure 4.17.
- The frequency domain signal at higher speeds became more pronounced after using TSA.
- After application of gravitational correction, 1X amplitudes of IAS measured with the wireless accelerometer increased with shaft drive speed. The other sensors show the same trend, see Figure 4.17.
- The profiles of the 2X, 3X and 4X amplitudes for all the sensors are closer. The amplitude difference is due to the position of the sensors resolution and sensitivity of each sensor, see Section 4.3.

CHAPTER FIVE

Test Rig Facilities and Data Acquisition Procedures

This chapter begins with an overview of the bearing test rig used to carry out the investigations. Specifications of the used coupling are listed. Moreover, the dial indicator steps of measuring parallel misalignment of the test rig are explained. In addition, different components and apparatus used are described. The data acquisition system, transducers and procedures used to perform the various experiments are described.

5.1 Introduction

The most useful monitoring technique used in condition monitoring of rotating machinery is vibration analysis (Randall, 2011). The main causes of vibration in rotating machinery are eccentric (material centre of mass not coincide with the geometrical centre), misaligned and unbalanced (due to additional mass) shafts and loose fittings, all of which can result in unexpected machine failure.

Traditionally, past research into rotor dynamics and vibration measurement used conventional wired accelerometers placed on the machine casing some distance from the likely source of vibration where it could be affected by vibration from all parts of the rig, including bearings, couplings, etc. The aim of this study is to develop a wireless accelerometer that can be placed directly on the rotating shaft to study rotor dynamics, detect rotor vibration and diagnose the cause or causes.

The experimental rig used was simple and industrially relevant. Faults could be introduced into the rig in a repeatable and controlled manner and the vibration measured to an acceptable level of accuracy. In addition, it provides real data similar to that recorded in an industrial situation. The test rig used instrumentation available within the Centre for Efficiency and Performance Engineering at the University of Huddersfield. The advantage of using an existing rig that was developed and used previously is ease of disassembling and re-assembling and also isolated from any other sources of vibrations.

The experiments carried out as part of this research using the test rig will be described in the following sections. In addition, the generic experiment steps and the facilities used will be explained, as well the data acquisition system.

5.2 Test Facility

5.2.1 Test Rig Components

The test rig is shown in Figure 5.1. It is driven by a 4kW, 3-phase, 4 pole electric induction motor coupled with a dynamic brake. The motor is coupled to the brake by four cylindrical steel shafts, which are coupled by three pairs of matched flexible couplings. Two bearing housings each contain one roller and one captive ball bearing support the shafts. The wireless accelerometer was mounted directly on the second shaft, see Figures 5.1 and 5.2, while the encoder (type RI32) was mounted directly on the induction motor rotor. Conventional wired piezoelectric accelerometers (of type SINOCERA) were positioned on the bearing housing; one vertically and the other horizontally to measure the lateral vibration. The speed and torque of the motor are controlled by a SIEMENS Micro Master Controller as shown in Figure 5.3. The drive shaft can be run at different speeds (up to a maximum of 1420 RPM) with different

applied torque loads to a maximum of 4.0 kW. The controller can be set to control the duration of the motor run.

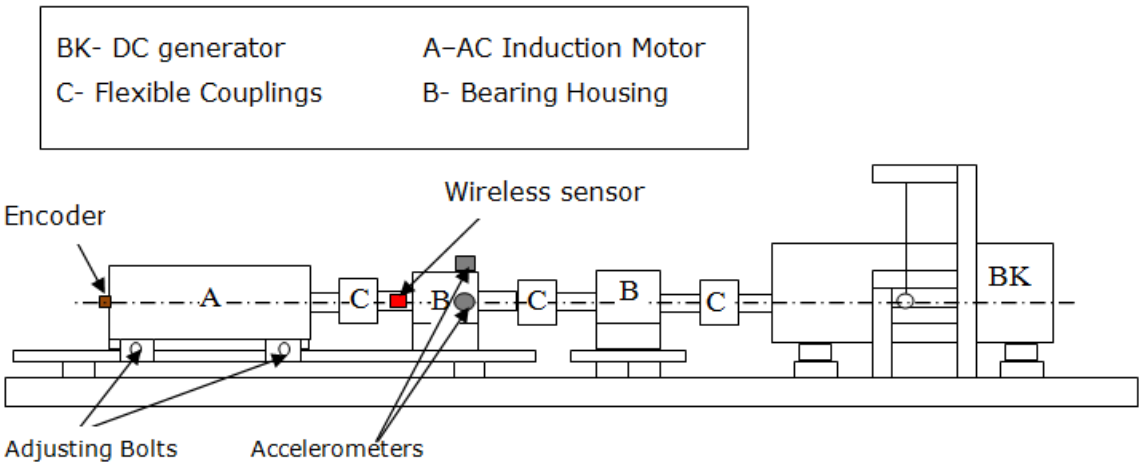

Figure 5.1 Complete test rig schematic and wireless sensor placement.

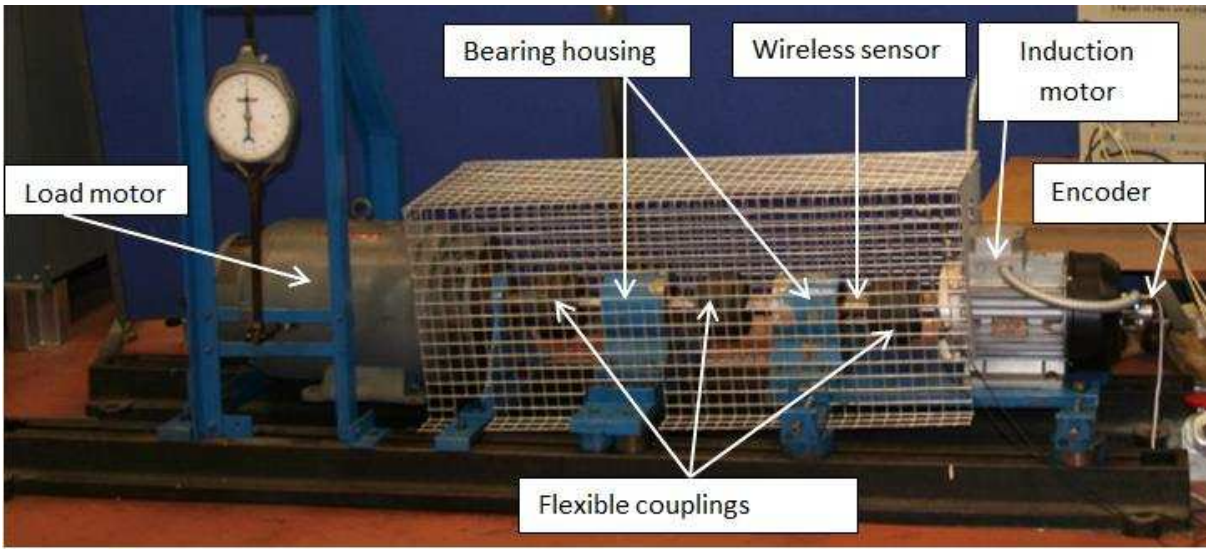

Figure 5.2 Test rig photo.

Figure 5.3 Test rig control panel.

5.2.2 Hard Rubber Coupling (HRC)

A hard rubber coupling is used to connect the various shafts, see Figure 5.2. HRC couplings are general purpose couplings with a flexible element which can accommodate a degree (max 0.4 mm at 4850 RPM) of misalignment and absorb vibration, see Figure 5.4. H type coupling, HRC130H, with taper lock bushing 1610 was used. The specification of the HRC130H was:

Table 5.1 Specification for Fenner Coupling HRC130H (Maryland, 2008)

Manufacturer	Fenner
Type	HRC130H
Size	130
Bore diameter	14-42 mm
Outer diameter	130 mm
Diameter of hub	105 mm
Length of hub	18 mm
Width of rubber	36 mm
Taper lock bush size code	1610
Mass	5.46 kg

Figure 5.4 HRC130H coupling.

5.2.3 Dial Indicator

Dial indicator, see Figure 5.5, is the most common tool that has been used to accurately measure the shaft alignment. The dial indicator used has a resolution of 0.01 mm which means for one revolution measures 1 mm. Using magnetic holder, the holder was mounted on one flange of the coupling and the indicator tip on second flange. Then the following steps are followed to align and misalign shafts, see Figure 5.6:

1. Move the indicator in the horizontal position and then set the scale to zero. To guarantee that the indicator in horizontal or vertical position, a sprit level is used, see Figure 5.6 (a).
2. Move the indicator 90^{o} to be in the vertical position. The reading will indicate the vertical degree of alignment, see Figure 5.6 (b).
3. Move the indicator another 90^{o} to be in the horizontal position again. The reading of indicator is divided by 2 to attain the horizontal degree of shafts alignment, Figure 5.6 (c).
4. By adjusting coupling positions in vertical and horizontal and repeating step 2 and 3, required degree of alignment was attained.
5. By tightening the shaft holders (Motor, bearing housing, Load) the target alignment degree was achieved.

Figure 5.5 Dial Indicator.

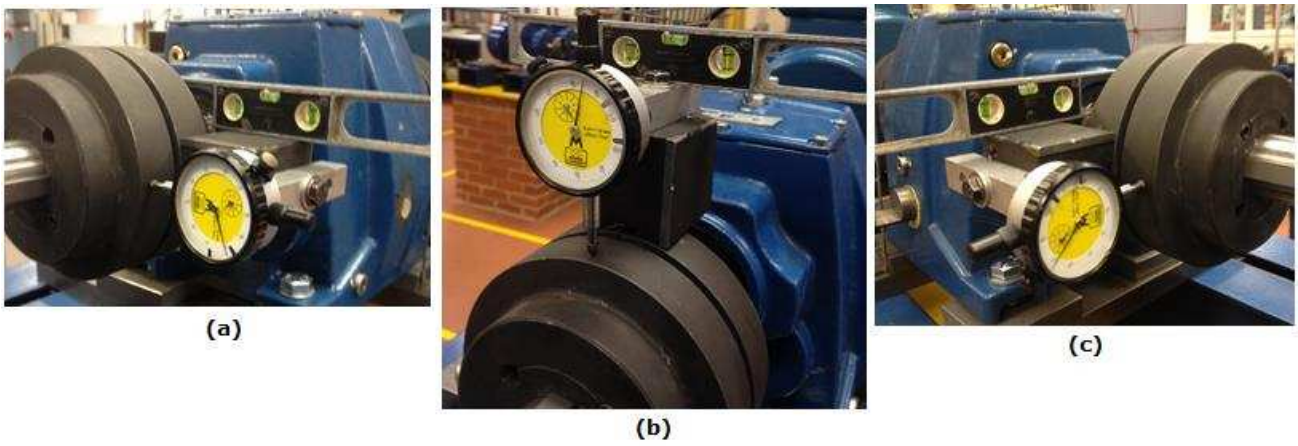

Figure 5.6 Alignment procedure using dial indicator

(a) zero the indicator horizontally (b) move the indicator vertically (c) read the indicator value and divide by 2.

5.2.4 Incremental Encoders

Incremental encoders determine the angular position of the shaft. They consist of a circular disc with equally spaced transparent and opaque segments around its the circumference, see Figure 5.7. The disc is mounted upon the shaft, which is mechanically connected to rotor of the induction motor to record its angular position.

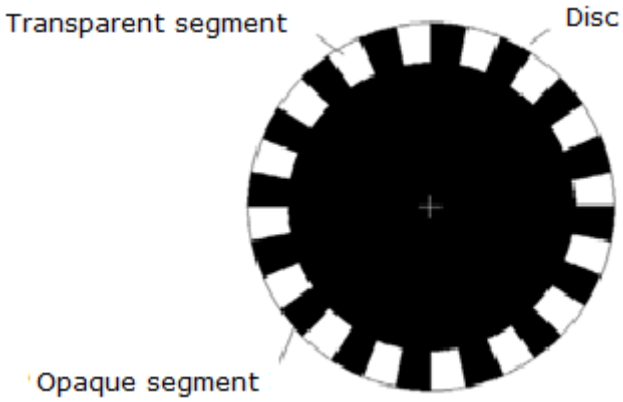

Figure 5.7 Incremental shaft encoder

A light emitter and a light receiver are located on opposite sides of the disc. As the disc rotates, the light is passed and blocked by the transparent and opaque segments respectively. Incremental shaft encoders are sensors capable of generating signals in response to rotary movement in conjunction with mechanical conversion devices, such as wheels or spindles. Figure 5.8 shows a photo of an incremental encoder manufactured by Hengstler.

Figure 5.8 Incremental shaft encoder type RI32 (Hengstler & Inc., 2009)

Encoders such as the RI32 are usually used to measure the IAS of rotating shafts and provide two outputs: the first was one pulse per revolution; the second was electrical pulse trains of 1000 pulses per revolution or 100 pulses per revolution. The time interval between two successive pulses is inversely proportional to the average speed of the encoder shaft (Li, Y., 2003a; Li, Y., et al., 2005). This kind of transducer is relatively cheap compared to laser encoders. Here the 1000 and 100 pulse trains provided measures of the rotation of the shaft and were used to benchmark the output from the wireless sensor.

5.2.5 Vibration Transducer

Accelerometers are the most popular vibration transducers used with rotating machinery (Scheffer & Girdhar, 2004). Figure 5.9 shows the two accelerometers used in these tests and Table 5.2 gives their specifications. Both are IEPE accelerometers, see Section 2.2.3.

Figure 5.9 SINOCERA accelerometers

Table 5.2 SINOCERA accelerometer specifications

Accelerometer	Sinocera (Vertical)	Sinocera (Horizontal)
Type	Piezoelectric	Piezoelectric
Model	YD-185TNC	YD-185TNC
Serial Number	SN00016	SN00039
Frequency range	0.5 Hz to 5000 Hz	0.5 Hz to 5000 Hz
Sensitivity (Calibration)	5.106 mV/ms^{-2}	4.960 mV/ms^{-2}
Operating voltage	12-24 VDC	12-24 VDC
Temperature	-20ºC to 120ºC	-20ºC to 120ºC

The accelerometers were attached to the bearing housing casing by threaded bronze studs, one in the vertical direction (SN00016) and the other in the horizontal direction (SN00039). The vibrations sensed by the accelerometers were connected to the data acquisition system by RF coaxial cable with TNC (Threaded Neill–Concelman) type connector (accelerometer output) and BNC (Bayonet Neill Concelman) type connector (Data acquisition input). Then, the data were sent to the computer via a USB port.

5.2.6 Laser Vibrometer

The principle of the laser vibrometer shown in Figure 5.10 (optoNCDT1300 from Micro-Epsilon) is optical triangulation. A light spot (wavelength 670 nm) is projected onto the target surface, the reflected light is focussed onto a sensitive element within the device by a receiving lens. Movement of the surface onto which the spot of light is focussed will cause a consequential movement of the image on the sensing element. This is translated by the vibrometer into a measure of the movement of the surface. The resolution of the sensor is 4µm (static) and 10µm (dynamic) (Micro-Epsilon, 2010).

Figure 5.10 OptoNCDT1300 (Micro-Epsilon, 2010).

5.3 Opto-interrupter

The encoder was mounted to the back end of the motor. The wireless accelerometer was mounted on the rotor about 635 mm away from the position of the encoder. To investigate the IAS from the wireless accelerometer, an opto-interrupter was mounted upon the flange of the flexible coupling closest to the wireless accelerometer, see Figure 5.12. It comprises a slotted disc and opto circuit. To generate a train of pulses, a circular disc has equally spaced transparent and opaque segments around its circumference. The disc is mounted upon a coupling, between first and second shafts as shown in Figure 5.12. The opto-interrupter passes current when there is no blockage of the light beam.

5.3.1 Slotted Disc Design

The 60 slots disc was designed to fit on the flange of the coupling. Figure 5.14 shows the dimensions of the disc. This design was done using Catia software which is compatible with the CNC machine software. The inner diameter of the disc was set to the outer diameter of the flange (106 mm) and mounted close to the wireless sensor, see Figure 5.12.

5.3.2 Opto-interrupter Circuit Design

Figure 5.13 shows the circuit for the opto-interrupter which was constructed from commercially available photo interrupters and an available single power supply operational amplifier (LM358) with simple passive components. The function of the photo interrupter is to change the output of the photo interrupter from low to high as the light beam passed through the gaps in the slotted disc. The output waveform of the opto-interrupter can be seen in Figure 5.14.

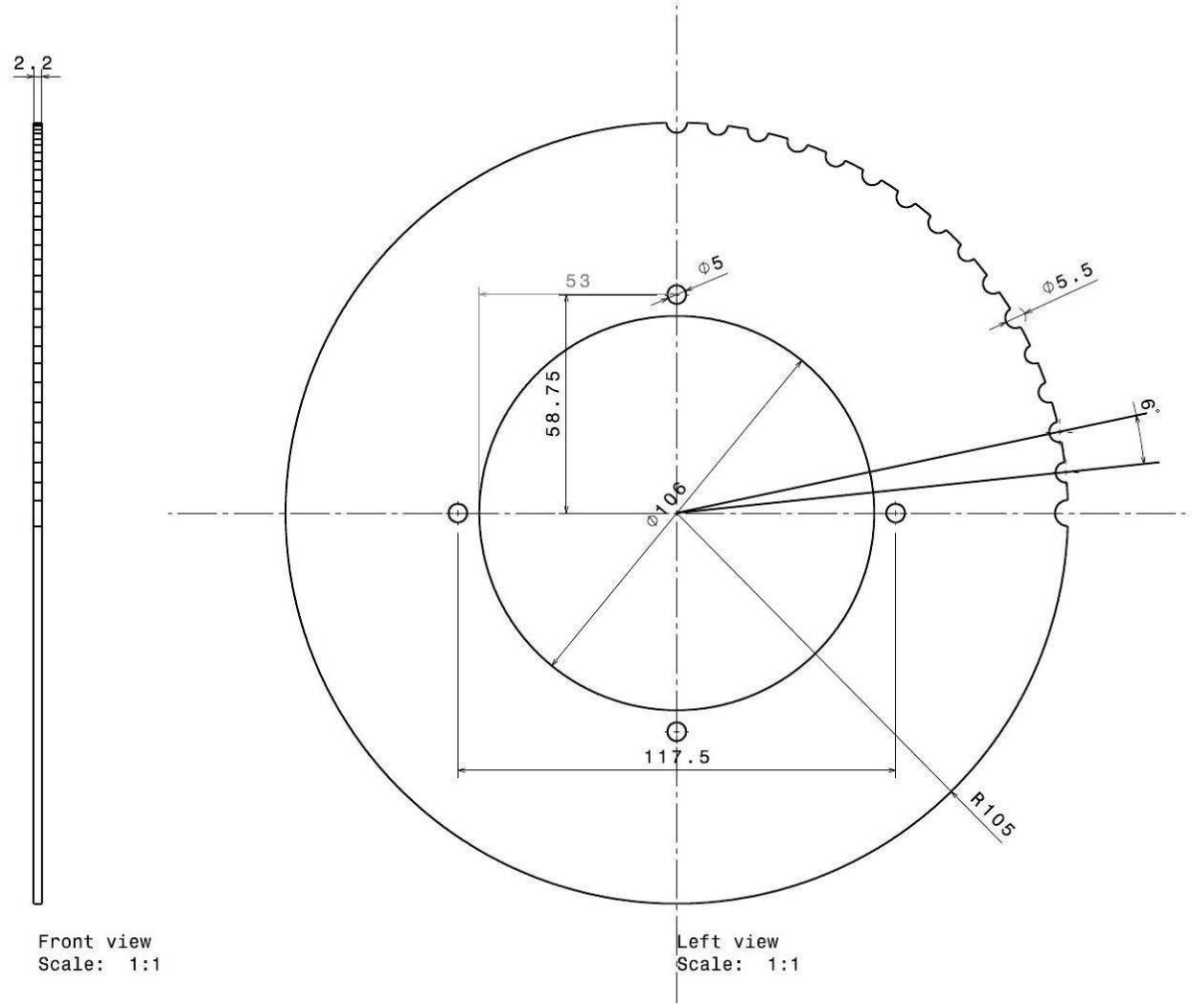

Figure 5.11 Circular disc design parameters.

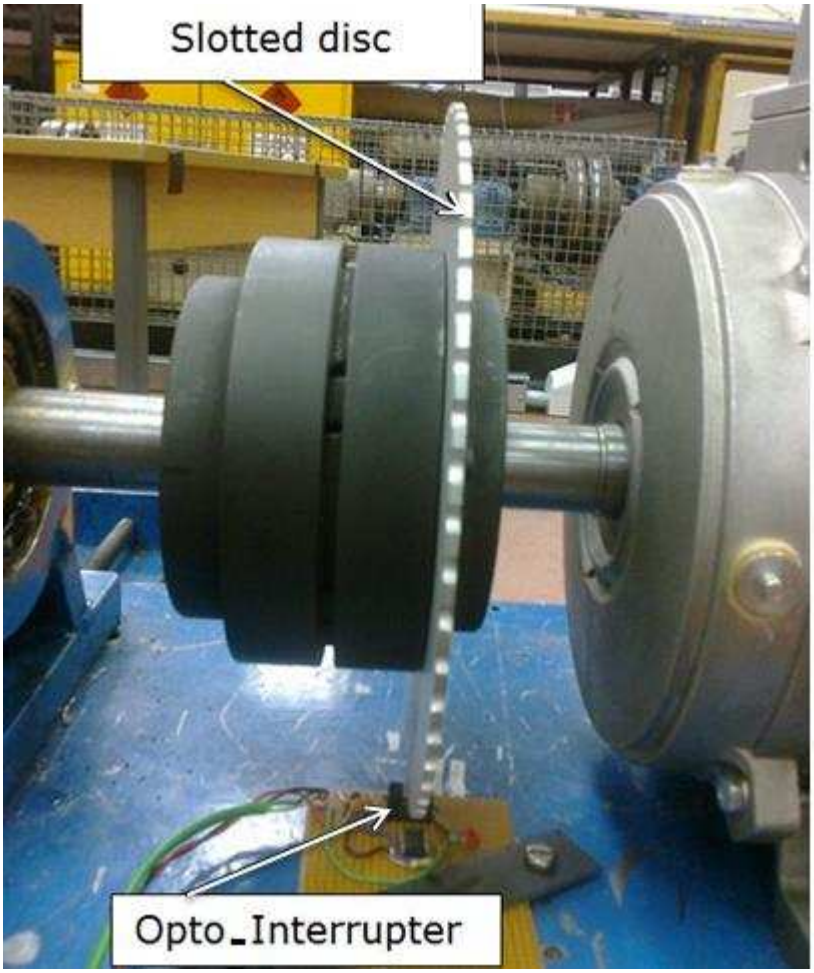

Figure 5.12 Circular disc and opto-interrupter installation

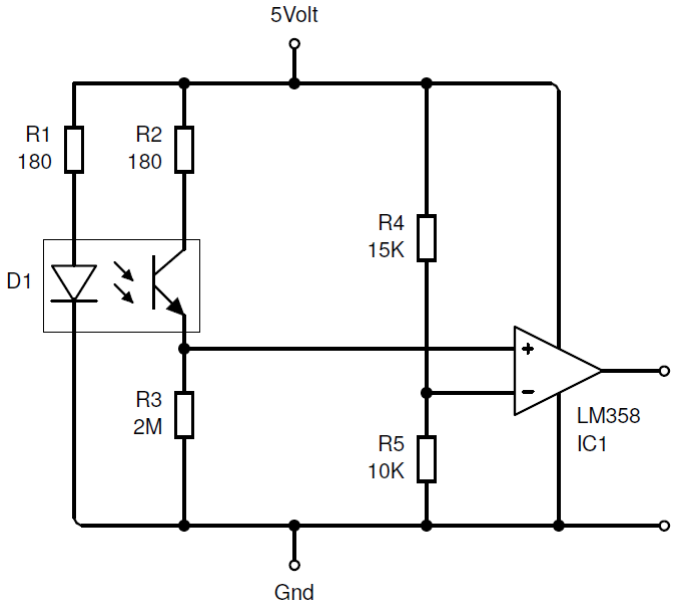

Figure 5.13 Opto-interrupter circuit

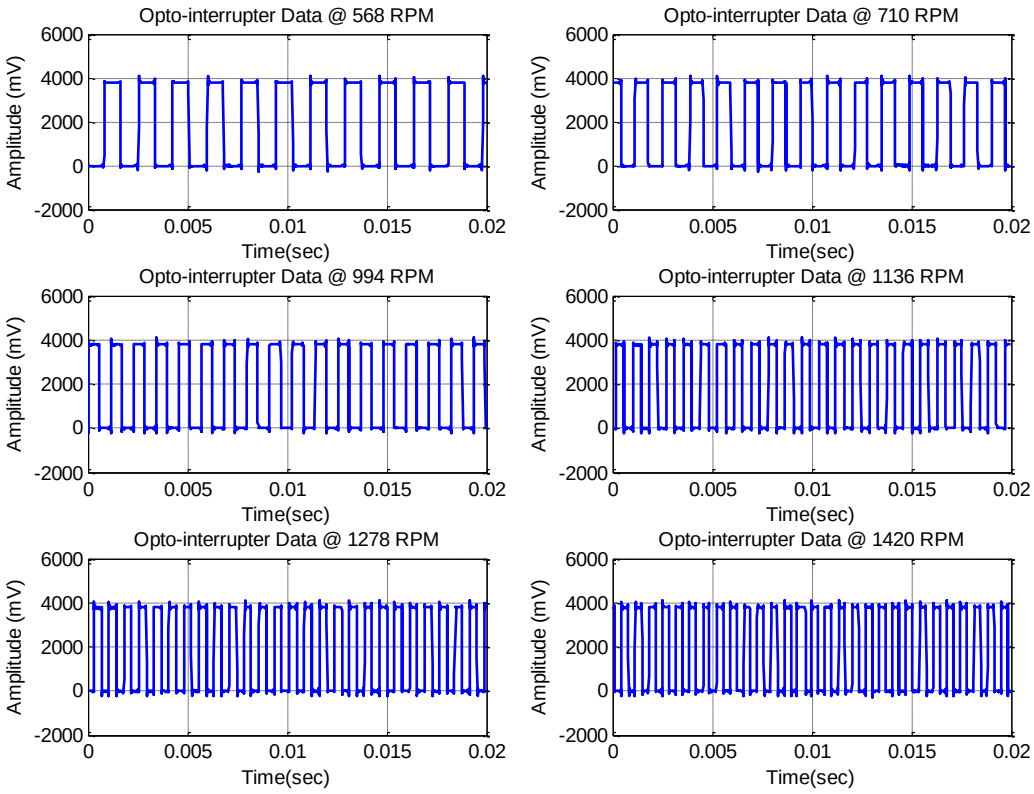

Figure 5.14 Opto-interrupter output waveform at different speeds

5.4 Dual Variable Filter

The Kemo dual variable filter is used as a low pass filter, see Figure 5.16. It has a frequency range of 1 Hz - 100 kHz (Kemo, 2011). In addition, it has two channels of high performance analogue filters, high gain and a flexible input front end. It provided a reliable general purpose filter amplifier.

5.5 Data Acquisition System (DAS)

The SINOCERA data acquisition system, type YE6232B as shown in Figure 5.15 possesses the following main features (Sinocera Piezotronics, 2011a):

- A 24-bit A/D parallel data acquisition system based on USB 2.0 interface,
- Voltage/IEPE input; 16 channel, built-in programmable gain amplifier and real-time digital filters,
- Supporting smart transducers (IEEE1451.4),
- Supporting multi-equipment cascading connection; suitable for multi-point testing,
- Built-in programmable gain amplifier and anti-filtering,
- Sampling frequency can be chosen by the software and varies from 375 Hz to 96000 Hz, and more specifications are listed in Table 5.3.

Figure 5.15 Volt Input Data Acquisitions System (SINOCERA YE6232B)(Sinocera Piezotronics, 2011a).

Figure 5.16 shows the signal acquisition system. The wireless receiver, which provides the duty cycle signal of the wireless accelerometer, was connected to the low pass filter with a variable cut off frequency (Dual variable filter). The low pass filter output and DCS signals were connected to the data acquisition system. The encoder, the opto-interrupter and laser vibrometer signals were also connected to the DAS as voltage. The wired accelerometers were connected to the channels in the IEPE mode. The sampling frequency was set to 96 kHz through the software YE7600. These signals were all sampled and recorded simultaneously. The software recorded the signals in parallel for further processing.

5.6 Data Acquisition Control Software

Figure 5.17 shows the program interfaces of YE7600 software (Sinocera Piezotronics, 2011b). YE7600 is general purpose data acquisition, conditioning and analysis software. It supports all instruments manufactured by SINOCERA and allows set up parameters for sampling, conditioning data format and signal sources. It has highly efficient data storage and fast data conversion to other formats such as MATLAB, Excel, etc., (Sinocera Piezotronics, 2011b). It is capable of time-domain analysis as well as frequency-domain. YE7600 contains various sampling triggers: manual, signal, hardware and from the waveform showing on the screen. The channels to be sampled could be set according to choice; the refreshing speed of the screen waveform is adjustable (Sinocera Piezotronics, 2011b).

Table 5.3 Specification of SINOCERA YE6232B data acquisition system (Sinocera Piezotronics, 2011a)

Channels	16 (Selectable)
A/D bits	24bit
Input Mode	V/IEPE/TEDS
IEPE Power Supply	4mA/+24VDC
Signal Input Range	≤±10VP
Signal Frequency Range	DC-30 kHz(-3dB±1dB)
Gain	×1, ×10, ×100
Filter	Independent anti-filtering
Accuracy	±0.5%
Sample Rate (Max.)	96 kHz/CH, Parallel
Interface	USB2.0
Trigger Modes	Signal trigger; External trigger
Temperature/Humidity	Operating temperature :0 to 50°C; Humidity: 20 to 80% RH
Dimensions (mm)	426W×88H×300D(H)
Weight	4 Kg
Power Supply	AC220V 50Hz/110V 60Hz DC12V (9 to18V)
Software	YE7600 General test & analysis software
Cable	Input cable, interface cable; power cable

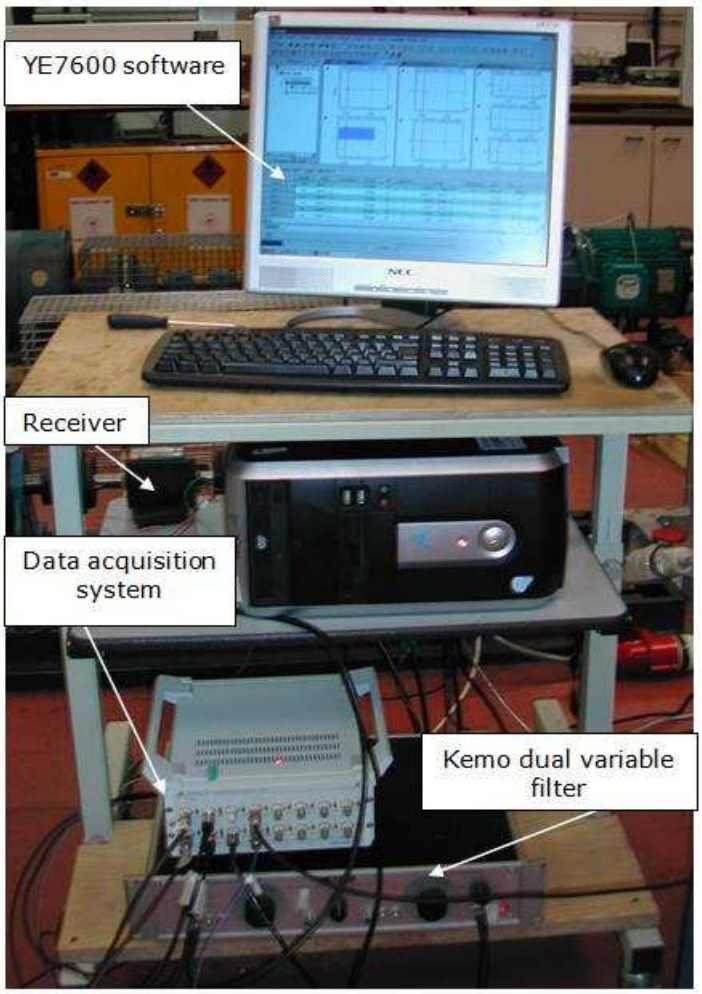

Figure 5.16 Data acquisition system and experimental set-up

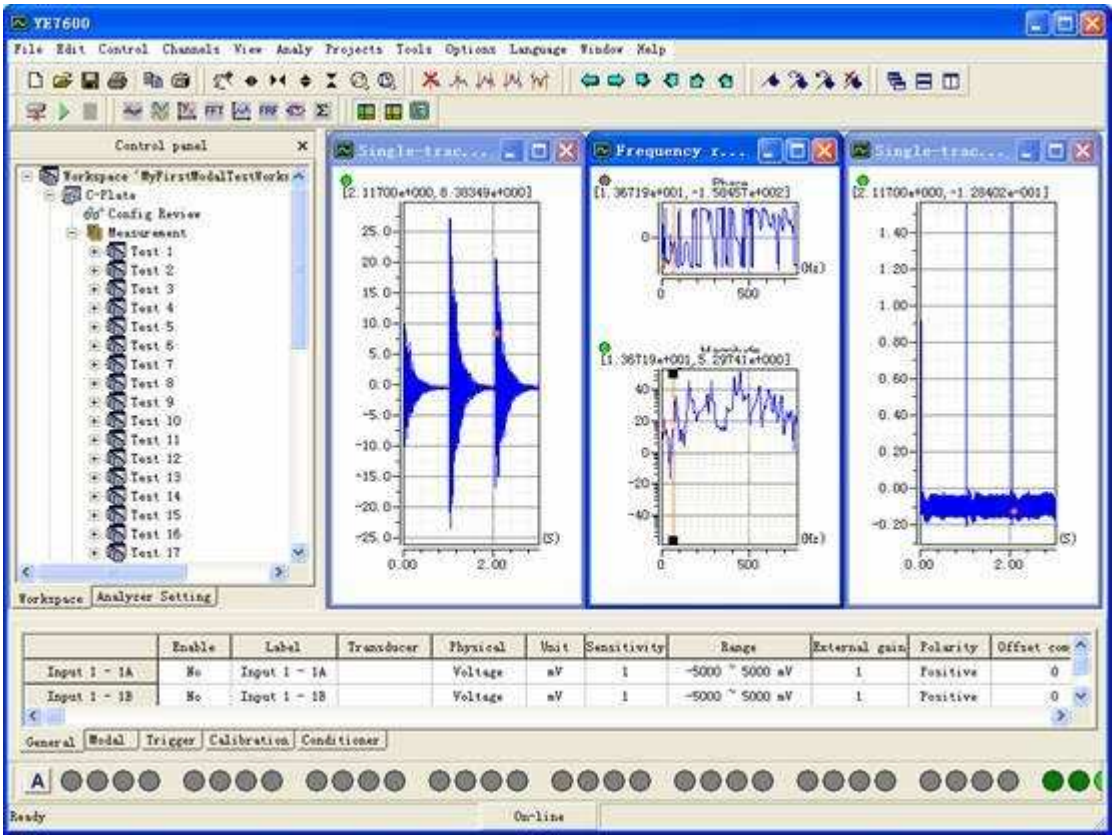

Figure 5.17 User interface of YE7600 software

5.7 Experimental and Data Collection Procedure

- The wireless accelerometer was mounted tightly and directly onto the shaft of the test rig; the sensitivity axis was in the tangential direction of rotation motion to eliminate the centripetal acceleration, see Figure 5-18. This has been done using shims to adjust the sensor in tangential direction to trade off the imperfection of sensor holder.

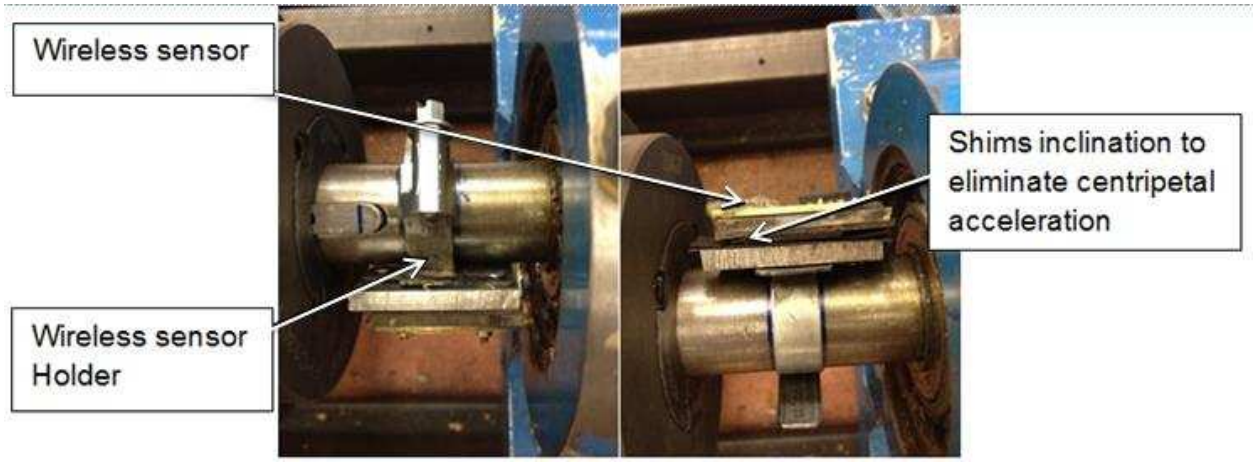

Figure 5-18 Wireless installation on shaft.

- The DCS signal was low-pass filtered to obtain the analogue form of the acceleration and then fed to the DAS. The DCS signal was recorded for each test carried out to be filtered and compared with the filtered one.
- Both the one pulse and 100 or 1000 pulses per revolution output cables were connected to data acquisition channels. The one pulse per revolution was used to calculate the average speed and the other outputs to calculate IAS.
- The data acquisition system (DAS) was connected to the computer through a USB lead.
- The YE7600 software was used to set up the chosen sampling rate (96 kHz) and the duration of recording at each test. Moreover, it records the data through DAS.
- Before starting the test, the oscilloscope mode of the software was used to ensure that the sensors were working correctly.
- The test rig control panel was set to the desired load, speed and time duration for each step of the test.
- Sufficient time (at least 10 minutes) was allowed for the test rig to "warm up" and reach steady state for each speed and load before starting any test. Then the collection of the data commenced via the DAS.
- The developed MATLAB code was used to process and analyse the recorded data.
- The data were collected in the time domain, and stored on the computer under different well-defined file names.
- Each test was repeated more than six times to ensure its repeatability.
- After collecting sufficient data, the rig was stopped and switched OFF at the mains.

CHAPTER SIX

Mathematical Model of a Multi-Shaft System

This chapter presents a mathematical model that simulates various vibration signals of the test rig. It begins with a literature review of rotor system misalignment modelling. It then describes the lumped mass method for modelling the test rig for a two rotor system. The derived equations are solved using the state space approach. The results of the model are presented. Then, a more advanced analysis method is used to model the four rotor system taking into account the bearings. In both models, the wireless sensor output is derived and explained.

6.1 Introduction

In industrial rotor bearing systems, rotor unbalance and shaft-to-shaft misalignment are two common and principal sources of vibration that are of major concern. A number of analytical methods have been applied to calculate unbalance response(Prabhakar, et al., 2001). However, limited research has been done on the vibrational characteristics of rotor systems that are due to shaft-to-shaft misalignment.

Shaft-to-shaft misalignment is a condition in which the shafts of the driving and driven machines are not on the same centre-line. Perfect alignment between the driving and driven machines cannot be attained in practice(Prabhakar, et al., 2001). Although acceptable alignment can be achieved before running the machine, it cannot be maintained during operation of the machine due to various factors such as the difference in thermal expansion of machines, foundation movement, etc.

Thus, misalignment is always present in a real machine and flexible couplings are used to compensate for misalignment between driving and driven shafts and to transmit rotary power without torsional slip(Prabhakar, et al., 2001). Li and He (Li, M. & He, 2009) studied the modelling of non-linear dynamic characteristics of an unbalanced rotor system due to parallel misalignment of two rotors under the action of non-linear oil film forces. When moving rotors are misaligned this will generally cause reaction forces and moments to be generated within the coupling which are often a major cause of machinery vibration which increases bearing wear, cause impacts between the rotor and the stator, and generates unpleasant and harmful noises (Li, M. & He, 2009).

Rivin (Rivin, 1986) proposed the classification of couplings as rigid, misaligned compensating, torsionally flexible and combined. The effect of coupling geometry, mass location and coupling mass unbalance on lateral vibrations of machines has been studied by Woodcock (Woodcock, 1977). Gibbons (Gibbons, 1976) derived the forces and moments acting at the coupling centres of articulation for different types of coupling in the presence of parallel misalignment. Arumugam and colleagues (Arumugam, 1995) predicted the reaction forces and moments for combined parallel and angular misaligned flexible couplings by assuming coupling transmitted forces represented by a half-sinusoid function having fundamental frequency equal to twice rotational speed. Sekhar and Prabhu (Sekhar, A. S. & Prabhu, 1995) developed a higher-order finite element model for a misaligned rotor coupling bearing system and numerically evaluated the effects of coupling misalignment on the second harmonic vibration response at different speeds.

Dewell and Mitchell (Dewell & Mitchell, 1984) determined the expected vibration frequencies for a misaligned metallic disc flexible coupling on the basis of an analysis of the structural vibrations produced by misalignment. Several investigators (Maten, 1970; Piotrowski, 2007)

have provided vibration identification charts which indicate that coupling misalignment generally produces a vibration component at twice the shaft speed frequency. Xu and Marangoni (Xu & Marangoni, 1994 a, 1994 b) showed that vibration responses due to coupling misalignment mainly occur at even integer multiples of the rotational speed. Sekhar and Rao (Sekhar, A. S. & Rao, 1996 a; Sekhar, A. S. & Rao, 1996 b) analysed vibrations due to misalignment in a rotor bearing system with flexible coupling. Lee and Lee (Lee & Lee, 1999) derived a dynamic model for misaligned rotor ball bearing systems driven through a flexible coupling by treating the reaction loads and deformations at the bearing and coupling elements as the misalignment effect.

The effect of parallel misalignment on the lateral and torsional responses of two rotors connected by a rigid mechanical coupling was analysed by Al-Hussain and Redmond (Al-Hussain & Redmond, 2002).

The magnitude of misalignment is not easy to evaluate on machinery that is running. A system's misalignment forces transmitted from a coupling to a shaft are mainly static, i.e. unidirectional and constant, and are difficult to measure externally with commercial instruments, as has been shown by Piotrowski (Piotrowski, 2007). However, it is possible to estimate the degree of misalignment of the rotor shafts through the measurement of the effect of these forces on the bearing vibrations (Saavedra, P. & Ramırez, D., 2004). Loads generated by misalignment are directly proportional to the degree of misalignment and the coupling stiffness. Because of this, vibration measurement is a good qualitative indicator for detecting the degree of misalignment in machinery while it is running (Saavedra, P. & Ramırez, D., 2004). The vibratory response of the bearings depends greatly on the frequency response functions between the coupling misalignment forces and the bearing (Saavedra, P. & Ramırez, D. , 2004).

In practice, the displacements between nearest neighbour rotors in some systems are coupled by the misalignment, and the dynamic performance of each is affected by the presence of the other (Li, M. & He, 2009).

Most previous work focused on the steady state vibrations of a misaligned rotor coupling bearing system. In this study, the modelling of steady state of a rotor system subjected to a displacement constraint due to the parallel misalignment between two rotors is undertaken. In addition, a model of a four rotor system under the effect of parallel misalignment has been developed and studied. In both cases the presence of the wireless accelerometer sensor is included in the model equation.

6.2 Mathematical Model Objectives

The major objectives of developing a mechanical model for the test rig are to:

1. Improve understanding of rotor dynamics in healthy and faulty conditions (parallel misalignment).
2. Gain an understanding of the changes in rotor vibration signature corresponding to parallel misalignment.
3. Obtain simulation results for healthy and faulty rotor behaviour for comparison with the results obtained from actual laboratory tests, and make an assessment of the accuracy of the simulation in the later chapters.

6.3 Two Rotor Model Developments

The following analysis, using a simplified approach, aims for a better understanding of the basic hypothesis on which this work is based: that vibration generated by misalignment is caused by periodic variations in the coupling stiffness while the shaft is rotating; i.e. the origin of the vibration is of a parametric nature. On this point, only the dependence of the coupling stiffness on the rotation angle will be considered. Further, its influence on the dynamic behaviour of the coupled rotors is discussed.

6.3.1 Test Rig Description

In general, a rotor system can be represented as in Figure 6.1. It consists of a motor (A) and a load (DC generator (BK) with torque measurement device) which are connected together mechanically by flexible coupling (C). The coupling reduces any extra forces on the system caused by imperfections such as misalignment between the motor shaft and the loader shaft, see Figure 6.2.

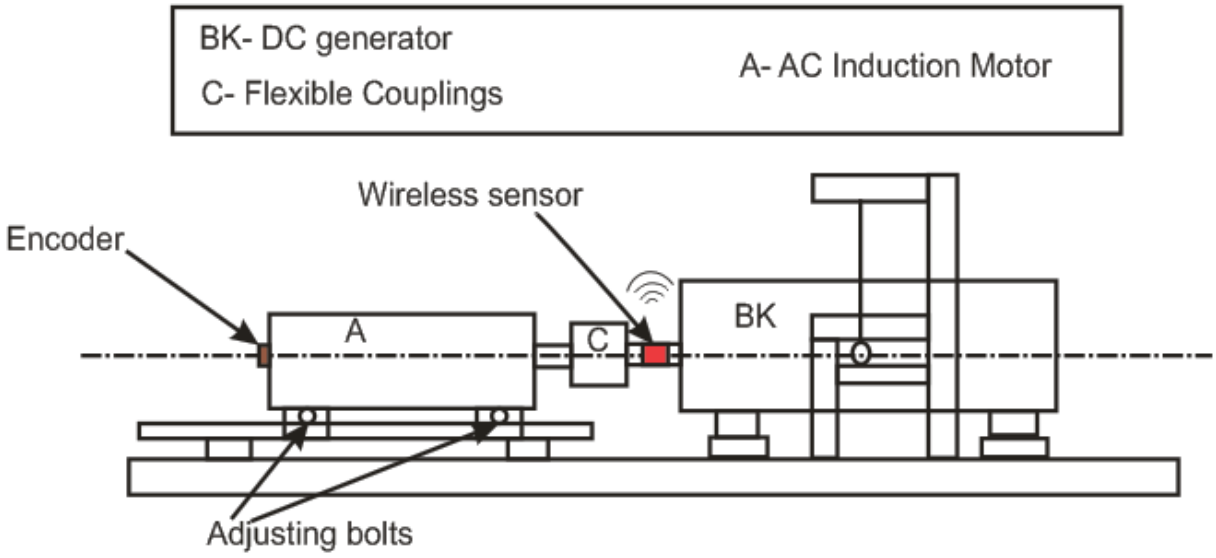

Figure 6.1 Schematic presentation of the test rig

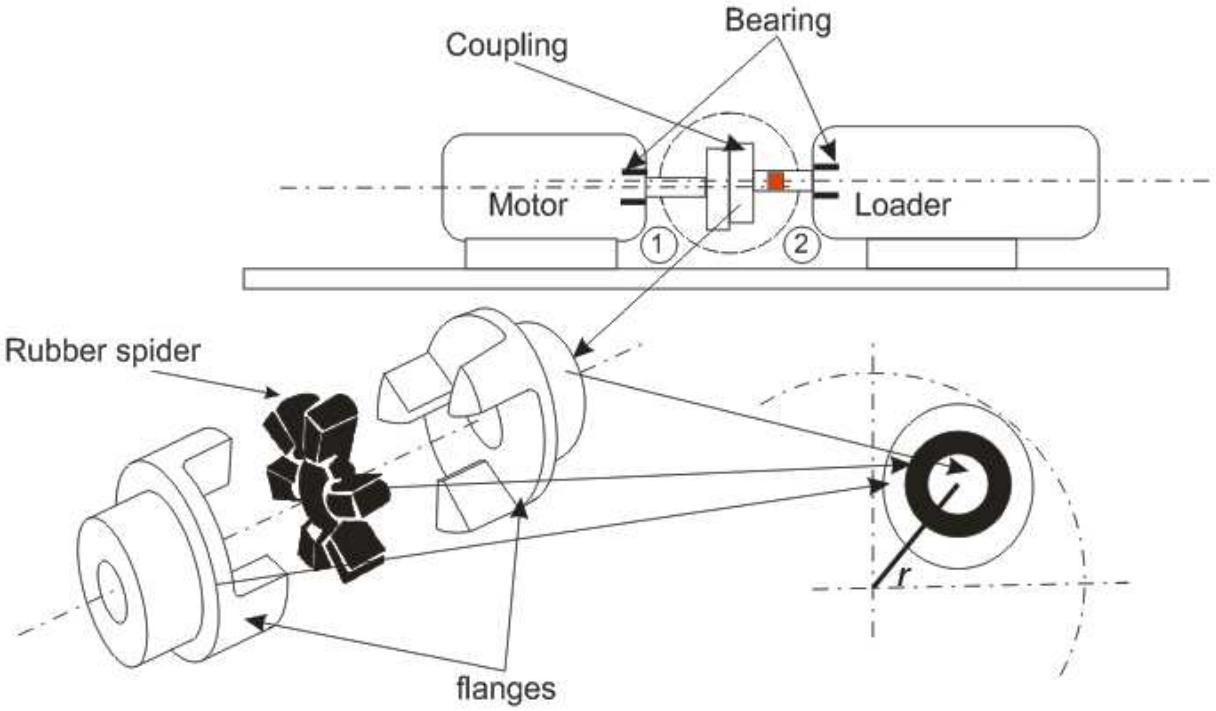

Figure 6.2 Schematic of simplified spider coupling as used in the model

6.3.2 Model of Rotor with Misalignment

The initial model considered comprises two shafts with masses m_1 and m_2 respectively. The shafts are connected by a flexible coupling composed of two three-jaw hubs and one six-legged intermediate elastomeric element, see Figure 6.2. For ease of modelling, the coupling is treated as three pins on one flange and three rings on other flange and with a rubber sleeve between the ring and pin at some distance of radius r from the shaft's centre see bottom right in Figure 6.2. This simplified construction retains the key features of the coupling, i.e. the ring and pin can move relatively in both radial and rotational directions due to the elastomeric rubber sleeve.

The system shown in Figure 6.2 can be modelled as illustrated in Figure 6.3. Two rigid shafts, mounted on motor and load bearings, are connected by the coupling with N pairs of pins/rings on each flange, each pair having a finite stiffness Kb, see Figure 6.3 (a). The system is assumed to be balanced dynamically and hence the exciting forces arise from misalignment and bearings only. More specifically they arise from varying forces in the coupling and bearing. In addition, it is also assumed that the pins on the flange of the first shaft are arranged equidistantly around the circumference of a circle centred on the centre of the shaft cross section, whereas on the second rotor the pins are equidistantly around the circumference of a circle displaced by $\boldsymbol{e_{12}}$ from the centre of the rotor, see Figure 6.2 and Figure 6.3 (b). Thus locus of the coupling pins on rotor 1 follow one circle, whereas those on rotor 2 follow a circle

of different diameter. The wireless accelerometer is mounted tangentially on the second rotor as illustrated in Figure 6.2.

The analysis of the motion commences with first rotor by applying the Euler-Lagrange equation of energy (App. A). The first rotor rotates at angular speed $\dot{\theta}_1$, and the second rotor at $\dot{\theta}_2$, see Figure 6.3 (b). $\dot{\theta}_2$ can vary with respect to $\dot{\theta}_1$. The variation in the angular speed will be related to the acceleration acting on wireless sensor.

The transitional acceleration that each rotor generates due to the supporting bearings is also derived.

The first shaft is considered to be rigid with a very large torsional inertia J_1, lateral stiffness value K_1, and displacements x_1, y_1, and θ_1. The second shaft has torsional inertia J_2, stiffness value K_2 and displacements x_2, y_2 and θ_2. This model considerably retains the physics of the test rig. The steps used to derive the equations of motion using the Lagrange Euler equation are presented in appendix A.

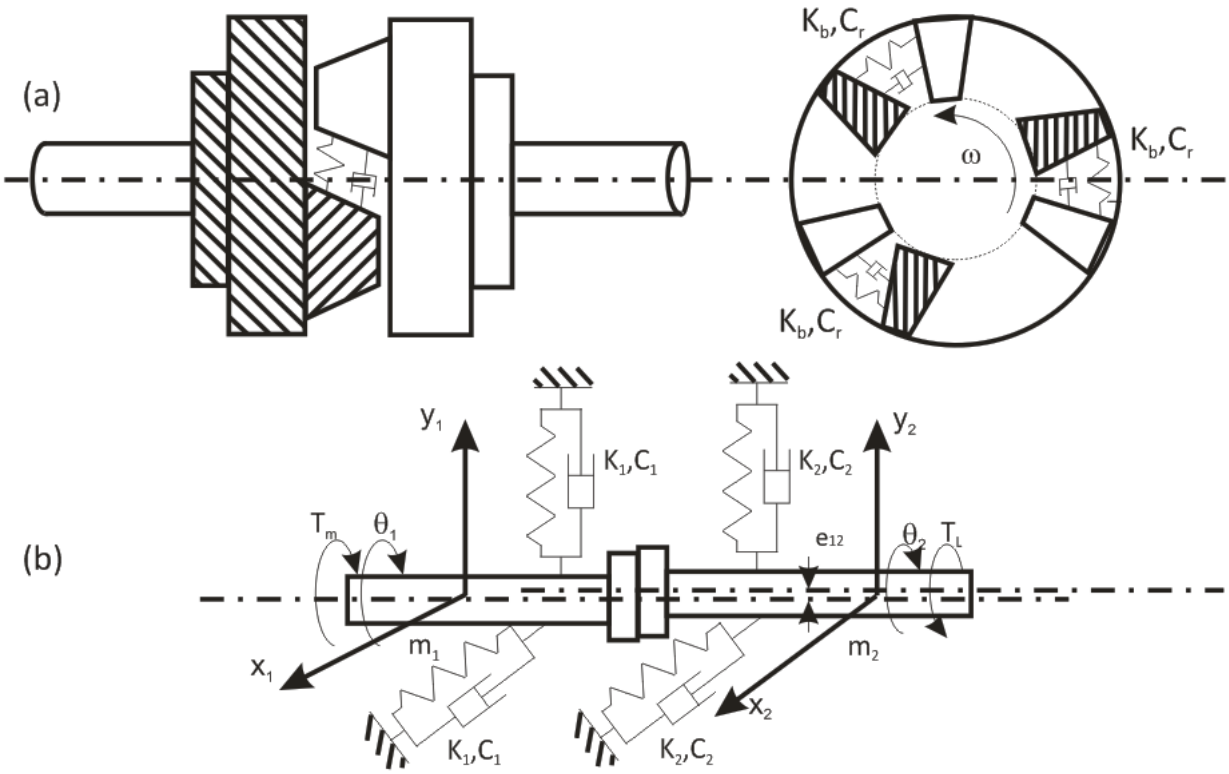

Figure 6.3 Schematic diagram of the vibrating systems
(a) couplings (b) shafts with misalignment

The model equations have been derived (see App. A) and can be written as(Lees, A. W., 2007 (a)):

$$m_1\ddot{x}_1 = -K_1x_1 + NK_b(x_1 - x_2) + NK_b\,\frac{e_{12}}{2}[cos(\theta_1 - \theta_0)](\theta_1 - \theta_2) + Fx_{12} - C_1\dot{x}_1 + dmforcex1$$

$$m_1\ddot{y}_1 = -K_1y_1 + NK_b(y_1 - y_2) - NK_b\,\frac{e_{12}}{2}[sin(\theta_1 - \theta_0)](\theta_1 - \theta_2) + Fy_{12} - C_1\dot{y}_1 + dmforcey1$$

$$J_1\ddot{\theta}_1 = -NK_b\,r^2(\theta_1 - \theta_2) - C_r\left(\dot{\theta}_1 - \dot{\theta}_2\right) - NK_b\,\frac{e_{12}}{2}sin(\theta_1 - \theta_0) + M_{x12} + Mg_{12} + T_m - dmtorque1 \quad \textbf{6.1}$$

$$m_2\ddot{x}_2 = -K_2x_2 - NK_b(x_1 - x_2) - NK_b\,\frac{e_{12}}{2}[sin(\theta_1 - \theta_0)](\theta_1 - \theta_2) - C_2\dot{x}_2 - Fx_{12} + dmforcex2$$

$$m_2\ddot{y}_2 = -K_2y_2 - NK_b(y_1 - y_2) + NK_b\,\frac{e_{12}}{2}[cos(\theta_1 - \theta_0)](\theta_1 - \theta_2) - C_2\dot{y}_2 - Fy_{12} + dmforcey2$$

$$J_2\ddot{\theta}_2 = +NK_b\,r^2(\theta_1 - \theta_2) - C_r\left(\dot{\theta}_1 - \dot{\theta}_2\right) - M_{x12} - Mg_{12} - T_L - dmtorque2$$

Where force excitations due to misalignment are:

$Fx_{12} = NK_b\,\frac{e_{12}}{2}sin(\theta_1 - \theta_0)$

$Fy_{12} = NK_b\,\frac{e_{12}}{2}cos(\theta_1 - \theta_0) - NK_be_{12}$

Torque excitation of coupling due to misalignment is:

$Mg_{12} = NK_b\,\frac{{e_{12}}^2}{2}sin(\theta_1 - \theta_0)$

Oscillating torque generated by coupling due to misalignment is:

$M_{x12} = NK_b\,\frac{e_{12}}{2}(x_1\,sin(\theta_1 - \theta_0) + y_1\,cos(\theta_1 - \theta_0) - x_2\,sin(\theta_1 - \theta_0) - y_2\,cos(\theta_1 - \theta_0))$

Oscillating torque generated by eccentric mass due to unbalance:

$dmtorque1 = 9.81e_cm_{e1}\,cos(\theta_1 - \theta_0)$

$dmtorque2 = 9.81e_cm_{e2}\,cos(\theta_2 - \theta_0)$

Oscillating forces generated by eccentric mass due to unbalance:

$$dmforcex1 = e_c{\dot{\theta}_1}^2 m_{e1}\,cos(\theta_1 - \theta_0)$$

$$dmforcey1 = e_c{\dot{\theta}_1}^2 m_{e1}\,sin(\theta_1 - \theta_0) \quad \textbf{6.2}$$

$$dmforcex2 = e_c{\dot{\theta}_2}^2 m_{e2}\,cos(\theta_2 - \theta_0)$$

$$dmforcey2 = e_c{\dot{\theta}_2}^2 m_{e2}\,sin(\theta_2 - \theta_0)$$

Where, $m_{e1} = m_1$, $m_{e2} = m_2$

J_1, J_2 = polar moments of inertia for motor rotor, second rotor and loader rotor,

$m_1\,m_2$ = the mass of the rotors,

$m_{e1}\,m_{e2}$ = the mass of the rotors at the physical eccentric centre,

e_{12}= the misalignment between shafts,

e_c= the geometric mass centre from rotational centre,

r = radius of the centre of coupling pin position on reference shaft,

T_m = the driving torque,

T_L = the torsional load,

N = the number of equivalent pins/rings in each flange,

K_b = the coupling stiffness of each pair of pin/ring,

C_1, C_2 = damping of rotors 1 and 2 respectively,

K1, K2 = stiffness of rotors 1 and 2 respectively, and

C_r= coupling critical damping.

Using the solver ODE45 (implements the Runge-Kutta (4,5) method) function available in MATLAB, the system given by Equations (6.1) can be solved to obtain displacements and velocity of rotors in the directions of interest. The accelerations: $\boldsymbol{a_x}$, $\boldsymbol{a_y}$, $\boldsymbol{a_w}$ and $\boldsymbol{a_t}$, respectively the lateral accelerations due to shaft bending or bearing clearances in the x and y directions, the angular acceleration due to rotational motion and the total tangential acceleration of the rotors, can be calculated by differentiating the corresponding velocities.

When the wireless accelerometer rotates in a circular path around a centre, its principal sensitivity axis also rotates and hence sensor output due to the relative change in direction of the earth's gravitational field is:

$$a_s = -\mathrm{g}\cos(\theta_2) \tag{6.3}$$

6.4 Output of Wireless Sensor

Figure 6.4 illustrates the relationship of different acceleration components at P where the wireless sensor is mounted. Decomposing these accelerations in the tangential direction, a representation of the electrical output waveform from the sensor can be obtained.

The accelerations at the sensor position can be found by decomposing $\boldsymbol{a_x}$ and $\boldsymbol{a_y}$ onto the tangential direction by:

$$\begin{aligned} \boldsymbol{a_{tx}} &= -\ddot{\mathrm{x}}_2\sin(\theta_2) \\ \boldsymbol{a_{ty}} &= \ddot{\mathrm{y}}_2\cos(\theta_2) \end{aligned} \tag{6.4}$$

Acceleration due to rotational angular acceleration is:

$$\boldsymbol{a_{tw}} = r_2\,\ddot{\theta}_2 \tag{6.5}$$

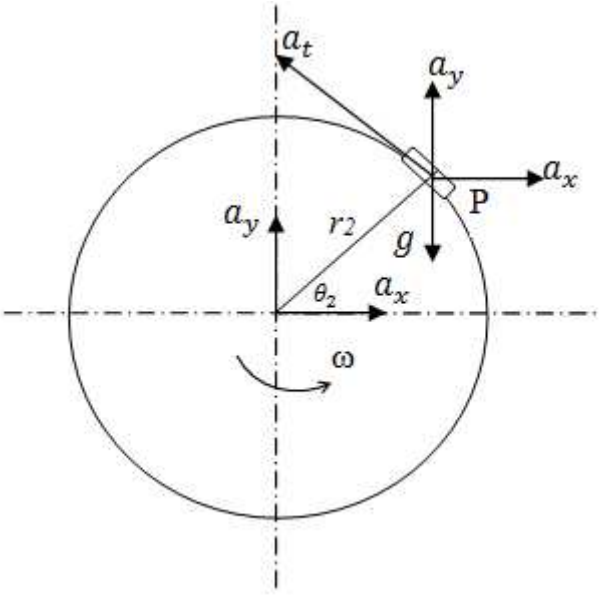

Figure 6.4 Schematic diagram of the wireless accelerometer mounted on rotor showing the different accelerations

Adding to yield the total acceleration in the tangential direction:

$$\boldsymbol{a_t = a_{tx} + a_{ty} + a_{tw}} \qquad \textbf{6.6}$$

The total sensor output $\mathrm{E_T}$ at P will be the sum of all accelerations in the tangential direction plus that due to gravitational effects, divided by the sensitivity of the sensor S:

$$\mathrm{E_T} = (\boldsymbol{a_t} + \boldsymbol{a_s})/\mathrm{S} \qquad \textbf{6.7}$$

The output of the wireless sensor shown in Equation (6.7) is due to a combination of different accelerations. These accelerations will be measured simultaneously by one sensor mounted on the surface of the shaft. That means it can detect different rotor problems which is a cost-effective approach. Moreover, it has the high sensitivity to incipient deviations and can produce a comprehensive assessment for the condition of the rotor system.

6.5 Simulation Study

To gain a better understanding of the dynamic behaviour of the rotor system and quantitative effects of different rotor faults, a simulation study was conducted based on a bearing test rig with layout shown in Figure 6.1 and rotor parameters shown in Table 6.1 (see also appendix B). The parameter for the damping coefficient was given a high value assuming that it is higher than critical damping of the system so that transient effects is minimised and the effect of misalignments are highlighted.

Table 6.1 Parameters for simulation study

Description	Symbol	Unit	Value
Shaft1 Diameter	D_1	m	0.030
Shaft1 Length	L_1	m	0.540
Shaft1 Mass	m_1	kg	12.73
Shaft2 Diameter	D_2	M	0.035
Shaft2 Length	L_2	M	0.760
Shaft2 Mass	m_2	kg	34.96
Radius of centre for the equivalent pin/ring	r	M	0.10
Coupling Damping	C_r	N/(m/s)	101.30
Coupling Stiffness	K_b	N/m	1.1×10^7
Rotor Stiffness	K_1,K_2	N/m	1.0×10^8
Moment of inertia	J_1	kg m^2	0.0061
Moment of inertia	J_2	kg m^2	0.0196
Eccentricity	e_c	M	10.0×10^{-4}
Misalignment (offset)	e_{12}	M	0.5×10^{-3}
Torsional load	T_L	Nm	50
Driving torque	T_m	Nm	50

6.6 Characteristics of Vibrations due to Misalignment

Figure 6.5 shows a typical result from numerical simulation studies when the motor operates at a speed of 750 RPM 0.5mm misalignment. It can be seen from Figure 6.5 (a) and (b) that waveforms of lateral accelerations: $\boldsymbol{a_x}$ and $\boldsymbol{a_y}$ are close to sinusoidal waves whereas the waveform of rotational acceleration $\boldsymbol{a_w}$ exhibits a complex fluctuation. These show that shaft misalignment leads to shaft fluctuations with different frequency contents in different directions.

Further examination of the results in the frequency domain found that the fundamental rotational component 1X dominates the spectra, as expected and as shown Figure 6.5 (c). The spectra show distinctive 2X components, which is the feature commonly used for diagnosing misalignments (Dewell & Mitchell, 1984; Sekhar, A. S. & Prabhu, 1995). The rotational acceleration, $\boldsymbol{a_w}$, shows more significant amplitudes at 2X whereas lateral vibrations exhibits distinctive components at 2X and 3X. These indicate that both rotational and lateral accelerations are sensitive to misalignment but with different frequency components. In general, these spectral features show that the model is adequate for exploring shaft misalignment and examining the output behaviour of the wireless accelerometer.

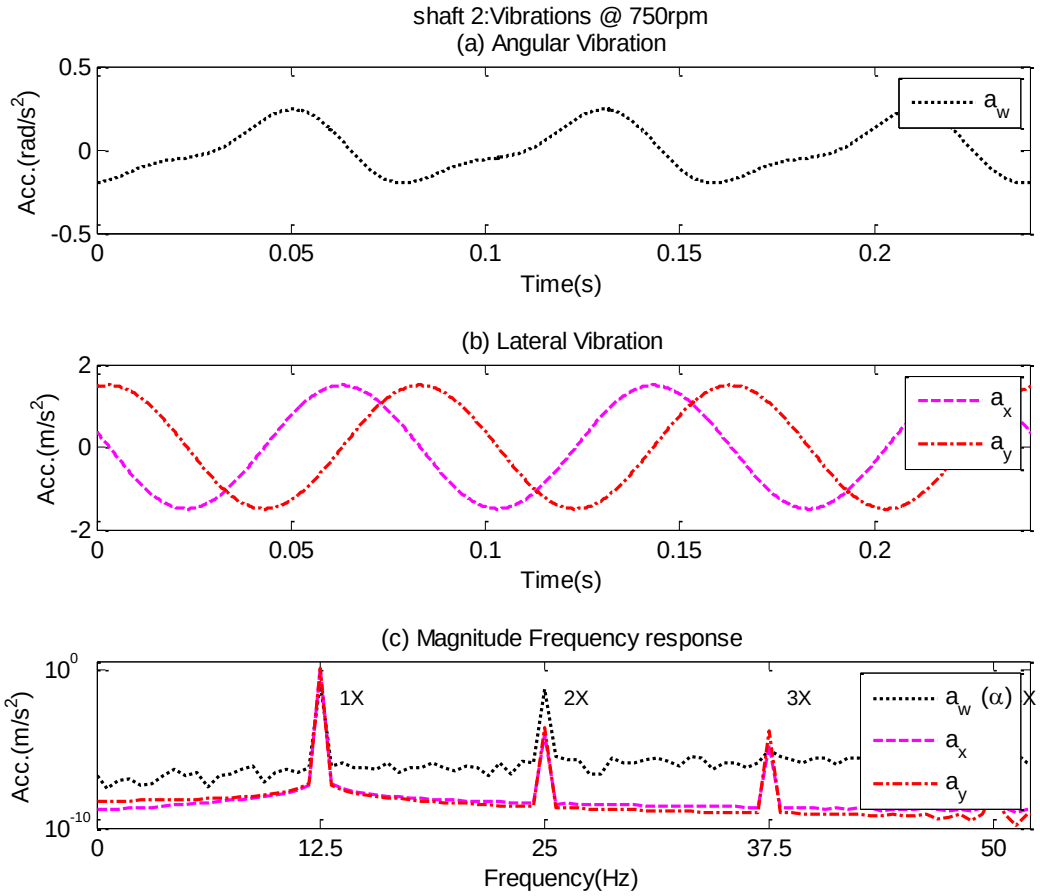

Figure 6.5 (a and b) waveforms for lateral and rotational acceleration, (c) waveform spectra.

Figure 6.6 (a) shows the tangential components: a_{tx}, a_{ty} and a_{tw} predicted at the accelerometer position due to accelerations: a_x, a_y and a_w. It can be seen that a_{tx} and a_{ty} fluctuate twice as fast as the original but with opposite phase. Combining these two components together produces a nearly steady value (a "DC" component). On the other hand, a_{tw} is in phase with a_t but with a much smaller magnitude due to the constant sensor position on the shaft surface. By combining the three components, the total acceleration a_t at P exhibits the same fluctuations as a_{tw} but with a clear DC shift due to the combination of a_{tx} and a_{ty}. The root mean squared (RMS) value of a_t is 1.448, slightly larger than the 1.059 of a_{tx} and a_{ty} and much greater than the value 0.002 of a_{tw}. This shows that the wireless sensor output will have a higher output than the other accelerations (a_{tx}, a_{ty}, a_{tw}) and hence be more sensitive to changes in acceleration due to faults.

In the frequency domain, the spectrum resulting from the combination of a_{tx} and a_{ty} is seen to have a low value except for sharp and distinct peaks at multiples of 12.5 Hz see Figure 6.6 (b). The spectrum for a_{tw} has a generally higher amplitude but without any distinct peaks. When combining the spectra of a_{tx} and a_{ty}, to obtain the spectrum of a_{txy}, it can be seen that the first four harmonics are clearly discernible. However, it can also be seen that the difference in

amplitude between $\boldsymbol{a_{tw}}$ and $\boldsymbol{a_t}$ is marginal at the lower harmonics 1X and 2X, indicating that these two components are mainly from the effects of rotational oscillation. On the other hand, amplitudes at 3X and 4X of $\mathbf{a_{txy}}$ show a distinctive increase, which means that the contribution from lateral vibration is more significant at these two components and that the combined ($\boldsymbol{a_t}$) spectrum is more sensitive to changes due to misalignments.

When considering the accelerometer output, gravitational acceleration of 9.81 ms^{-2} has to be included which results in the waveform shown in Figure 6.7 (a). This superimposition alters the spectrum at only 1X, i.e. increases it by 9.81 ms^{-2}. Other spectral features remain the same, as shown.

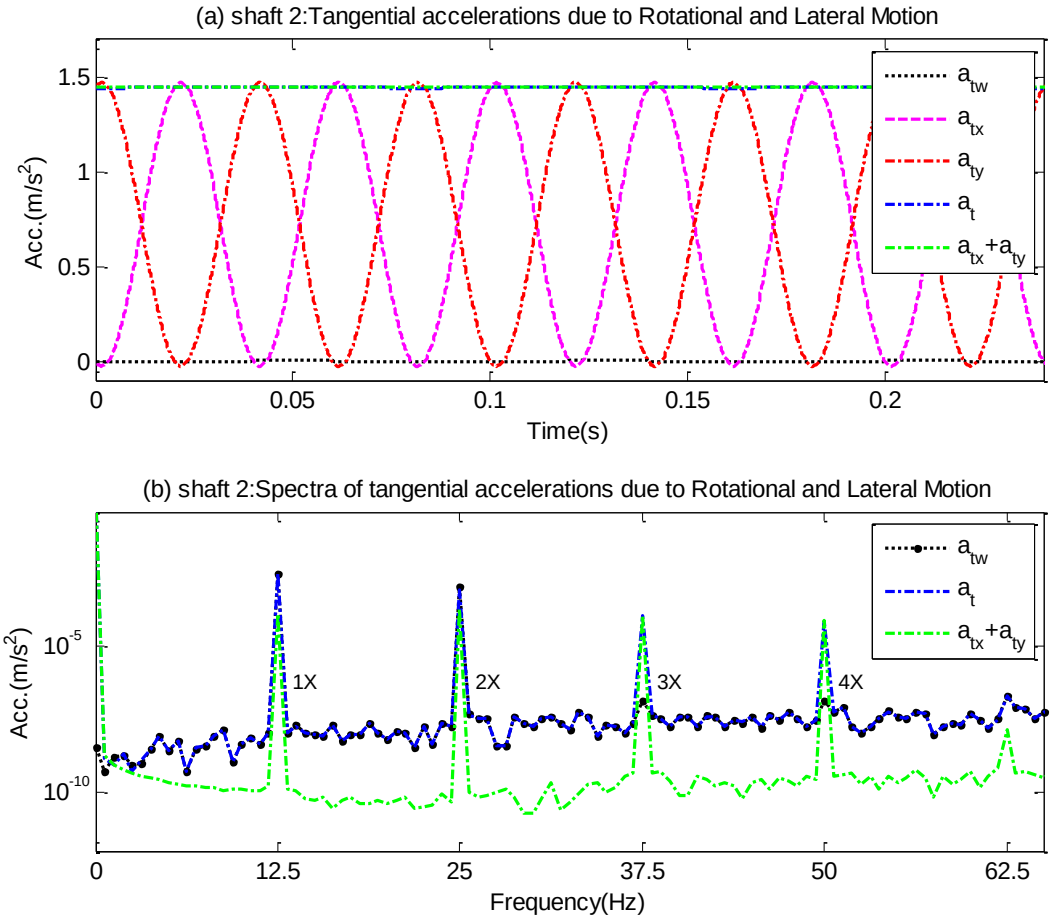

Figure 6.6 (a) Time domain waveforms, (b) spectra of lateral and rotational acceleration at sensor position predicted by model

To validate model results, the test rig shown in Figure 6.1 was run at 729 RPM with 0.5 mm misalignment. The measured waveforms from the wireless sensor given in Figure 6.8 with the same condition exhibit the same response as the model. The speed used is slightly smaller than that used in the model. The main features of the model are achieved experimentally. In the frequency domain, the spectrum of measured waveform show similarity to the model output spectrum.

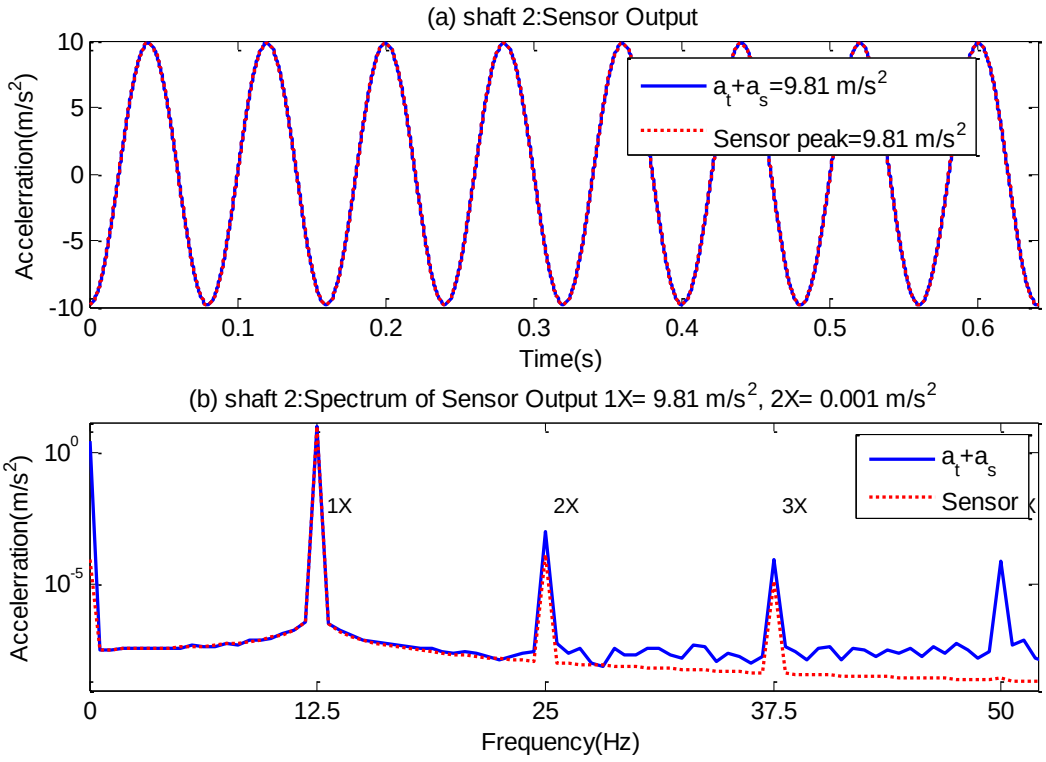

Figure 6.7 Predicted waveforms and spectrum from a wireless accelerometer

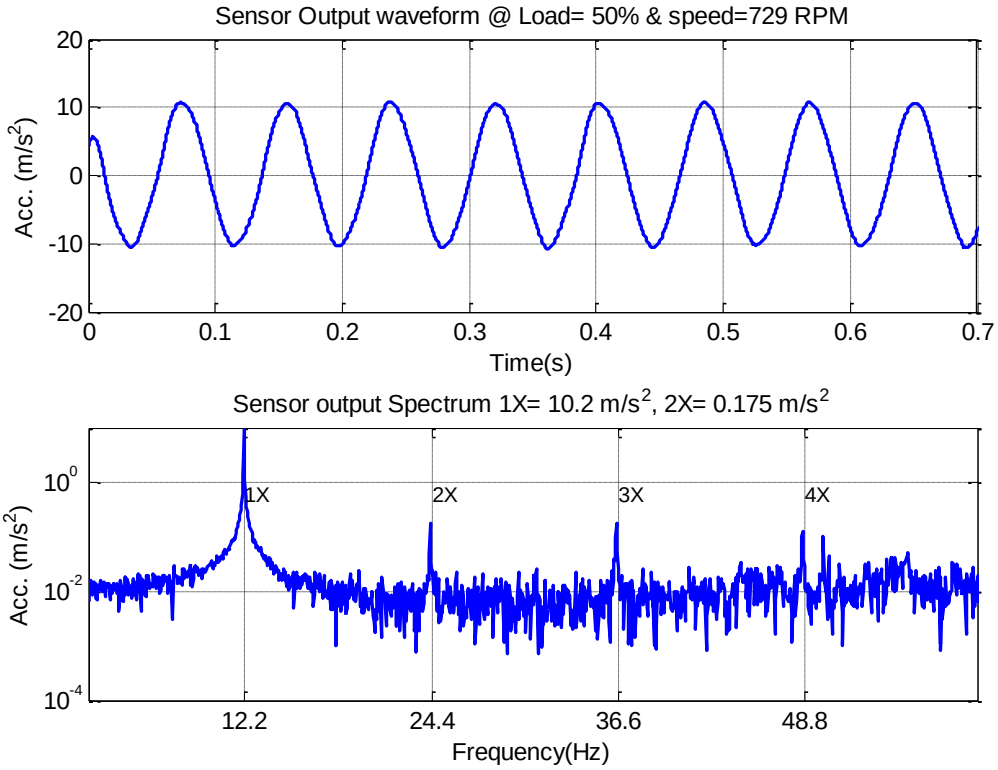

Figure 6.8 Measured waveform and its spectrum from a wireless accelerometer at 729 RPM and 0.5mm misalignment

The spectrum is dominated by peaks at 1X and 2X, but the measured response also has other peaks not caused by forces acting on the shaft. These will include the power line frequency and other complicated mechanical responses. To remove this noise from the spectrum, the same data were processed using time synchronous averaging (TSA) (Harris, C. M., 1988) triggered by a synchronized repetitive pulse (see Section 4.7). In this case, one tachometric pulse per shaft turn was used. This process enhances the synchronous spectral components (at multiple frequencies of shaft speed) and reduces the amplitude of the non-synchronous components (i.e. random noise and periodic vibrations with frequencies at non-integer multiples of the shaft speed). Figure 6.9 shows the order spectrum of synchronous time averaged vibration waveform from the wireless sensor obtained using an order number of 200 averages and 10 revolutions. This means that 200 chunks of 10 periods are averaged to eliminate unsynchronised noise within the signal. It can be seen from this order spectrum that the TSA procedure has removed the spectral contribution of the electrical frequencies and enhanced the order harmonics of the shaft speed (1X, 2X, 3X,..) compared to measured signal before application of TSA Figure 6.8. This allows the focus to be on the mechanical vibration, so that it is easier to diagnose the source of the vibration.

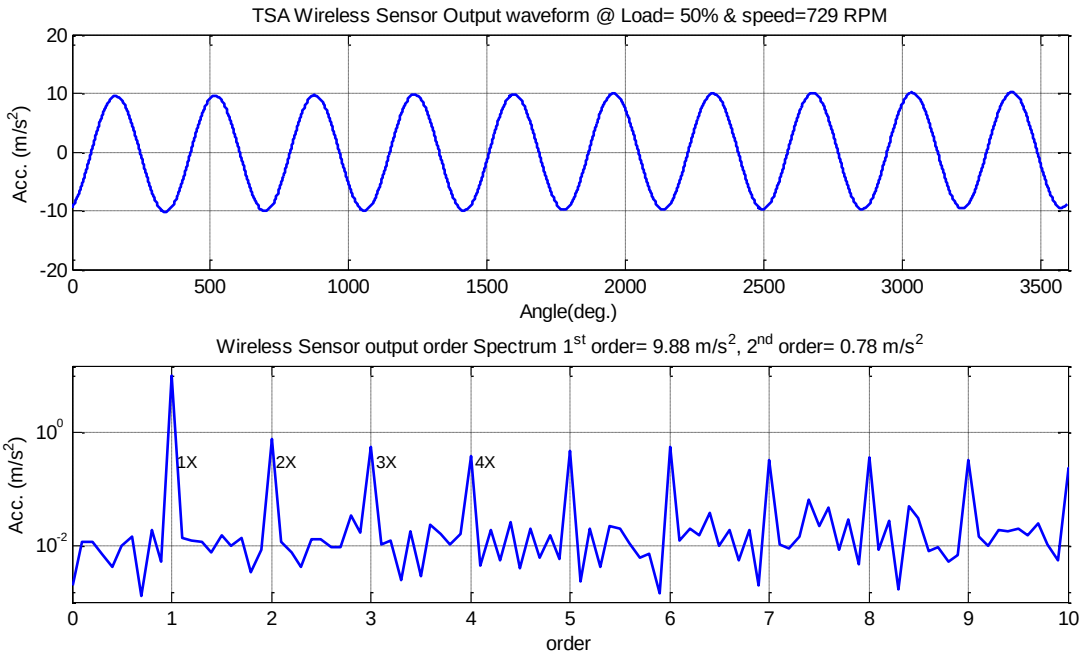

Figure 6.9 Measured waveform and its spectrum from a wireless accelerometer at 729 RPM and 0.5mm misalignment after application of TSA.

6.7 Characteristics of Spectral Amplitude with Misalignment and Speed

To examine further the changes of spectral amplitude for misalignment diagnosis a simulation study was performed under different motor speeds and different degrees of misalignment. Figure 6.10 shows the amplitude changes for the first four harmonics of the second shaft. It represents the combination of all accelerations $\mathbf{a_t}$ ($\mathbf{a_{txy}}$ and $\mathbf{a_{tw}}$) and the rotational ($\mathbf{a_{tw}}$).

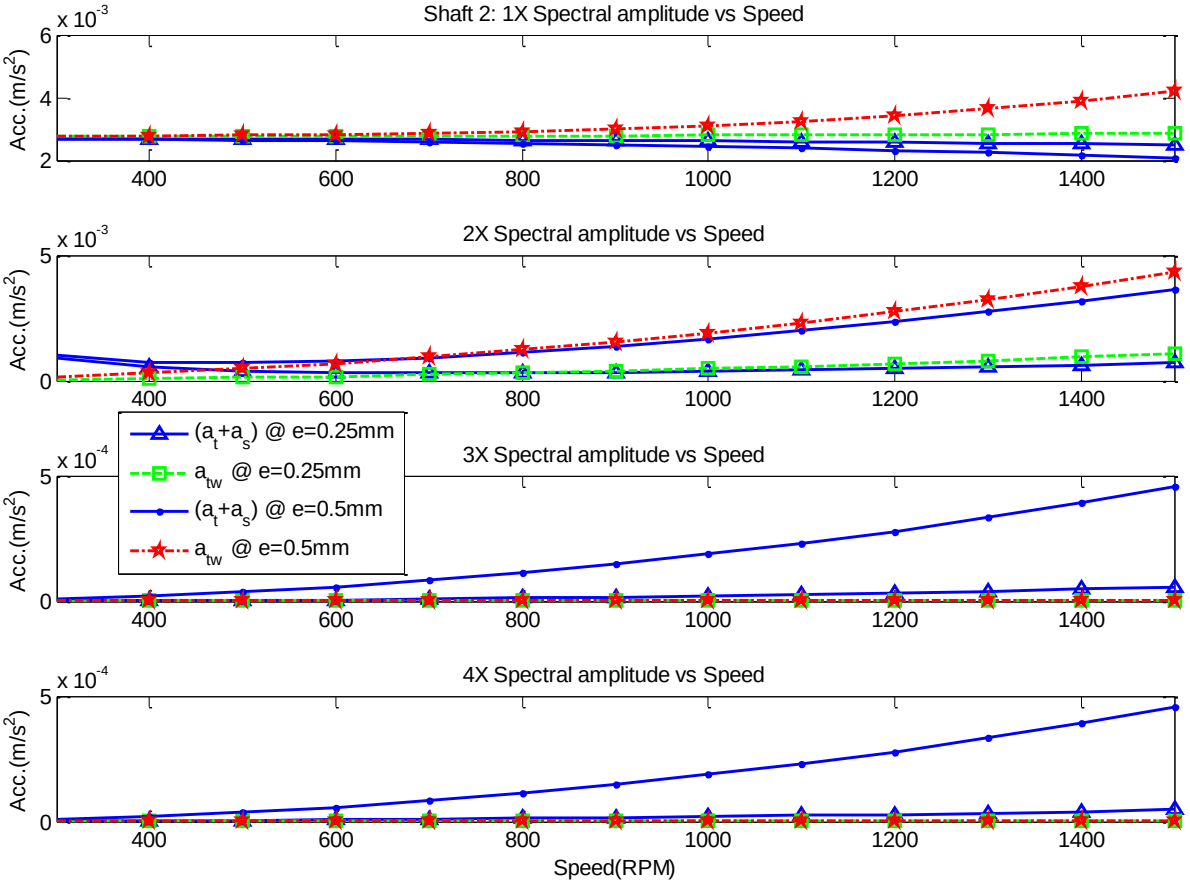

Figure 6.10 Spectral amplitude versus speeds for different misalignments (shaft 2)

By comparing relative spectral amplitudes of combination ($\boldsymbol{a_t}$ +$\boldsymbol{a_s}$) and $\mathbf{a_{tw}}$ at different rotation speeds and misalignment, it can be observed that:

The amplitude of the 1X spectral peak from combination ($\boldsymbol{a_t}$+$\boldsymbol{a_s}$) after subtraction 9.81 m/s^2 exhibits small changes with increasing shaft speeds and with the degree of misalignment. However, it is lower than that of rotational ($\boldsymbol{a_{tw}}$) at small and high degree of misalignment. It is concluded that the amplitude at 1X is not suitable for misalignment detection.

The amplitude of the 2X spectral peaks from both combination and rotation increases with both shaft speed and the degree of misalignment. In each case of misalignment the peaks for combination and rotation ($\boldsymbol{a_{tw}}$) had similar amplitudes. It thus is a good indicator of misalignment at higher speed.

Figure 6-10 also shows that the amplitude of 3X for the combined acceleration increases with both shaft speed and the degree of misalignment. It is especially noticeable that there is a large relative increase for the higher degree of misalignment (i.e. e increases from 0.25 to 0.5 mm). The amplitude of the 3X peak due to rotational does not change with speed or misalignment. Thus the 3X peak from combination could be a good indicator of misalignment. However, the absolute amplitudes of the 3X peak are about 1000 times less than the values for the 1X and 2X peaks, which may an important factor when considering measurement accuracy. A very similar situation is observed with the 4X peak.

In general, the amplitude variations of combined acceleration at 2X, 3X and 4X could be a good indicator of misalignment. However, the magnitudes of the 3X and 4X peaks were very low and would be influenced by measurement noise. It is concluded that the amplitude of combination and rotational at 2X can be a basis for misalignment detection which is the common characteristics used for misalignment detection (Dewell & Mitchell, 1984; Sekhar, A. S. & Rao, 1996 a).

6.8 Multi Rotor Machine Model Development

The model derived in the previous section is extended to a four rotor system. Applying the same principles and manipulation techniques, the model of the test rig with four rotors was derived. This was done to better understand the different rotors dynamics due to parallel misalignment.

6.8.1 Model of Misaligned Rotors

In general, a rotor system can be represented in Figure 6.11. It consists of a motor and a loader (DC generator with torque measurement device) which are mechanically connected together by two shafts and three flexible couplings. As previously, the coupling reduces extra forces on the system caused by any forms of imperfections such as misalignment between the motor shaft and the loader shaft, as shown in Figure 6.11.

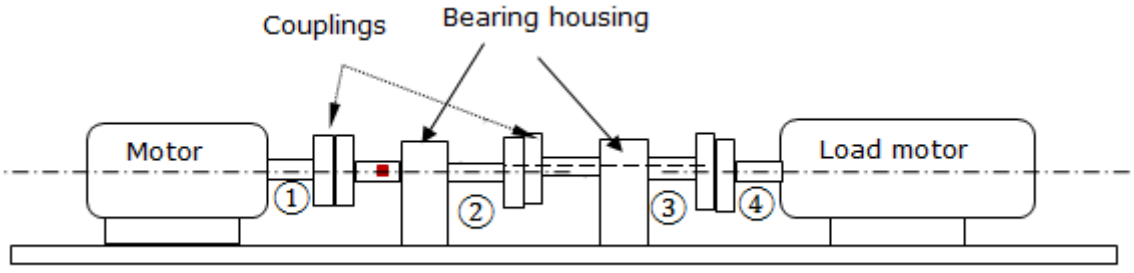

Figure 6.11 System schematic of system with four shafts and three simplified spider couplings for modelling

6.8.2 Model of Rotor with Misalignment

The model considered comprises four shafts with mass m_1, m_2, m_3 and m_4 respectively. The shafts are connected by three flexible couplings. Each coupling is composed of two three-jaw hubs and one six-legged intermediate elastomeric element as described above in Section 5.2.2 and shown in the bottom right of Figure 6.2.

The system shown in Figure 6.11 can be simplified as depicted in Figure 6.12. Two rigid shafts, mounted on ball-rolling bearings, are connected by the coupling with N pairs of pins/rings on each flange, each pair having a finite stiffness K_b. The system is assumed to be balanced dynamically and hence the exciting forces arise only from misalignment and bearings, more specifically they arise from varying forces in the coupling and bearing. In addition, it is also assumed that the pins on the flange of the third shaft are arranged around a circle centred on the centre of the shaft cross section whereas on the second and forth rotor the pins are again positioned on a circle displaced by $\boldsymbol{e_{23}}$ and $\boldsymbol{e_{34}}$ from the centre of the rotor as illustrated in Figure 6.2 and Figure 6.12. The wireless accelerometer is mounted tangentially on the second rotor as shown in Figure 6.11.

The analysis of the motion commences with first rotor by applying the Euler-Lagrange energy equation. The first rotor rotates at speed $\dot{\theta}_1$, the second, third and fourth rotors at $\dot{\theta}_2$, $\dot{\theta}_3$, and $\dot{\theta}_4$ respectively and each can vary as shown in Figure 6.12. The variation in the angular speed is directly related to the acceleration acting on the wireless sensor. The transitional acceleration that each rotor experiences due to the supporting bearings is also derived.

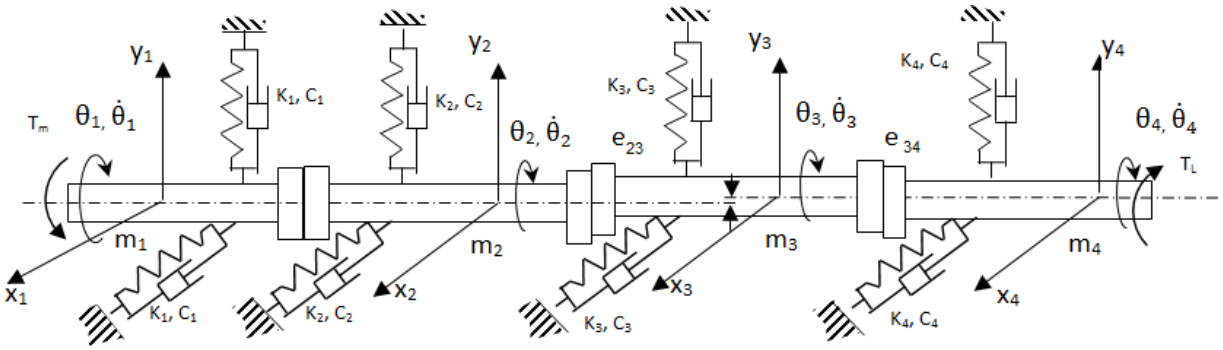

Figure 6.12 Schematic diagram of the vibrations modes

Note the locus of the coupling pins: on rotor 1, 2 and 4 follows the same circular motion, whereas those on rotor 3 follow a circle of different diameter, see Figure 6.12. The first shaft is considered to be rigid and has very large torsional inertia J_1 and lateral stiffness value K_1. It has displacements x_1, y_1, θ_1. The fourth shaft has torsional inertia J_4 and stiffness value K_4 and displacements x_4, y_4, θ_4. Similarly, shafts two and three have torsional inertias J_2 and J_3, stiffness's K_2 and K_3 and displacements x_2, y_2, θ_2 and x_3, y_3, θ_3 respectively. The model equations have been derived (see Appendix A) and can be written as:

$$
\begin{aligned}
m_1\ddot{x}_1 &= -K_1x_1 + N\mathrm{K_b}(x_1 - x_2) + N\mathrm{K_b}\,\frac{e_{12}}{2}[cos(\theta_1 - \theta_0)](\theta_1 - \theta_2) - C_1\dot{x}_1 + Fx_{12} + dmforcex1\\
m_1\ddot{y}_1 &= -K_1y_1 + N\mathrm{K_b}(y_1 - y_2) - N\mathrm{K_b}\,\frac{e_{12}}{2}[sin(\theta_1 - \theta_0)](\theta_1 - \theta_2) - C_1\dot{y}_1 + Fy_{12} + dmforcey1\\
J_1\ddot{\theta}_1 &= -N\mathrm{K_b}\,r^2(\theta_1 - \theta_2) - C_{r1}\left(\dot{\theta}_1 - \dot{\theta}_2\right) + M_x12 + Mg12 + T_m - dmtorque1
\end{aligned}
\qquad \textbf{6.8}
$$

$$
\begin{aligned}
m_2\ddot{x}_2 &= -K_2x_2 - N\mathrm{K_b}(x_1 - x_2) - N\mathrm{K_b}\,\frac{e_{12}}{2}[cos(\theta_2 - \theta_0)](\theta_1 - \theta_2) - Fx_{12}\\
&\quad -N\mathrm{K_b}(x_2 - x_3) - N\mathrm{K_b}\,\frac{e_{23}}{2}[cos(\theta_2 - \theta_0)](\theta_2 - \theta_3) + Fx_{12} - C_2\dot{x}_2 + dmforcex2\\
m_2\ddot{y}_2 &= -K_2y_2 - N\mathrm{K_b}(y_1 - y_2) + N\mathrm{K_b}\,\frac{e_{12}}{2}[sin(\theta_1 - \theta_0)](\theta_1 - \theta_2) - Fy_{12}\\
&\quad -N\mathrm{K_b}(y_2 - y_3) + N\mathrm{K_b}\,\frac{e_{23}}{2}[sin(\theta_2 - \theta_0)](\theta_2 - \theta_3) - C_2\dot{y}_2 + Fy_{23} + dmforcey2\\
J_2\ddot{\theta}_2 &= +N\mathrm{K_b}\,r^2(\theta_1 - \theta_2) + C_{r1}\left(\dot{\theta}_1 - \dot{\theta}_2\right) - M_{x12} - Mg_{12}\\
&\quad -N\mathrm{K_b}\,r^2(\theta_2 - \theta_3) - C_{r2}\left(\dot{\theta}_2 - \dot{\theta}_3\right) + M_{x23} + Mg_{12} - dmtorque2
\end{aligned}
\qquad \textbf{6.9}
$$

$$
\begin{aligned}
m_3\ddot{x}_3 &= -K_3x_3 + N\mathrm{K_b}(x_2 - x_3) + N\mathrm{K_b}\,\frac{e_{23}}{2}[cos(\theta_2 - \theta_0)](\theta_2 - \theta_3) - Fx_{23}\\
&\quad +N\mathrm{K_b}(x_3 - x_4) + N\mathrm{K_b}\,\frac{e_{34}}{2}[cos(\theta_3 - \theta_0)](\theta_3 - \theta_4) - C_3\dot{x}_3 + Fx_{34} + dmforcex3\\
m_3\ddot{y}_3 &= -K_3y_3 + N\mathrm{K_b}(y_2 - y_3) - N\mathrm{K_b}\,\frac{e_{23}}{2}[sin(\theta_2 - \theta_0)](\theta_2 - \theta_3) - Fy_{23}\\
&\quad +N\mathrm{K_b}(y_3 - y_4) - N\mathrm{K_b}\,\frac{e_{34}}{2}[sin(\theta_3 - \theta_0)](\theta_3 - \theta_4) - C_3\dot{y}_3 + Fy_{34} + dmforcey3\\
J_3\ddot{\theta}_3 &= +N\mathrm{K_b}\,r^2(\theta_2 - \theta_3) + C_{r2}\left(\dot{\theta}_2 - \dot{\theta}_3\right) - M_{x23} - Mg_{23}\\
&\quad -N\mathrm{K_b}\,r^2(\theta_3 - \theta_4) - C_{r3}\left(\dot{\theta}_3 - \dot{\theta}_4\right) + M_{x34} + Mg_{34} - dmtorque3
\end{aligned}
\qquad \textbf{6.10}
$$

$$
\begin{aligned}
m_4\ddot{x}_4 &= -K_4x_4 - N\mathrm{K_b}(x_3 - x_4) + N\mathrm{K_b}\,\frac{e_{34}}{2}[cos(\theta_4 - \theta_0)](\theta_3 - \theta_4) - C_4\dot{x}_4 - Fx_{34} + dmforcex4\\
m_4\ddot{y}_4 &= -K_4y_4 - N\mathrm{K_b}(y_3 - y_4) + N\mathrm{K_b}\,\frac{e_{34}}{2}[sin(\theta_4 - \theta_0)](\theta_3 - \theta_4) - C_4\dot{y}_4 - Fy_{34} + dmforcey4\\
J_4\ddot{\theta}_4 &= +N\mathrm{K_b}\,r^2(\theta_3 - \theta_4) + C_{r3}\left(\dot{\theta}_3 - \dot{\theta}_4\right) - M_{x34} - Mg_{34} - T_L - dmtorque4
\end{aligned}
\qquad \textbf{6.11}
$$

Where the excitation forces and torques are:

The force excitations due to misalignment are:

$$Fx_{12} = -N\mathrm{K_b}\,\frac{e_{12}}{2}sin(\theta_1 - \theta_0)$$

$$Fy_{12} = N\mathrm{K_b}\frac{e_{12}}{2}cos(\theta_1 - \theta_0) - NKbe_{12}$$

$$Fx_{12} = -N\mathrm{K_b}\,\frac{e_{23}}{2}sin(\theta_2 - \theta_0)$$

$$Fy_{23} = N\mathrm{K_b}\frac{e_{23}}{2}cos(\theta_2 - \theta_0) - NKbe_{23}$$

$$Fx_{34} = -N\mathrm{K_b}\frac{e_{34}}{2}sin(\theta_3 - \theta_0)$$

$$Fy_{34} = N\mathrm{K_b}\frac{e_{34}}{2}cos(\theta_3 - \theta_0) - N\mathrm{K_b}e_{34}$$

Torque excitations of coupling due to misalignment are:

$$Mg_{12} = -N\mathrm{K_b}\frac{e^2{}_{12}}{2}sin(\theta_1 - \theta_0)$$

$$Mg_{23} = -N\mathrm{K_b}\frac{e^2{}_{23}}{2}sin(\theta_2 - \theta_0)$$

$$Mg_{34} = -N\mathrm{K_b}\frac{e^2{}_{34}}{2}sin(\theta_3 - \theta_0)$$

Oscillating torque generated by coupling due to misalignment:

$$M_{x_{12}} = N\mathrm{K_b}\frac{e_{12}}{2}[-x_1 cos(\theta_1 - \theta_0) + y_1 \sin(\theta_1 - \theta_0) + x_2 cos(\theta_1 - \theta_0) - y_2 \sin(\theta_1 - \theta_0)]$$

$$M_{x_{23}} = N\mathrm{K_b}\frac{e_{23}}{2}[-x_2 cos(\theta_2 - \theta_0) + y_2 \sin(\theta_2 - \theta_0) + x_3 cos(\theta_2 - \theta_0) - y_3 \sin(\theta_2 - \theta_0)]$$

$$M_{x_{34}} = N\mathrm{K_b}\frac{e_{34}}{2}[-x_3 cos(\theta_3 - \theta_0) + y_3 \sin(\theta_3 - \theta_0) + x_4 cos(\theta_3 - \theta_0) - y_4 \sin(\theta_3 - \theta_0)]$$

Torsional oscillating torque generated by eccentric mass due to unbalance:

$$dmtorque1 = 9.81e_c m_{e1}\cos(\theta_1 - \theta_0)$$

$$dmtorque2 = 9.81e_c m_{e2}\cos(\theta_2 - \theta_0)$$

$$dmtorque3 = 9.81e_c m_{e3}\cos(\theta_3 - \theta_0)$$

$$dmtorque4 = 9.81e_c m_{e4}\cos(\theta_4 - \theta_0)$$

Where, e_c is the geometric mass centre from rotational centre;

Lateral oscillating forces generated by eccentric mass due to unbalance:

$$dmforcex1 = e_c\dot{\theta}_1{}^2 m_{e1} cos(\theta_1 - \theta_0)$$

$$dmforcey1 = e_c\dot{\theta}_1{}^2 m_{e1} sin(\theta_1 - \theta_0)$$

$$dmforcex2 = e_c\dot{\theta}_2{}^2 m_{e2} cos(\theta_2 - \theta_0)$$

$$dmforcey2 = e_c\dot{\theta}_2{}^2 m_{e2} sin(\theta_2 - \theta_0)$$

$$dmforcex3 = e_c\dot{\theta}_1{}^2 m_{e3} cos(\theta_3 - \theta_0)$$

$$dmforcey3 = e_c\dot{\theta}_3{}^2 m_{e3} sin(\theta_3 - \theta_0)$$

$$dmforcex4 = e_c\dot{\theta}_1{}^2 m_{e4} cos(\theta_4 - \theta_0)$$

$$dmforcey4 = e_c\dot{\theta}_4{}^2 m_{e4}\cos(\theta_4 - \theta_0)$$

And

J_1, J_2, J_3, J_4 = polar moments of inertia for motor rotor ,second rotor and loader rotor,

$m_1\ m_2\ m_3\ m_4$ = the mass of the rotors and loader,

e_c = the geometric mass centre from rotational centre,

e_{12}, e_{23}, e_{34} = the misalignment between shafts,

r = radius of the centre of coupling pin position on reference shaft,

T_m = the driving torque,

T_L = the tortional load,

N = the number of equivalent jaws in each flange,

C_1, C_2, C_3, C_4 = damping coefficients of rotor1, 2, 3 and 4 respectively,

K_1, K_2, K_3, K_4 = stiffness coefficients of rotor1, 2, 3 and 4 respectively,

C_{r1}, C_{r2}, C_{r3} = coupling critical damping,

K_b = the coupling stiffness of each pair of jaws,

When the wireless accelerometer rotates in a circular path around a centre, its principal sensitivity axis also rotates and hence sensor output due to the relative change in direction of the earth's gravitational field is as given in Equation (6.2).

Using the ODE45 function available in MATLAB, Equations (6.8 - 6.11) can be solved to obtain displacements and velocities of rotors in the directions of interest. Then accelerations: $\boldsymbol{a_x}$, $\boldsymbol{a_y}$, $\boldsymbol{a_w}$ and $\boldsymbol{a_t}$ of the rotors can be calculated by differentiating the corresponding velocities.

6.9 Simulation Study

For a better understanding of the dynamic behaviour of the four shaft rotor system, a simulation study was conducted based on a bearing test rig with the arrangement shown in Figure 6.10 and rotor parameters as in Table 6.2 (see also Appendix B). The stiffness coefficients (K_1, K_2, K_3, K_4 and Kb) were selected with a high value so that transient effects were minimised and effects due to misalignments were highlighted. Consequently, the coupling damping coefficients (C_{r1}, C_{r2}, C_{r3}) will be affected by stiffness value of coupling (Kb)

Table 6.2 Parameters for simulation study

Description	Symbol	Unit	Value
Shaft 1 Diameter	D_1	m	0.030
Shaft 1 Length	L_1	m	0.540
Shaft 1 Mass	m_1	kg	12.730
Shafts 2,3 Diameter	$D_{2,3}$	M	0.035
Shafts 2,3 Length	$L_{2,3}$	M	0.380
Shafts 2,3 Mass	$m_{2,3}$	kg	7.460
Shaft 4 Diameter	D_4	M	0.040
Shaft 4 Length	L_4	M	0.760
Shaft 4 Mass	m_4	kg	34.960
Radius of centre for the equivalent	r	M	0.100
Coupling Damping	C_{r1}	N/(m/s)	75.565
Coupling Damping	C_{r2}	N/(m/s)	80.923
Coupling Damping	C_{r3}	N/(m/s)	105.359
Coupling Stiffness	Kb	N/m	$1.1x10^7$
Rotor Stiffness	K_1,K_2,K_3,K_4	N/m	1.0×10^8
Moment of inertia	J_1	kg m^2	0.0061
Moment of inertia	J_2,J_3	kg m^2	0.0082
Moment of inertia	J_4	kg m^2	0.0196
Eccentricity	e_c	m	$10.0x\ 10^{-4}$
Misalignment (offset)	e_{12}	m	$0.02x\ 10^{-3}$
Misalignment (offset)	e_{23}, e_{34}	m	$0.5x\ 10^{-3}$
Torsional load	T_L	Nm	50.0
Driving torque	T_m	Nm	50.0

6.10 Characteristics of Vibrations due to Misalignment

Figure 6.13 shows typical results from the numerical simulation studies when the motor operated at shaft speed of 1500 RPM. It can be seen from Figure 6.13 ("a"s and "b"s) that the waveforms of the lateral accelerations, a_x and a_y, are sinusoidal waves, whereas the waveform of rotational acceleration a_w exhibits a more complex waveform. These show that shaft misalignment leads to shaft fluctuation in different directions and the waveforms will have different frequency contents.

Figure 6.13 ("c"s) shows that in the frequency domain the fundamental rotational harmonic, 1X, dominates the spectra. As was found in the two rotor model, the spectra also show distinctive 2X components (Dewell & Mitchell, 1984; Sekhar, A. S. & Prabhu, 1995). For the 2X peak the rotational acceleration consistently shows the greatest amplitude. The lateral vibrations exhibit distinctive components at 2X, 3X and 4X. These indicate that both rotational and lateral accelerations are sensitive to misalignment but at different frequency components. In general, these spectral features show that the model is adequate for exploring shaft misalignment and examining the output behaviour of the wireless accelerometer.

Figure 6.14 ("a"s) shows the tangential components of the accelerations: a_{tx}, a_{ty} and a_{tw} predicted at sensor position due to accelerations: a_x, a_y and a_w. It can be seen that a_{tx} and a_{ty} fluctuate twice as fast as their original (a_x, a_y) but with opposite phase. Combining these two components together produces a nearly steady value. On the other hand, a_{tw} retains the same phase but with a difference in magnitude due to the sensor position on shaft surface being fixed. By combining the three components, the total acceleration a_t at P is dominated by a_{tw} but with a clear DC shift due to the combination of a_{tx} and a_{ty}.

The RMS value of a_t on shaft 2 is 2.6682, much larger than 0.0098 of a_{tw} and close to 2.6685 of the combination of a_{tx} and a_{ty} (a_{txy}). This shows that the wireless sensor output will have a_{txy} dominated output and hence more sensitive to changes due to faults.

In the frequency domain, the spectrum resulting from the combination of a_{tx} and a_{ty} is similar to that of a_{tw} but has lower amplitudes, shown in Figure 6.14 ("b"s). The spectrum from the full combination of a_{txy} and a_{tw} exhibits noticeable differences at various shaft frequencies. In particular, the amplitude difference between a_{tw} and a_t is marginal at 1X and 2X, showing that these two components are mainly from the effects of rotational variations. However, amplitudes at 3X and 4X show a distinctive increase, which means that the contribution from lateral vibration is more significant at these two components and that the combined spectrum is more sensitive to changes due to misalignments.

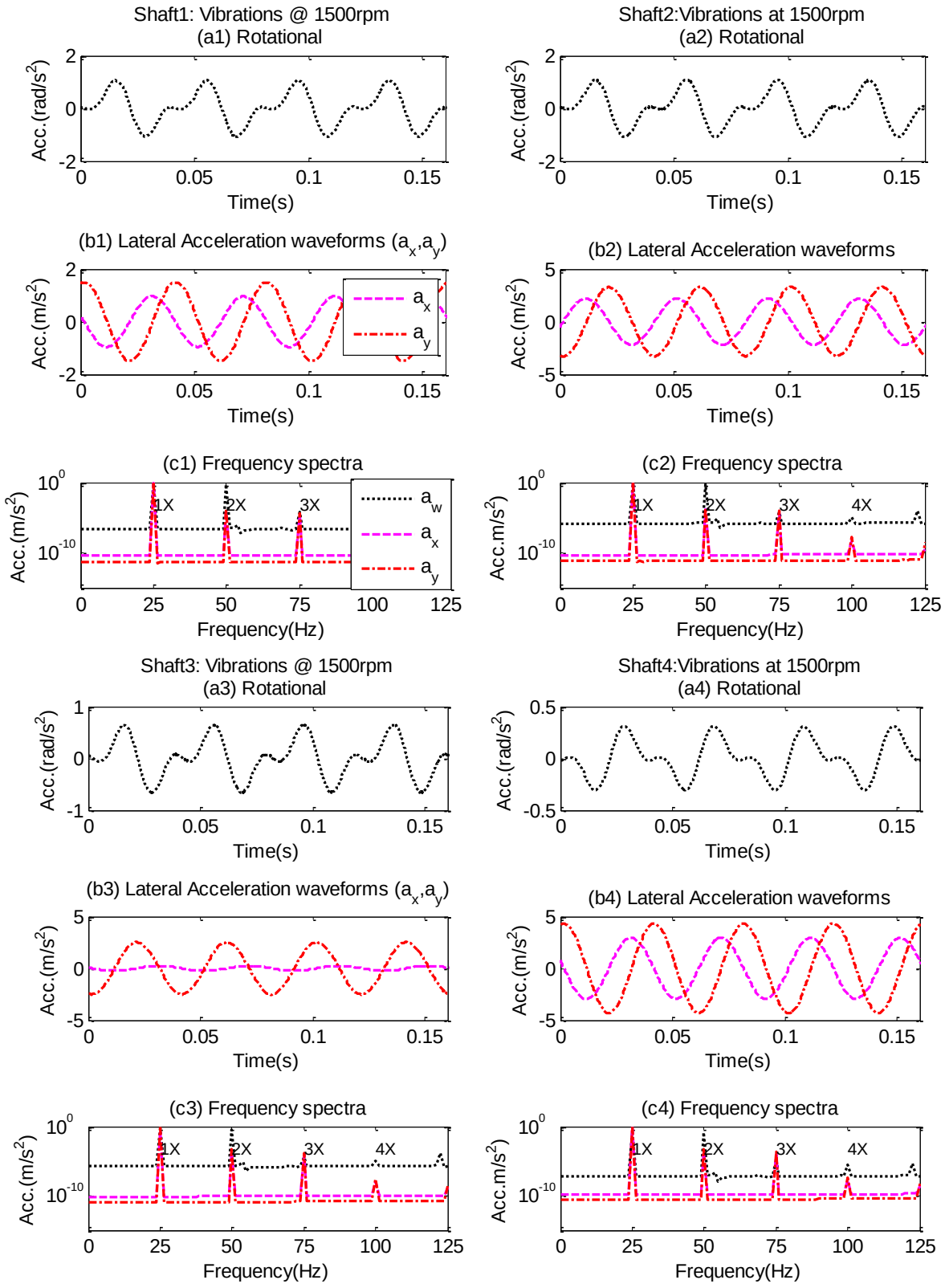

Figure 6.13 Predicted time domain waveforms and spectra of lateral and rotational acceleration for four shaft model.

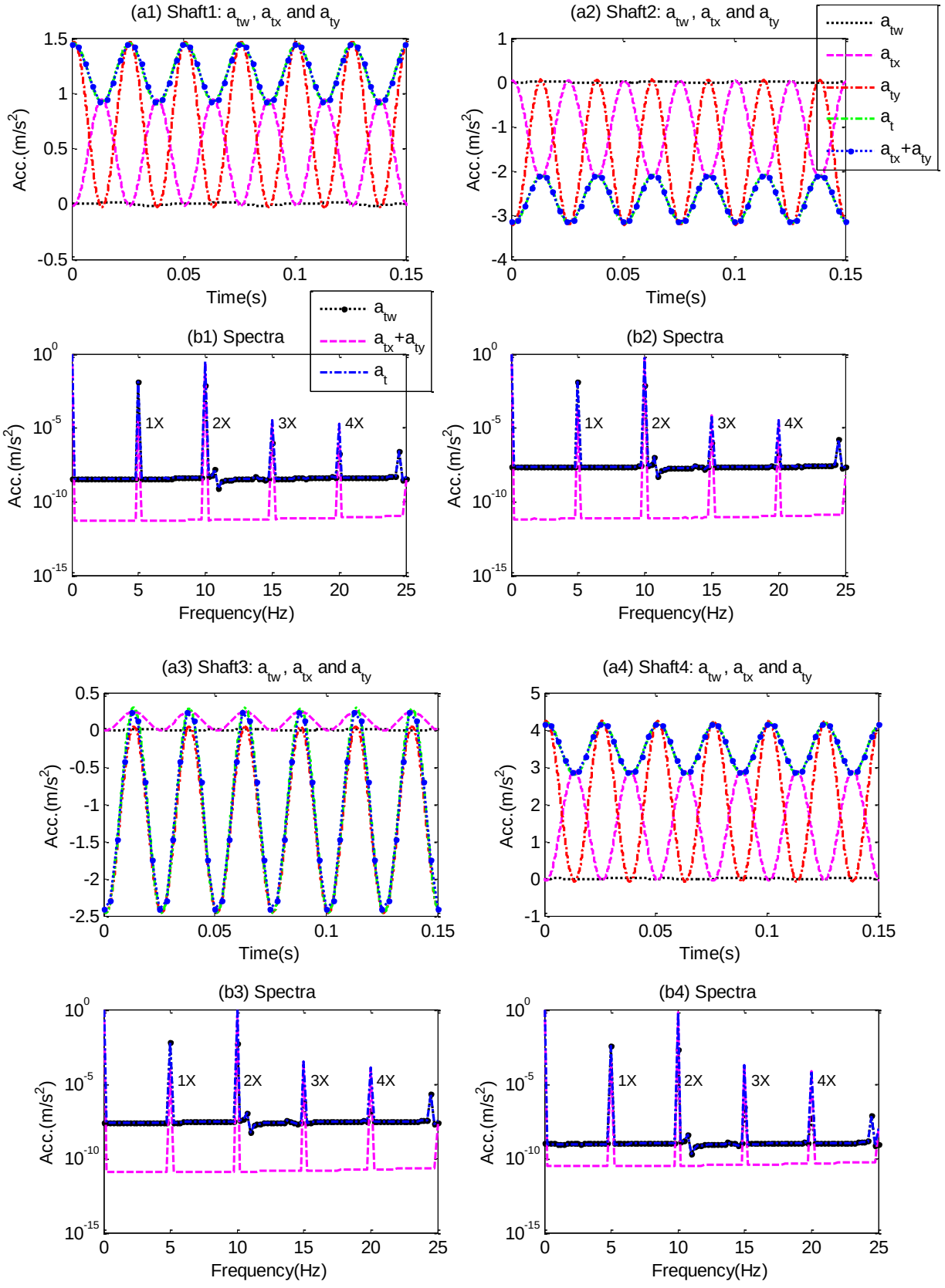

Figure 6.14 Predicted waveforms and spectra of lateral and rotational acceleration at sensor position for four shaft model.

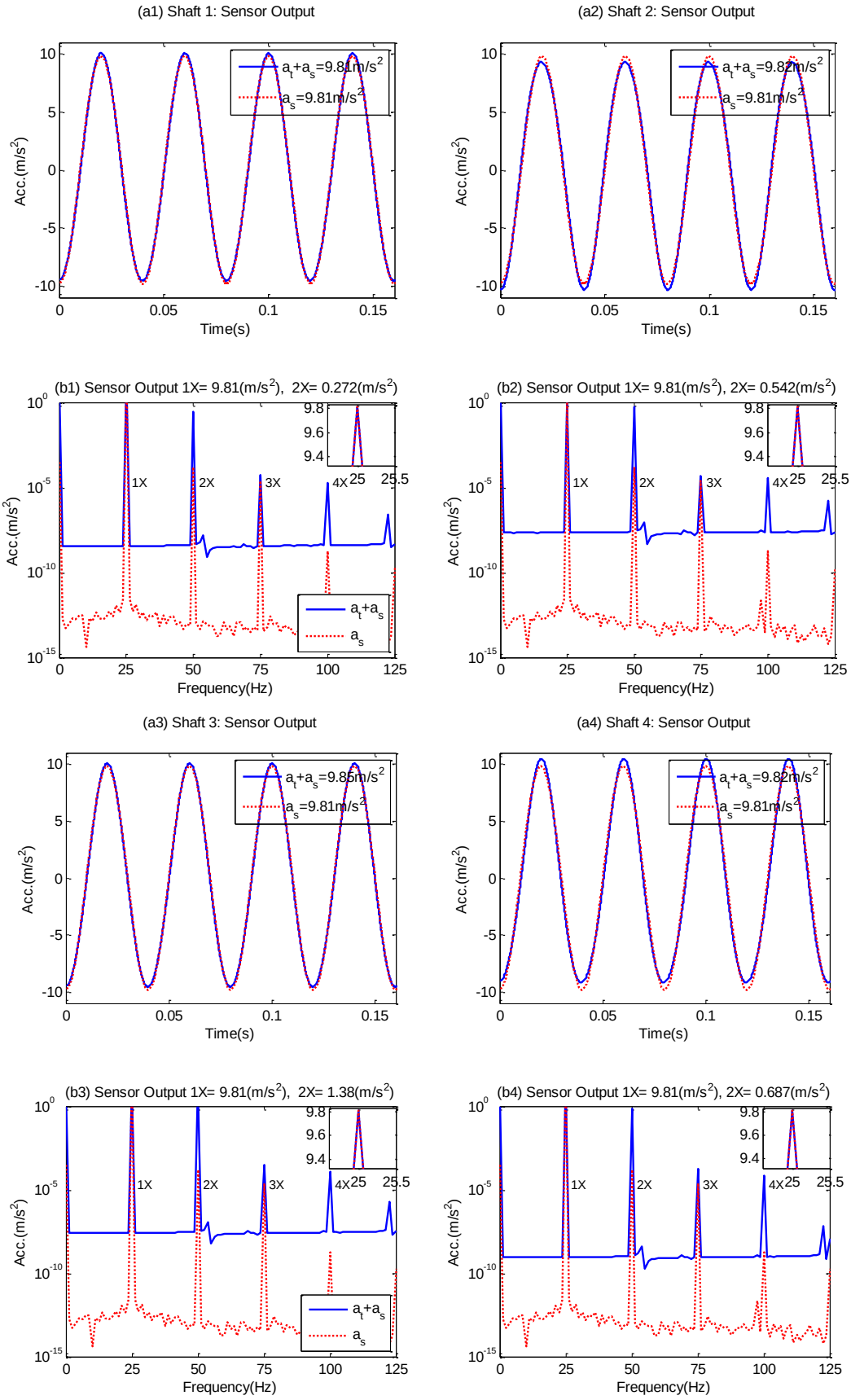

Figure 6.15 Predicted time waveforms and spectrum from a wireless accelerometer for four shaft model.

For the sensor output, gravitational acceleration $9.81ms^{-2}$ has to be superimposed on waveform $\boldsymbol{a_t}$ which results in a waveform shown in Figure 6.15 ("a"s). This superimposition alters the spectrum only at 1X, i.e. increases it by an amount of 9.81 ms^{-2}. Other spectral features remain the same, see Figure 6.15 ("b"s).

6.11 Characteristics of Spectral Amplitude with Misalignment and Speed

To examine further the changes of spectral amplitude for use with misalignment diagnosis a simulation study was performed under different motor speeds and different degrees of misalignment with the four shaft model. Figure 6.16 shows the change in amplitude of the first four harmonics with change in shaft speed for two levels of misalignment (0.25 mm and 0.50 mm). By comparing amplitudes of the combined ($\mathbf{a_t}$+$\mathbf{a_s}$) and the rotation ($\mathbf{a_{tw}}$) accelerations (shaft 2), it can be observed that:

The amplitude at 1X for the combined acceleration has small change for either increase in shaft speed or degree of misalignment. Additionally the combined acceleration is consistently lower than that for rotational motion. Thus the peak at 1X is not suitable for misalignment detection which agrees with the findings of Dewell & Mitchell (Dewell & Mitchell, 1984).

The amplitude of the 2X harmonics, for the combined acceleration, increases with both shaft speed and degree of misalignment. The acceleration for the rotational variation follows a similar trend but at much lower amplitudes. 2X has the possibility of being a good indicator of misalignment at higher speeds.

The amplitude of the 3X harmonic, for the combined acceleration, increases noticeably with shaft speed for the higher level of misalignment. There is an increase in combined acceleration with increase in misalignment regardless of speed. On the other hand, the amplitude values of 3X peak for rotational variation have small change for different speeds and degree of misalignment. Both accelerations amplitude values are 4 orders lower than that of 2X, which may be influenced by measurement accuracy.

Similar with the 4X peak, the amplitude for the combination increases with shaft speed and the degree of misalignment and might be of use as a secondary indicator for a misaligned shaft. However, the amplitude of 4X for the rotational variation does not change either with shaft speed or misalignment and hence it is not an effective misalignment indicator.

In general, the amplitude variation of the combined acceleration at 2X, 3X and 4X can be a good indicator of misalignment. However, the peaks at 3X and 4X have very low amplitudes and can be influenced by measurement noise. Thus the amplitudes of rotational oscillation only at 2X can be used for misalignment detection.

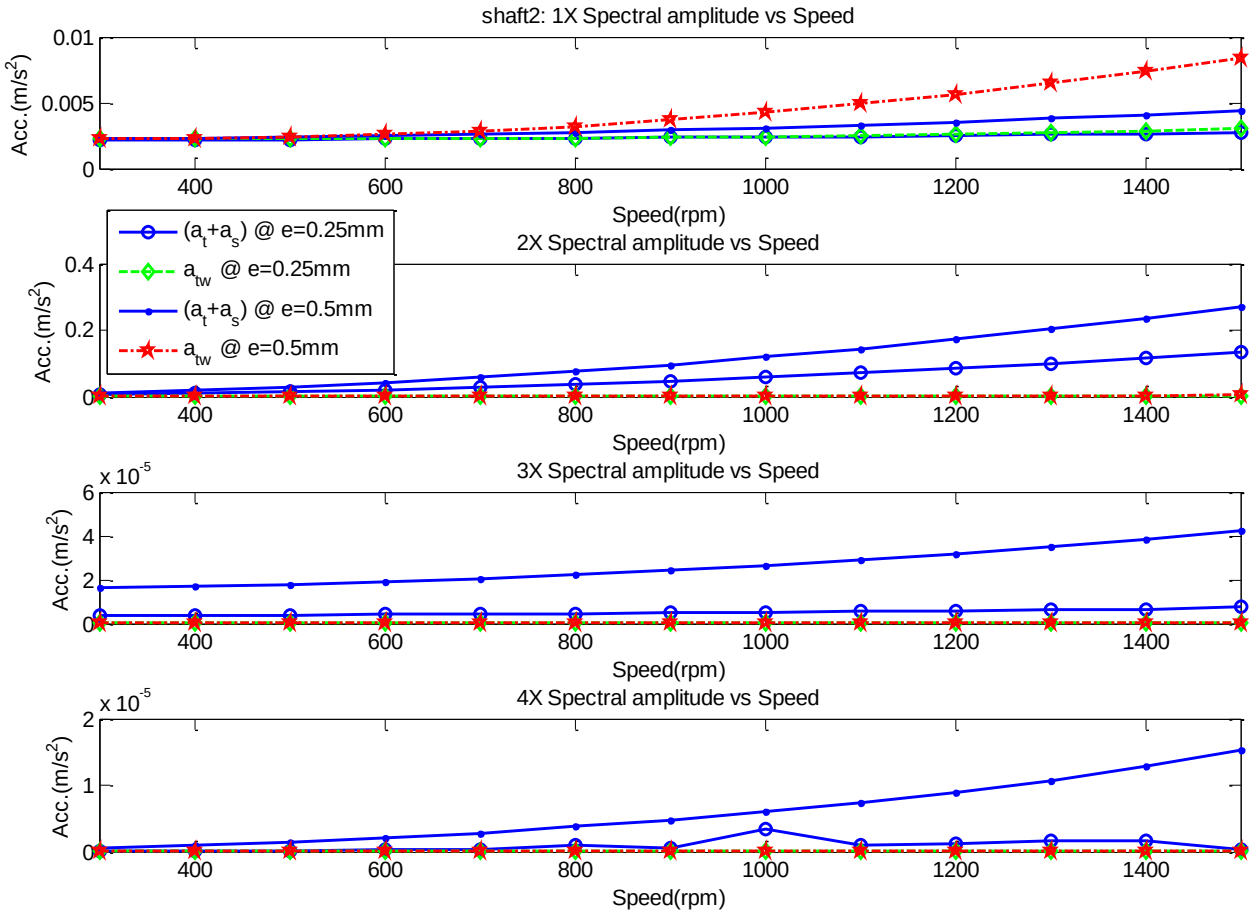

Figure 6.16 Predicted spectral amplitude versus speeds and misalignment for four shaft model.

6.12 Case Study

A specific case is now presented to further understanding of the behaviour of the above model and illustrate performance model output features.

This example uses the above model (multi-rotor) with rotational speed of 1500 RPM and at 0.5 mm degree of misalignment between rotors 2, 3 and 3, 4. The right side of Figure 6.17 shows the vibration acceleration spectral response. Note that the force arises purely from the eccentricity of 0.1 mm from the machining on one of the coupling jaws.

No mass unbalance has been applied to the rotors. Although the acceleration in the Figure 6.17 is plotted on a logarithmic scale, the 2X components of excitation are significant for the rotational accelerations whereas the lateral ones are smaller. This is due to the coupling forces acting on jaws radially.

The left side of Figure 6.17 shows the basic waveforms of the rotational and lateral displacements. For the rotational case, the first and second shaft's displacement waveforms

are 90° out phase with displacements of third and fourth shafts. This represents the fluctuations in the shafts caused by the misalignment relative to the third shaft.

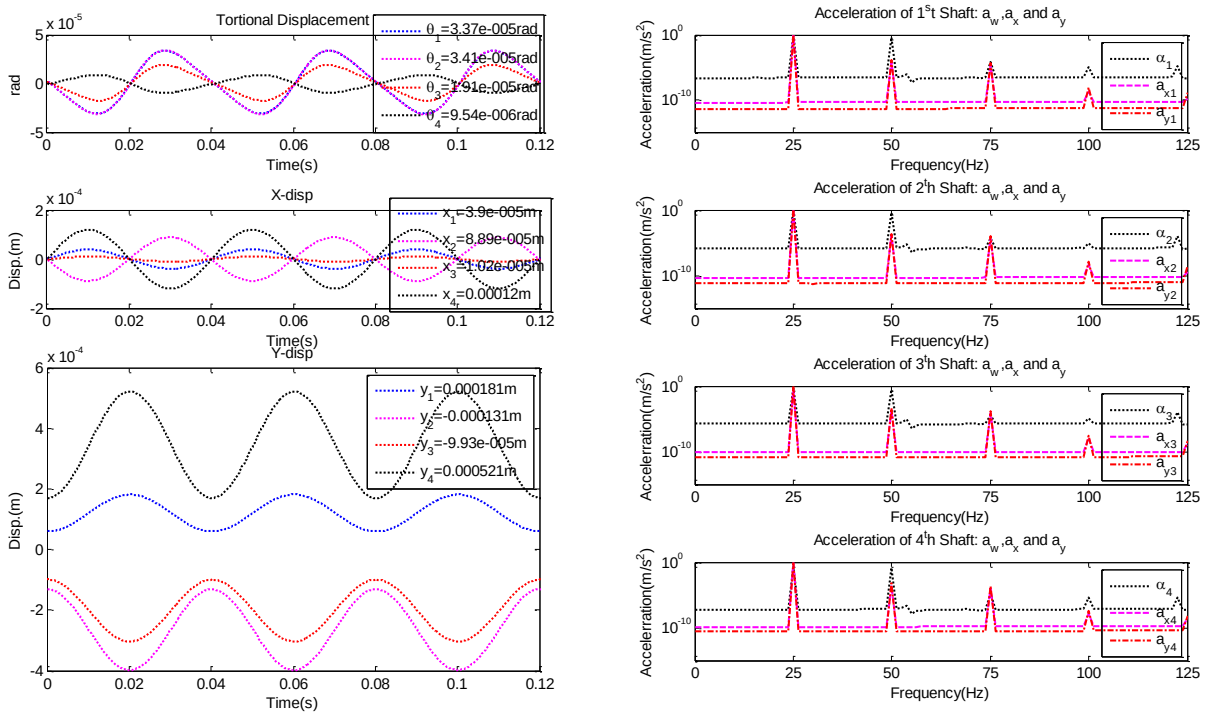

Figure 6.17: Displacement and acceleration response with rotor at 1500 RPM (misalignment 0.5 mm)

The displacements waveforms in the x-direction of the first and third shafts are in phase as are the second and fourth shafts, but the two couples are 90° out phase. For the y-direction displacements waveforms of the first and second shafts are in phase with positive waveforms generated by the reaction forces acting in that direction. However, the y-direction displacements for the second and fourth shafts are in phase but negative due the direction of the forces acting being in the opposite direction to those operating on the first and second shafts. The coupling jaw was forced upward by the misalignment in the y-direction. As a result of this force, the reaction force was in the opposite direction and will show as a displacement in the y-direction.

6.13 Summary

The main objective of developing the mathematical model of the test rig has been completed. This study focuses on the steady state vibrations of a misaligned rotor coupling bearing system. The steady state of rotors system subjected to a displacement restriction due to the parallel misalignment is included for both two and four rotor systems. The simulation predicts the results of vibrations in the x and y direction concurrent with the rotational and tangential. Moreover, the different harmonics of tangential accelerations (wireless) in the frequency domain show that 1X is overlaid by a factor of 9.81 ms^{-2} which is due to gravitational

attraction of the wireless sensor. Other components clearly follow the speed of the rotor. The measured wireless accelerometer waveforms show the same trends as the predicted results, see Figure 6.7, Figure 6.8 and Figure 6.9. The spectral amplitude of the simulation confirms that the second harmonic of the running speed is best for detection of misalignment confirming the previous studies (Huer & Zhaojian, 2010; Jalan & Mohanty, 2009; Lees, A. W., 2007 (a), 2007 (b); Nakhaeinejad & Ganeriwala, 2009; Tejas, H. Patel & Ashish, K. Darpe, 2009; Zhou, Wang, Feng, & Du, 2011).

Using the same principle, the four rotor system was modelled using the parameters shown in Table 6.2. The misalignment conditions between 2, 3 and 3, 4 at different speed have shown different dynamics for each rotor for the combination signal ($\boldsymbol{a_t}$+$\mathbf{a_s}$). The waveforms were characterised by change in their magnitude according to the mechanical state of the neighbouring rotor. The spectral amplitude of the system shows that the combination accelerations are capable of detecting parallel misalignments, as depicted in Figure 6.16. Moreover, the spectral amplitudes of the second harmonic of running speed is able to separate different cases of misalignment conditions.

The displacement study of rotor behaviour shows that rotors exchange their vertical oscillations according to the forces generated by the misalignment. For instance, Figure 6.17 shows the displacement behaviour of all rotors when the first and second rotors are subjected to 0.5 mm misalignment. The rotational displacements of first and second rotors are in phase with each other, the third and fourth are in phase with each other but out of phase with the first and second. In the x-direction rotors vibrate at different magnitudes and phases. In the y-direction, positive and negative displacements represent the different movements of rotors. These show that the reaction forces due to misalignment drive the rotors to move in opposite directions, where the jaws of couplings clearance exchange positions in the y-direction, and hence force the rotors to react in such manner.

Both models demonstrate their capability of differentiating between 0.25 mm and 0.5 mm degrees misalignment.

CHAPTER SEVEN

Modelling and Measuring the Dynamic Characteristics of a Misaligned Rotor

This chapter introduces a literature review of parallel misalignment in rotors. Then it investigates a novel approach for monitoring shaft parallel misalignment using a wireless accelerometer which can be mounted directly on a rotating shaft. It is suggested that such a measurement system can more effectively diagnose rotating shaft faults because its signal to noise ratio is high due to direct nature of the sensor installation and combined response measurements. Both theoretical analysis and experimental results show that the scheme outperforms IAS measurement when detecting shaft misalignments.

7.1 Introduction

Shaft misalignments cause not only additional dynamic load but also machine vibration which accelerates machine deterioration. In industry, 30% of a machine's downtime is due to the poorly aligned machines (Hariharan, V., et al., 2009). Misalignment is estimated to cause over 70% of rotating machinery's vibration problems (Bognatz, 1995).

The basic types of misalignment are parallel and angular, as shown in Figure 7.1. Generally, shaft misalignment is a combination of both parallel and angular types in vertical and horizontal directions. Parallel misalignment generates more vibrations than angular misalignment(Nakhaeinejad & Ganeriwala, 2009).

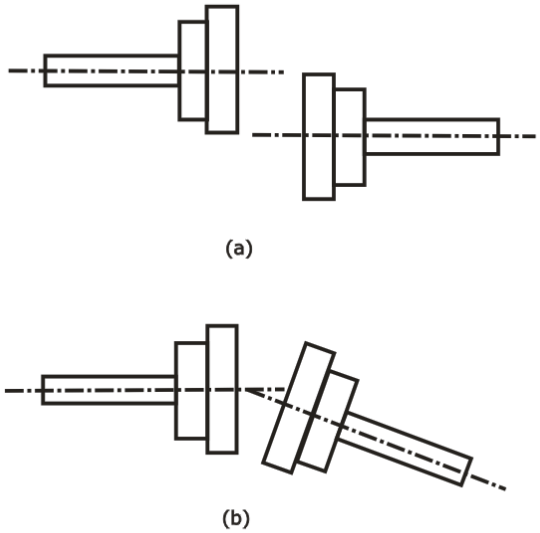

Figure 7.1 Basic types of shaft misalignment (a) parallel; (b) angular (Xu & Marangoni, 1994 a).

Gibbons (Gibbons, 1976) was the first to derive the misalignment reaction forces separate from those generated in different types of couplings. Vance (Vance, 1988) and Goodman (Goodman, 1989) observed that misalignment is present due to improper machine assembly and sometimes due to thermal distortion of the bearing housing supports, both of which result in abnormal rotating preload. These authors have pointed out that perfect alignment between the driving and driven shafts during machine operation cannot be attained.

Despite the rapid increase in the understanding of rotor dynamics in the last decade, no analysis satisfactorily explains the range of observed phenomena (Hariharan, Vaggeeram & Srinivasan, 2011). Hence, an in-depth study to provide accurate knowledge of the vibration characteristics would be very helpful for understanding and diagnosing rotor misalignment in order to avoid any resulting failure or damage (Tejas, H. Patel & Ashish, K. Darpe, 2009).

A number of researchers have found that shaft vibration due to coupling misalignment can be substantial for even small degrees of misalignment and occurs predominantly at the second harmonic, 2X, of the rotor speed but a 4X component can also be present (Xu & Marangoni, 1994 a).

When a misaligned shaft is supported by rolling-element bearing, these characteristic frequencies of the bearings may also appear and high axial vibration levels occur. Tejas and Ashish (Tejas, H. Patel & Ashish, K. Darpe, 2009) found from the measured forces that the presence and type of misalignment (parallel or angular misalignment) has significant influence on the harmonic content of the misalignment excitation forces.

Stephen (Stephen, Hines, & Edmondson, 1999) found that, in some cases, up to 50% percent of the expected bearing life can be lost with an offset misalignment as small as 0.127 mm. Stephen also showed that angular misalignment has a much smaller impact on bearing life than parallel misalignment. Recently, Lees (Lees, A. W., 2007 (a), 2007 (b)) has confirmed these findings and reported that parallel misalignment in rigidly coupled rotors generated excitation at twice the rotor speed.

From the literature, it is clearly seen that misalignment produces high vibration levels in bearings and couplings. The degree of vibration is influenced by the machine speed and the stiffness of the coupling, i.e., rubber couplings which have a lower damping coefficient are more tolerant and tend to produce less vibration (Piotrowski, 2007).

In general, the majority of misalignment studies have been theoretical and experimental investigations relatively limited. The outcomes of those studies may not be accurate since, in reality, there are usually many more sources of vibration in an actual rotor system than those included in the model equations. All the experimental studies used wired accelerometers which were invariably attached to the bearing housing and so measured shaft dynamics which could have been considerably attenuated.

In this study to investigate the consequences of parallel misalignment, a wireless accelerometer is mounted directly on a shaft to measure the dynamics. A theoretical analysis has been conducted to better understand the dynamic outputs of the accelerometer. A test evaluation of the performance of the wireless accelerometer in detecting the seeded misalignment is benchmarked by the independent measurement of instantaneous angular speed (IAS) (Gu, et al., 2006; Li, Y., et al., 2005). IAS has been chosen because it is minimally influenced by bearing house vibrations.

To evaluate the predicted performance of wireless sensor in detecting parallel misalignment a test study was conducted based on a bearing test rig which has a similar layout shown in

Figure 6.1 and can be induced conveniently with different degrees of misalignment. The setting of this experiment is detailed in the next section.

7.2 Shaft Alignment

For the sake of studying shaft misalignment effects, the shafts must first be aligned. The aligned system is taken as a basis for creating desired misalignment system. The shaft alignment was performed on the rotors of the test rig. Alignment in both vertical and horizontal directions was conducted in turn to achieve best possible alignment results.

The detailed alignment procedure for the test rig shown in Figure 5.6 were given in Section 5.2.3. After multiple alignment adjustments in vertical and horizontal directions, good alignment was almost achieved. The maximum allowable coupling alignment tolerance for the flexible coupling (HRC130) used was 0.4 mm at 4250 RPM in parallel and 1 degree in angular misalignments. This tolerance specifies the mechanical or fatigue limits of the coupling and its components (Piotrowski, 2007). Since the maximum speed of the test rig used in this study is 1420 RPM, the tolerance of coupling misalignment can be higher than that given earlier. The rotor misalignment or offset is measured in millimetres (mm). The misalignment coupling and rotor tolerance can be changed when connected to the system. The parallel offset induced to the test rig was chosen relatively medium (according to (Nakhaeinejad & Ganeriwala, 2009) and max. speed used) to examine the detectability of wireless sensor for such level of misalignment. When the motor is operated at high speeds, good shaft alignment is especially critical. Therefore, the 0.6 mm parallel misalignment is acceptable as low speed as 1420 RPM.

7.3 Experiment Setup

The test rig is described in Section 6.3.1 and shown in Figure 6.1 and 6-2. A MEMS wireless accelerometer sensor was mounted directly on the second shaft as shown in Figure 7.2. The principal sensitivity axis of the sensor was along the tangential direction of shaft rotation. To benchmark the results from the wireless sensor, a shaft encoder was mounted at the end of the induction motor. Both the wireless channel and encoder channel were measured simultaneously at a sampling rate of 96 kHz. At this rate, the duty cycle signal (DCS) from wireless sensor and the frequency modulated (FM) signal from the encoder can be recorded accurately.

During post-processing, the DCS signal was low pass filtered to obtain the acceleration signal in the tangential direction. The pulse train signal was processed by a FFT-based demodulation algorithm (Gu, et al., 2006) to obtain the IAS. As only relative detection performance is required between the wireless sensor and the shaft encoder; the angular speed was compared directly, rather than converting it into angular acceleration.

Two tests were conducted. The first test was the baseline measurement under which the system was adjusted with minimal difference between the two flanges of the coupling, between the motor and the loader by a dial indicator (see Section 5.2.3), see Figure 5.6. The dial indicator is used to align the coupling flanges vertically and horizontally. Both data measured from wireless accelerometer and encoder was recorded. The load was set to 50% of rated load through the experiment.

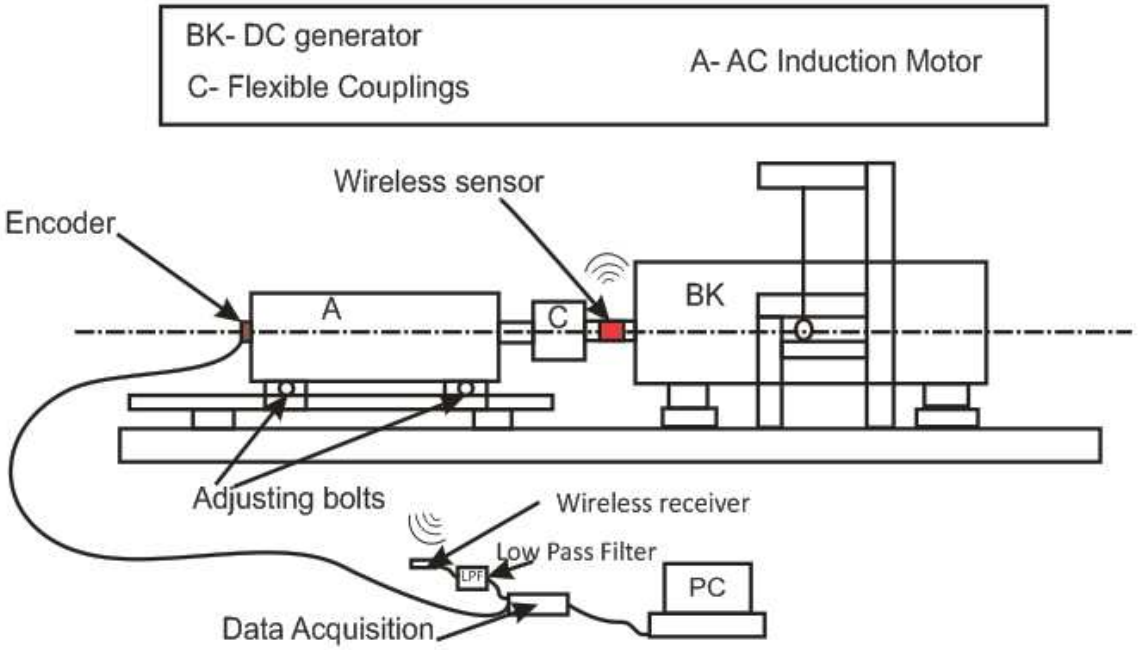

Figure 7.2 Schematic presentation of the test rig setting.

The second test records the measurements from both wireless and encoder when the centre-line of one flange was offset by 0.64 mm from the centre-line of the other. This offset was achieved using the dial indicator with resolution of 0.01 mm. In each test measurements were taken at shaft running speeds: 300, 450, 600, 750, 1050 and 1200 RPM. The speeds are set by the control panel.

7.4 Results and Discussion

Figure 7.3 shows typical result of measurements made with the wireless accelerometer for the two given misalignment conditions at shaft speed 755 RPM (measured).

Although careful adjustment was made to minimise the misalignment between shafts, the baseline measurement still shows distinctive oscillations. Its spectrum in Figure 7.3 (a2) shows that there are clear and distinct peaks at 1X and 2X, and there is a series of peaks at 3X and 4X, which can be distinguished from background noise. This indicates that the baseline oscillation may be caused mainly by problems of eccentricity and torque fluctuation due to the driving motor. The series of peaks at 2X, 3X, and 4X, due to the misalignment is consistent

with model predictions. It is concluded that the spectral peaks at 2X, 3X and 4X can be an effective and reliable indicator for shaft misalignment.

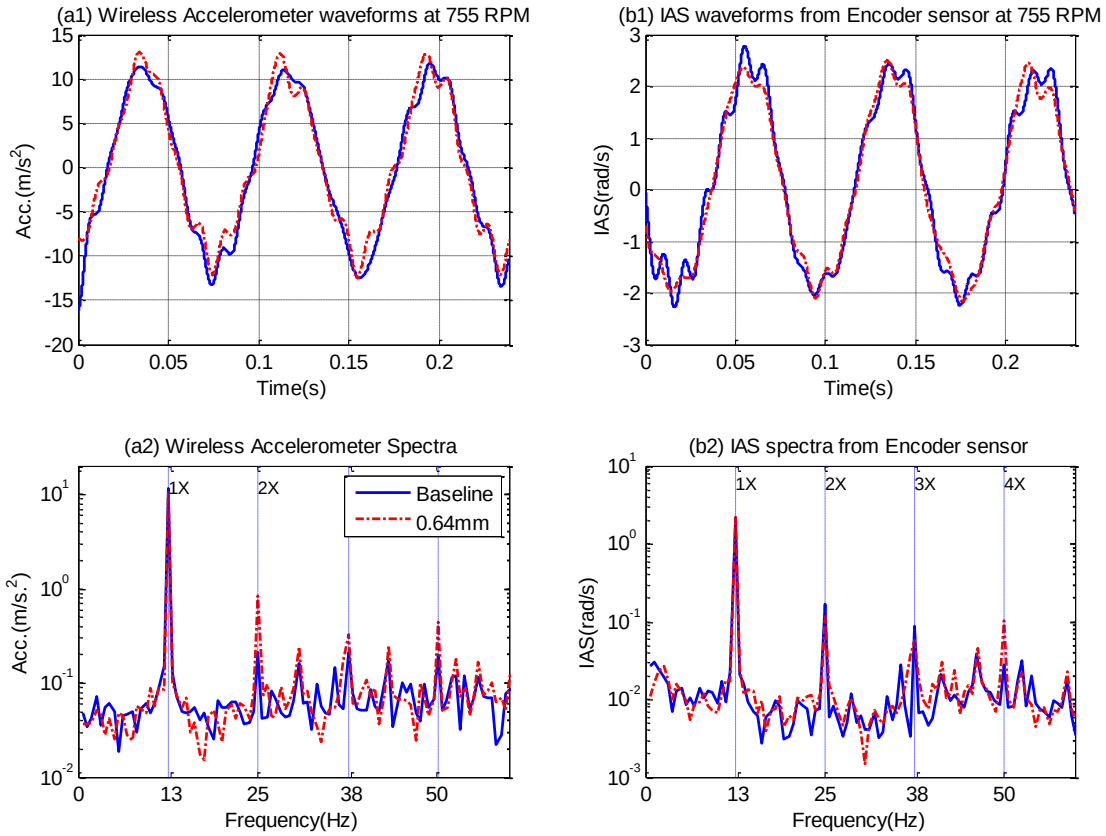

Figure 7.3 Time domain waveforms and spectra for two degrees of misalignment.

The IAS signals from the encoder, see Figure 7.3 (b2), show hardly any changes in the amplitudes of the peaks at 1X and 2X due to the increase in misalignment. Surprisingly, the spectrum shows an amplitude decrease at 3X and increase at 4X, which is inconsistent with wireless accelerometer readings. This is due to more noise influences the encoder output since it is far position from the coupling.

Figure 7.4 shows the variation trend of peak spectral amplitudes with speed. The spectral amplitudes at 1X from both wireless and encoder shows are not capable of separating different cases. However, the spectral amplitudes obtained from the wireless accelerometer at 2X, 3X and 4X show an increase with speed, which is consistent with model predictions. These peaks show good performance in separating the misalignment from the baseline when speed is higher than 600 RPM.

On the other hand, with the encoder only at 2X did the spectral amplitudes in the IAS spectrum show the expected trend. Nevertheless, it allows the misalignment to be separated

from the baseline at speeds higher than 1000 RPM, which is much lower in detection performance compared with that of wireless sensor.

Figure 7.5 shows the normalized spectra of the predicted accelerations and the measured accelerations obtained from the wireless sensor and the corresponding instantaneous angular acceleration (IAA) from encoder. Note the two shaft speeds were 755 RPM and 1200 RPM. It is easily observable that all three sets of data have the same peak frequencies. It is clear that the acceleration predicted by the model has no background noise due to the simplifying assumptions made, whereas the measured spectra from wireless and encoder contain substantial amounts of noise generated by such effects as friction, damping and residual unbalance. The spectral amplitudes of all signals increased with degree of misalignment and speed. The second harmonic, 2X, is the component that changes most with respect to the degree of misalignment, as expected.

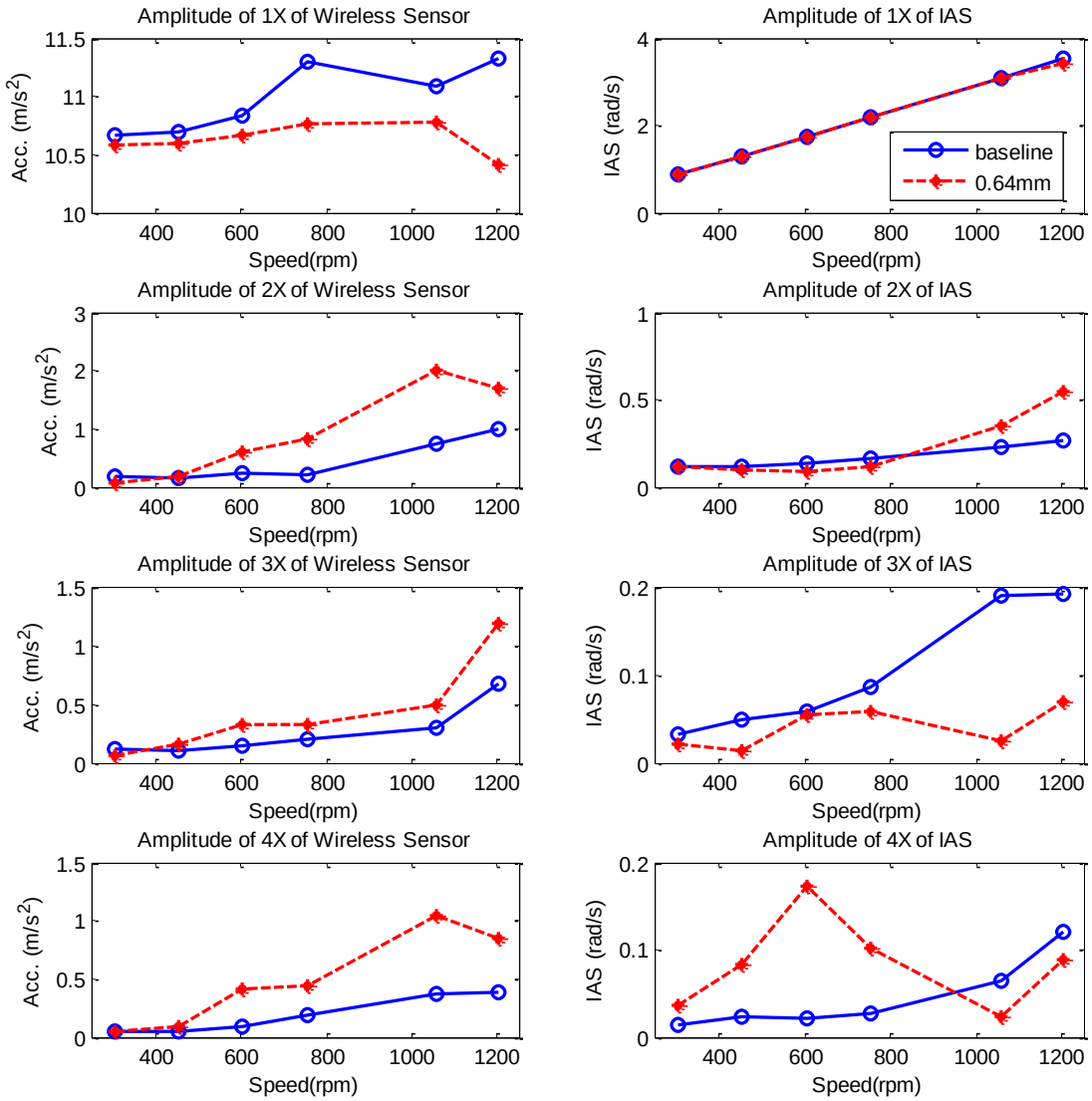

Figure 7.4 Measured spectral peak amplitudes versus speed and degree of misalignment

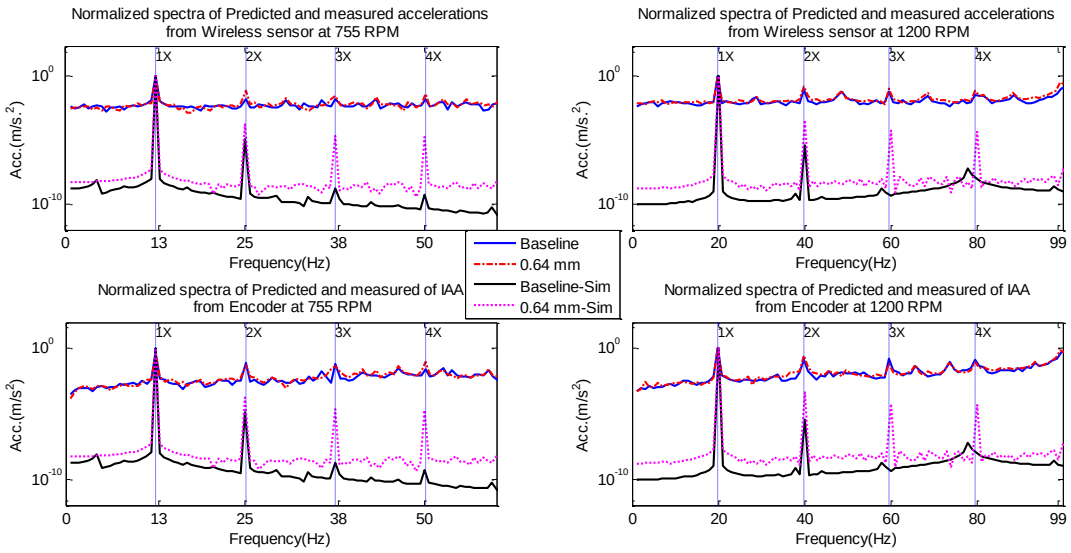

Figure 7.5 Predicted and measured acceleration from wireless and encoder

7.5 Summary

A wireless accelerometer to monitor shaft problems has been investigated. A model of the pin type coupling-roller-ball bearing system with misalignment was derived in Chapter 6 to simulate the dynamics of a misaligned shaft system at different speeds. Through experiment and simulation, the validity of the model and use of the wireless accelerometer as a measurement device has been successfully verified over a range of relevant operating speeds. The spectra obtained from both the model and measurement show that misalignment can be detected and characterized primarily by the spectral amplitudes at 2X, 3X and 4X of shaft running speed. Because these components consist of both rotational and lateral vibrations, the detection performance of the wireless measurement scheme is considered to produce better results than IAS measurements because of wireless high SNR compared to that of IAS (see Figure 7.3).

CHAPTER EIGTH

A Comparative Study of Misalignment Detection using a Novel Wireless Sensor with Conventional Wired Sensors

This chapter reports a systematic comparison between the wireless sensor and three common sensors (a laser vibrometer, an accelerometer and a shaft encoder), for detection of shaft misalignment using the bearing test rig described in Chapter 5. The four sensors were used to simultaneously measure dynamic responses to seeded misalignment faults: IAS from the encoder, bearing house acceleration from the accelerometer, shaft displacements from the laser vibrometer and angular acceleration from the wireless accelerometer. These responses were then compared in both the time and frequency domains for detecting and diagnosing different levels of shaft misalignment. Results show the effectiveness of the wireless accelerometer in detecting the faults.

8.1 Introduction

A misaligned rotor generates a very complicated dynamic response due to imprecisions in rotor and machine construction including bearing stiffness, types of coupling, manufacturing and installation accuracies, mounting base dynamics, lubrication performance, thermal deformations, etc. Many different models (Sekhar, A. S. & Prabhu, 1995; Vance, 1988) have been developed to include these influences in different ways. Although these models have produced good predictions in particular cases, they are not so generic as to include all the factors. This means that the dynamics of a shaft can be accurately determined only through experimental study.

The most common way to measure shaft dynamics for diagnosis of shaft related problems is to place an accelerometer on a bearing house. Obviously, because of the attenuation and distortion due to bearing structure dynamics, it is difficult to obtain the true dynamic behaviour of the shaft. To avoid the influences of the sensor position, it is sensible to place a sensor on the shaft directly. Thanks to the advancement in low cost and low power MEMS sensors, it has been possible to develop a cost-effective measurement scheme by placing a wireless accelerometer on the rotating shaft for monitoring the dynamics of the shaft and achieve a more accurate fault diagnosis.

To confirm the acceptability of the wireless accelerometer as a measurement device for monitoring shaft dynamics, this chapter presents a comparative study of the monitoring of shaft misalignments using the wireless accelerometer mounted directly on a shaft and three conventional sensors: laser vibrometer, wired accelerometer and shaft encoder.

8.2 Test Facility and Method

The bearing test rig, shown in Figure 8.1, was used in this experimental study, and has been described in Section 5.2. The construction allows the study of different types of misalignments such as angular and parallel misalignments in different parts of the shaft system, but here we were focused only on parallel misalignment. The wireless accelerometer was mounted directly on the shaft closest to the motor shaft while an encoder was mounted at the rotor end of the induction motor as shown in Figure 8.1 and Figure 8.2.

8.2.1 Encoder

An incremental shaft encoder type RI32, shown in Figure 5.8 and described in Section 5.2.4, was used to measure the Instantaneous Angular Speed (IAS)(Li, Y., et al., 2005). It has two outputs: one pulse per revolution and 100 pulses per revolution.

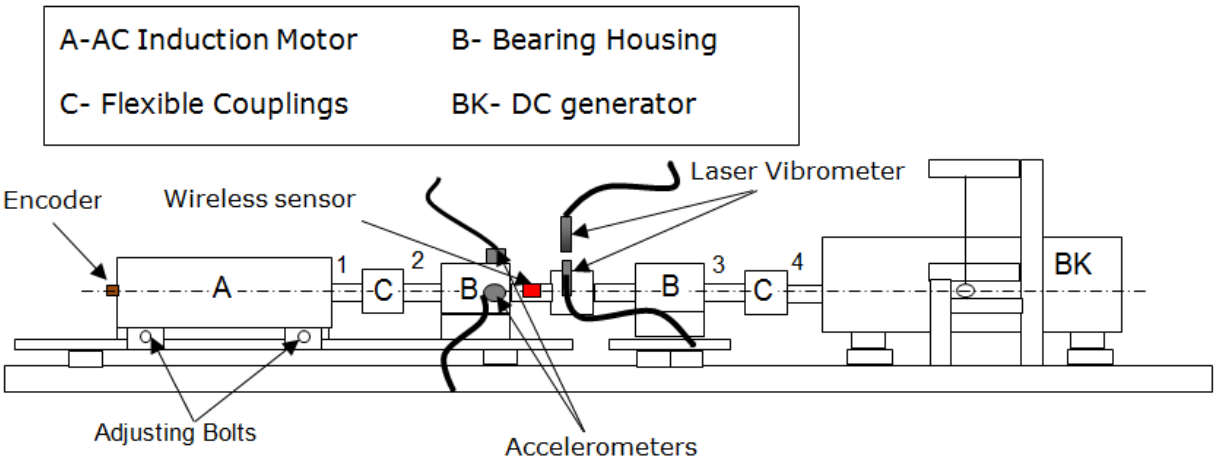

Figure 8.1 Test rig schematic showing sensor placements.

8.2.2 Laser Vibrometer

A photo of the OptoNCDT1300 (Micro-Epsilon, 2010) laser vibrometer is shown in Figure 5.9 and the principle of operation of the device is described in Section 5.2.6.Figure 8.2 shows the laser vibrometers installation within the test rig.

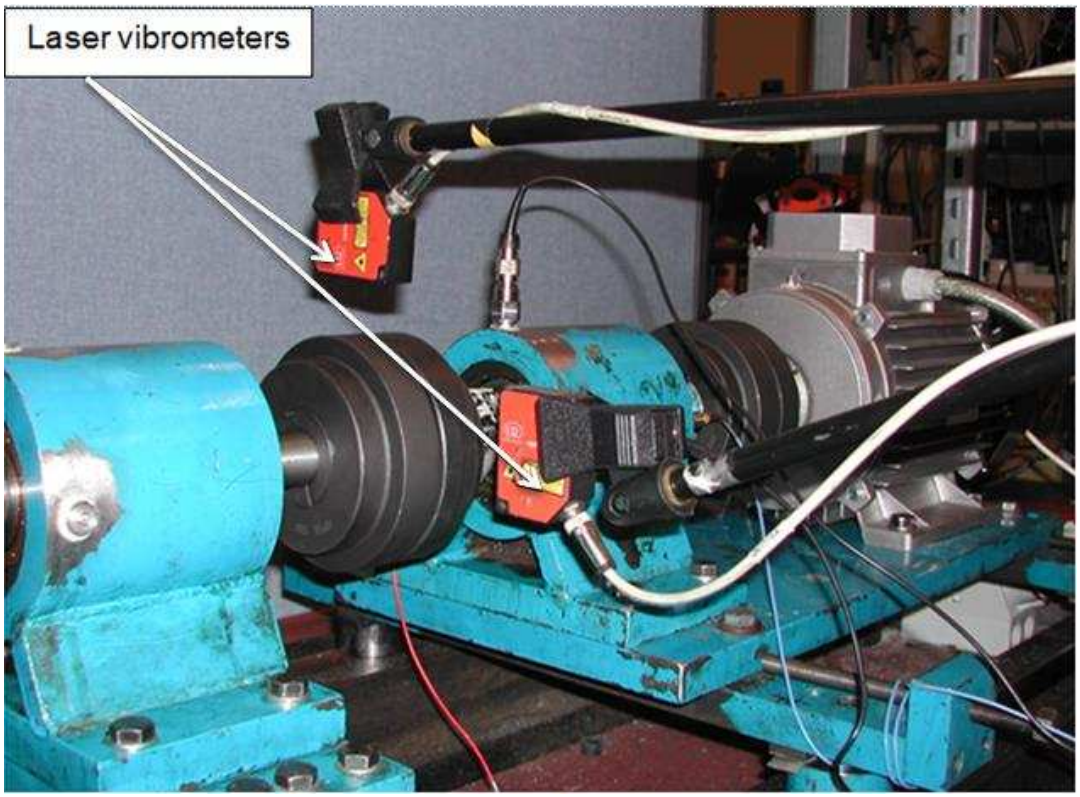

Figure 8.2 Test rig showing Laser Vibromters placements.

8.2.3 Accelerometer

The accelerometers used are SINOCERA piezoelectric based type YD-185TNC accelerometers which have a flat frequency response in the range 0.5 Hz to 5000 Hz. The sensitivity of the vertical positioned sensor (SN00016) is 5.106 mV/ms^{-2} and the horizontal positioned sensor (SN00039) is 4.960 mV/ms^{-2}. The slight difference in sensitivity of the two accelerometers will not change the measured vibration. Both operate under 12-24 VDC. A photo of the accelerometers is shown in Figure 5.10.

The wireless MEMS accelerometer was mounted directly on the second shaft connecting to the shaft of the motor as shown in Figure 8.3. The principal sensitivity axis of the sensor is tangential to the direction of shaft rotation as depicted schematically on the right hand side in Figure 8.3.

To benchmark the results from the wireless sensor, a shaft encoder was mounted at the end of the induction motor. Two wired accelerometers were connected to the bearing housing close to the motor as shown in Figure 8.1. Two laser vibrometers were installed to monitor the shaft vibration in both vertical and horizontal directions as shown in Figure 8.1 and 8-2. As in previous tests, all sensor channels were measured simultaneously through the DAS (YE7600) at a sampling rate of 96 kHz.

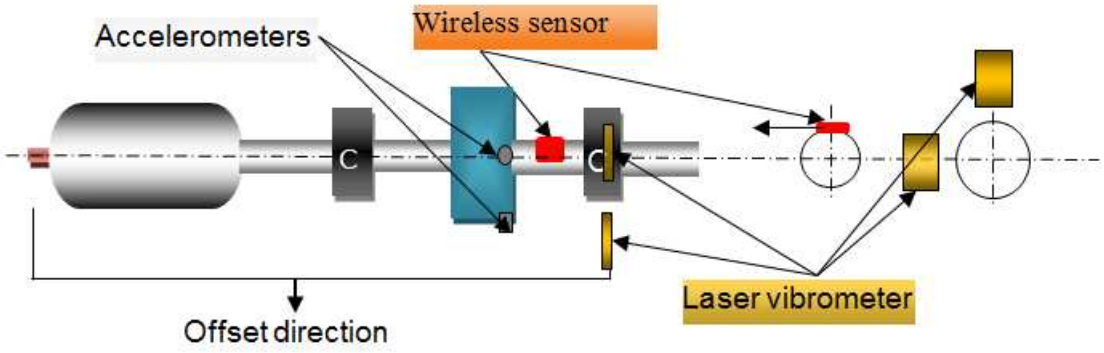

Figure 8.3 Schematic diagram of misaligned shaft (Top view).

As in the previous tests, the DCS from the wireless sensor was low pass filtered (100 Hz) to obtain the acceleration signal in the tangential direction. An FFT based demodulation algorithm was applied to the encoder pulse train signal to obtain the IAS (Gu, et al., 2006). As before, the angular speed was used directly for comparison, it was not converted into angular acceleration. The waveforms obtained from the accelerometers were compared directly. The displacement from the laser vibrometer was compared for relative performance with the other sensors.

8.3 Test Procedure

The test rig was operated under a fixed load of 50% of the rated load (2kw) but at different speeds: 284, 426, 568, 710, 852, 994, 1136, 1278 and 1420 RPM to examine the frequency response and sensitivity of the wireless sensor. Prior to commencing each test, different shafts of the rig were tuned for minimal misalignment (baseline condition) which was confirmed through a static measurement using a dial meter and dynamic measurements of all the sensors. The data was then collected from all sensors simultaneously as the baseline reference.

Using the dial meter given in Section 5.2.3 and the way used shown in Figure 5.6, the first level of misalignment between shafts 2 and 3 was set at 0.3 mm in a horizontal direction at which repeatable results were made with all sensors. The test rig was then run under this operating condition and data collected. This step was repeated for other higher misalignment levels: 0.4 mm and 0.5 mm.

The collected data sets were then processed using a MATLAB program to perform comparisons of time waveforms and frequency spectra.

8.4 Results and Discussion

8.4.1 Waveform Variation

Figure 8.4 shows typical waveforms from a wireless sensor for baseline condition and a 0.3 mm offset misalignment and shaft speeds 284 and 1420 RPM. As can be seen from the top row of Figure 8.4, the time domain of the signal from the wireless accelerometer for the baseline condition showed clear periodic oscillations at the shaft speed. This may be due to unavoidable misalignment of other shafts in the system and also the shaft radial fluctuation (IAS). The introduction of the 0.3 mm offset misalignment generated significant changes in the waveform, both in shape and amplitude (Peak-to-Peak difference between baseline and 0.3 mm was 1.505 m/s^2 low speed, 5.657 m/s^2 high speed). The higher the speed was, the greater the effects. These changes give a good indication that the wireless sensor will detect and diagnose the presence of misalignment.

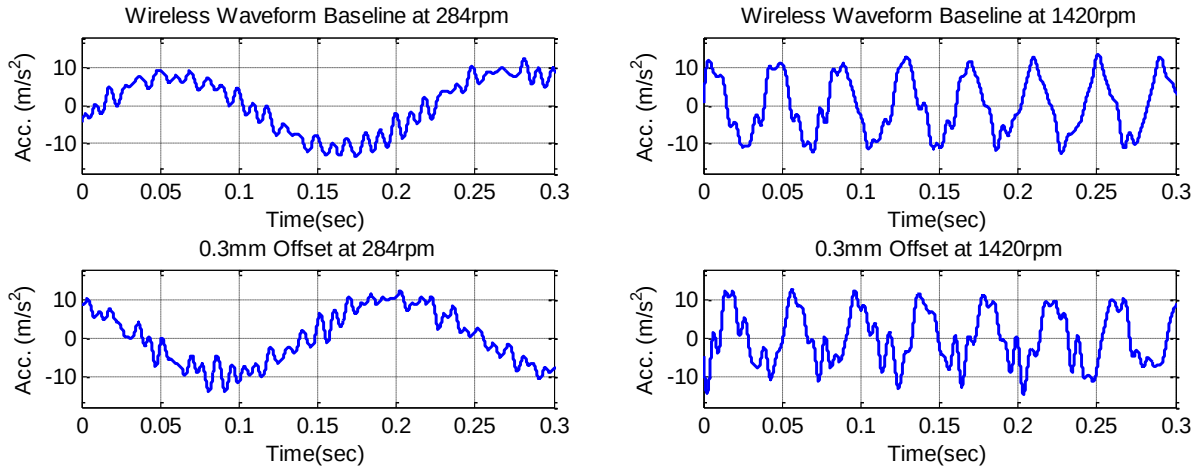

Figure 8.4 Wireless sensor waveforms at low and high speeds and two misalignment conditions.

Figure 8.5 show the IAS waveforms obtained from the encoder 100 pulses per revolution, using time interval method explained in Section 4.4.1, for baseline condition and a 0.3 mm offset misalignment and shaft speeds 284 and 1420 RPM. The figure shows the variations about the mean value of the average speed (29 and 148 rad/s). At low speed waveform exhibits small change (decrease) in amplitude (-0.070 rad/s Peak) when the 0.3 mm misalignment was introduced whereas there was a significant decrease at the higher speed (-8.885 rad/s Peak). However, these changes are clear from the waveforms amplitude decrease when 0.3 mm induced at high and low speed.

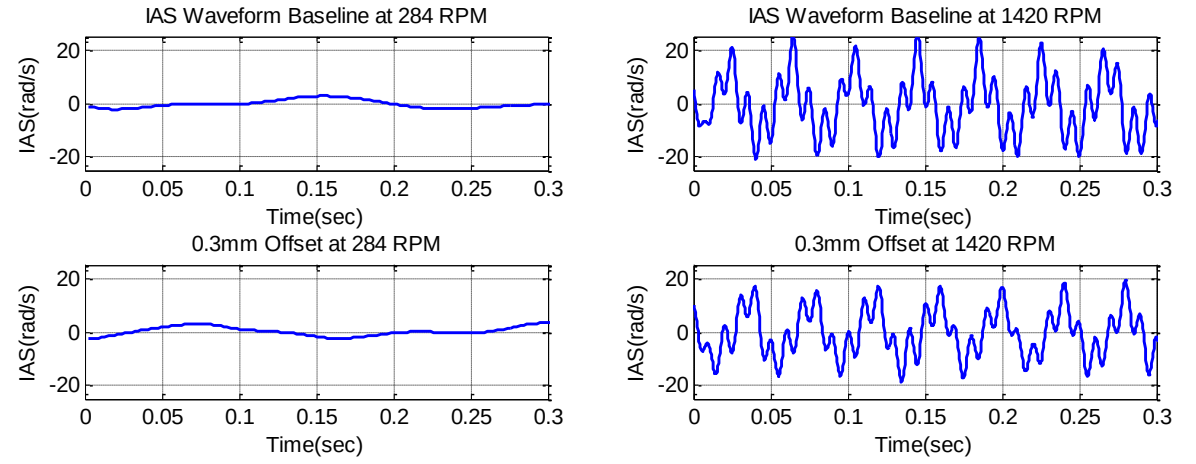

Figure 8.5 IAS waveforms at low and high speeds and two misalignment conditions.

Figure 8.6 presents the outputs of the wired accelerometers in the vertical and horizontal directions. The waveforms were badly contaminated by high frequency noise, making the periodic feature difficult to distinguish. At low speed the horizontal waveform exhibit small change in amplitude (0.573 m/s^2 Peak) when the 0.3 mm misalignment was introduced whereas there was a significant increase at the higher speed (0.866 m/s^2 Peak). On the

vertical side, at low speed the waveforms demonstrate significant change in amplitude (1.027 m/s^2 Peak) when the 0.3 mm introduced whereas there was a small increase at high speed (0.507 m/s^2 Peak). In addition, the horizontal vibration waveform amplitudes are slightly higher than that of the vertical, and increase with misalignment level.

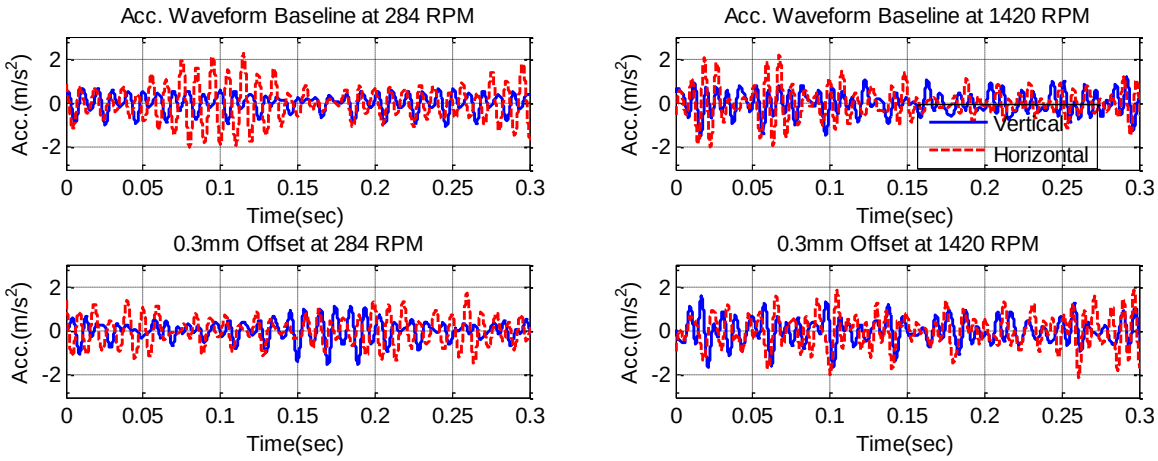

Figure 8.6 Accelerometers waveforms at low and high speeds and two misalignment conditions.

The displacement waveforms from the laser sensor are shown in Figure 8.8. The waveforms show clear periodicity with respect to the shaft rotation. The vertical waveforms amplitude exhibits a very small decrease (-0.002 mm Peak) at the lower speed when the 0.3 mm misalignment is introduced, whereas at the higher speed the amplitude increases (0.006 mm Peak). On the horizontal side, the waveforms amplitude demonstrate decrease (-0.025 mm Peak) at the low speed and also decrease (-0.028 mm Peak) at high speed. Although the amplitude is decreased at low and high speed of horizontal direction, it shows that the change is higher than that of vertical one. However, the most obvious difference between waveforms is that the displacement in the horizontal direction is lower than that in the vertical. Since the laser vibrometr was directed to the coupling as shown in Figure 8.2, the flexible coupling forces acting in the horizontal direction were constrained by the hard rubber, see Figure 8.7. Therefore, the target flange of the coupling compensates that by acting in the vertical direction.

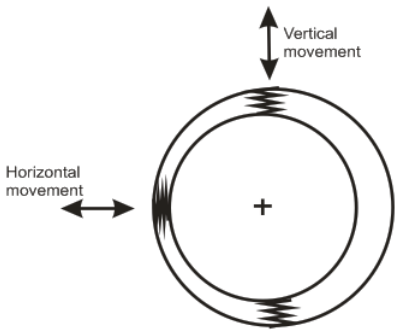

Figure 8.7 Coupling constraint horizontally due to horizontal offset.

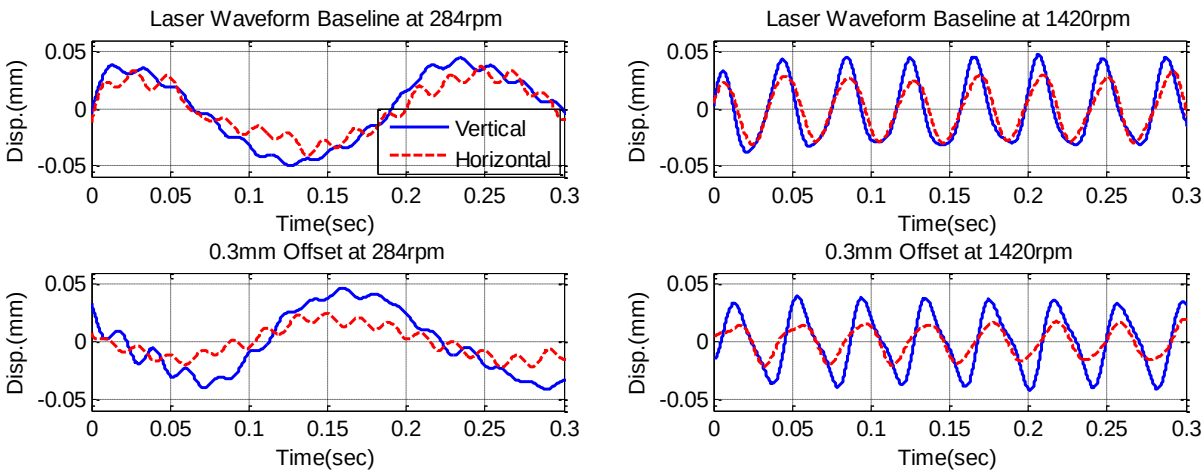

Figure 8.8 Laser vibrometers waveforms at low and high speeds and two misalignment conditions.

From the above waveform based analysis, the wireless sensor and accelerometers are more likely to detect the misalignment than the other sensors.

8.4.2 Spectrum Variation

To investigate further the measured responses and identify whether they could accurately differentiate the baseline and misaligned conditions, an FFT was applied to obtain corresponding spectra for the wireless accelerometer, IAS, wired accelerometers and the laser vibrometers, as shown in Figure 8.9, Figure 8.10, Figure 8.11 and Figure 8.13 respectively.

Figure 8.9 shows the wireless sensor spectra. The high amplitude peak at 1X running speed was mainly due to the gravitational effects due to its rotation around the shaft in a vertical plane (9.81 m/s^2). The faint higher harmonics represented inevitable rotor unbalance or misalignment in the baseline spectrum. Comparing the spectra for baseline and misaligned cases, it can be seen that at the lower speed the amplitude of the peak at 2X running speed showed little change when the misalignment fault of 0.3 mm was seeded into the system. However, there was a significant increase (from 0.391 to 1.069 m/s^2) at the higher speed due to effect of unbalance forces caused by the misalignment. The magnitude of the harmonic peaks at frequencies above 2X showed only marginal increases at the higher speed, showing the misalignment had less effect on high frequency vibration. The considerable amplitude increase at 2X is considered an indication of misalignment.

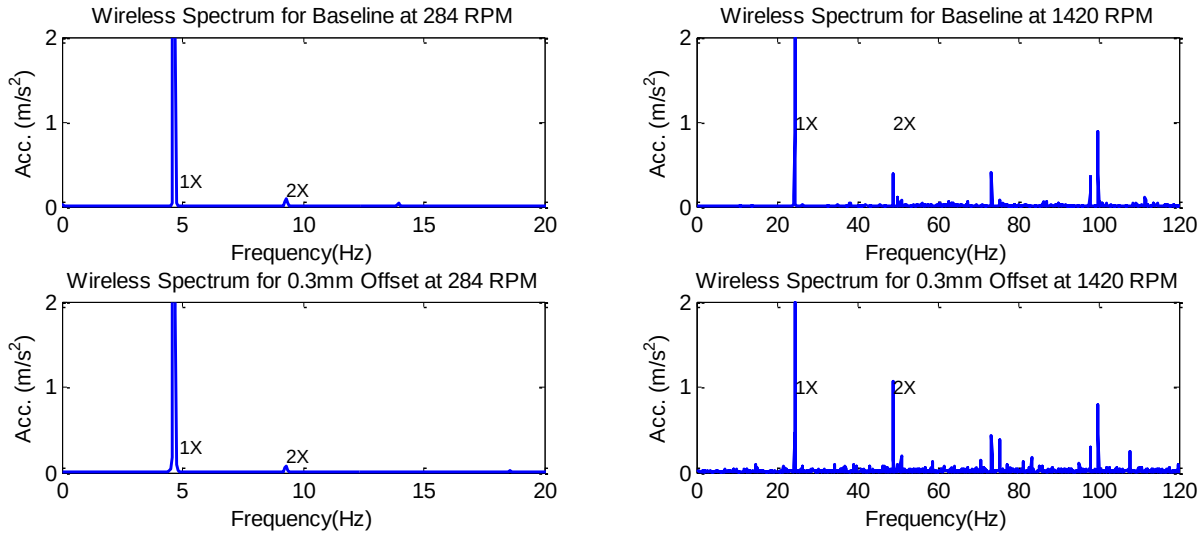

Figure 8.9 Spectra of wireless sensor waveforms at low and high speeds and two misalignment conditions.

The encoder spectra in Figure 8.10 showed a substantial increase in the amplitude of the 1X peak in the baseline and misaligned spectra with increase in rotor speed. For the lower speed, introducing the misalignment reduced the 1X peak slightly, but small reduced the 2X peak (from 0.429 to 0.369 rad/s). At the higher speed introducing the misalignment significantly increased the magnitude of the 1X peak, however the amplitude of the 2X peak is decreased by introducing the misalignment (from 0.718 to 0.416 rad/s). The small change in spectral amplitude of 2X, in this condition, is due to the position of the encoder at the far end of the shaft.

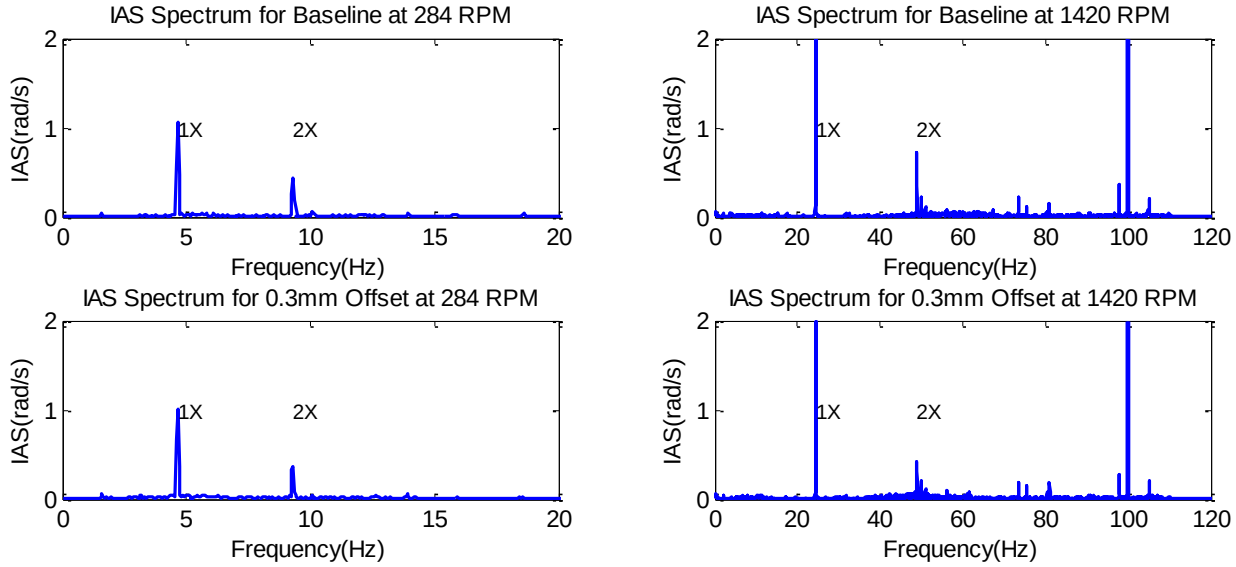

Figure 8.10 Spectra of encoder (IAS) waveforms at low and high speeds and two misalignment conditions.

Figure 8.11 presents the spectra of the signal from the wired accelerometers for low and high speeds, with and without the seeded misalignment. At the lower speed the seeding of the misalignment fault significantly increased the amplitudes of the 1X and 2X peaks. The magnitude of increase of 2X peaks was for horizontal (from 0.00126 to 0.00244 m/s^2) whereas in vertical (from 0.00065 to 0.00085 m/s^2). The horizontal accelerometer shows much greater increases than the vertical. At the higher speed, the introduction of the misalignment fault produced a small but significant increase in the peaks at 1X and 2X. The 2X peaks change in horizontal was decreased (from 0.112 to 0.109 m/s^2) whereas increased in vertical direction (from 0.118 to 0.121 m/s^2), but a large increase in the amplitude of the peak from the horizontal and vertical accelerometer at 3X.

The laser vibrometer spectra in Figure 8.12 show that both vertical and horizontal peak amplitudes at 1X for both speeds decreased when the misalignment fault was introduced. In addition the corresponding 1X peaks decreased with increase in rotor speed. Comparison of the 1X and 2X amplitudes obtained show that the horizontal value was consistently lower than that of the vertical. At low speed, the 2X peaks change in horizontal was decreased (from 0.002 to 0.001 mm) whereas increased in the vertical direction (from 0.0012 to 0.0024 m/s^2). At high speed, the 2X peaks change in horizontal was decreased (from 0.0025 to 0.00232 mm) and also decreased in vertical direction (from 0.0021 to 0.0019 mm).

From the above discussion, it is clear that the 2X amplitude increases and decreases according to the corresponding sensor of both speed and misalignment level. However, the wireless sensor produces more significant consistent increase than that of other sensors.

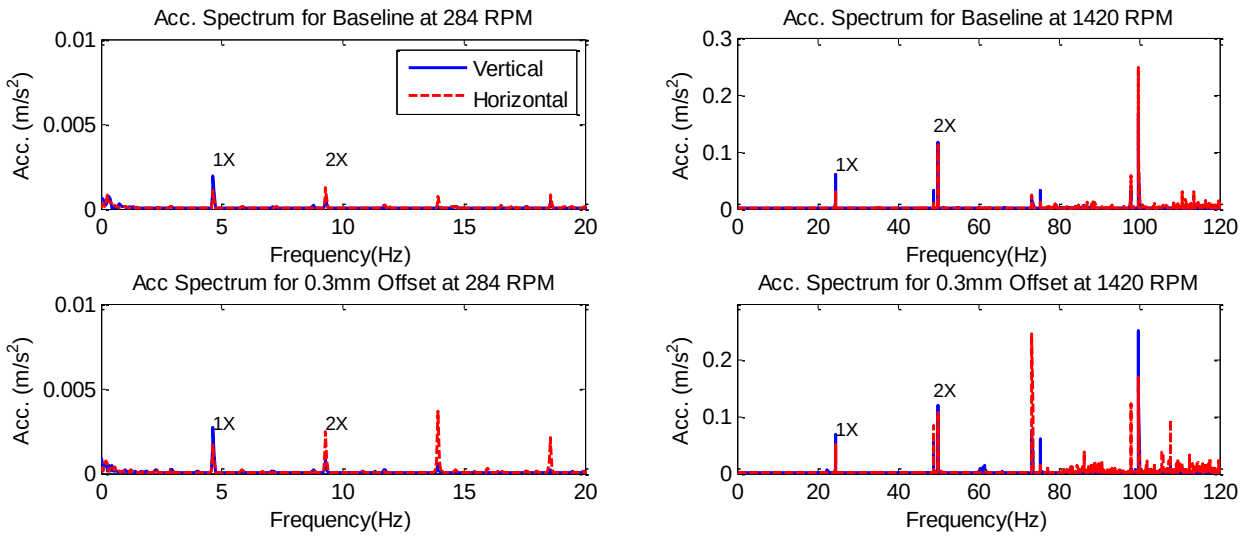

Figure 8.11 Spectra of waveforms from wired accelerometers at low and high speeds and two misalignment conditions.

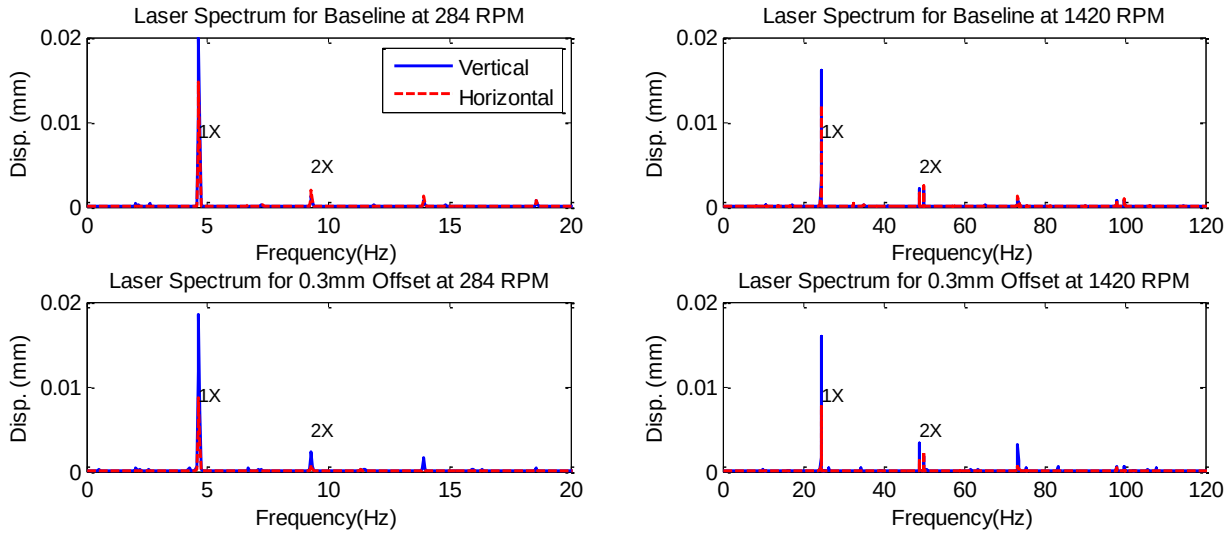

Figure 8.12 Spectra of laser vibrometer waveforms at low and high speeds and two misalignment conditions.

8.5 Detection and Diagnosis Performance

To provide more accurate results for misalignment diagnosis and comparison between sensors, the peak amplitudes at 1X and 2X running speed were extracted and represented as a function of rotor speed, see Figure 8.13 and Figure 8.14.

Comparing the spectral amplitude trends of different sensors with misalignment levels, Figure 8.13 shows that 1X components of wireless sensor, encoder and laser vibrometer were not able to separate baseline and misaligned cases. However, the vertical and horizontal wired accelerometers show clear differences between baseline and the different misalignment levels. The horizontal accelerometer shows better separation between baseline and misalignment levels as the speed increases, but there is no discrimination between different levels of misalignment. This argument proves that the misalignment cannot be clearly found based on the amplitude of 1X running speed for all the sensors (Hariharan, V., et al., 2009; Lees, A. W., 2007 (a), 2007 (b); Piotrowski, 2007; Saavedra, P. & Ramırez, D. , 2004; Xu & Marangoni, 1994 a).

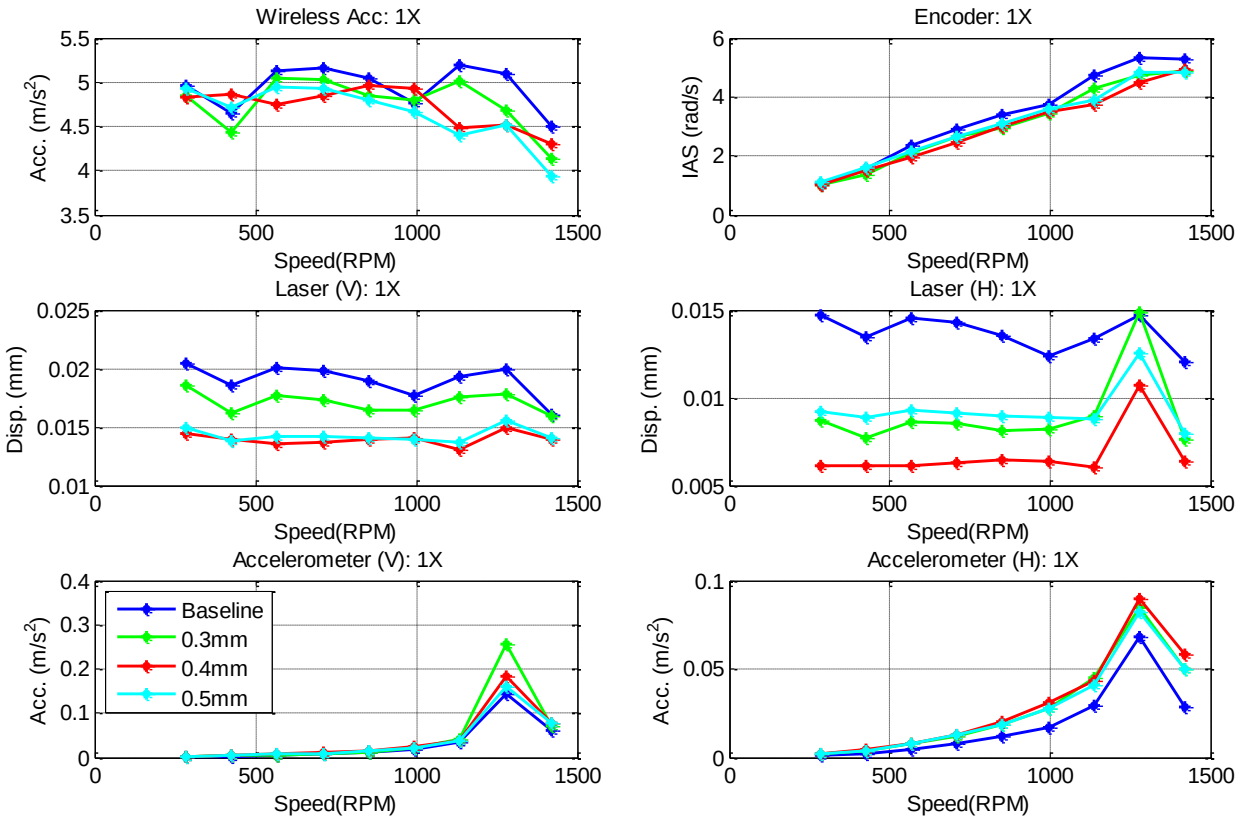

Figure 8.13 Amplitudes of spectral peaks at 1X running speed versus speed and misalignments.

The amplitude of the 2X peak is shown in Figure 8.14 reveals that the wireless accelerometer, wired accelerometers and encoder could be used for misalignment diagnosis as there are definite differences in amplitude between misalignment levels. Also the difference in levels tends to increase with rotor speed. However, although the vertical laser vibromrter appears best separating between baseline and different levels of misalignment with rotor speed, the levels of misalignment were not consistent mainly between 0.3 and 0.4mm. The wireless sensor can produce a peak value that increases consistently with misalignment level and rotor speed. These results agree with the wireless sensor model results of (Arebi, Gu, & Ball, 2011) and with results reported by other researchers (Sekhar, A. S. & Prabhu, 1995; Vance, 1988).

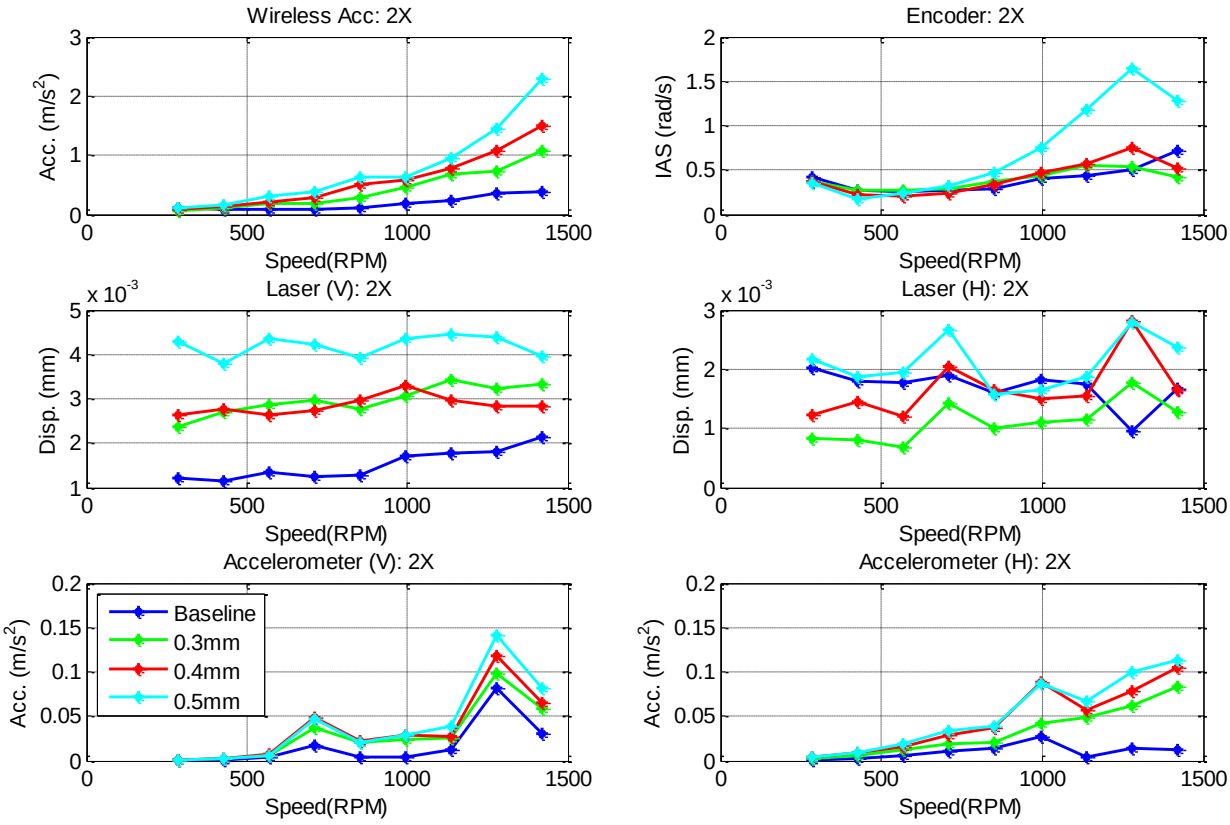

Figure 8.14 Amplitudes of spectral peaks at 2X running speed versus speed and misalignments.

8.6 Summary

The comparison of signals from the different sensors showed a slight change in the amplitude of the signals for different levels of misalignment. Generally, the amplitude increases with speed, but its overall level did not show a consistent trend with increasing misalignment probably because of high frequency noise from other vibrations.

Spectral analysis showed a peak at 1X running speed component of all sensors failed to differentiate different levels of misalignment. However, the spectral peak at 2X allowed the misalignments to be separated with different degrees of success depending on the sensors used:

- The wireless sensor produces full separation of different misalignment levels and shows a unique increasing trend with speed.
- IAS allowed separation of the high misalignment level at high speeds.
- Vertical displacement from the vibrometer shows misalignment separation from the baseline but is not consistent with misalignment levels.
- Horizontal acceleration shows a very similar performance to that of the wireless sensor, but its trend is not consistent with increasing speed.

8.7 Investigation of Detectability of Small Degrees of Misalignment

The relative small value of shaft misalignment can have significant impact on roller element bearing, seals, and couplings. Stephen (Stephen, et al., 1999) found that, in some cases, up to 50% percent of the expected bearing life can be lost with as small as a 0.127 mm horizontal misalignment.

The aim of this study is to test the efficiency of the wireless accelerometer in detecting smaller values of the seeded misalignment, 0.1 mm and 0.2 mm. This investigation uses the model developed in Chapter 6 with 4 rotors. The parameters used in this study are the same as given in Table 6.2. Also, the eccentricity was kept at 0.02 mm and the residual misalignment between shafts 3 and 4 was assumed constant at 0.01 mm.

8.7.1 Simulation Results and Discussion

8.7.2 Modelled Characteristics of Vibrations due to Misalignment

Figure 8.15 shows the results obtained from a numerical simulation study of the wireless accelerometer when the rotor speed was 1500 RPM. Figure 8.15 (a) shows the tangential components: a_{tx}, a_{ty} and a_{tw} predicted by the sensor due to accelerations: a_x, a_y and a_w. It can be seen that a_{tx} and a_{ty} fluctuate twice as fast as a_{tw}. Combining these two components together produces a sinusoidal waveform. a_{tw} follows the shaft rotation due to the sensor being rigidly located on the shaft surface. By combining the three components, the total acceleration a_t predominantly exhibits the features of a_{tw} but with the features of a_{tx} and a_{ty} imposed on it. The peak magnitude of a_{tx}, a_{ty} and a_{tw} in the baseline are 0.035, 0.017 m/s^2 and 0.017 rad/s^2 respectively.

In the frequency domain, the spectrum resulting from the combination of a_{tx} and a_{ty} is similar to that of a_{tw} but has lower amplitude, see Figure 8.15 (b). The spectrum from the full combination of a_{txy} and a_{tw} exhibits noticeable peaks at multiples of the shaft frequency. In particular, the amplitude difference between a_{tw} and a_t is marginal at 2X, showing that this component is mainly due to the effects of rotational oscillation.

For 0.1 mm misalignment, the predicted output of the sensor is as shown in Figure 8.16 (a). It can be seen that a_{tx} and a_{ty} have the same characteristics as for the healthy case except the amplitude is increased hugely (Peak 0.318 and 0.296 m/s^2 respectively). a_{tw} keeps the same phase and also same magnitude (Peak 0.017 rad/s^2). The total acceleration a_t at the sensor position exhibits much the same features as a_{tw} but with a DC shift due to the combination of a_{tx} and a_{ty}.

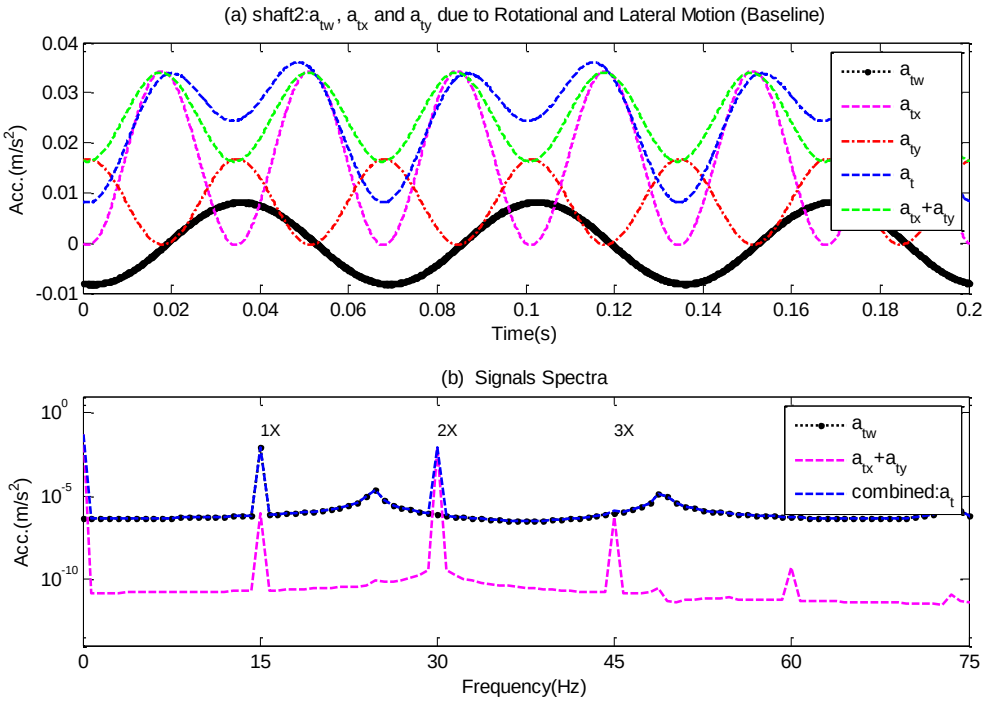

Figure 8.15 Simulated baseline rotational, lateral and tangential signals from wireless accelerometer at 1500 RPM: (a) Waveforms, (b) Spectra.

In the frequency domain, see Figure 8.16 (b), the spectrum resulting from the combination of $\boldsymbol{a_{tx}}$, $\boldsymbol{a_{ty}}$ and $\boldsymbol{a_{tw}}$ is similar with that of $\boldsymbol{a_{tw}}$. In terms of frequency content the peak at 1X has amplitude no larger than the peak at 2X. The spectrum from the full combination of $\boldsymbol{a_{tx}}$ $\boldsymbol{a_{ty}}$ and $\boldsymbol{a_{tw}}$ exhibits noticeable differences at 1X rotor speed compared with the baseline condition.

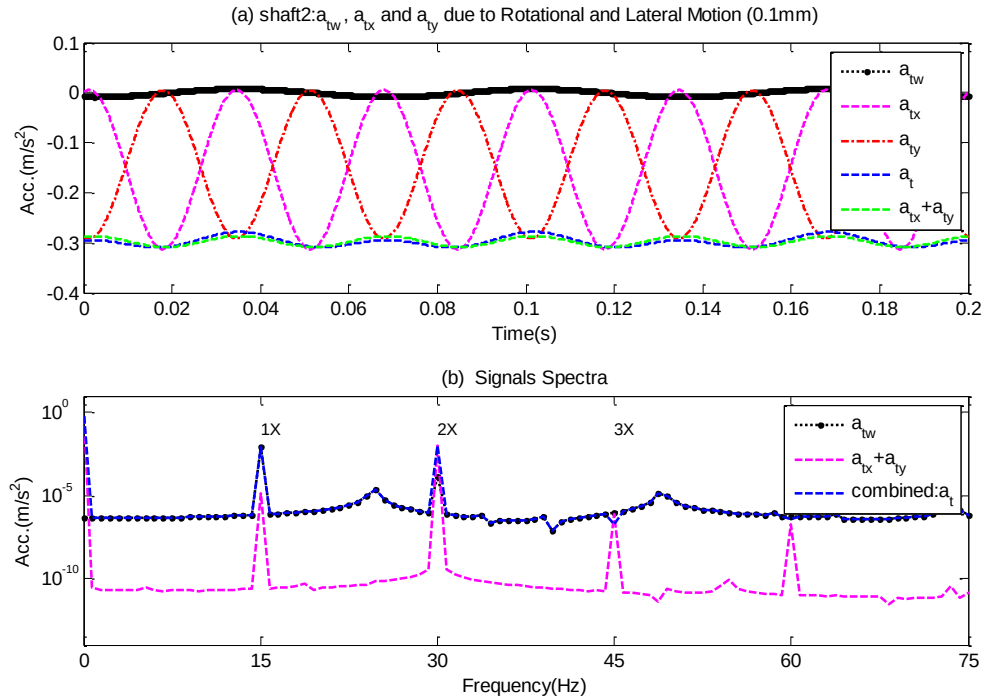

Figure 8.16 Simulated rotational, lateral and tangential signals from wireless accelerometer at 1500 RPM with 0.1 mm misalignment: (a) Waveforms, (b) Spectra.

For 0.2 mm misalignment the predicted output of the sensor is as shown in Figure 8.17 (a). It can be seen that $\boldsymbol{a_{tx}}$ and $\boldsymbol{a_{ty}}$ have the same characteristics as for the 0.1 mm misalignment but with greater amplitude (0.71 and 0.644 m/s^2 respectively). $\boldsymbol{a_{tw}}$ retains the same phase and same magnitude (0.017 rad/s^2). The total acceleration $\boldsymbol{a_t}$ at the sensor position exhibits much the same features as $\boldsymbol{a_{tw}}$ but with a DC shift due to the combination of $\boldsymbol{a_{tx}}$ and $\boldsymbol{a_{ty}}$.

In the frequency domain, see Figure 8.17 (b), the spectrum resulting from the combination of $\boldsymbol{a_{tx}}$ and $\boldsymbol{a_{ty}}$ is similar with that of $\boldsymbol{a_{tw}}$. In terms of frequency content the peak at 1X has lower amplitude than the peak at 2X. The combined spectrum of $\boldsymbol{a_{txy}}$ and $\boldsymbol{a_{tw}}$ exhibits noticeable differences at 2X rotor speed compared with the baseline condition.

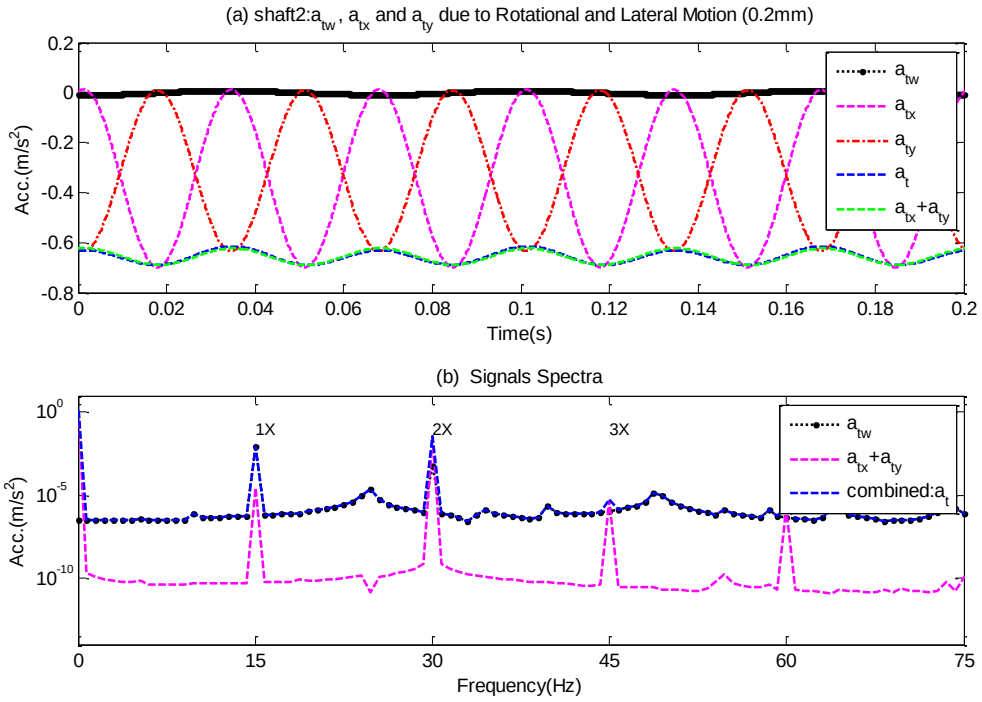

Figure 8.17 Simulated rotational, lateral and tangential signals from wireless accelerometer at 1500 RPM with 0.2 mm misalignment: (a) Waveforms, (b) Spectra.

8.7.3 Modelled Characteristics of Spectral Amplitude

To examine further the changes in predicted spectral amplitude for the 0.1 mm and 0.2 mm misalignments, a simulation study was performed under different motor speeds. Figure 8.18, Figure 8.19, and Figure 8.20 show the predicted variation in amplitude of the first four harmonics, 1X, 2X, 3X and 4X, with rotor speed for the combined, rotational and lateral acceleration spectra respectively. By comparing amplitudes between combination ($\boldsymbol{a_t}$), rotational ($\boldsymbol{a_{tw}}$) and lateral ($\boldsymbol{a_{txy}}$) it was observed that:

The amplitude of the first harmonic peak, 1X, for the combined acceleration ($\boldsymbol{a_t}$) increased with speed and also increased with increase in misalignment. Also, the magnitude of the peak was very small. Both rotational ($\boldsymbol{a_{tw}}$) and lateral ($\boldsymbol{a_{txy}}$) accelerations also showed very small

amplitudes but now the amplitude did increase with speed and the three misalignment conditions could be distinguished. However, the small amplitude of the accelerations could be influenced by measurement noise. It is concluded that the amplitude at 1X is not suitable for misalignment detection.

The predicted amplitude of the peak at 2X is much larger than the peak at 1X for all three accelerations and also increases with speed. The magnitude of the 2X peak for combined acceleration ($\boldsymbol{a_t}$) was the highest, but did not discriminate between the baseline and 0.1 mm misalignment and so may have problems detecting incipient faults. The rotational acceleration ($\boldsymbol{a_{tw}}$) did discriminate between the baseline and 0.1 mm misalignment and so would probably better for detecting incipient faults. This means that the wireless sensor is capable of detecting this small degree of misalignment. The 2X feature for detecting misalignment follows what was derived and observed in previous chapters.

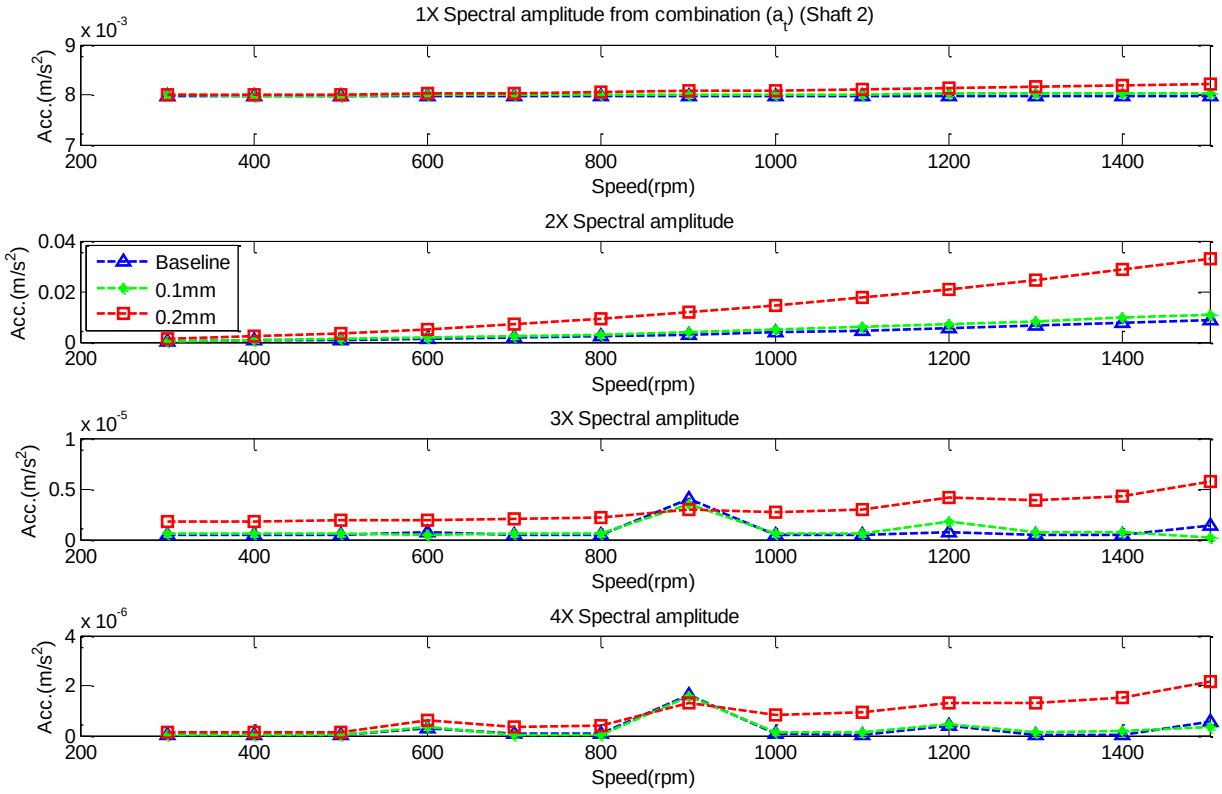

Figure 8.18 Amplitudes of spectral harmonics as a function of rotor speed (Combined, a_t)

The amplitude of the 3X peak appeared to clearly distinguish the 0.2 mm misalignment certainly at higher speeds, though there was some variability in the rotational acceleration ($\boldsymbol{a_{tw}}$). However, for this particular peak only the combined acceleration was able to distinguish the 0.2 mm misalignment and then only at higher speeds. However, the predicted magnitudes of these peaks were in the order of 10^{-6} ms^{-2} which would be very difficult to detect in practice.

The predicted amplitudes of the 4X peaks are again of the order of 10^{-5} ms^{-2}. Only the lateral acceleration, a_{txy} offers a consistent trend and distinguishes the 0.2 mm misalignment. There appears to be a difference between the baseline and 0.1 mm misalignment but it is so small (about 10^{-6} ms^{-2}) as not to be significant.

It is concluded that the magnitudes of the 3X and 4X peaks of the combined and rotational accelerations cannot be used as indicators of small degree of misalignment. The peaks appeared in the 3X and 4X in the rotational accelerations at 600,900, 1200 and 1500 are due to the closeness of these speeds to the system resonance frequency. Consequently, the combinational accelerations at 3X and 4X are affected by these changes in the response of the rotational accelerations.

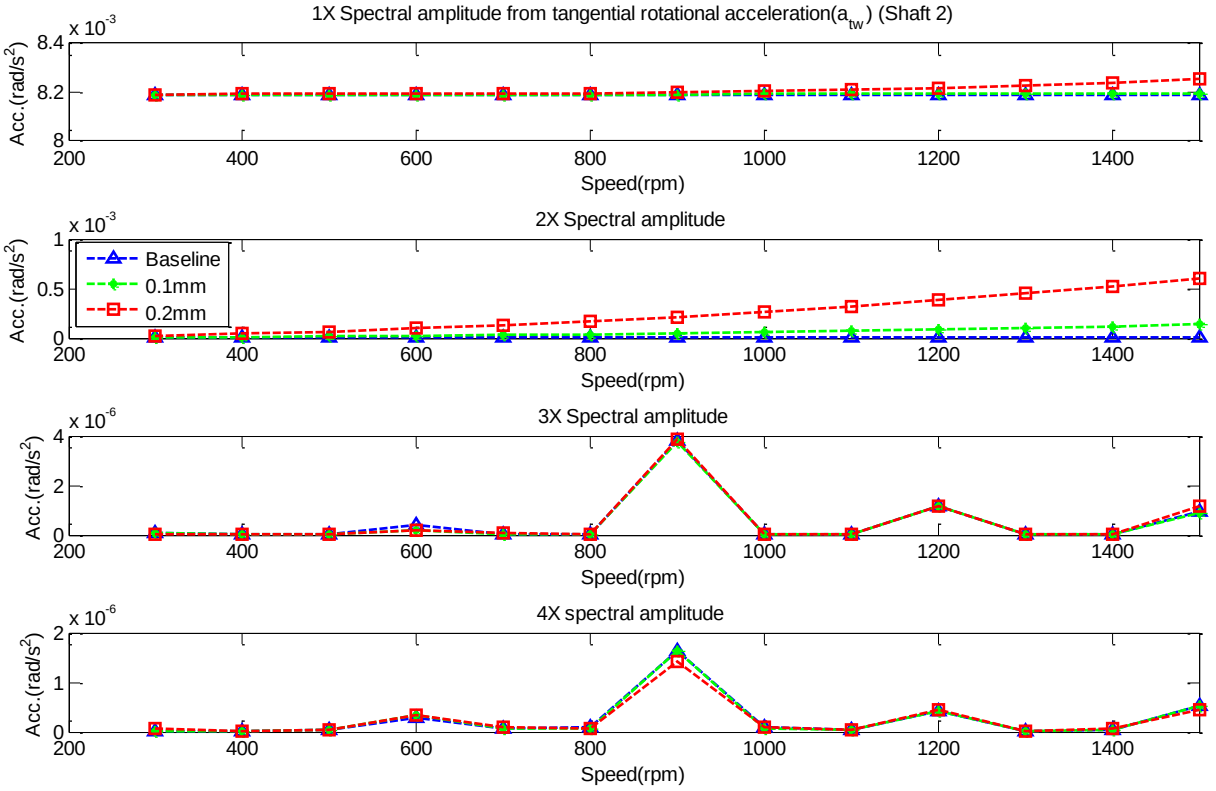

Figure 8.19 Amplitudes of spectral harmonics as a function of rotor speed (Rotational, a_{tw})

In general, the amplitude variations for each of the combined, lateral and rotational accelerations at the 2X harmonic peak could be good indicators of small degrees of misalignment. However, although the rotational acceleration separates the cases clearly, it has low magnitude compared to combination. On the other hand, although the 1X peaks for rotational and lateral acceleration could separate different cases of misalignment at high speed, it has relatively low amplitude and can be influenced by measurement noise.

It was concluded that the 2X acceleration peaks were best for misalignment detection confirming the findings of previous researchers (Jalan & Mohanty, 2009; Lees, A. W., 2007 (a), 2007 (b); Redmond, Irvin & Al-Hussain, 2001; Saavedra, P. & Ramırez, D. , 2004; Sekhar, A. S. & Prabhu, 1995; Xu & Marangoni, 1994 a).

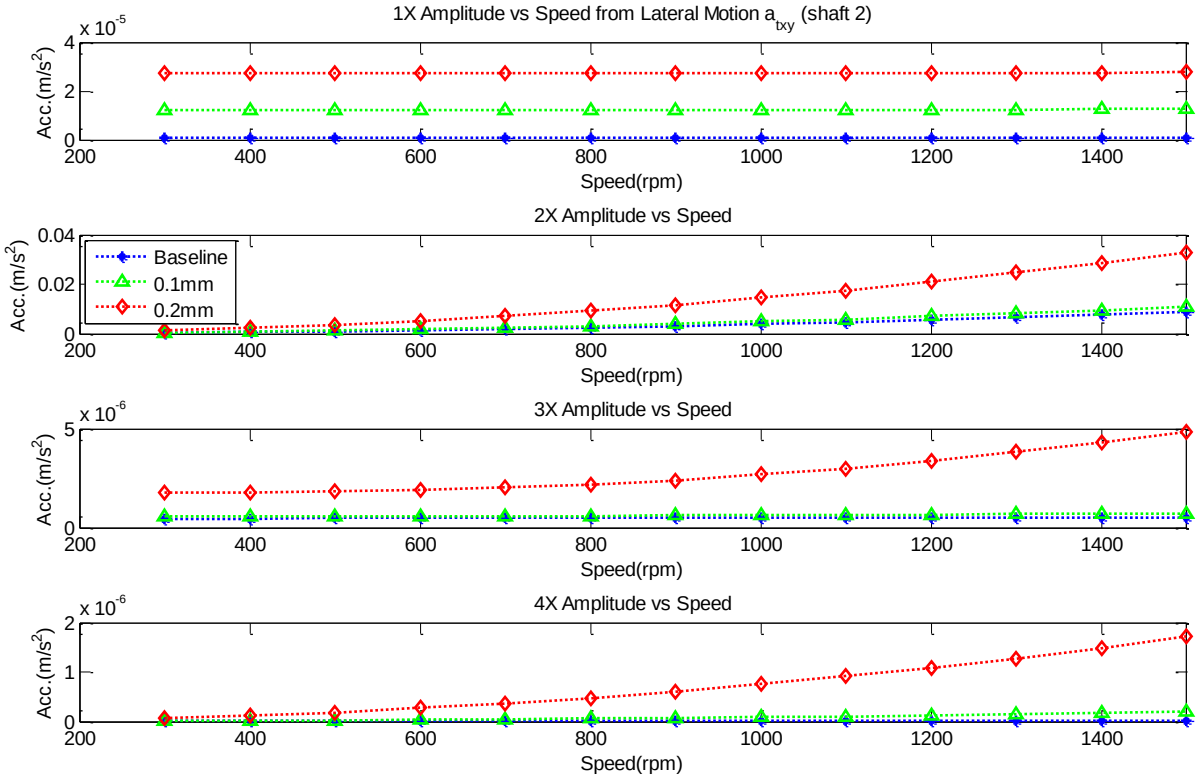

Figure 8.20 Amplitudes of spectral harmonics as a function of rotor speed (Lateral, a_{txy})

8.8 Experiment Setup

To verify the results from the model at 0.1 mm and 0.2 mm degrees of misalignment, an experiment was carried out. In this experiment the same test rig setup as shown in Figure 8.21 is used. The test procedure carried was similar to that described in Section 8.3. Table 8.1 presents measured residual values of the misalignment degrees using a dial indicator. Since the dial indictor measures the horizontal through 180°, the value is divided by 2 in order to get the effective value of measured degree of misalignment.

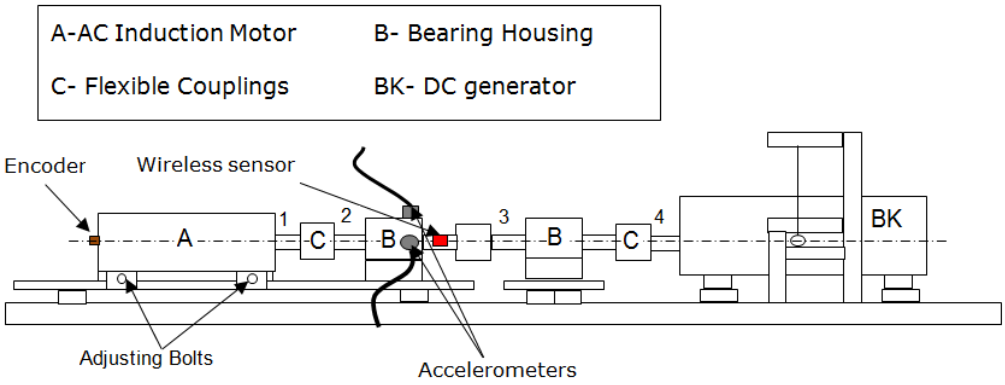

Figure 8.21 Test rig schematic and wireless sensor, encoder and accelerometers placement.

Table 8.1 Measured misalignment

Condition	Vertical	Horizontal	Effective Horizontal misalignment
Baseline	+0.03 mm	+0.00 mm	+0.00 mm
0.1mm	+0.12 mm	+0.21 mm	+0.105 mm
0.2mm	+0.21 mm	+0.41 mm	+0.205 mm

8.9 Results and discussion

8.9.1 Waveform Variation

Figure 8.22 shows typical waveforms from a wireless sensor for baseline, 0.1 mm and 0.2 mm misalignments at shaft speeds of 284 and 1420 RPM. As demonstrated by the top row of Figure 8.22, the output of the wireless sensor for the baseline case shows clear periodic oscillations. There is a large amplitude relatively low frequency signal corresponding to the rotor rotation frequency of about 4.7 Hz (284 RPM) on which is imposed a much smaller, higher frequency oscillation. When the 0.1 mm and 0.2 mm misalignments were seeded there was a small increase in waveform amplitudes. At low speed, the peak amplitude of baseline, 0.1 mm and 0.2 mm was 25.45, 26.31 and 25.55 m/s2 respectively whereas at high speed, 29.37, 30.03 and 29.72 m/s2. In addition, the waveform shape also showed considerable change for 0.2 mm misalignment level at the higher speed. These are good indications for detecting and diagnosing the occurrence of misalignments.

IAS waveforms from the encoder in Figure 8.23 show similar periodic oscillations to those of the wireless accelerometer. With the higher degree of misalignment (0.2 mm) there was a slight decrease in waveform amplitude at the lower speed, but an increase in waveform amplitude was observed at the higher speed. At low speed, the peak amplitude of baseline, 0.1 mm and 0.2 mm was 5.84, 6.89 and 7.36 m/s^2 respectively whereas at high speed, 43.67, 44.59 and 40.45 m/s^2 respectively.

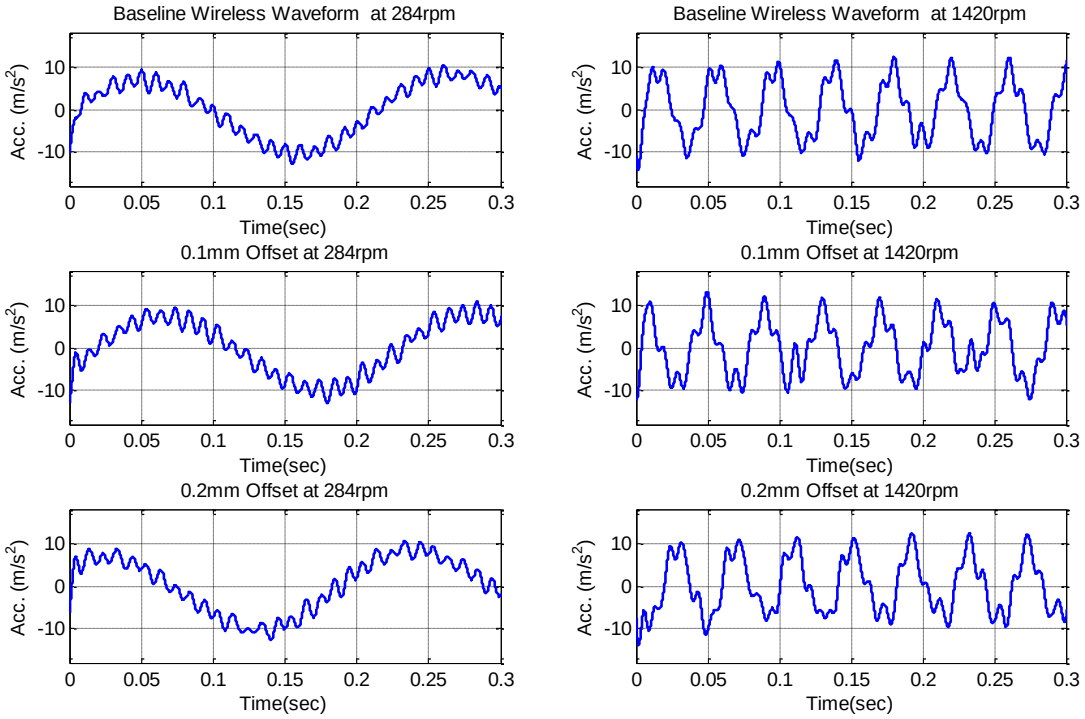

Figure 8.22 Wireless sensor waveforms for baseline, 0.1 mm and 0.2 mm misalignments at low and high speeds.

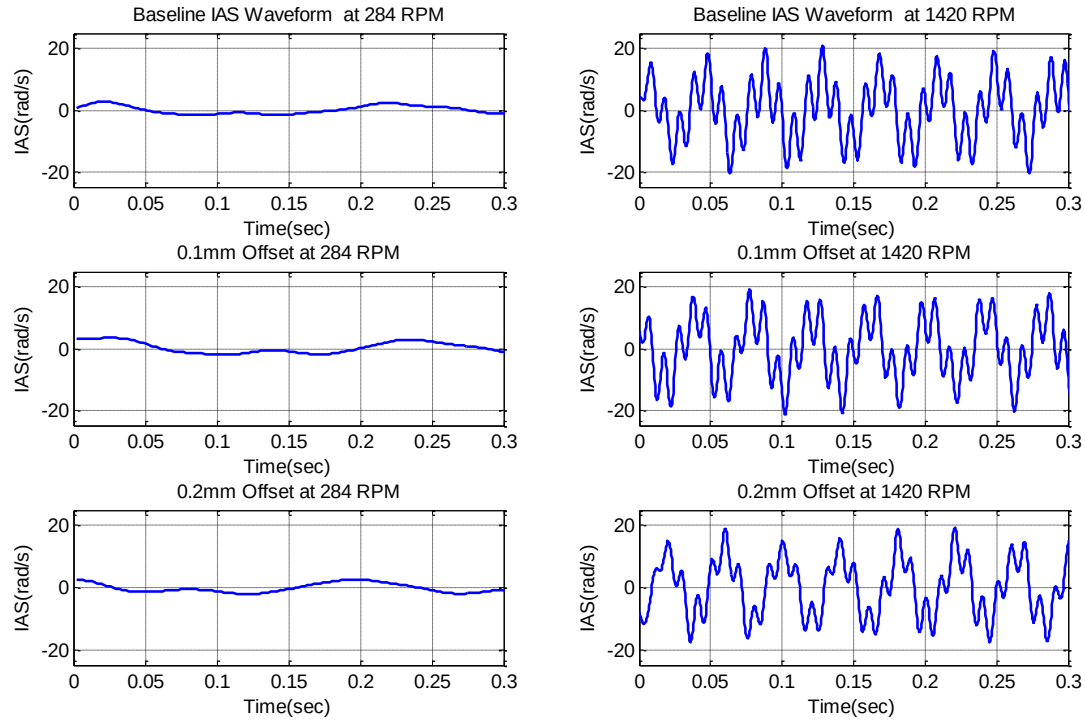

Figure 8.23 Waveforms for baseline, 0.1 mm and 0.2 mm misalignments at low and high speeds.

Figure 8.24 illustrates the outputs of the vertical and horizontal wired accelerometer sensors. The waveforms were badly contaminated by high frequency noise, making the periodic feature hard to observe. The waveform amplitudes exhibited small change with different degrees of misalignment at low speed but significant increase at high speed. At low speed, the peak amplitude of baseline, 0.1 mm and 0.2 mm in the horizontal direction was 1.986, 1.989 and 1.649m/s^2 respectively whereas at high speed, 3.129, 3.435 and 3.994 m/s^2. On the vertical direction, the peak amplitude of baseline, 0.1 mm and 0.2 mm in the vertical direction was 1.199, 1.863 and 2.242 m/s^2 respectively whereas at high speed, 1.211, 2.214 and 2.460 m/s^2. In addition, the horizontal vibration waveform amplitudes were slightly higher than for the vertical accelerometer, and increase with misalignment levels as shown in Figure 8.24. The generated forces in the couplings manifested the characteristics of lateral vibration. It is clear the horizontal shift of the rotor made the rotor showed greater movement in that direction rather than in the vertical direction. The reaction forces in the vertical direction will force the shaft to vibrate more in the horizontal direction due to misalignment offset. These lateral forces impact on the overall rotor vibration in the tangential direction. The wireless sensor will pick up these forces in the tangential direction with the same frequency content as acceleration but different amplitude.

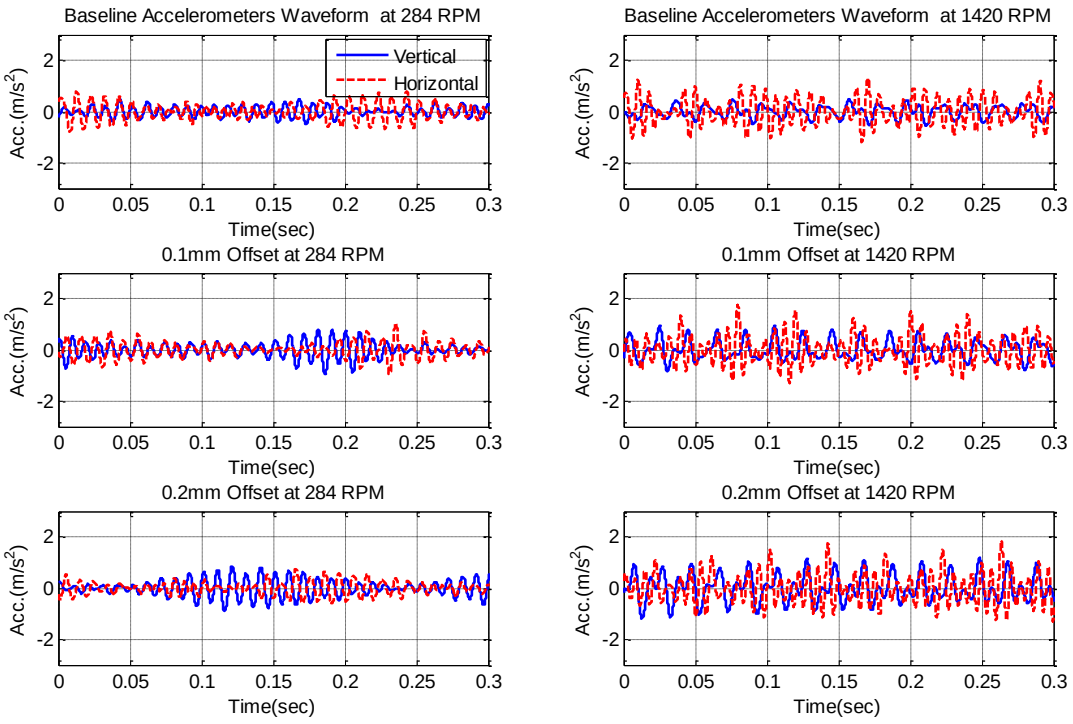

Figure 8.24 Wired accelerometers waveforms for baseline, 0.1 mm and 0.2 mm misalignments at low and high speeds.

8.9.2 Variation in Amplitude of Spectral Peaks

For additional analysis, the 1X and 2X harmonic peaks for baseline, 0.1 mm and 0.2 mm misalignments were measured as a function of rotor speed, see Figure 8.25 and Figure 8.26 respectively. For the peak at the first harmonic, 1X, only the encoder detected the misalignment, see Figure 8.25.

For the 2X peak, see Figure 8.26, the wireless accelerometer was able to detect the higher level of misalignment for speeds above 400 RPM, and the lower level of misalignment above about 1000 RPM. Above 1000 RPM the baseline, 0.1 mm and 0.2 mm misalignments the trends were quite separate and distinct. The encoder, while not giving a uniform trend did clearly distinguish between the three levels of misalignment above 500 RPM. The wired accelerometers did not provide consistent readings able to detect the fault. The wireless accelerometer outperforms all the other sensors in detecting small degrees of misalignment.

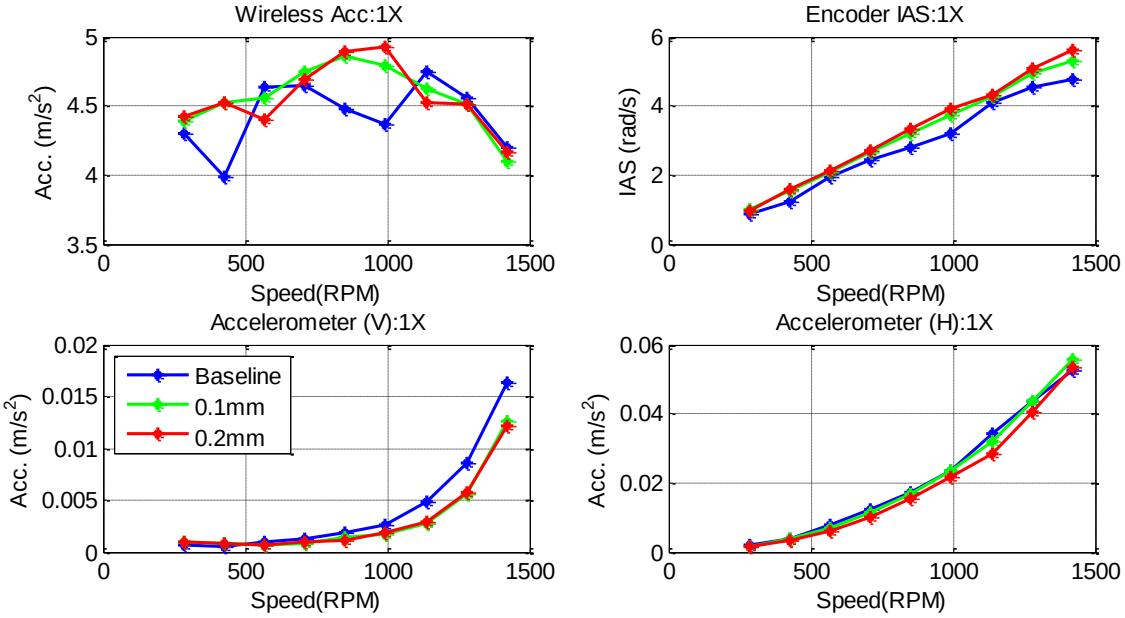

Figure 8.25 Amplitude of first harmonic, 1X, versus speed for baseline, 0.1 mm and 0.2 mm misalignments.

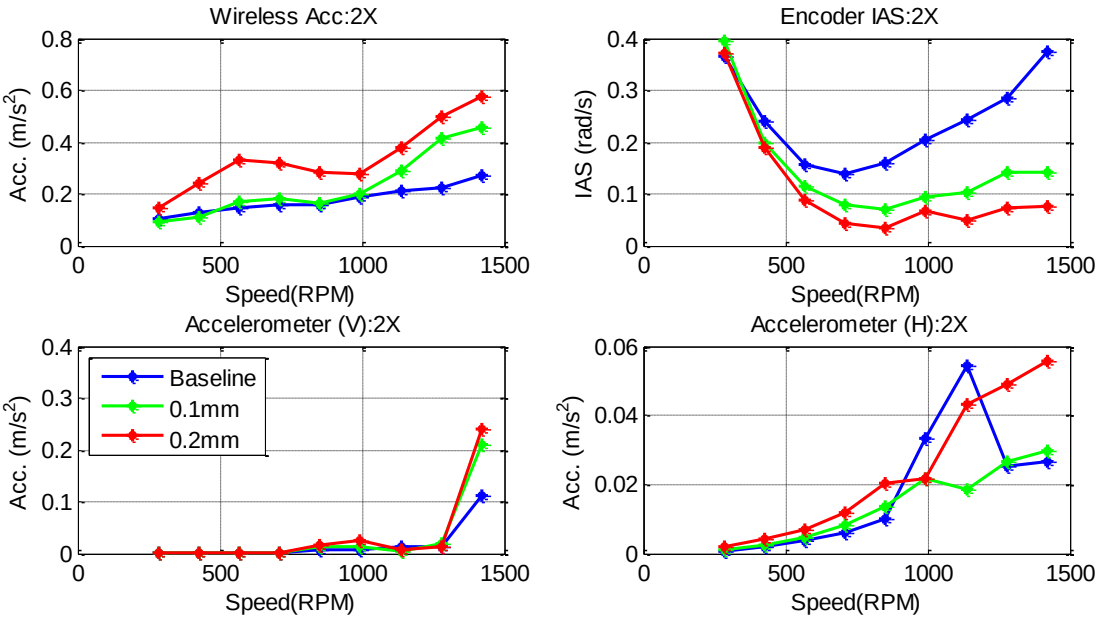

Figure 8.26 Amplitude of second harmonic, 2X, versus speed for baseline, 0.1 mm and 0.2 mm misalignments.

8.10 TSA Wireless signal in angular domain

To study the effectiveness of TSA, the raw data from wireless sensor was processed using this technique (refer to Section 4.7) to suppress the noise generated by other parts of the test rig.

In addition, the effective acceleration acting on the wireless sensor was obtained by eliminating variation in gravitational effect due to the angular position of the MEMS wireless accelerometer (refer to Section 4.7.1). The next section explains the procedure used and the results obtained.

8.10.1 Characteristics of TSA Wireless Signals after Elimination of Gravitational Effects

Gravitation effects removal algorithm discussed in Section 4.7.1 is applied to wireless measured data at different operating conditions of Figure 8.22. The signals examined were for nine different rotor speeds between 284 and 1420 RPM. The result obtained shown in Figure 8.27 represents the tangential acceleration in the angular domain. It is clear that the waveforms show the increase in the amplitude of the acceleration with respect to the shaft speed with 5 revolutions and 200 orders. In addition, a small change in the waveform shape is shown with respect to the operating condition.

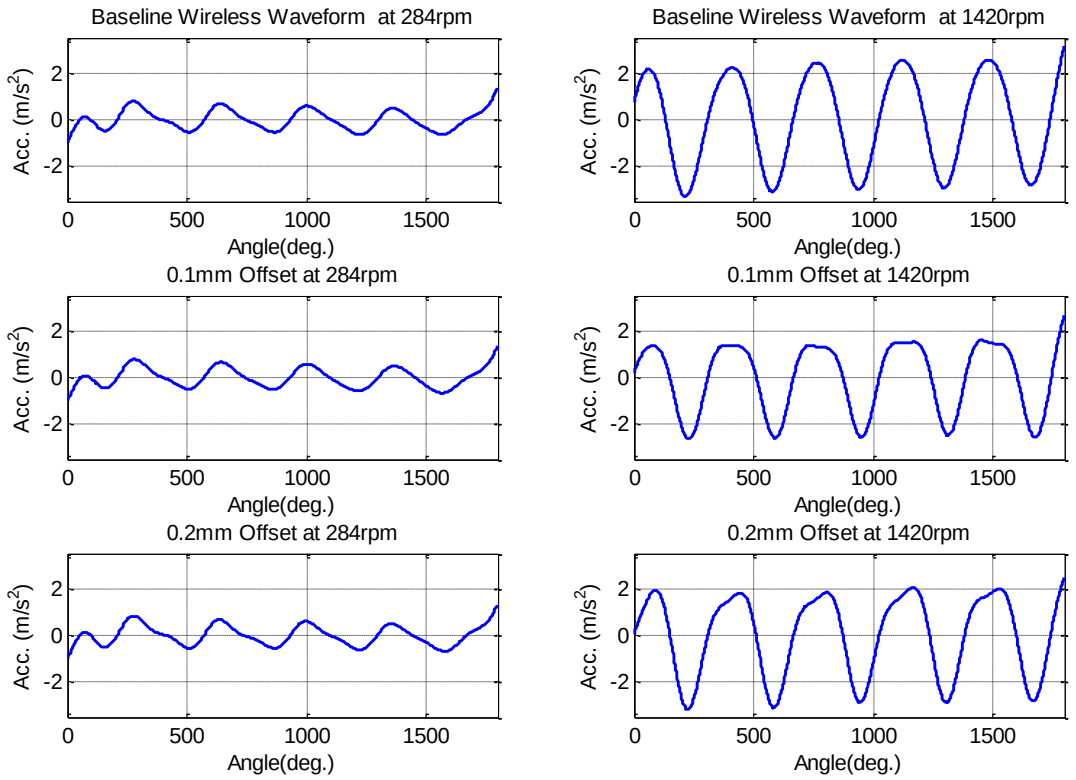

Figure 8.27 Wireless sensor waveforms for baseline, 0.1 mm and 0.2 mm misalignments at low and high speeds after applying TSA and gravitational correction.

8.10.2 Order Spectra of TSA wireless Signals

Figure 8.28 shows order spectral amplitudes of the first and second order in the order spectrum of both the TSA signals before application of gravitational correction and after given in Figure 8.27. For the 1st order peak the spectral amplitudes of the TSA waveforms varying between 8.5 and 9.87 m/s^2. The decrease in values above 1000 RPM was due to the gravity characteristics of the MEMS accelerometer refer to Section 3.12, 4.7.2. After eliminating g the amplitude of the 1st order peak shows a fairly linear increase trend with rotor speed, this represented the acceleration in the tangential direction and follows the expected trend. Although the elimination of g from TSA waveforms changes the waveform shape, the new waveforms preserve the characteristic of the waveforms before elimination g. It can be seen from Figure 8.28 that the 2nd order peak followed the same trend. The detection scheme of misalignment is shown clearly in 2nd order of spectra after application of gravitational correction compared to that of normal spectra shown in Figure 8.26.

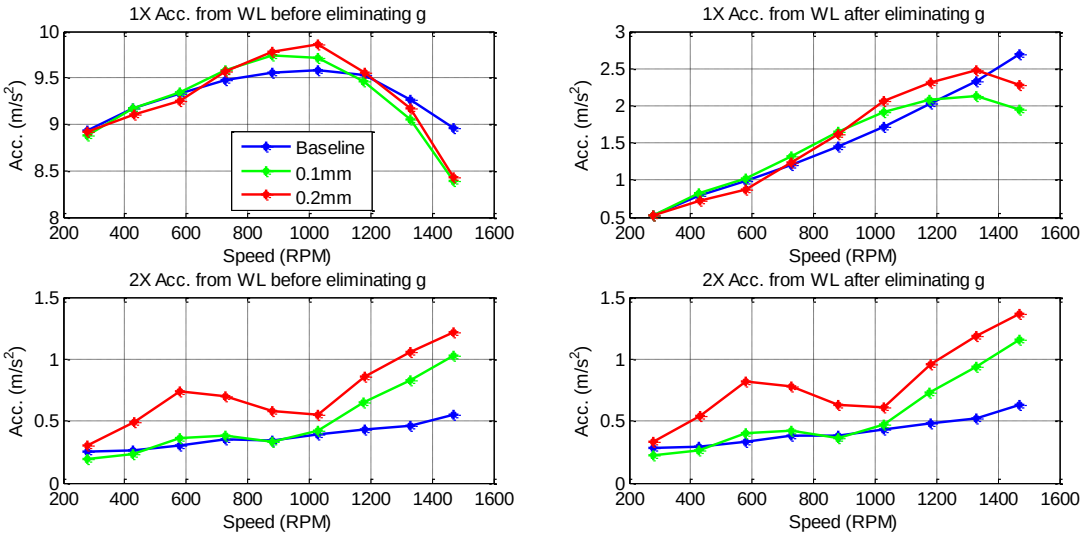

Figure 8.28 Comparison of 1X and 2X spectral peaks for the wireless accelerometer before and after eliminating gravitational effects.

8.11 Summary

From the above simulation and experimental investigation of small degrees of misalignment, it is clear that the wireless sensor is capable of detecting misalignments of 0.1 mm and 0.2 mm. The waveforms from the simulation exhibited changes in signal amplitudes generated by the fault condition. The spectral amplitude for different misalignment conditions and rotor speeds from simulation demonstrates the 2X harmonic of running speed clearly separates the different degrees of misalignment.

The experimental study shows that the waveforms exhibited small changes in magnitude at different misalignment conditions and rotor speeds. Also, the amplitude of the 2X harmonic in the spectrum of the wireless accelerometer shows clear separation between the different misalignments, whereas the other sensors failed to separate them. This shows the potential effectiveness of the wireless sensor in detecting small degrees of misalignment. Although the analysis showed that the amplitude of the 1X spectral peak of different conditions from the encoder separated, it is not related to the misalignment. The 2X peak in the spectrum of the horizontal wired accelerometer was able to separate the degrees of misalignment below 878 RPM but the vertical one could not.

The wireless sensor was better able than the other sensors to detect a low degree of shaft misalignment using the second harmonic of the signal. There was agreement between measured and simulated results in detecting such faults.

The wireless acceleration from the wireless sensor was processed using the TSA algorithm. The results show that unwanted vibrations from nearby sources were eliminated, and the resulting waveforms were smoother.

By eliminating gravitational effects from the TSA signal, an increase trend in resulted waveform amplitudes was noticeable. The amplitude of the 1^{st} order spectral peak showed an increasing trend with speed, but the amplitude of the 2^{nd} order peak increased with rotor speed both before and after elimination of g, as illustrated in Figure 8.28. This means that the characteristics of resulted waveform preserved its characteristics and increase the detection performance.

CHAPTER NINE

Identification Of Rotor Unbalance using Wireless Sensor

This chapter reports the use of the bearing test rig to conduct a systematic comparison of the wireless sensor and two other common sensors: a wired accelerometer and a shaft encoder for the detection of shaft unbalance. These three sensors were used to measure simultaneously the dynamic response of the rotor shaft: IAS from the encoder, bearing housing acceleration from the wired accelerometers and angular acceleration from the wireless sensor. These responses were then compared in both the time and frequency domains for detecting and diagnosing different levels of shaft unbalance. Results show the effectiveness of the wireless accelerometer in detecting the faults.

9.1 Introduction

The greatest challenge in condition monitoring is the detection and diagnosis of a fault before it becomes critical. The nature of rotating machinery means any fault in a rotor such as unbalance, misalignment, cracks, etc. will generate unwanted vibration. Hence, vibration measurements can be used to identify those defects qualitatively. Many researchers have studied such faults using only vibration measurements (Adiletta, Guido, & Rossi, 1997; Guido & Adiletta, 1999; Hubinger, Gattringer, Bremer, & Mayrhofer, 2012; Jalan & Mohanty, 2009; Li, M. & He, 2009; Loparo, Adams, Wei, Abdel-Magied, & Afshari, 2000; Sudhakar & Sekhar, 2011; Xu & Marangoni, 1994 a, 1994 b).

Model based methods are usually used to identify faults in rotor systems. Using advanced signal processing techniques such as wavelet transforms and Hilbert transforms, faults can be identified at an early stage of occurrence and also can be distinguished from one another. Model based methods are used to identify likely location and magnitude of the fault. Many researchers have successfully identified rotor faults using model based methods. Platz and Markert (Platz & Markert, 2001) identified rotor faults using model based methods that included virtual loads generated in the system due to the faults. Prabhakar and colleagues (Prabhakar, et al., 2001) used this approach for the identification of unbalance and cracks acting simultaneously in a rotor bearing system. Korkua and colleagues (Korkua, et al., 2010) identified unbalance using vibration signals from an induction motor and verified the results experimentally by introducing different levels of fault severity into a test rig. Bachschmid and Pennacchi (Bachschmid & Pennacchi, 2003) developed methods to test the accuracy of results obtained with model based techniques to identify faults in rotating machines. They also tested those methods using both machine response simulated by mathematical models and experimental data on a real machine. Sinha et al. (Sinha, Jyoti K, Lees, & Friswell, 2004) proposed a method that can estimate unbalance and misalignment of a flexible rotating machine from a single run-down. They also demonstrated their method robustness using experimental data.

Based on different symptoms, diagnosis of faults can be accomplished by applying classical or inference methods (Isermann, 2005). Lees, et al. (Lees, A., et al., 2009) have given a detailed review on the use of model based identification of rotating machines. They described different models for identifying rotor faults and their applications. Recently, Jalan and Mohanty (Jalan & Mohanty, 2009) identified unbalance and misalignment experimentally in a rotor bearing system using a model based method.

In the present work, theoretical and experimental fault models have been used to identify rotor unbalance. The parameters for the misalignment model given in Chapter 6 have been used. Both methods simulate identification of unbalance fault in the rotor system shown in

Figure 8.1. The unbalance fault was experimentally identified using the wireless sensor and the results compared with those obtained from the wired sensors.

9.2 Basic Theory and Definitions

9.2.1 Unbalance

Unbalance happens in a rotating machine due to uneven distribution of a rotor's, i.e., mass centreline and the geometric centre do not coincide on each other. Unbalance rotors generate vibration to be transmitted to the bearings and other parts of the machine during operation.

Uneven mass distribution can be due to material faults, design errors, manufacturing and assembly errors, and especially faults occurring during operation of the machine (Saleem, Diwakar, & Satyanarayana, 2012). In order to get better performance, more cost-effective operation and ultimately fatigue failure can be avoided by reducing unbalance vibrations to acceptable grade (Iso1940-1, 2003).

The unbalance amount of mass (m) distanced (r) from the centreline of rotation (see Figure 9.1) is expressed as:

$$U = m \times r \tag{9.1}$$

Where, *m*: unbalance mass in kg

r: distance from unbalance mass to rotor centreline in metres

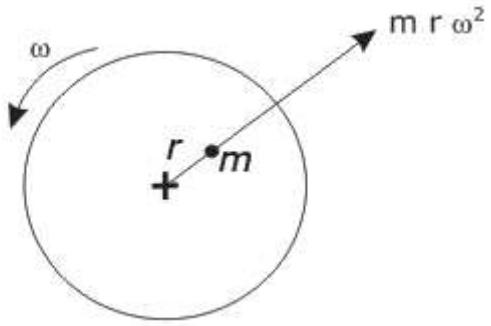

Figure 9.1 Unbalance Force (Centrifugal force).

The centrifugal force cause the vibration is expressed as:

$$F = m \times r \times \omega^2 \tag{9.2}$$

Where, *F*: force (N)

m: mass (kg)

r: radius (meter)

ω: speed (rad/sec)

The centrifugal force changes its direction as the rotor rotates. This force acts repeatedly on the bearing and causes vibration of the whole machine. Centrifugal force increases proportionally to the square of the increase in speed. If the speed doubles, the centrifugal force is quadrupled.

The unbalance quality grade (G) represents the value of the vibration caused by the unbalance mass (Iso1940-1, 2003). In addition, the rotor unbalance value is applicable, as long as the rotor mass is a typical percentage of the rotor mass. Moreover, the rotor distance between the holding bearings can contribute to the rotor unbalance.

The permissible residual unbalance e_{per} can be calculated on the basis of a selected balance quality grade G (from Table C. 1) by the following equation:

$$e_{per} = \frac{G \times 1000}{\Omega(rad/s)} \tag{9.3}$$

Where,

e_{per}: the permissible residual unbalance, expressed in gram millimetres (g.mm/kg);

G: the selected balance quality grade, expressed in millimetres per second (mm/s);

Ω: the angular velocity in radians per seconds (rad/s);

In addition, permissible residual unbalance U_{per} for a given speed and balance quality grade G can be computed based on Figure C. 1 by multiplying e_{per} by the rotor mass.

9.2.2 Calculations of permissible residual unbalance

Using equation 9.3 permissible residual unbalance for rotor mass 7.46kg at maximum speed of 1420 RPM with unbalance quality grade of G6.3 as:

$$e_{per} = \frac{6.3 \times 1000}{148.7} = 42.4 \ g.mm/kg$$

The eccentricity e can be expressed as 42.2 μm

The permissible residual unbalance

$$\mathrm{U_{per}} = 42.4\ \mathrm{g.mm/kg} \times 7.46\ \mathrm{kg} = 316.1\ \mathrm{g.mm}\ (0.3161\ \mathrm{kg.mm})$$

Using equation 9.2, the centrifugal force results from residual unbalance at maximum speed (148.7 rad/s):

$$\mathrm{F_{per}} = 0.3161\ \mathrm{kg.mm} \times (148.7)^2 = 7.0\ \mathrm{N}$$

The unbalance caused by first mass 400g at radius of 18 mm can be calculated using equation 9.1 as:

$$\mathrm{U_{0.4}} = 0.4\ \mathrm{kg} \times 18\ \mathrm{mm} = 7.2\ \mathrm{kg.mm}\ (7.2 \times 10^{-3}\ \mathrm{kg.m})$$

$$\mathrm{F_{0.4}} = 7.2 \times 10^{-3}\ \mathrm{kg.m} \times (148.7)^2 = 159.2\ \mathrm{N}$$

For the second mass 500g at radius of 25mm

$$\mathrm{U_{0.5}} = 0.5\ \mathrm{kg} \times 25\ \mathrm{mm} = 12.5\ \mathrm{kg.mm}\ (12.5 \times 10^{-3}\ \mathrm{kg.m})$$

$$F_{0.5} = 12.5 \times 10^{-3}\ \text{kg.m} \times (148.7)^2 = 276.4\ \text{N}$$

Comparing the residual unbalance of the rotor to the added masses, it is clear that the added masses exert higher centrifugal forces on the bearing than the residual one. These forces will contribute to the increase of the vibration of the rotor.

The unbalance quality grade G of both unbalance masses can be estimated using Figure C. 1 after computing residual specific unbalance e_{per} to each mass as:

$$e_{per} = \frac{400\text{g} \times 18\text{mm}}{7.46\text{kg}} = 965.15\ {}^{\text{g.mm}}/_{\text{kg}}$$

$$e_{per} = \frac{500\text{g} \times 25\text{mm}}{7.46\text{kg}} = 1675.6\ {}^{\text{g.mm}}/_{\text{kg}}$$

The unbalance quality grade for masses 400g and 500g are G100 and G250 respectively corresponding to Figure C. 1. According to Table C. 1 G100 is equivalent to complete reciprocating engines for cars, trucks and locomotives whereas G250 is equivalent to crankshaft drives, inherently unbalanced, rigidly mounted.

9.2.3 Types of unbalance

There are three types of unbalance(Maccamhaoil & Kjaer, 1989):

Static unbalance is the eccentricity of the centre of gravity of a rotor from the centreline of rotation (see Figure 9.2 (a)).

Couple (Moment) unbalance is where the mass axis intersects the running axis. For example: a cylinder shown in Figure 9.2(b), it is possible to add two equal masses placed symmetrically about the centre of gravity (C_g) but positioned 180° from each other. The rotor is statically balanced but when the rotor turns, the two masses shift in the inertia and hence no longer aligned with the centreline of rotation.

Dynamic unbalance illustrated in Figure 9.2(c) is usually a combination of static and couple unbalance and is the most common type of unbalance found in rotors.

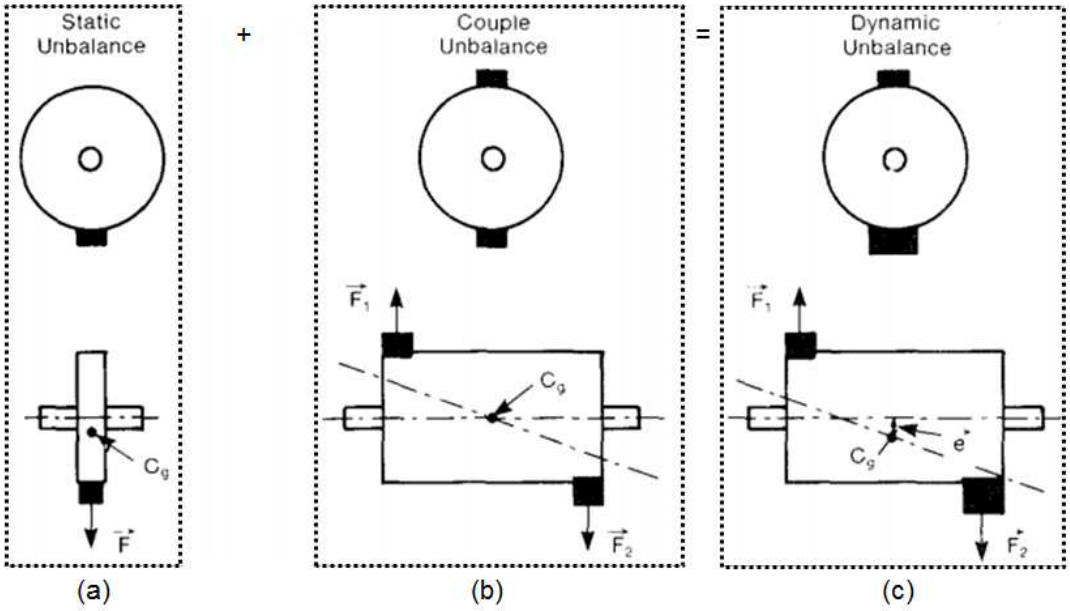

Figure 9.2 Unbalance Types (Maccamhaoil & Kjaer, 1989).

9.2.4 Unbalance Detection

Vibrations due to irregular mass distribution occur due to centrifugal force exerted by the heavier side of the rotor during the rotating machine's speed of operation. As the speed increases the amplitude at 1X is also increases for the same unbalance mass. This increase in amplitude value is due to the increase of centrifugal force (Saleem, et al., 2012). Therefore vibration signature and orbits plots have been used as methods of machinery unbalance detection and diagnosis. In addition, recently (Saleem, et al., 2012) used deflected shapes of rotor in detecting rotor unbalance. In this study, two unbalance masses are mounted to the second shaft to examine the capability of the wireless sensor in detecting force changes acting on the second rotor.

9.3 Rotor Unbalance Masses Model

A rotor unbalance fault has been simulated using the same mathematical model presented in Chapter 6 (Table 6.2). The same simulation parameters were used and a 0.02 mm and 0.01mm residual misalignment and unbalance assumed respectively. The oscillating forces generated by unbalance mass and eccentricity due to misalignment were added to equation (6.2) of second shaft as given in equation (9.4). The mass of the rotor that the unbalance mass was attached was 7.46 kg. To understand the dynamic response of rotor to unbalance, different unbalance masses (0.2, 0.4, 0.6, 0.8 kg) were attached to the second shaft at constant radial location of (e_u) 18 mm from its centre. The residual degree of misalignment was assumed as 0.02 mm. The torsional load applied was set to 50% of rated load. The simulation analysis was carried out at angular speeds 300, 500, 700, 900, 1100, 1300, 1500

RPM simultaneously at each mass. The following equations (9.4) represents the effect of unbalance masses on the the second shaft of the model.

$$\begin{aligned} dmtorque2 &= 9.81 e_{12} m_{e2} \cos(\theta_1 - \theta_0) + 9.81 e_u m_u \cos(\theta_1 - \theta_0) \\ dmforcex2 &= e_{12} \dot{\theta}_2^{\,2} m_{e2} \cos(\theta_2 - \theta_0) + e_u \dot{\theta}_2^{\,2} m_u \cos(\theta_2 - \theta_0) \\ dmforcey2 &= e_{12} \dot{\theta}_2^{\,2} m_{e2} \sin(\theta_2 - \theta_0) + e_u \dot{\theta}_2^{\,2} m_u \sin(\theta_2 - \theta_0) \end{aligned} \quad \textbf{9.4}$$

Where, $\mathrm{m_{e2}} = \mathrm{m_2}$, $e_{12} = eccentricity\ due\ to\ misalignment$

$m_u = unbalance\ mass$, $e_u = eccentricity\ due\ to\ unbalance\ mass$

To examine the effect of different masses on the spectral amplitude a simulation study was performed for different motor speeds (300 to 1500 RPM) for each mass. Figure 9.3, Figure 9.4 and Figure 9.5 present the predicted amplitude changes for the first 4 harmonics.

By comparing relative amplitudes of tangential accelerations of combined ($\boldsymbol{a_t}$), lateral ($\boldsymbol{a_{txy}}$) and rotational ($\boldsymbol{a_{tw}}$) of the second rotor it can be observed that:

The amplitude of the 1X peak for combined and rotational accelerations remains almost constant over the range of speeds tested but discriminated between unbalance cases. It means that amplitude at 1X for either of these plots is predicted to be suitable for unbalance detection. The rotational ($\mathbf{a_{tw}}$) acceleration manifest the combined ($\mathbf{a_t}$) because the lateral acceleration ($\mathbf{a_{txy}}$) were very small ($\approx 10^{-5}$ ms^{-2}). This prediction increases the potential of wireless sensor unbalance detection.

On the other hand, the 2X peak all accelerations increased in amplitude with mass increase but the combined acceleration has the highest amplitude at different unbalance masses. Compared by 1X, it is concluded that the 2X peak is unlikely to be a good indicator of small unbalance mass.

The predicted amplitudes of the spectral peaks at 3X and 4X rotor speed are consistently very small ($<\approx 10^{-5}$ ms^{-2}) and so would be extremely difficult to measure.

The results show that the small change of the mass of 0.2 kg can be predicted and hence the unbalance cases can be discriminated at 1X running speed. Moreover, the spectral peaks at 2X, 3X and 4X are very small compared to 1X and hence cannot be used to detect unbalance.

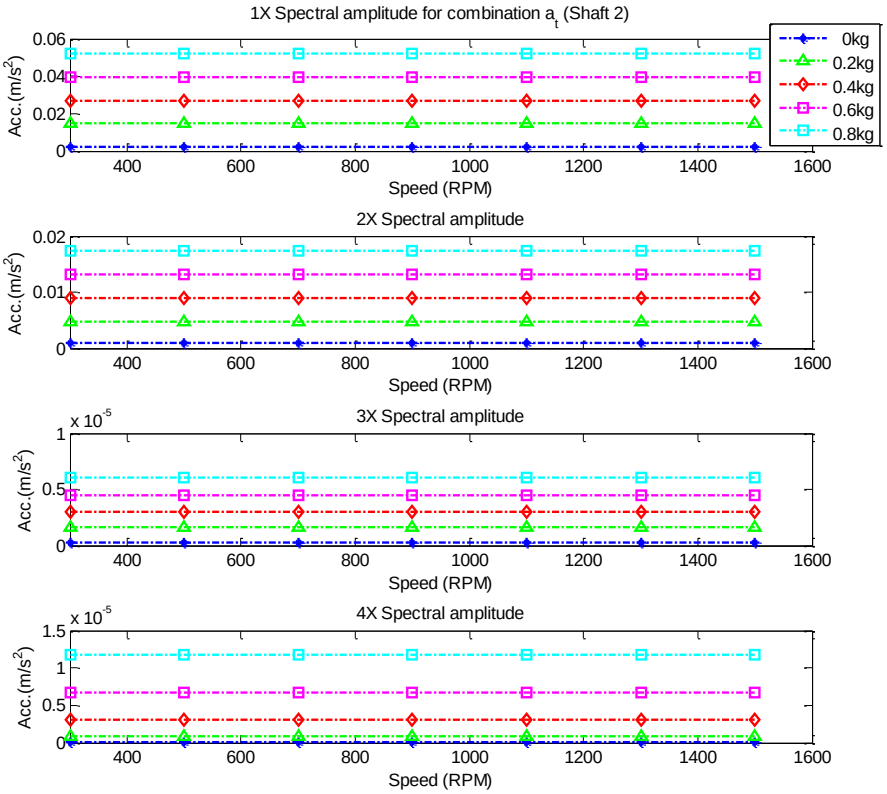

Figure 9.3 Predicted spectral amplitudes of combination tangential accelerations from wireless accelerometer.

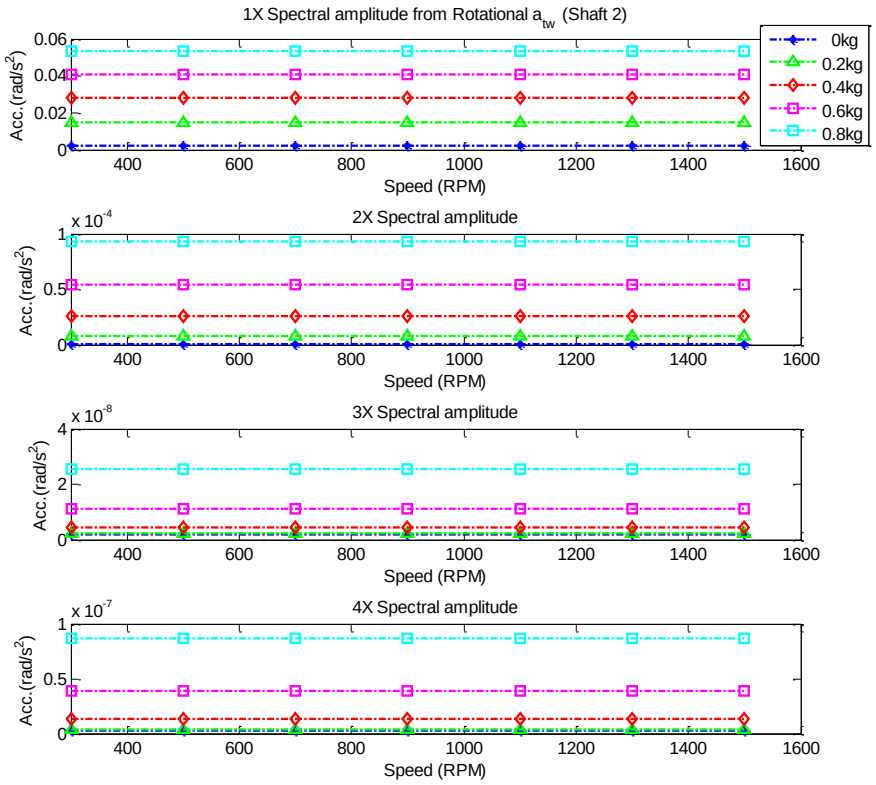

Figure 9.4 Predicted spectral amplitudes of rotational accelerations from wireless accelerometer.

9.4 Rotor Unbalance Simulation

Using the simulation model described in Section 9.3, the unbalance masses chosen in the experimental study were examined. To introduce unbalance into the system a mass of 400 g was attached to the second rotor at a radial location of 18 mm from its centre, see Figure 9.14. A second mass of 100 g was attached to the holder as shown in Figure 9.14 at a radial location of 25 mm from the centre. The total mass of the second unbalance was 500 g. The residual degree of misalignment was assumed as 0.02 mm. The torsional load applied was set to 50%. The simulation analysis was carried out at angular speed 1500 RPM.

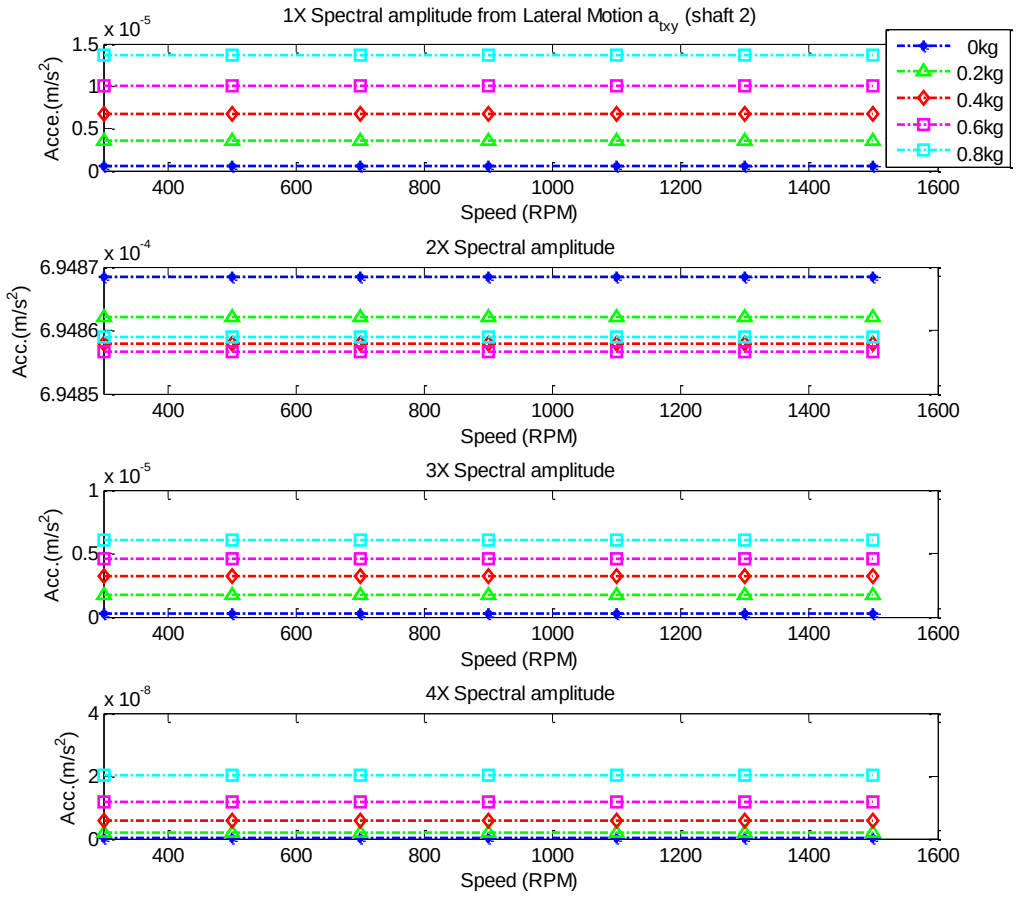

Figure 9.5 Predicted spectra of lateral accelerations from wireless accelerometer.

9.5 Simulation Results and Discussion

9.5.1 Characteristics of Vibrations due to Unbalance

Figure 9.6 shows a typical result from a numerical simulation study when the motor operated at a speed of 1500 RPM. It can be seen from first column, baseline condition (no unbalance mass applied), waveforms of lateral accelerations: $\boldsymbol{a_x}$, and $\boldsymbol{a_y}$ are close to sinusoidal waves whereas the waveform of rotational acceleration $\boldsymbol{a_w}$ exhibits a faster rate of noisy sinusoidal fluctuation. The values presented in Figure 9.6 represent the peak value.

The two unbalance masses were attached to the rotor, first one and then the second. The same general waveforms were obtained from the model, but the amplitudes of the signals increased relative to those obtained with no unbalance mass (see Figure 9.6). The frequency response of the waveforms also showed some changes; the lateral accelerations $\boldsymbol{a_x}$, and $\boldsymbol{a_y}$ show a substantial increase in amplitude though the distinctive peak at 1X rotor speed and the subsidiary peak at 2X remain. The magnitude of the rotational acceleration $\boldsymbol{a_w}$ remains much the same, the peaks at 1X and 2X are still present but the larger the unbalance mass the noisier the signal, especially at higher rotor speeds. These indicate that both rotational and lateral acceleration are sensitive to the problem of unbalance. In general, these spectral features show that the model is adequate for exploring shaft unbalance using the output of the wireless accelerometer.

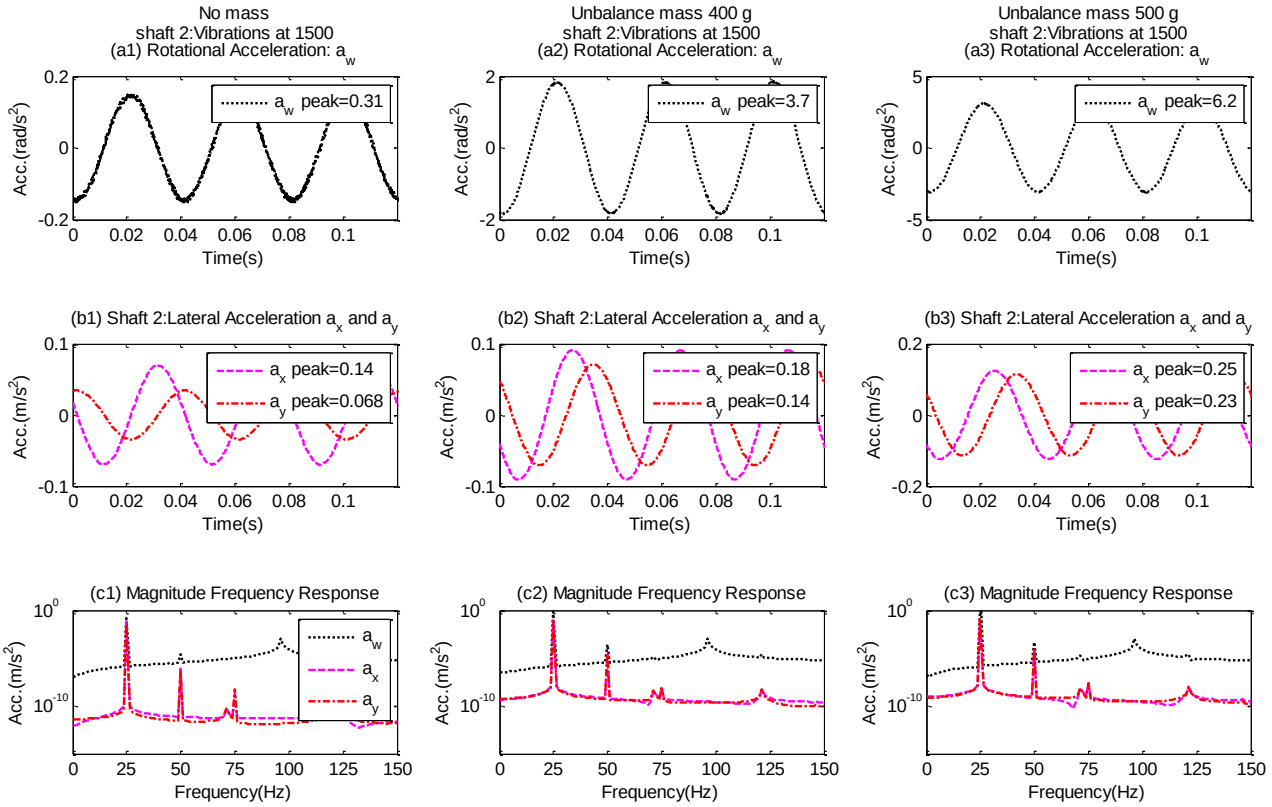

Figure 9.6 Predicted waveforms and spectra of lateral and rotational accelerations from wireless accelerometer.

Further analysis of the predicted output of the wireless sensor, see Figure 9.7 (a) shows the tangential components: $\boldsymbol{a_{tx}}$, $\boldsymbol{a_{ty}}$ and $\boldsymbol{a_{tw}}$ extracted from accelerations: $\boldsymbol{a_x}$, $\boldsymbol{a_y}$ and $\boldsymbol{a_w}$. It can be seen that $\boldsymbol{a_{tx}}$ (peak 0.070 m/s^2) and $\boldsymbol{a_{ty}}$ (peak 0.034 m/s^2) oscillate twice as fast as the original signal (see Figure 9.6 (b1, b2 and b3)) but they have shifted phase. This double oscillation in the tangential direction was caused by fast change of the angular displacement (θ_2). Combining these two components together produces a sinusoidal waveform. On the other hand, $\boldsymbol{a_{tw}}$ keeps the same phase ($\boldsymbol{a_w}$) but with a difference in magnitude (peak $\boldsymbol{a_w}$= 0.308 and

$\boldsymbol{a_{tw}}$= 0.005 rad/s^2) due to the constant of sensor position on shaft surface. By combining the three components, the total acceleration, $\boldsymbol{a_t}$, at sensor position exhibits mainly the feature of $\boldsymbol{a_{tw}}$ but with a shifted sinusoidal due to the combination of $\boldsymbol{a_{tx}}$ and $\boldsymbol{a_{ty}}$.

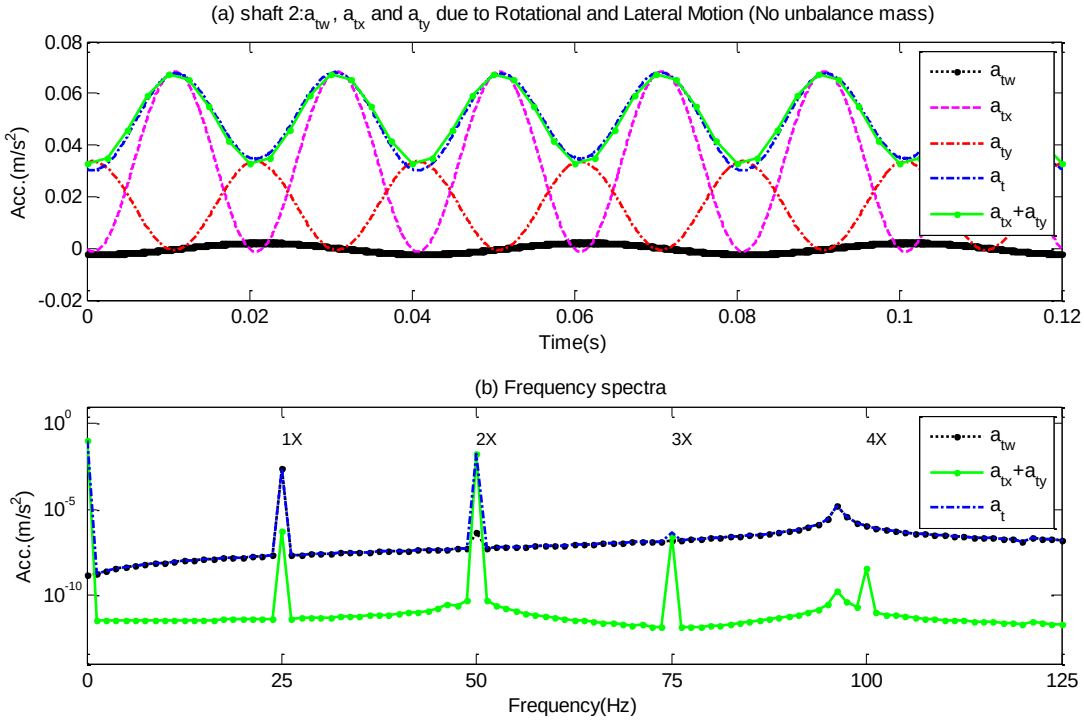

Figure 9.7 Predicted waveforms and spectra of rotational, lateral and tangential accelerations from wireless accelerometer at 1500 RPM with no unbalance mass.

In the frequency domain, the spectrum resulting from the combination of $\boldsymbol{a_{tx}}$ and $\boldsymbol{a_{ty}}$ is similar to that of $\boldsymbol{a_{tw}}$ but has a lower amplitude, see Figure 9.7 (b). Generally the spectra of the combined accelerations $\boldsymbol{a_{txy}}$ and $\boldsymbol{a_{tw}}$ exhibit considerably different amplitudes, however, at 2X rotor speed the amplitude difference is marginal, showing that this component is mainly due to rotational oscillation.

For the unbalance mass of 400 g (case 1) the predicted output of the wireless accelerometer is shown in Figure 9.8 (a). It can be seen that $\boldsymbol{a_{tx}}$ and $\boldsymbol{a_{ty}}$ have much the same characteristics as when no unbalance mass was present except the amplitude is increased noticeably (peak 0.091 and 0.071 m/s2 respectively). On the other hand, $\boldsymbol{a_{tw}}$ shows a very large increase in amplitude (peak 0.056 rad/s^2) but keeps the same phase as $\boldsymbol{a_w}$. The time domain signal of the total acceleration, $\boldsymbol{a_t}$, at the sensor position exhibits the main features of $\boldsymbol{a_{tw}}$ but with the combined sinusoid of $\boldsymbol{a_{tx}}$ and $\boldsymbol{a_{ty}}$ superimposed.

In the frequency domain, the spectrum has a large peak at 1X rotor speed contributed by $\boldsymbol{a_{tw}}$ and a second large and distinct peak at 2X rotor speed contributed by the combination of $\boldsymbol{a_{tx}}$ and $\boldsymbol{a_{ty}}$. However, the peak at 1X has the lower amplitude, see Figure 9.8 (b). The spectrum

for the full combination of $\boldsymbol{a_{txy}}$ and $\boldsymbol{a_{tw}}$ exhibits a noticeable difference at 1X running speed compared with baseline, Figure 9.7 (b).

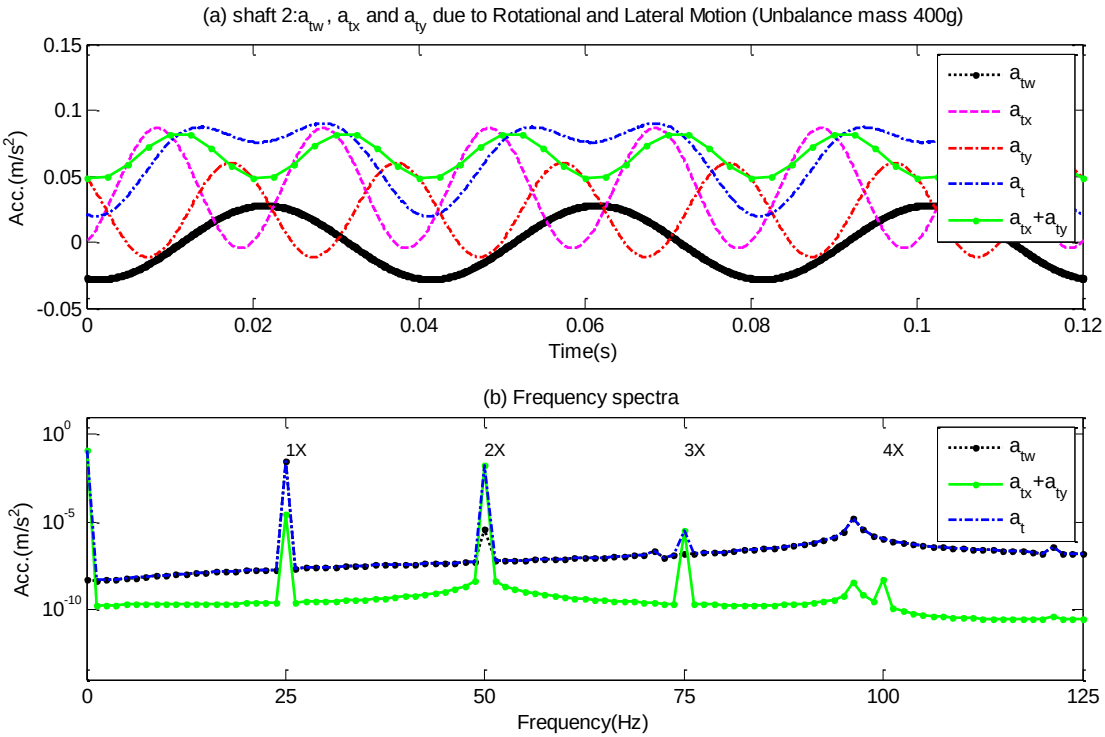

Figure 9.8 Predicted waveforms and spectra of rotational, lateral and tangential accelerations from wireless accelerometer at 1500 RPM with unbalance mass 400 g.

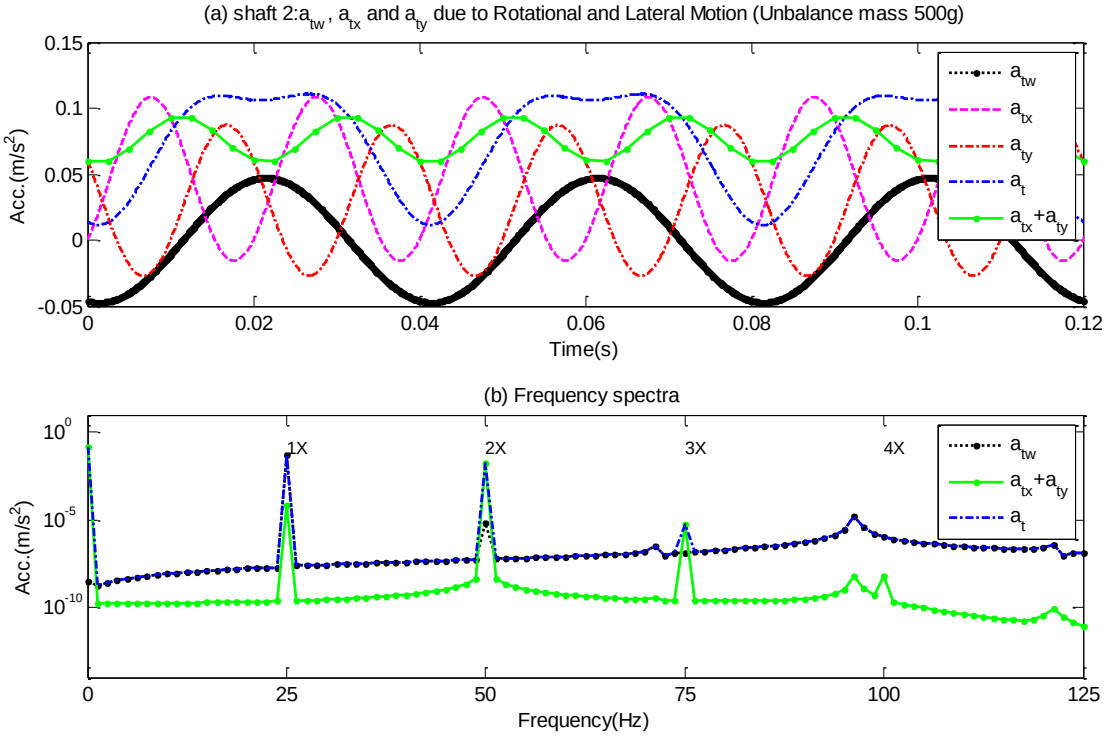

Figure 9.9 Predicted waveforms and spectra of rotational, lateral and tangential accelerations from wireless accelerometer at 1500 RPM with unbalance mass 500 g.

For unbalances mass 500 g (case 2) the outputs of the sensor, see Figure 9.9 (a), shows marked similarities to those obtained for case 1 but with a significant increase in signal amplitude (peak $\boldsymbol{a_{tw}}$= 0.0948 rad/s^2, $\boldsymbol{a_{tx}}$= 0.124 m/s^2 and $\boldsymbol{a_{ty}}$= 0.114 m/s^2). Again, $\boldsymbol{a_{tw}}$ keeps the same phase as $\boldsymbol{a_w}$. As with case 1 the time domain signal of the total acceleration, $\boldsymbol{a_t}$, at the sensor position exhibits the main features of $\boldsymbol{a_{tw}}$ but with the combined sinusoid of $\boldsymbol{a_{tx}}$ and $\boldsymbol{a_{ty}}$.

In the frequency domain, as for case 1, the combined spectrum, $\boldsymbol{a_t}$, has a large peak at 1X rotor speed contributed by $\boldsymbol{a_{tw}}$ and a second large and distinct peak at 2X rotor speed contributed by the combination of $\boldsymbol{a_{tx}}$ and $\boldsymbol{a_{ty}}$. The distinctive spectral peak at 1X, due to $\boldsymbol{a_{tw}}$ is the main feature commonly used to diagnose unbalance (Hubinger, et al., 2012; Loparo, et al., 2000; Sudhakar & Sekhar, 2011; Xu & Marangoni, 1994 a).

9.5.2 Characteristics of Spectral Amplitude

To examine further the changes of spectral amplitude a simulation study was performed for different motor speeds (300 to 1500 RPM) and the two unbalance masses. Figure 9.10, Figure 9.11 and Figure 9.12 present the predicted spectral amplitude changes for the first 4 harmonics of combination ($\boldsymbol{a_t}$), rotational ($\boldsymbol{a_{tw}}$) and lateral ($\boldsymbol{a_{txy}}$) tangential accelerations respectively.

By comparing relative amplitudes of combined ($\boldsymbol{a_t}$), lateral ($\boldsymbol{a_{txy}}$) and rotational ($\boldsymbol{a_{tw}}$) accelerations it can be observed that:

The amplitude of the 1X peak for combined and rotational accelerations remains almost constant over the range of speeds tested but discriminated between grades of unbalance. It means that amplitude at 1X for either of these plots is predicted to be suitable for unbalance detection. For lateral acceleration the plots separated the different degrees of unbalance but the difference was small ($<10^{-2}$) for lower speeds.

On the other hand, the 2X peak for the combined and lateral accelerations increased in amplitude with rotor speed but did not separate the different degrees of unbalance. The 2X peak for rotational acceleration increased with speed but separated the different degrees of unbalance only at the lowest speed (below 700 RPM). It is concluded that the 2X peak is unlikely to be a good indicator of unbalance.

The predicted amplitudes of the spectral peaks at 3X and 4X rotor speed are consistently very small ($<\approx 10^{-5}$ ms^{-2}) and so would be extremely difficult to measure. For the combined and lateral accelerations the amplitude of the 3X peak remained almost constant over the range of speeds tested but discriminated between degrees of unbalance cases. However, at 4X rotor speed no discrimination for combination but there is some differentiation for lateral

acceleration. However, the rotational acceleration shows very small (≈ 10^{-6} ms^{-2}) magnitude and can't differentiate between different cases. The changes in the 3X peaks for combination and rotational acceleration could be a secondary indicator for unbalance.

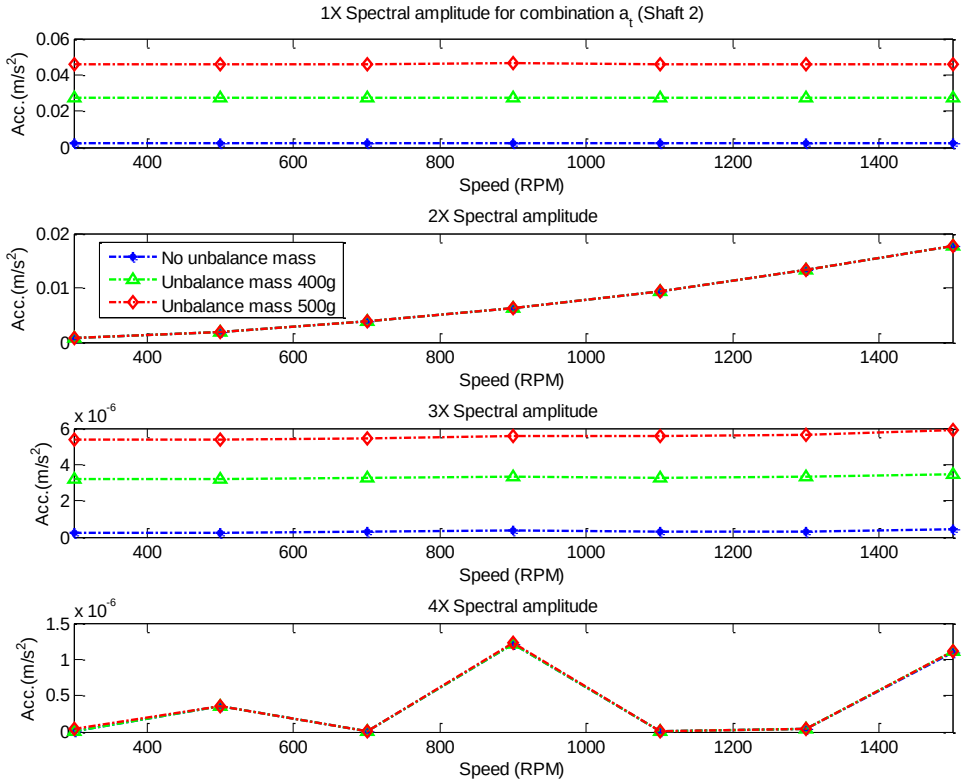

Figure 9.10 Predicted amplitudes of 1X, 2X, 3X and 4X spectral peaks as functions of rotor speed and degree of unbalance (Combined acceleration, at,).

It is concluded that the amplitude variation of both combined and rotational accelerations at 1X could be a good indicator of mass unbalance. The variation in amplitude of the 1X peak for combined, rotational and lateral accelerations can be used for unbalance detection which confirms what researchers has been found (Adiletta, et al., 1997; Hubinger, et al., 2012; Jalan & Mohanty, 2009; Li, M. & He, 2009; Suphattana & Surawatpunya, 2010; Xu & Marangoni, 1994 a).

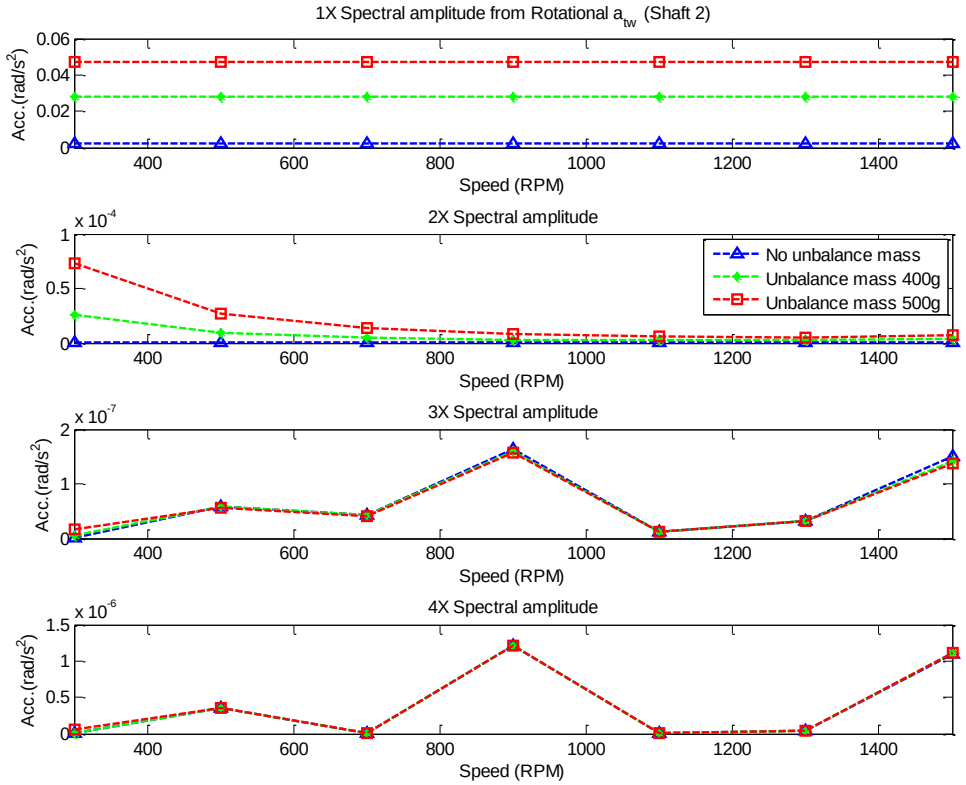

Figure 9.11 Predicted amplitudes of 1X, 2X, 3X and 4X spectral peaks as functions of rotor speed and degree of unbalance (Rotational acceleration aw)

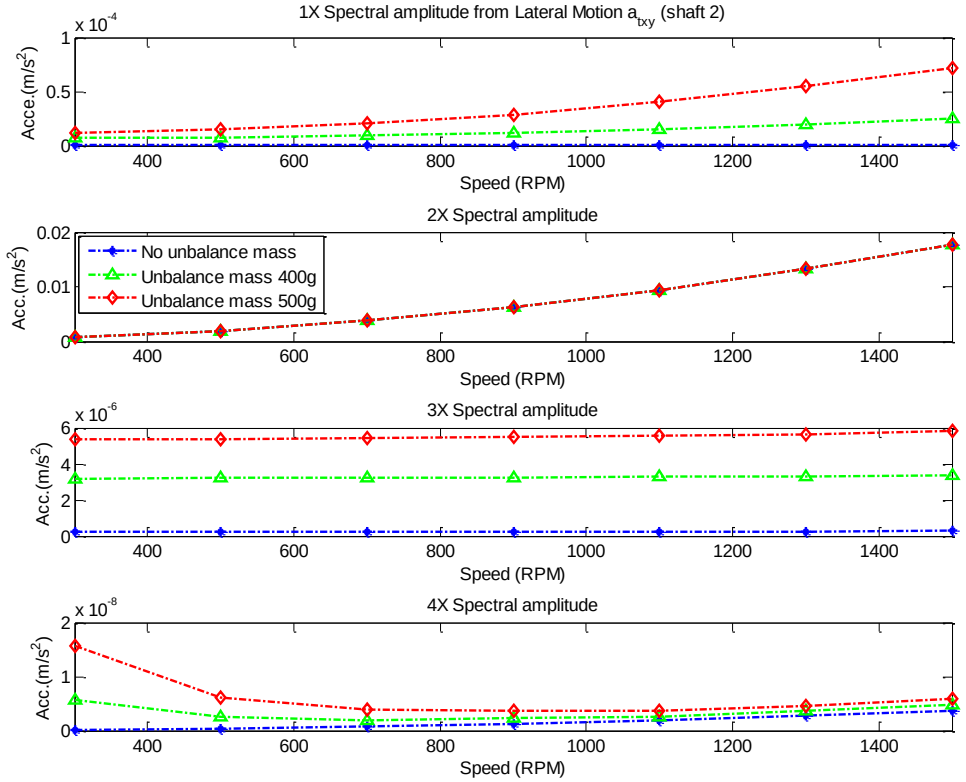

Figure 9.12 Predicted amplitudes of 1X, 2X, 3X and 4X spectral peaks as functions of rotor speed and degree of unbalance (Lateral acceleration atxy)

9.6 Experiment Setup

To validate the predictions of the theoretical model, a practical experiment was carried out. The test rig described in Chapter 5 was used, see Figure 5.1. The wireless accelerometer was mounted on the second shaft. The wired accelerometers were mounted on the housing bearing on which the shaft rested. The unbalance mass (mass holder) was then mounted on the second shaft on the other side of the bearing, as shown in Figure 9.13. An encoder used to determine IAS was mounted to the end of motor shaft. The residual misalignment between shaft 2 and shaft 3 was 0.20 mm vertically and 0.24 mm horizontally (measured statically by dial indicator).

Figure 9.14 show the mass holder and the mass mounted on the second shaft. The holder mass 400 g was considered as unbalance case 1. The mass 100 g was added by mounting it on the holder to become 500 g and was considered as unbalance case 2. The distances from the longitudinal centre axis of the rotor to the centres of the masses are shown in Figure 9.14.

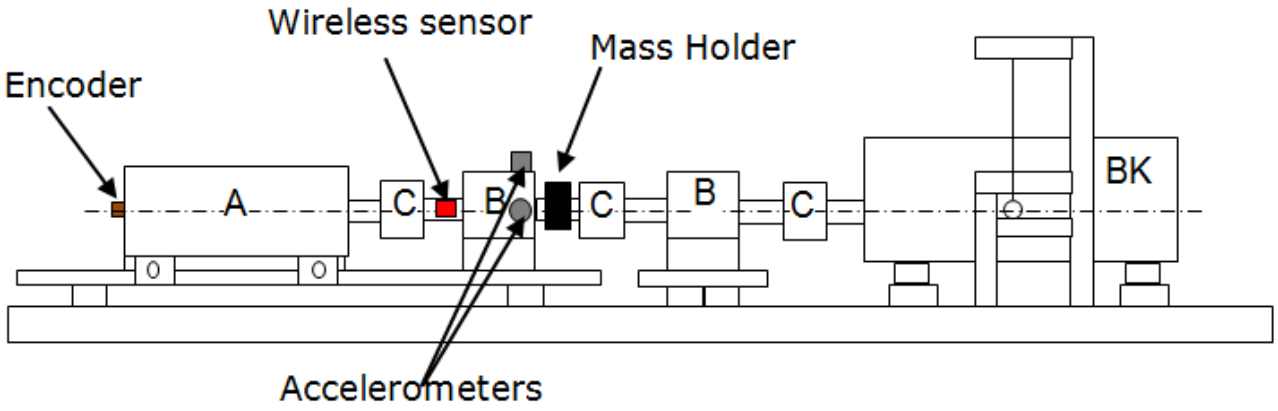

Figure 9.13 Test rig schematic and wireless sensor placement.

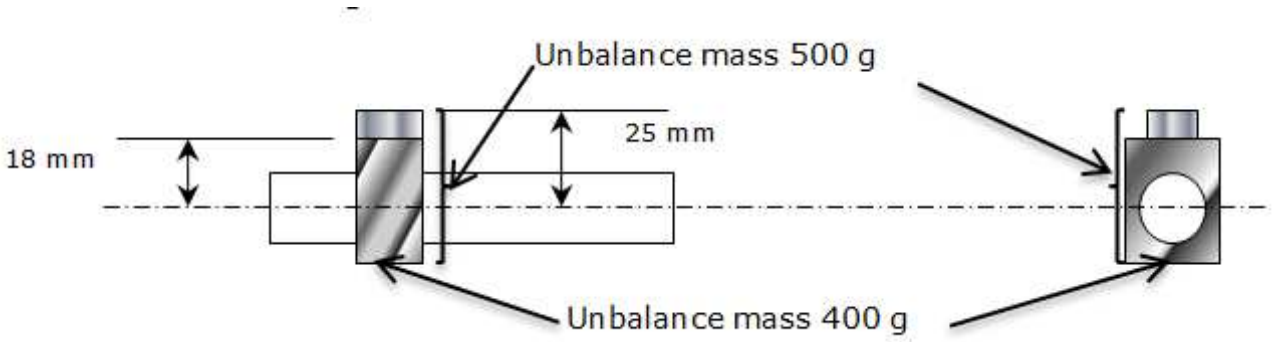

Figure 9.14 Schematic diagram of mass holder and mass position.

9.7 Test Procedure

1. The torsional load was set to 50% of rated load (4kw).
2. The test rig was run for 10, 20, 30, 40, 50, 60, 70, and 80% of rated speed (1420 RPM). The data from the various sensors was collected simultaneously.
3. The holder (400 g) was mounted on the second shaft as shown in Figure 9.13, and then step 2 was repeated.
4. A mass of 100 g was added to the holder (total mass 500 g) and firmly attached to the holder as shown in Figure 9.14, and then step 2 was repeated.
5. The collected data from step 2, 3 and 4 was subjected to analysis using MATLAB code to study the effect of unbalance masses on the rotor. A wireless sensor was used together with wired accelerometers and encoder which were used to benchmark the performance of the wireless sensor.

9.8 Experiment Results and Discussion

9.8.1 Waveform Variations

Figure 9.15 shows typical waveforms from a wireless accelerometer for balanced shaft and shaft with two unbalance masses, at speeds 276 and 1176 RPM. The top row of Figure 9.15, for the baseline case shows that the outputs of the wireless sensor are periodic oscillations at the shaft fundamental. The addition of an unbalance mass (holder) causes a small increase in waveform amplitude (Peak change from 28.241 to 28.270 m/s^2 at low speed, and 27.742 to 27.889 m/s^2) with a slight change in waveform shape at both lower and higher speeds. These are good indications for detecting and diagnosing the occurrence of unbalance. This behaviour agrees with the predicted results from the model. The addition of an unbalance mass (100 g) causes a small increase in waveform amplitude (Peak change from 28.270 to 29.062 m/s^2 at low speed, and 27.889 to 28.328 m/s^2) with a slight change in waveform shape at both lower and higher speeds.

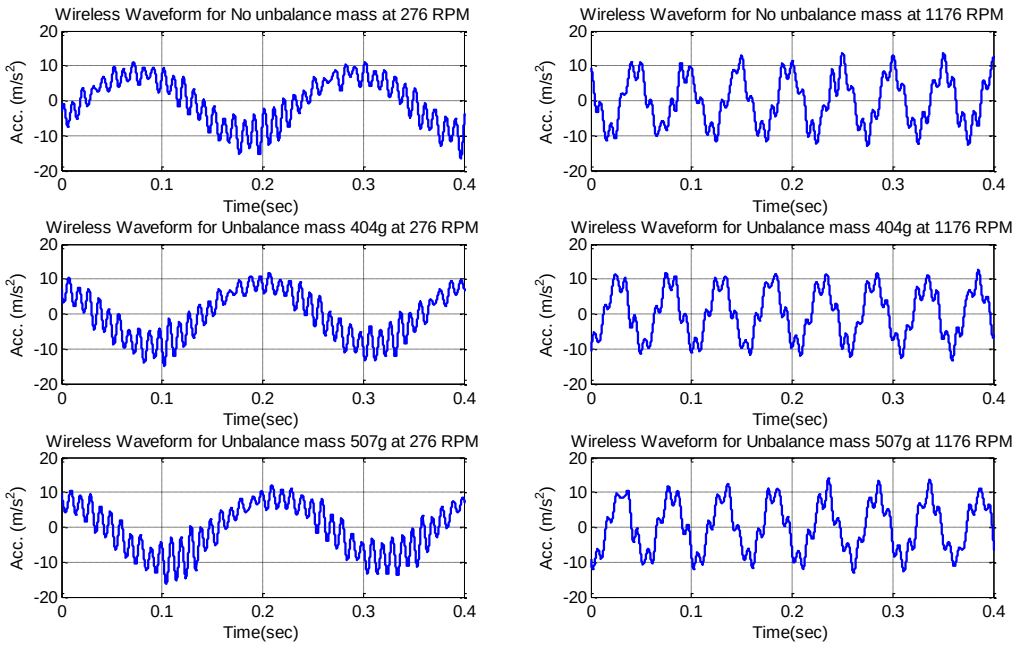

Figure 9.15 Measured wireless accelerometer waveforms at low and high speeds for baseline and two unbalance masses (400 g and 500 g)

Figure 9.16 shows typical signals from the wired accelerometers for both vertical and horizontal directions. The waveforms of vertical accelerometer are higher than that of the horizontal due to the residual misalignment in this direction given earlier. The vertical waveform amplitudes exhibit significant changes with different degrees of unbalance at low speed (peak 1.357, 1.612 and 1.628 m/s^2) whereas there are small decreases at high speed (peak 3.063, 2.871 and 2.432 m/s^2). On the other hand, the horizontal waveform amplitudes exhibit small fluctuation changes with different degrees of unbalance at low speed (peak 0.799, 0.765 and 0.805 m/s^2) whereas at high speed (peak 1.104, 1.013 and 1.01 m/s^2). It can be seen from the figure that the amplitudes of the vertical vibration waveform are increasing at low speed with different cases of unbalance whereas the horizontal fluctuating from high to low and then high. Therefore, the vertical accelerometer has the potential of detecting unbalance than the vertical.

IAS waveforms from the encoder presented in Figure 9.17 show periodic oscillation following the rotor speed. With unbalance the waveform showed a slight decrease and increase in amplitude at low speed (peak 0.834, 0.823 and 0.902 rad/s). However, an increase in waveform amplitudes was observed at high speed (peak 4.245, 4.141 and 4.317 rad/s). Fluctuations of speed were clearly exhibited by the waveforms' shape, mainly at high speed.

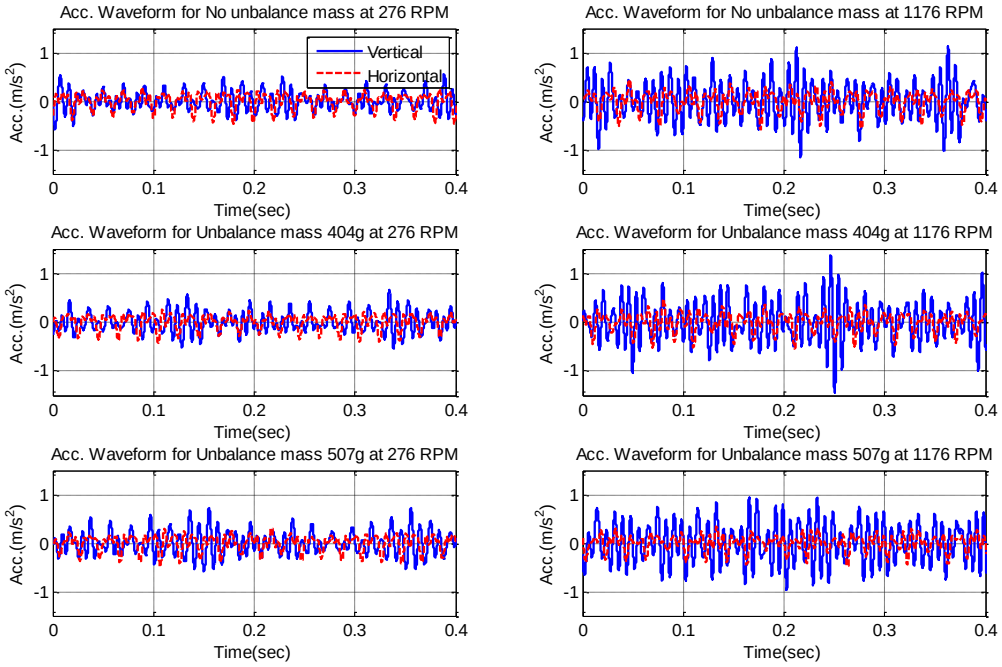

Figure 9.16 Measured wired accelerometer waveforms at low and high speeds for baseline and two unbalance masses (400 g and 500 g).

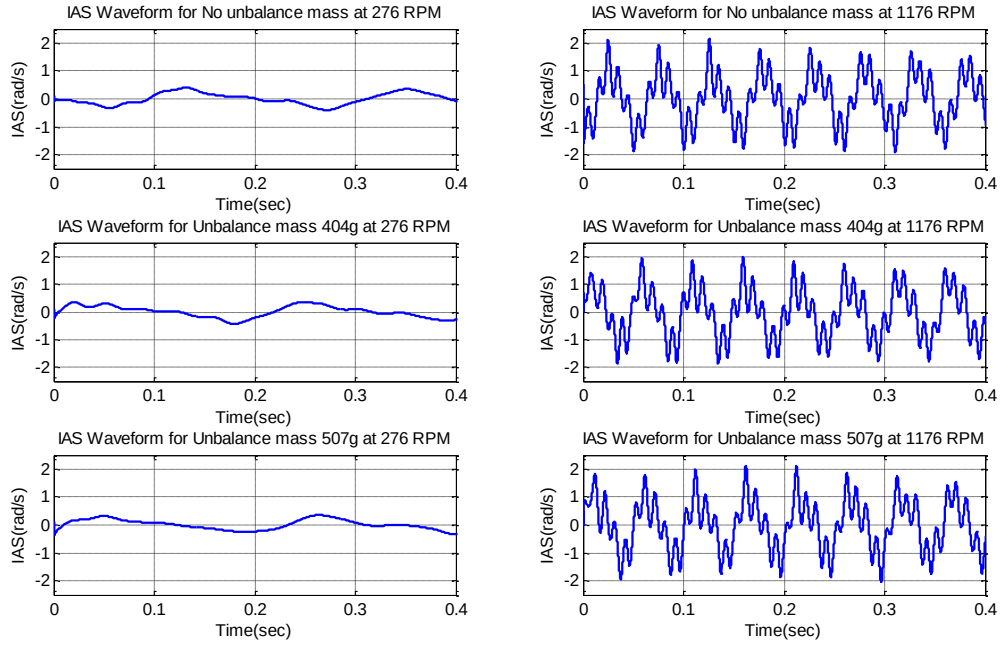

Figure 9.17 Measured IAS waveforms at low and high speeds for baseline and two unbalance masses (400 g and 500 g)

9.8.2 Variations in Spectral Peak Amplitudes

To obtain a better appreciation of the diagnosis of unbalance and comparison between sensors, the amplitude at spectral peaks at 1X and 2X runing speed were extracted from their spectra and presented with respect to shaft speed, see Figure 9.18 and Figure 9.20 respectively.

Comparing the trends between different sensors for different degrees of unbalance, it can be seen from Figure 9.18 that the wireless sensor can not only produce a clear difference between baseline and both cases of seeded unbalance, but also full separation between different cases of unbalance for all speeds. These results agree with the wireless sensor model predictions in the previous section and with results reported by other researchers (Jalan & Mohanty, 2009; Xu & Marangoni, 1994 a).

The 1X peak from the encoder shows that IAS is unable to detect mass unbalance because the position of the encoder is far from the unbalance rotor.

The 1X peak for the wired accelerometers shows good differentiation for the larger of the unbalanced masses at high speed. But there is very poor discrimination between baseline and the 400 g mass unbalance which strongly suggest this is not a good method for detecting incipient mass balance faults.

For the 2X peak component, see Figure 9.20, only the IAS signal from the encoder shows a clear difference between baseline and the seeded mass unbalances for shaft speeds above 400 RPM, but did not distinguish between the two seeded faults. This proves that mass unbalance cannot be clearly detected based on the amplitude of 2X peak for any of the sensors tested.

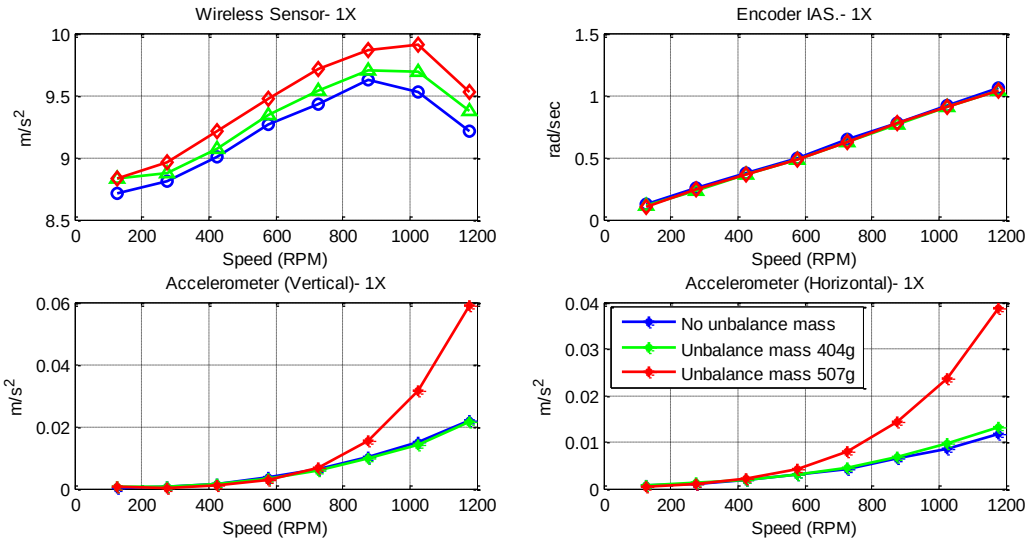

Figure 9.18 Amplitudes of the first harmonic, 1X shaft speed, for wireless sensor, wired accelerometers and encoder as a function of shaft speed and degree of mass unbalance.

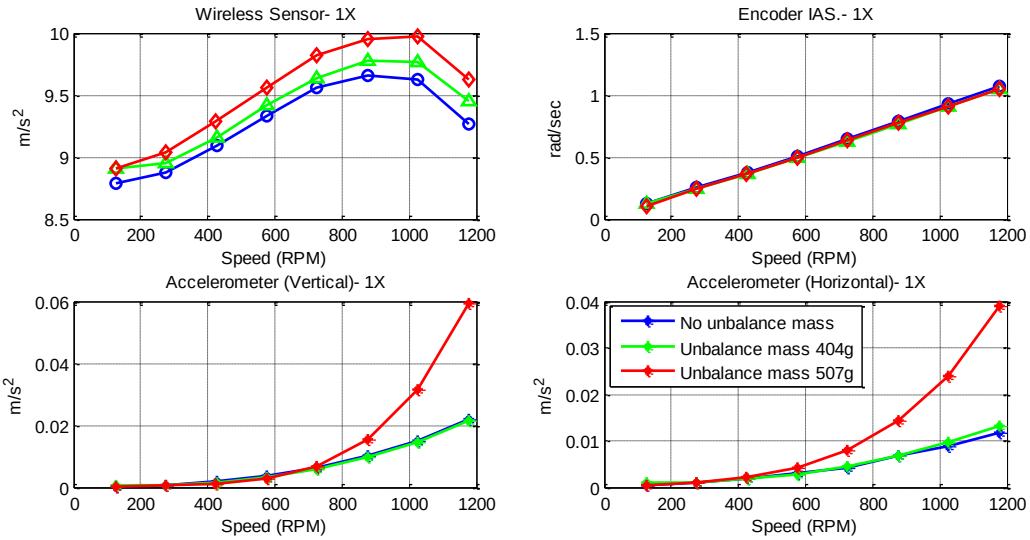

Figure 9.19 Amplitudes of the first harmonic, 1X shaft speed, for wireless sensor, wired accelerometers and encoder as a function of shaft speed and degree of mass unbalance after application of TSA processing.

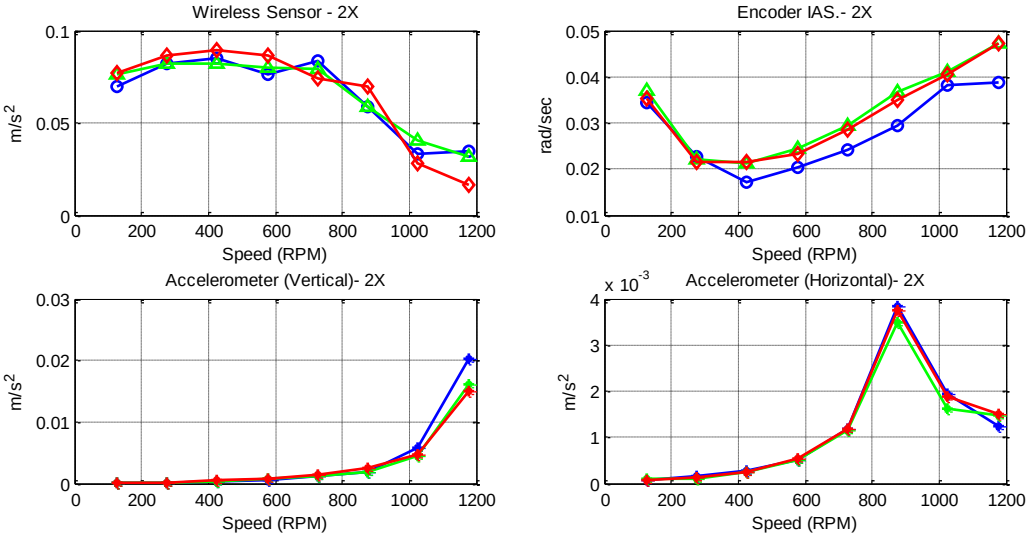

Figure 9.20 Amplitudes of the second harmonic, 2X shaft speed, for wireless sensor, wired accelerometers and encoder as a function of shaft speed and degree of mass unbalance.

Applying TSA to all the signals, for the 1st order peaks there is an improvement in discrimination for the wireless accelerometer, see Figure 9.19. For the other signals there is little or no significant change. For the 2nd order peaks, applying TSA does not result in a significant improvement in the usefulness of any of the signals, see Figure 9.21.

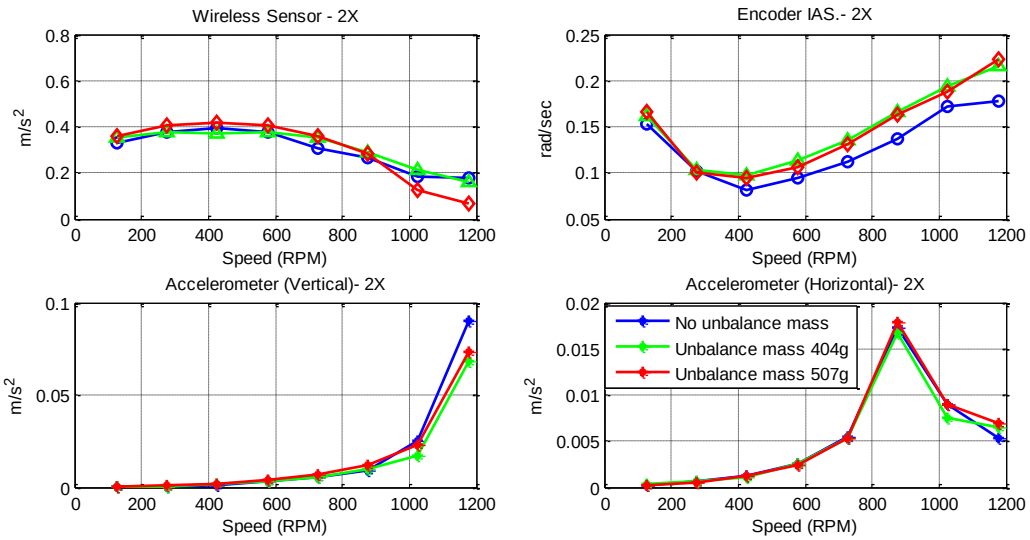

Figure 9.21 Amplitudes of the second harmonic, 2X shaft speed, for wireless sensor, wired accelerometers and encoder as a function of shaft speed and degree of mass unbalance after application of TSA processing.

9.9 Summary

A wireless accelerometer has been investigated as an effective means to monitor shaft unbalance. The model developed in Chapter 6 was used to simulate the dynamics of an unbalanced shaft system at different speeds. Through experiment and simulation, the validity of the model and measurement scheme has been successfully verified for a wide range of operating speeds.

Both measured and simulated spectra show that rotor shaft unbalance can be characterized primarily by the amplitude of the spectral peak at 1X shaft running speed, from which unbalance detection can be extracted. Because these components produce both rotational and lateral vibrations, the detection performance of the wireless accelerometer is much better than IAS and conventional wired vibration measurements.

The comparison of the waveforms from the different sensors has shown a small change in the amplitude of the signals for different degrees of seeded unbalance. Generally the amplitude of waveforms increases with speed, but its overall level did not show a consistent trend with the successive changes of unbalance level because of high frequency noise from other vibrations, see Figure 9.15, Figure 9.16 and Figure 9.17.

The spectral analysis shows that the amplitude of the spectral peak at 2X running speed failed to differentiate between different degrees of unbalance for both normal and order spectra for all sensors see Figure 9.20 and Figure 9.21.

However, the amplitude of the spectral peak at 1X running speed allows the grade of unbalance to be separated, but with varying degrees of success depending on the sensors used (see Figure 9.18 and Figure 9.19):

- The wireless sensor produces full separation of different grades of unbalance.
- Encoder (IAS) is not capable of separating the different grades of unbalance.
- Vertical acceleration from the wired accelerometer discriminated the unbalance condition from the baseline but only at a high grade of unbalance and speed.
- Horizontal acceleration shows clear unbalance separation but only at high speed.

CHAPTER TEN

Conclusions and Recommendations for Future Work

This chapter summarises the achievements of this research Thesis and explains how the aim and objectives stated in Chapter One were achieved. A summary of the author's contributions to knowledge and the novel aspects of the research are also included. Finally, recommendations for future work relating to the development and use of a wireless accelerometer are provided.

10.1 Review of Aim, Objectives and Achievements

This chapter describes the achievements and contributions to knowledge made by this research work. This thesis met its aim of developing and testing an accurate and sensitive MEMS wireless accelerometer suitable for application to a rotating shaft by demonstrating the use of a MEMS inertial sensor for modal analysis of rotating machinery. It also has addressed the development of MEMS based wireless accelerometer.

This research has focused on the investigation of rotor dynamics using a novel wireless sensor. Theoretical analysis and experimental studies were carried out on rotor vibration signal characteristics, and a selection of signal processing methods and techniques were implemented to investigate the effect of seeded rotor faults on the vibration signal. The key achievements of the research work reported in this thesis are detailed below.

The aim of this work was: To develop and test an accurate and sensitive MEMS wireless accelerometer suitable for application to a rotating shaft. This has been achieved; a MEMS based wireless accelerometer has been designed, constructed and successfully used in the detection and diagnosis of mass unbalance, misalignment and measure IAS of a rotating shaft.

Sensor improvement:

Objective 1: Developing a wireless sensor unit and deploy it on rotating shaft.
Achievement 1: The design and implementation of the wireless sensor has been achieved using a MEMS accelerometer (ADXL202) and digital communication modules. The bandwidth and centre frequency of the acceleration signal were set to desired values. The output of this sensor was acquired by the receiver and filtered using a low pass filter in order to reconstruct the analogue form of the acceleration. Also, the digital form of the output was acquired for later processing. Both digital and filtered signals were recorded by the data acquisition system. Using a wired MEMS accelerometer, the frequency response of a rotating shaft was determined to benchmark the new sensor. The result shows the closeness of their responses. The sensitivity of the wireless sensor was determined according to the data sheet of the ADXL202. It confirms the capability of wireless sensor in detecting small rotor faults.

Objective 2: Develop a more accurate sensor system for measurement of rotor dynamics.
Achievement 2: Due to the vibration of rotating shaft, movement of the battery could occur and hence the output of the sensor could change. Consequently, the battery was placed under the PCB and secured by screws as described in Section 3.5.1. In addition, the dynamic response of the wireless sensor showed that the position of the wireless sensor on the shaft affected the DC value of the acceleration signal, refer to Section 3.12. Thus, the position of the sensor must not change during diagnostic tests once it had been installed. Experiment showed

that 0^o (see Figure 3.27) gave the highest DC shift. The transfer function of the wireless sensor showed that the sensor can be used for rotor dynamic fault detection, since it showed acceptable response within the range of interest (1 Hz to 25 Hz both –ve and +ve of sensitivity direction).

Objective 3: Benchmark the new sensing system.
Achievement 3: In order to benchmark the new sensor, two wired accelerometers were used. The results of the frequency response experiment are presented in Section 3.9.4, and showed the similarity between the wireless and two wired sensors taking into account their proximity to the wireless sensor. The results presented demonstrate the capability of wireless sensor to capture vibration direction and its magnitude.

Objective 4: Investigate the characteristics of the rotor dynamics including IAS extraction methods and factors that might cause a difference between IAS and wireless sensor measurements.
Achievement 4: The speed measurements were investigated using shaft speed Equation 4.2. The derived Equation 4.7 shows the relationship between the maximum error and the measurement parameters. In order to obtain an accurate measure of IAS, the resolution should be configured as low as possible, based on the measurement system. Figure 4.1 shows that the resolution of the wireless sensor decreased as speed increased, whereas the opto-interrupter and encoder increases. This can be justified by gravitational effect removal from wireless sensor waveforms.

Thus, the results of the tests showed clear differences between the IAS from wireless sensor and the other two sensors before removing gravitational effect. The results from the experiment on resolution reported in Section 4.3.2 show that the rotor condition has a major effect on IAS measurements. From Table 4.2, the spectral amplitudes of IAS from different sensors can be summarized:

- All three sensors clearly indicate the presence of vibration fluctuations at the highest level of misalignment. However, at the medium level of misalignment the encoder appears the least reliable and the wireless sensor the most reliable for indicating vibration fluctuations. Moreover, the wireless sensor appears the most sensitive of the three devices at the smallest level of misalignment. However, in the aligned case the wireless sensor, at 3X and 4X running speed, hardly captures the IAS because of the closeness of resolution of the sensor and the signal amplitude.
- The spectral peak at 2X running speed can be used to capture shaft speed fluctuations.
- It is clear from resolution plot (Figure 4.1) that the resolution of both encoder and opto-interrupter were directly proportional to the rotational frequency whereas the wireless

sensor resolution decreased as rotational frequency increases due to gravitational effect of MEMS accelerometers.

The resolution of wireless accelerometer changed with respect to the alignment condition and so is capable of small fault detection.

Since there is a difference in resolution between the wireless sensor and other sensors, the IAS from wireless sensor was compared with that of encoder and opto-interrupter. The algorithm used to obtain the IAS from the wireless accelerometer was based on integration of the raw acceleration signal. It was found that the acceleration obtained from the wireless signal varied with the relative directions of the earth's gravitational field and accelerometer axis. Therefore a TSA signal from wireless was used to eliminate g (gravitational correction) .The acceleration signal from the wireless sensor without the gravitational effect showed close agreement with the IAS from encoder and opto-interrupter, as shown in Figure 4.14. Therefore, to detect IAS by MEMS accelerometer, gravitational effect must be eliminated.

Objective 5: Measure the IAS and vibration of the system using conventional methods.
Achievement 5: The conventional transducers were used to benchmark the new sensor. It was found that the response of the new sensor was indicative to that of encoder and Opto-interrupter sensors. For instance, the response of the wired MEMS was found to be close to that of the wireless sensor. In addition, the IAS and IAA spectral response obtained from wireless sensor and encoder demonstrated a clear agreement in spectral content, see Figure 4.10.

Rotor Modelling:

Objective 6: Develop an accurate model that takes into account the dynamics of the couplings.
Achievement 6: Two rotor systems have been modelled. The equations have been solved using the state space method. A computer simulation program has been developed. The various lateral and rotational acceleration signals and their tangential counterpart have been discussed in Section 6.6. The model results were verified and evaluated from the wireless signals obtained experimentally. Both sets of results agreed in terms of frequency content as shown in Figure 6.7 and Figure 6.8.

Objective 7: Develop a more accurate model that takes into account the dynamics of misalignment, eccentricity and unbalance;
Achievement 7: The two rotor system was extended to a four rotor model. The new model took into account misalignment, eccentricity and unbalance. Different degrees of misalignment at different speeds were studied. In this simulation study, unbalance and eccentricity were

kept constant. In addition, the misalignment was induced between first and second rotors but the other rotors were maintained unchanged (residual misalignment, eccentricity and unbalance). The model spectral amplitude trend confirms that peak at 2X running speed is the major component that can be used to discern misalignment, see Figure 6.16.
The model also confirms the capacity of the wireless sensor for rotor fault detection. Moreover, the model allowed investigation of the net forces acting on the couplings due to misalignment using the displacement characteristics (Figure 6.17). Rotor 1 and rotor 2 showed displacements that were opposite and 90^{o} out of phase in the vertical direction whereas in the horizontal direction rotor 2 was subjected to greater forces than rotor 1 but was still out of phase by 90^{o} as shown in Figure 6.17.

Objective 8: Study characteristics of the rotor dynamics based on the model and measurement under normal and misalignment conditions.
Achievement 8: The results from experiment and simulation show the validity of the model and measurement scheme were successfully verified over a wide range of operating speeds, as presented in Figure 7.4 and Figure 6.16 respectively. The spectra from both the measured and numerical results confirm that misalignment can be detected and characterized primarily from the amplitude of the spectral peak at 2X shaft running speed. In addition, the comparison between simulation and measured spectra of wireless sensor and encoder acceleration spectra confirms the effectiveness of wireless sensor in detecting different misalignment degrees at different operating speeds, see Figure 7.5.

Objective 9: Study the characteristics of the rotor dynamics based on the model and measurement under normal and unbalanced conditions.
Achievement 9: The experimental results successfully validated the model and measurement scheme over a wide range of operating speeds as presented in Figure 9.10 and Figure 9.18 respectively. Both the measured and predicted spectra confirm that unbalance can be detected and characterized primarily by the spectral peak at 1X shaft running speed. The wireless sensor detects both rotational and lateral vibrations, and can separate baseline and different unbalanced rotors condition.

Rotor Diagnosis:

Objective 10: Develop more advanced analysis techniques for rotor dynamics based fault diagnosis, i.e. to differentiate between unbalance and misalignment.
Achievement 10: To minimise noise in the signals measured by the wireless accelerometer and the other sensors time synchronous averaging (TSA) was used. The results from this process gave good results and there was an increase in the strength of the signals. This technique led to a new approach to analysis of the wireless acceleration signal. The new method extracted the effects of gravity from the measured wireless acceleration see Section

4.7.1. The unbalance results confirmed an increase in the peak at 1st order (1X) running speed with rotor speed (Figure 9.19). On the other hand, misalignment results confirmed an increase in the peak at 2nd order (2X) running speed with rotor speed (Figure 8.28). In addition, this approach was used to compare the IAS from wireless and encoder and opto-interrupter and was successfully achieved, see Chapter 4.

Objective 11: Benchmark the diagnostic performance of the wireless accelerometer with conventional vibration measurements using wired contact accelerometers and non-contact laser displacement systems.
Achievement 11: A comparative study of different types of conventional transducers is given in Chapter 8 which also shows the performance of the new sensor. The laser vibrometer, encoder and accelerometers were used to benchmark the wireless sensor performance. The results proved the wireless sensor outperforms these three conventional sensors in diagnosing rotor misalignment condition.

Objective 12: Study characteristics of the rotor dynamics based on the model and measurement.
Achievement 12: The results from measurements and simulation (Chapters 7 and 9) confirm the agreement of rotor misalignment and unbalance spectral characteristics with previous studies. Moreover, the measured results from the wireless sensor were verified both by measurements made with the encoder and validated the predicted simulation results.

Objective 13: Develop more advanced analysis techniques for rotor dynamics based on fault detection (TSA).
Achievement 13: TSA was applied to sensor signals to enhance rotor dynamics fault detection. The results show increase in signal amplitude due to noise reduction and suppression of unrelated signals. In addition different approaches were used to obtain the IAS signals from wireless and other conventional signals. The gravitational correction of IAS has presented acceptable way of measuring the IAS by the new wireless sensor.

The algorithm used to extract IAS from the encoder and opto-interrupter was based on a FFT (Hilbert Transform) and the results obtained provide solid evidence the agreement with IAS from wireless sensor, see Section 4.6 and 4.7.3.

Application of the TSA and the gravitational correction brought values of the IAS from all three sensors into close proximity.

Objective 14: Develop more advanced techniques for IAS based diagnosis.
Achievement 14: The IAS extraction has been studied in terms of the resolution and measurement error as shown in Table 4.1. Chapter 4 elaborates on IAS measurements from both wireless and encoder. The study shows the difference in measured IAS signals from

wireless sensor and encoder in Figure 4.1. However, the IAS from wireless is well correlated to that obtained from encoder. The high IAS resolution of wireless sensor increases the potential of misalignment detection than the encoder and opto-interrupter at low speed. Table 4.2 shows the effect of degree of misalignment on IAS spectral amplitude. It confirms that all sensors at a high degree of misalignment capture large speed fluctuations. Moreover, the spectral peaks at 2X running speed are large enough to be measured. Consequently, the change in resolution of wireless sensor with respect to alignment is confirming its capability of detecting small faults.

10.2 Conclusions:

10.2.1 Wireless Accelerometer Node Design

1. The bandwidth of the new accelerometer is set to 500 Hz and the centre frequency to 1.838 kHz. It can be changed by changing R_{set} and the $C_{x,y}$ values, see Section 3.5.
2. The power consumption range of the wireless sensor has been found (2.7-3VDC) refer to Section 3.7.
3. The battery and the antenna must be held tightly to PCB to eliminate any possible vibrations, as shown in Figure 3.11 and described in Section 3.8.
4. It was found that change in power of the transmitted signal could be maintained by the fixed power supply of the receiver.
5. The low pass filtered DCS signal from the wireless sensor was found as DC shifted by the product of amplitude of DCS signal and percentage of on-time ($a_0 = K.D$). The frequency of the remaining ripples around DC is equal to the centre frequency of the DCS signal.
6. The sensitivity of the wireless sensor was 275 mV/g.
7. The calibration of the wireless sensor has been conducted using two wired sensors. It has been found that their responses are very similar though with some amplitude difference, see Figure 3.15. To improve the frequency response of wireless sensor, the modified response was used to rectify the wireless measurements as explained in Section 3.9.4.
8. The transfer function of the sensor presented in Figure 3.18 shows that sensor response is linear within the frequency range of interest for rotor dynamic diagnosis.
9. Based on theoretical prediction of tangential and centripetal accelerations acting on the sensor, the wireless sensor must be aligned tangentially to the rotor surface in order to nullify the effect of centripetal acceleration.
10. The dynamic characteristics of the wireless sensor on the rotor show that the DC shift of the output can vary according to the position of the sensor on the rotor. The change of the DC shift with respect to sensor position on the rotor show the sensitivity of the

sensor to the different dynamics of each point on the rotor (centre of mass), and hence the sensor must be fixed in one position during rotor health monitoring.

11. It has been found that by controlling the angle of inclination of the sensor, increasing or decreasing of the DC shift can be obtained.
12. The analysis showed that possible communication errors due antenna installation were negligible. In addition, the sensor noise analysis demonstrated high signal to noise ratio. Moreover, the study of sensor resolution also confirmed that the sensor is capable of measuring possible rotor vibrations and high potential of small fault detection.
13. Finally, all the above procedures demonstrated the effectiveness and accuracy of the wireless accelerometer for rotor dynamics health monitoring.

10.2.2 Instantaneous Angular speed (IAS)

The research has shown that it is possible to develop a wireless sensing system to detect the IAS of rotary shaft and confirmed the following:

1. The IAS results obtained from the developed wireless sensor can be compared to that obtained from a contact encoder.
2. The wireless acceleration signal has high signal-to-noise ratio which will increase the possibility of small fault detection compared to IAA from encoder.
3. The information conveyed by the IAS from wireless accelerometer is promising for rotor fault detection.
4. From the IAS shown in Figure 4.10 (a), it can be seen that the rotational frequency and its higher order harmonics can be resolved by both wireless and encoder signals. The IAS from the wireless sensor shows lower noise levels in the high frequency range but much higher amplitudes in the low frequency range.
5. Although the wireless accelerometer used is bandwidth limited by the active low pass filter, the information used in the extraction of IAS shows acceptable features for fault diagnosis.
6. The discussion in Section 4.6.1 concluded that by applying TSA and gravitational correction to the acquired signals, IAS waveforms characteristics from wireless become closer to those obtained from encoder and opto-interrupter, as shown in Figure 4.14. Moreover, the order of the spectral amplitude of the IAS from wireless sensor changed in the sense that the peaks at 1X running speed increased with speed rather than decreasing as shown in Figure 4.15 and Figure 4.17.
7. In general, the results obtained provide solid evidences for effectiveness of TSA in IAS extraction from wireless sensor.

10.2.3 Simulation Results of System Model

1. The two-rotor system mathematical model developed as part of this research has been examined under a number of different operating conditions.
2. This simplified model retained the key features of the coupling and bearing. Two rigid shafts, mounted on motor and load bearing were connected by a coupling with N pairs of pins/rings on each flange, each pair having a finite stiffness Kb as shown in Figure 6.3 (a). The system was assumed to be balanced dynamically and hence the exciting forces arise only from seeded misalignment. More specifically they arise from varying forces in the coupling and bearing. The wireless accelerometer is mounted tangentially on the second rotor as illustrated in Figure 6.2.
3. The analysis of the motion commenced with first rotor by applying the Euler-Lagrange energy equation (Appendix A). The variation in the angular speed is related to the acceleration acting on wireless sensor. In addition, the transitional acceleration of each rotor due to rotational movement in its supporting bearings is derived.
4. The model was validated against a set of experimental results (see Section 6.5). The predicted results shown in Figure 6.7 are very similar to the experimental results in Figure 6.9. It was concluded that the wireless sensor can play a significant role in the remote detection of rotor faults such as misalignment under different operation conditions.
5. The mathematical simulation showed that the spectral peak at 2X running speed in combined acceleration spectrum from the wireless sensor is capable of detecting the misalignment, as illustrated in Figure 6.10.
6. The measured and simulated results were validated against one another, and it was concluded that the results were close enough for the model to be accepted as a practical basis for predictions concerning wireless fault detection.
7. A similar simulation study of a four rotor system showed that at high speed the waveforms of the lateral acceleration exhibit sinusoidal fluctuation whereas the rotational exhibit a greater rate of fluctuation, as shown in Figure 6.13. These fluctuations show that shaft misalignment leads to shaft fluctuation in all directions but with different frequency contents.
8. Further examination of the results in the frequency domain found that the fundamental rotational component 1X dominates the spectra, as shown in Figure 6.13(c). Moreover, the spectra also show distinctive 2X components, which is the main feature commonly used for diagnosing misalignments (Dewell & Mitchell, 1984; Sekhar, A. S. & Prabhu, 1995). These indicate that both rotational and lateral accelerations are sensitive to misalignment but at different frequencies. In general, these spectral features show that the model is adequate for exploring shaft misalignment and predicting the resulting signals from a wireless sensor.

9. At the wireless sensor position, the simulation results show that tangential accelerations ($\boldsymbol{a_{tx}}$, $\boldsymbol{a_{ty}}$ and $\boldsymbol{a_{tw}}$) along the sensitivity axis fluctuate twice as fast as the original but with shifted phase, as shown in Figure 6.14 (a). Moreover, by combining the three components, the total acceleration $\boldsymbol{a_t}$ exhibits mainly the feature of $\boldsymbol{a_{tw}}$ but with a clear DC shifts due to the combination of $\boldsymbol{a_{tx}}$ and $\boldsymbol{a_{ty}}$.
10. In the frequency domain, the spectrum from the full combination of $\boldsymbol{a_{txy}}$ and $\boldsymbol{a_{tw}}$ exhibits noticeable differences at various shaft frequencies. In particular, the amplitude difference between $\boldsymbol{a_{tw}}$ and $\boldsymbol{a_t}$ is marginal at 1X and 2X, showing that these two components are due mainly to rotational oscillation. Therefore, the combined spectrum is more sensitive to changes due to misalignments.
11. The sensor output waveform is superimposed by the acceleration due to gravity, 9.81 ms^{-2}. This affects the spectrum at only 1X; the other features remain the same as shown in Figure 6.15.
12. The simulated spectral amplitude changed with different degrees of misalignment and different motor speeds but it was found that the amplitude of the spectral peak at 2X for the combined accelerations increased with both shaft speed and the degree of misalignment (Dewell & Mitchell, 1984) as shown in Figure 6.16. It was thus a good indicator for misalignment at high speed. In general, the amplitude variation of the combined acceleration peaks at 3X and 4X can be indicators of misalignment. However, 3X and 4X have very low amplitude and can be influenced by measurement noise (see Section 6.11).
13. The case study in Section 6.12 predicted the displacement behaviour of the four shafts with respect of misalignment. It was shown that:
    a. The rotational displacements of rotors 1 and 2 are out of phase with rotors 3 and 4, as illustrated in Figure 6.17. That means the rotors are fluctuating angularly according to the different misalignment generated forces.
    b. The displacements waveforms in the x-direction of first and third shafts are in phase, as are the second and fourth shafts, but the two couples are 90° out of phase.
    c. The displacement waveforms in the y-direction of first and fourth shafts are in phase with positive waveforms, whereas the second and third shafts are in phase but with negative waveforms and so move in the opposite direction. The forces acting on the first pair are thus in the opposite direction to the forces acting on the second pair.

10.2.4 Characteristics of Rotor Dynamics based on Model and Measurement under Misalignment

1. Through experiment and simulation, the validity of the model and sensor measurement were successfully verified over a wide range of operating speeds. Although the amplitude of the waveforms obtained from the encoder for IAS and from the wireless sensor for acceleration showed only small changes with degree of misalignment, it is clear from the spectra that the wireless sensor was effective in detecting the misalignment, as shown in Figure 7.3.
2. The spectral amplitudes of both sensors show the peak at 2X running speed can be used for misalignment detection see Figure 7.4. Both measured and predicted spectra for the wireless sensor and encoder show that the spectral amplitudes of all signals increased with increase in misalignment and speed.
3. Previous studies of rotor misalignment and the experiment results confirmed that the second peak harmonic at 2X is the component that changes most with respect to the degree of misalignment, see Figure 7.5. Because the 2X, 3X and 4X components consist of both rotational and lateral vibrations, as explained in Chapter 6, it proves the effectiveness of new detection scheme performance compared with IAS measurements scheme.

10.2.5 Comparative Study of Misalignment Detection using a Wireless Sensor and Conventional Wired Sensors

10.2.5.1 High level of misalignment (0.3, 0.4, 0.5 mm)

Form the experimental results, the vibration waveforms from different sensors showed small changes for different misalignment levels. However, the amplitude generally increased with speed, but did not show a consistent trend with change in misalignment level because of high frequency vibrations from other sources, see Figure 8.4, Figure 8.5, Figure 8.6, Figure 8.8.

The amplitudes of the spectral peak at 1X running speed for all sensors failed to separate different levels of misalignment. However, the 2X peak could differentiate the level of misalignment level but with different degrees of success depending on the sensor used:

- The wireless sensor fully separated the different misalignment levels and showed a uniquely increasing trend with speed (Figure 8.14).
- IAS from the encoder consistently separated the high misalignment levels at high speeds (Figure 8.14).

- The vertical displacement from the laser vibrometer separated misalignment from the baseline signal but was not consistent with degree of misalignment and speed (Figure 8.14).
- The horizontal acceleration signal from the wired accelerometer showed a very similar performance to the wireless sensor, but its trend oscillated at low speeds (Figure 8.14).

10.2.5.2 Low Level of Misalignment (0.1, 0.2mm)

The simulated results for the spectral peaks at 1X, 2X, 3X and 4X running speed for combined, rotational and lateral acceleration are presented in Figure 8.18, Figure 8.19 and Figure 8.20 respectively and show the possibility of detecting low degrees of misalignment:

1. It was concluded that the amplitude at 1X was not suitable for misalignment detection.
2. The peak at 2X succeeded in detecting misalignment at 0.2mm clearer than 0.1mm.
3. The predicted values of the 3X and 4X peaks are so small ($\sim 10^{-5}$ m/s^2) that they are likely to be swamped by system noise and cannot be relied on.

The experimental investigations of small degrees of misalignment (0.1 mm and 0.2 mm) demonstrated that the amplitude of the spectral peak at 1X running speed only the encoder could separate misalignment levels. For the spectral peak at 2X running speed, only the wireless sensor could clearly separate the different levels of misalignment with speeds (Figure 8.26). The 2X spectral peak of the horizontal wired accelerometer was able to differentiate between levels of misalignment below 878 RPM, but the vertical one could not (Figure 8.26).

The wireless sensor outperformed the other sensors in detecting the small levels of misalignment. There was agreement between simulated and measured results in detecting such levels of misalignment.

The measured accelerations from wireless sensor subjected to TSA algorithm resulting smoother waveforms in the angular domain. By eliminating gravitational effects from wireless signals in the angular domain, an increase in the waveform amplitudes was noticeable. Consequently, the 1st order spectral amplitude peak showed increasing trend with speed increase, but the 2nd order peak not changed as shown in Figure 8.28.

10.2.6 Identification of Rotor Unbalance using Wireless Sensor

The simulation results showed that the combined and rotational tangential accelerations have shown small change in 2X peak amplitude for different grades of mass unbalance. However, at the 1X peak amplitude the differences became clear. As the unbalanced mass increased the lateral tangential acceleration came close to the combined and rotational accelerations as shown in Figure 9.7, Figure 9.8 and Figure 9.9. The spectra of all the tangential accelerations demonstrated clear separation of the different degrees of unbalance for different speeds at 1X.

The 3X and 4X spectral components were very small in magnitude and hence would be difficult to measure in the presence of noise. Consequently, the 1X spectral peak appeared best for unbalance detection as proven in previous studies (Adiletta, et al., 1997; Hubinger, et al., 2012; Jalan & Mohanty, 2009; Li, M. & He, 2009; Suphattana & Surawatpunya, 2010; Xu & Marangoni, 1994 a).

Based on model results, the wireless measurement scheme was used to investigate the problem of monitoring unbalanced shafts. Experimental work successfully validated the model over a wide range of operating speeds. The experimental results showed the detection performance of the wireless measurement sensor was much better than the IAS and vibration measurements (Figure 9.18).

Experiments using different sensors have shown slight changes in the amplitude of the signals for different degrees of unbalance (Figure 9.15, Figure 9.16, Figure 9.17). The waveforms of all sensors exhibited small changes at low speed but bigger changes at high speeds with increase in mass unbalance grade. However, the shape of the waveforms was only slightly changed and did not give a clear differentiation between different cases. The spectral analysis showed that the amplitude of the 2X peak for all sensors failed to detect the unbalance fault (Figure 9.20). However, the amplitude of the 1X peak was able to separate the different unbalance cases with different degrees of success depending on the sensor used:

- The wireless sensor produced full separation of the different degrees of unbalance and showed a unique increase with speed.
- The encoder (IAS) was not capable of separating the different cases.
- Vertical acceleration from the wired accelerometer separated only the higher grade of unbalance and then only at high speed.
- Horizontal acceleration from the wired accelerometer showed clear unbalance separation but only at high speed.

The simulation and experimental results presented unequivocal evidence for the effectiveness of wireless sensor in detecting the rotor unbalance.

10.3 Novel Measurement Scheme Summary

The research Thesis presents a novel wireless sensor for condition monitoring of rotor dynamics. It incorporates a number of novel and important issues not previously reported by other researchers or practitioners:

❖ **Novel Aspect One:**

The author believes that the novel wireless accelerometer prototype captures the same static vibration (the sensor not moving) as the wired accelerometer and dynamic vibration (the sensor rotating on shaft). Also, the predicted dynamic characteristics successfully correlated

with the measured ones (see Chapters 3, 6, 7 and 8). This novel wireless sensor determined the tangential acceleration of the rotating shaft.

❖ **Novel Aspect Two:**

The use of the new sensor to measure the IAS of a rotating shaft showed the effectiveness of the new device. With advanced signal processing, the measured IAS was close to counterpart IAS from encoder and opto-interrupter.

❖ **Novel Aspect Three:**

The dynamic model of a rotor with seeded misalignment and unbalanced mass faults and with an attached wireless sensor for remote detection and diagnosis is entirely novel.

❖ **Novel Aspect Four:**

The actual use of wireless sensor for remote detection and diagnosis of rotor misalignment is entirely novel. No work has been found describing in any detail the wireless accelerometer analysis of vibration under different misaligned rotor operating conditions.

❖ **Novel Aspect Five:**

The actual use of wireless sensor for remote detection and diagnosis of rotor unbalance is entirely novel. No work has been found describing in any detail the wireless accelerometer analysis of vibration under different unbalanced rotor operation conditions.

10.4 The Contributions to Knowledge made by this Thesis

The First Contribution:

The application of wireless accelerometer vibration analysis for remote detection and diagnosis of rotor faults has not been previously investigated.

The Second Contribution:

The author could not find any reports of using a MEMS wireless sensor deployed on a rotating shaft for IAS measurement.

The Third Contribution:

The author could not find any reports of using a MEMS wireless sensor deployed on rotating shaft for misalignment detection and diagnosis.

The Fourth Contribution:

The author could not find any reports of using a MEMS wireless sensor deployed on rotating shaft for detection and diagnosis of mass unbalance.

The Fifth Contribution:

The modelling of a two flexible rotor bearing system in association of the use of a wireless sensor to study the forces acting between two shafts and the use of a Lagrange-Euler equation

to represent the rotor dynamics (eccentricity, unbalance and misalignment) has not previously been approached in this way.

The Seventh Contribution:

The modelling of a four flexible coupled rotor bearing system (including tangential accelerations acting in the direction of wireless sensor sensitivity axis) to study the four shafts dynamics (eccentricity, unbalance and misalignment) has not previously been attempted.

The Eighth Contribution:

No reports have been found of using TSA for processing of signals from a remote wireless sensor for detection and diagnosis of rotor misalignment. The author believes that the use of the TSA signal processing technique to analyse the MEMS gravity based sensor of a flexible coupled rotors bearing system is unique.

10.5 Recommendations for Future Work on Wireless Sensor

Recommendation 1:

The MEMS wireless accelerometer PCB prototype needs to be miniaturised for ease of installation. This might be achieved using a smaller antenna. The components and battery need to fit tightly to avoid parasitic vibration. Moreover, the sensor holder should be designed to ensure that the sensor axis is radial and the sensor positioned tangentially at the rotor surface.

Recommendation 2:

One of the main issues with the wireless sensor was its power consumption and the consequent requirement of periodic battery replacement. Power harvested from the ambient vibration could help the sensor to be self-powered making the wireless sensor more independent.

Recommendation 3:

The use of a number of transmitter frequencies, multiple wireless MEMS sensors could be utilised to simultaneously perform modal analysis and health monitoring of multiple rotors.

Recommendation 4:

More experimental work is needed to further evaluate the sensitivity and reliability of the proposed detection method on a simple rotor system, (e.g. a single rotor) to gain a better understanding of the effect of other vibration sources on the measured vibration signal.

Recommendation 5:

Use the model to predict the dynamic characteristics of a rotor with eccentricity, misalignment and mass unbalance. Use a wireless sensor to measure and analyse the corresponding acceleration signals. This study would investigate the differences between signals due to eccentricity, misalignment and mass unbalance and combinations of these faults.

Recommendation 6:

Investigate the use of a data acquisition system with a substantially higher sampling rate to increase the resolution of the data and better results could be achieved.

Recommendation 7:

By miniaturise the MEMS wireless accelerometer, it is possible to deploy where conventional accelerometers too hard to be mounted.

Recommendation 8:

By embedding a processing unit, a smart wireless accelerometer could be developed which process the data inside the node and transmit key features only.

Recommendation 9:

Conventional encoder based IAS measurements are unable to measure very low speed machines such as the input of a wind turbine and output of press machines. The wireless accelerometer allows the measurement of IAS at nearly zero speed. It is recommended investigating the extension of this scheme to low speed machines.

References

Adiletta, G., Guido, A., & Rossi, C. (1997). Nonlinear dynamics of a rigid unbalanced rotor in journal bearings. Part I: theoretical analysis. *Nonlinear Dynamics, 14*(1), 57-87.

Al-Hussain, K. M., & Redmond, I. (2002). Dynamic Response of Two Rotors Connected by Rigid Mechanical Coupling with Parallel Misalignment. *Journal of Sound and Vibration, 249*(3), 483-498. doi: http://dx.doi.org/10.1006/jsvi.2001.3866

Analog Devices, I. (2009). ADXL202E Data sheet 2009, from http://www.analog.com/static/imported-files/data_sheets/ADXL202E.pdf

Andrejašic, M. (2008). *Mems accelerometers.* Paper presented at the University of Ljubljana. Faculty for Mathematics and Physics, Department of Physics, Seminar.

Arebi, L., Gu, F., & Ball, A. (2011). *Misalignment Detection using a Wireless Sensor Mounted on a Rotating Shaft*. Paper presented at the Proc. of the 24th Int. Congress on Condition Monitoring and Diagnostics Engineering Management

Arumugam, P., Swarnamani, S. and Prabhu, B. S. (1995). Effects of coupling misalignment on the vibration characteristics of a two stage turbine rotor. *ASME Des. Engng Tech. Conf, 84*, 1049-1054.

Bachschmid, N., & Pennacchi, P. (2003). Accuracy of fault detection in real rotating machinery using model based diagnostic techniques. *JSME International Journal Series C, 46*(3), 1026-1034.

Barron, D. R. (1996). *Engineering Condition Monitoring: Practice, Methods and Applications*: Longman.

Bejarano, F. A., Jia, Y., & Just, F. (2009). Crack Identification of a Rotating Shaft with Integrated Wireless Sensor. *International Journal On Smart Sensing and Intelligent Systems, 2*(4), 564-578.

Belanger, P. R. (1992, 12-14 May 1992). *Estimation of angular velocity and acceleration from shaft encoder measurements.* Paper presented at the Robotics and Automation, 1992. Proceedings., 1992 IEEE International Conference on.

Bhargavi, N. (Producer). (2011). PWM DAC Using MSP430 High-Resolution Timer, MSP430 Applications. *Application Report, Texas Instruments, SLAA497*.

Bognatz, S. R. (1995). Alignment of critical and non critical machines. *Orbit,* 23–25.

Braun, S. (2011). The synchronous (time domain) average revisited. *Mechanical Systems and Signal Processing, 25*(4), 1087-1102.

Braut, S., Zigulic, R., & Butkovic, M. (2008). Numerical and experimental analysis of a shaft bow influence on a rotor to stator contact dynamics. *Strojniški vestnik, 54*(10), 693-706.

Cabanas, M., Gonzalez, F., Rojas, C., Melero, M., Norniella, J., Orcajo, G., . . . Nuno, F. (2011). A New Portable, Self-Powered and Wireless Instrument for the Early Detection of Broken Rotor Bars in Induction Motors. *Industrial Electronics, IEEE Transactions on, PP*(99), 1-1.

Charles, P., Sinha, J. K., Gu, F., Lidstone, L., & Ball, A. D. (2009). Detecting the crankshaft torsional vibration of diesel engines for combustion related diagnosis. *Journal of Sound and Vibration, 321*(3–5), 1171-1185. doi: http://dx.doi.org/10.1016/j.jsv.2008.10.024

Chen, C.-Y., & Kuan, C.-H. (2000). Design and calibration of a noise measurement system. *Instrumentation and Measurement, IEEE Transactions on, 49*(1), 77-82.

Chung, H. C., Enomoto, T., Loh, K., & Shinozuka, M. (2004). *Real-time visualization of bridge structural response through wireless MEMS sensors.* Paper presented at the NDE for Health Monitoring and Diagnostics.

Chung, H. C., Enomoto, T., & Shinozuka, M. (2003). *MEMS-type accelerometers and wireless communication for structural monitoring.* Paper presented at the The 2nd MIT Conferences on Fluid and Solid Mechanics, Cambridge, MA.

Collacott, R. A. (1997). *Mechanical Fault Diagnosis and Condition Monitoring*. London, UK.: Chapman and Hall.

Crawford, A. R., & Crawford, S. (1992). *The simplified handbook of vibration analysis: Introduction to Vibration Analysis Fundamentals, Volume I* (Vol. 1): Computational Systems.

Dalpiaz, G., & Rivola, A. (1997). Condition monitoring and diagnostics in automatic machines: comparison of vibration analysis techniques. *Mechanical Systems and Signal Processing, 11*(1), 53-73.

De Silva, C. W. (2005). *Vibration and shock handbook*: CRC.

Dewell, D., & Mitchell, L. (1984). Detection of a misaligned disk coupling using spectrum analysis. *Journal of Vibration, Acoustics, Stress &. Reliability Design, 106*(3), 9-16.

Edwards, S., Lees, A., & Friswell, M. (1998). Fault diagnosis of rotating machinery. *Shock and Vibration Digest, 30*(1), 4-13.

Elwenspoek, M., & Wiegerink, R. (2001). *Mechanical Microsensors*: Springer.

Feldman, M., & Seibold, S. (1999). Damage diagnosis of rotors: application of Hilbert transform and multihypothesis testing. *Journal of Vibration and Control, 5*(3), 421-442.

Fraden, J. (2010). Handbook of modern sensors: physics, designs, and applications

Gardner, J. W. (1994). *Microsensors: principles and applications*: Wiley.

Gibbons, C. B. (1976). Coupling misalignment forces. *Proceedings of 5th Turbomachinery Symposium, ,Gas Turbine Laboratories*(Texas A&M University), 111-116.

Goodman, M. (1989). *Dynamics of Rotor – Bearing Systems*. London: Unwin Hyman Ltd.

Gu, F., Yesilyurt, I., Li, Y., Harris, G., & Ball, A. (2006). An investigation of the effects of measurement noise in the use of instantaneous angular speed for machine diagnosis. [doi: 10.1016/j.ymssp.2005.02.001]. *Mechanical Systems and Signal Processing, 20*(6), 1444-1460.

Guido, A., & Adiletta, G. (1999). Dynamics of a Rigid Unbalanced Rotor with Nonlinear Elastic Restoring Forces. Part II: Experimental Analysis. *Nonlinear Dynamics, 19*(4), 387-397.

Hariharan, V., & Srinivasan, P. (2011). Vibration analysis of parallel misaligned shaft with ball bearing system. *Songklanakarin Journal of Science and Technology, 33*, 1.

Hariharan, V., Srinivasan, P., & Engg, K. (2009). Vibration analysis of misaligned shaft -ball bearing system. *Indian Journal of Science and Technology, 2*(9).

Harris, C. M. (1988). *Shock and Vibration Handbook*. New York: McGraw-Hill.

Harris, C. M., & Piersol, A. G. (2010). *Harris' shock and vibration handbook* (Vol. 6): McGraw-Hill New York.

Hengstler, & Inc. (2009). Technical Datasheet Incremental Encoder RI32 Retrieved 1/2/2009, from http://www.hengstler.com/en/products/shop.php,catID=1011&artID=34

Hsu, T.-R. (2008). *MEMS & Microsystems: Design, Manufacture, and Nanoscale Engineering*: John Wiley & Sons.

Hubinger, S., Gattringer, H., Bremer, H., & Mayrhofer, K. (2012). *Acceleration of Unbalanced Rotors.* Paper presented at the Mathematical Modelling.

Huer, S., & Zhaojian, Y. (2010, 23-25 July 2010). *Study on Lateral Vibration Responses of Misalignment Rotor-Bearing Systems Based on Linear Torsion Excitation.* Paper presented at the Information Engineering and Electronic Commerce (IEEC), 2010 2nd International Symposium on.

Isermann, R. (2005). Model-based fault-detection and diagnosis – status and applications. *Annual Reviews in Control, 29*(1), 71-85. doi: http://dx.doi.org/10.1016/j.arcontrol.2004.12.002

ISO1940-1. (2003). Mechanical vibration - Balance quality requirements for rotors in a constant (rigid) state *Part 1: Specification and verification of balance tolerances* (Vol. ISO 1940): ISO.

ISO10816-3. (2009). Mechanical vibration -- Evaluation of machine vibration by measurements on non-rotating parts --

Part 3: Industrial machines with nominal power above 15 kW and nominal speeds between 120 r/min and 15 000 r/min when measured in situ, from https://www.iso.org/obp/ui/#iso:std:50528:en

ISO-10816-1. (1995). Mechanical vibration - Evaluation of machine vibration by measurements on non-rotating parts - Part 1: General Guidelines.

ISO/16063-21. (2003). Methods for the calibration of vibration and shock transducers *Vibration calibration by comparison to a reference transducer*. Geneva: ISO.

Jalan, A. K., & Mohanty, A. R. (2009). Model based fault diagnosis of a rotor–bearing system for misalignment and unbalance under steady-state condition. [doi: 10.1016/j.jsv.2009.07.014]. *Journal of Sound and Vibration, 327*(3–5), 604-622.

Jardine, A. K., Lin, D., & Banjevic, D. (2006). A review on machinery diagnostics and prognostics implementing condition-based maintenance. *Mechanical Systems and Signal Processing, 20*(7), 1483-1510. doi: citeulike-article-id:6931368 doi: 10.1016/j.ymssp.2005.09.012

Jardine, A. K. S., Lin, D., & Banjevic, D. (October 2006). A review on machiner diagnostics and prognostics implementing condition-based maintenance *Mechanical Systems and Signal Processing, 20*(7), 1483-1510.

Kang, C., Hsu, W., Lee, E., & Shiau, T. (2011). Dynamic analysis of gear-rotor system with viscoelastic supports under residual shaft bow effect. *Mechanism and Machine Theory, 46*(3), 264-275.

Kelly, A. (1997). *Maintenance Strategy*. Oxford: Butterworth-Heinemann.

Kemo, I. (2011). Kemo Dual Variable Filter Type 1Hz- 100kHz, from http://www.china-yec.com/en/products_details.asp?id=221

Kenjo, T., & Nagamt, S. (1985). Permanent-Magnet and Brushless. DC Motors

Korkua, S., Jain, H., Lee, W.-J., & Kwan, C. (2010, 9-13 May 2010). *Wireless health monitoring system for vibration detection of induction motors.* Paper presented at the Industrial and Commercial Power Systems Technical Conference (I&CPS), 2010 IEEE.

Kovacs, G. T. (1998). *Micromachined transducers sourcebook*: WCB/McGraw-Hill New York, NY.

Lee, Y. S., & Lee, C. W. (1999). Modelling and Vibration Analysis of Misaligned Rotor-Ball Bearing Systems. [doi: DOI: 10.1006/jsvi.1997.1301]. *Journal of Sound and Vibration, 224*(1), 17-32.

Lees, A., & Friswell, M. (1997). The evaluation of rotor imbalance in flexibly mounted machines. *Journal of Sound and Vibration, 208*(5), 671-683.

Lees, A., Sinha, J., & Friswell, M. (2009). Model-based identification of rotating machines. *Mechanical Systems and Signal Processing, 23*(6), 1884-1893.

Lees, A. W. (2007 (a)). Misalignment in rigidly coupled rotors. *Journal of Sound and Vibration, 305*(1–2), 261-271. doi: http://dx.doi.org/10.1016/j.jsv.2007.04.008

Lees, A. W. (2007 (b)). *Misalignment in Rigidly Coupled Flexible Rotors*. Paper presented at the IMAC-XXV: Conference & Exposition on Structural Dynamics.

Levinzon, F. A. (2008). *Ultra-low-noise 10 V/g compact IEPE seismic accelerometer.* Paper presented at the Proceedings of the 26th International Modal Analysis Conference.

Li, M., & He, L. (2009). The dynamics of a parallel-misaligned and unbalanced rotor system under the action of non-linear oil film forces. *Mechanical Engineering Science, 224*(Part C).

Li, Y. (2003a). The Measurement of Instantaneous Angular Speed Using Programmable Interval Timer 82C54 (Vol. Internal Report, pp. 1-6).

Li, Y. (2003b). The Measurement of Instantaneous Angular Speed Using Programmable Interval Timer 82C54 (pp. 1-6).

Li, Y., Gu, F., Harris, D., & Ball, A. D. (2005). The Measurement of Instantaneous Angular Speed. *International Journal of Mechanical Systems and Signal Processing, 19*(4), 786-805.

Li, Y., Gu, F., Harris, G., Ball, A., Bennett, N., & Travis, K. (2005). The measurement of instantaneous angular speed. [doi: 10.1016/j.ymssp.2004.04.003]. *Mechanical Systems and Signal Processing, 19*(4), 786-805.

Liang, B. (2000). *Condition Monitoring and Fault Diagnosis of Induction Motors.* PhD Thesis, Manchester School of Engineering, Department of Mechanical Engineering, Manchester, UK.

Linx. (2009 A). ANT-418-SP Data sheets Retrieved Revised 11/05/12, from https://www.linxtechnologies.com/resources/data-guides/txm-xxx-lr.pdf

Linx. (2009 R). LR Series Receiver Module Data Guide Retrieved Revised 11/05/12, from https://www.linxtechnologies.com/resources/data-guides/rxm-xxx-lr.pdf

Linx. (2009 T). LR Series Transmitter Module Data Guide Retrieved Revised 11/05/12, from https://www.linxtechnologies.com/resources/data-guides/txm-xxx-lr.pdf

Loparo, K. A., Adams, M. L., Wei, L., Abdel-Magied, M. F., & Afshari, N. (2000). Fault detection and diagnosis of rotating machinery. *Industrial Electronics, IEEE Transactions on, 47*(5), 1005-1014. doi: 10.1109/41.873208

Lynch, J. (2004). *Overview of wireless sensors for real-time health monitoring of civil structures.* Paper presented at the Proceedings of the 4th International Workshop on Structural Control.

Lynch, J. P., Law, K. H., Straser, E. G., Kiremidjian, A. S., & Kenny, T. W. (2000). *The development of a wireless modular health monitoring system for civil structures.* Paper presented at the MCEER Mitigation of Earthquake Disaster by Advanced Technologies (MEDAT-2) Workshop.

MacCamhaoil, M., & Kjaer, B. (1989). Static and Dynamic Balancing of Rigid Rotors.

Maryland, M. (2008). HRC Coupling, 2010, from web: http://mdmetric.com

Maten, S. (1970). Program machine maintenance by measuring vibration velocity. *Hydrocarbon Processing, 49(9)*, 291-296.

Mathew, J., & Davis, A. (1998). *Handbook of Condition Monitoring: techniques and methodology ,Common Vibration Monitoring Techniques* London: Chapman & Hall

Matthew, J. (1987). Machine Condition Monitoring Using Vibration Analysis. *Acoustic Australia, 15*, 7-13.

McFadden, P. D., & Toozhy, M. M. (2000). Application of Synchronous Averaging to Vibration Monitoring of Rolling Element Bearing. *Mechanical Systems and Signal Processing, 14*(6), 891-906. doi: http://dx.doi.org/10.1006/mssp.2000.1290

Michael, M. (2005). *Introduction to MEMS.* EECS 414 lectures, University of Michigan, Michigan USA.

Micro-Epsilon. (2010). optoNCDT, Laser Triangulation Displacement Sensors, 2010, from http://www.micro-epsilon.de/download/products/cat--optoNCDT--en.pdf

Mobley, R. K., & Davies, A. (1998). *Condition Based Maintenance. In: Handbook of Condition Monitoring*. London: Chapman & Hall.

Mohd-Yasin, F., Korman, C. E., & Nagel, D. J. (2003). Measurement of noise characteristics of MEMS accelerometers. *Solid-State Electronics, 47*(2), 357-360. doi: http://dx.doi.org/10.1016/S0038-1101(02)00220-4

Nakhaeinejad, M., & Ganeriwala, S. (2009). Observations on Dynamic Responses of Misalignments. [Tech Note, SpectraQuest Inc]. (Sep. 2009).

Nicholas, J., Gunter, E., & Allaire, P. (1976). Effect of Residual Shaft Bow on Unbalance Response and Balancing of a Single Mass Flexible Rotor—Part I: Unbalance Response. *Journal of Engineering for Power, 98*, 171.

Pereira, L. A., & da Silva Gazzana, D. (2004, 2-6 Nov. 2004). *Rotor broken bar detection and diagnosis in induction motors using stator current signature analysis and fuzzy logic.* Paper presented at the Industrial Electronics Society, 2004. IECON 2004. 30th Annual Conference of IEEE.

Piotrowski, J. (2007). *Shaft alignment handbook* (Vol. 3): Crc Press.

Platz, R., & Markert, R. (2001). *Fault models for online identification of malfunction in rotor systems*. Paper presented at the Transactions of the 4th International Conference on Acoustical and Vibratory Surveillance, Methods and Diagnostic Techniques, France.

Prabhakar, S., Sekhar, A., & Mohanty, A. (2001). Vibration analysis of a misaligned rotor coupling bearing system passing through the critical speed. *Proceedings of the Institution of Mechanical Engineers, Part C: Journal of Mechanical Engineering Science, 215*(12), 1417-1428.

Qi, K., He, Z., Li, Z., Zi, Y., & Chen, X. (2008). Vibration based operational modal analysis of rotor systems. [doi: 10.1016/j.measurement.2007.11.009]. *Measurement, 41*(7), 810-816.

Randall, R. B. (2011). *Vibration-based condition monitoring: industrial, aerospace and automotive applications*: John Wiley & Sons.

Redmond, I. (2010). Study of a misaligned flexibly coupled shaft system having nonlinear bearings and cyclic coupling stiffness—Theoretical model and analysis. [doi: 10.1016/j.jsv.2009.09.039]. *Journal of Sound and Vibration, 329*(6), 700-720.

Redmond, I., & Al-Hussain, K. (2001). Misalignment as a source of vibration in rotating shaft systems. *System, 1*, 47.

Reilly, S., Leach, R., Cuenat, A., Awan, S., & Lowe, M. (2006). Overview of MEMS sensors and the metrology requirements for their manufacture. *National Phsycial Laboratory*.

Remond, D. (1998). Practical performances of high-speed measurement of gear transmission error or torsional vibrations with optical encoders. *Measurement Science and Technology, 9*(3), 347.

Resor, B. R., Trethewey, M. W., & Maynard, K. P. (2005). Compensation for encoder geometry and shaft speed variation in time interval torsional vibration measurement. [doi: 10.1016/j.jsv.2004.10.044]. *Journal of Sound and Vibration, 286*(4–5), 897-920.

Richey, R. (1999). Measure tilt using PIC16F84A & ADXL202. *Microchip Technology Inc*.

Rivin, E. I. (1986). Design and application criteria for connecting couplings. *Trans. ASME Mechanisms, 108*(Transm. Automn Des), 96-104.

Saavedra, P., & Ramırez, D. (2004). Vibration analysis of rotors for the identification of shaft misalignment Part 1: theoretical analysis. *Mechanical Engineering Science, 218 Part C*(C18203 ©IMechE 2004).

Saavedra, P., & Ramırez, D. (2004). Vibration analysis of rotors for the identification of shaft misalignment Part 2: Experimental validation. *Mechanical Engineering Science, 218 Part C*(C18203 ©IMechE 2004).

Saleem, M. A., Diwakar, G., & Satyanarayana, M. (2012). Detection of Unbalance in Rotating Machines Using Shaft Deflection Measurement during Its Operation. *IOSR*.

Sarkimaki, V., Tiainen, R., Ahola, J., & Lindh, T. (2005). *Wireless technologies in condition monitoring and remote diagnostics of electric drives; requirements and applications.* Paper presented at the Power Electronics and Applications, 2005 European Conference on.

Sasi, A. B., Payne, B., Gu, F., & Ball, A. D. (2001). *The exploitation of instantaneous angular speed for condition monitoring of electric motors.* Paper presented at the Proceedings of the 14th International Congress on Condition Monitoring and Diagnostic Engineering Management, Manchester, UK.

Sasi, A. Y. B., Gu, F., Li, Y., & Ball, A. D. (2006). A validated model for the prediction of rotor bar failure in squirrel-cage motors using instantaneous angular speed. [doi: 10.1016/j.ymssp.2005.09.010]. *Mechanical Systems and Signal Processing, 20*(7), 1572-1589.

Sasi , A. Y. B., Gu, F., Payne , B., & Ball, A. (2004). Instantaneous angular speed monitoring of electric motors. *Journal of Quality in Maintenance Engineering, 10*(2), 123-135.

Sasi, Y. A. (2005). *The Exploitation of Instantaneous Angular Speed for Machinery Condition Monitoring.* PhD Thesis, School of Mechanical, Aerospace and Civil Engineering, Manchester, UK.

Scheffer, C., & Girdhar, P. (2004). *Practical machinery vibration analysis and predictive maintenance*: Access Online via Elsevier.

Sekhar, A. S., & Prabhu, B. S. (1995). Effects of coupling misalignment on vibrations of rotating machinery. [doi: DOI: 10.1006/jsvi.1995.0407]. *Journal of Sound and Vibration, 185*(4), 655-671.

Sekhar, A. S., & Rao, A. (1996 a). Vibration analysis of rotor coupling bearing system with misaligned shafts. *41st ASME International Gas Turbines and Aeroengine Congress and Exhibition, paper 96-GT-12*.

Sekhar, A. S., & Rao, A. (1996 b). Crack versus misalignment in rotor coupling bearing system. *J. Mach. Vibr, 5*, 179-188.

Shinozuka, M., Feng, M. Q., Chou, P., Chen, Y., & Park, C. (2004). *MEMS-based wireless real-time health monitoring of bridges.* Paper presented at the the 3rd International Conference on Earthquake Engineering.

Sinha, J. K. (2005). On standardisation of calibration procedure for accelerometer. *Journal of Sound and Vibration, 286*(1–2), 417-427. doi: http://dx.doi.org/10.1016/j.jsv.2004.12.004

Sinha, J. K., Lees, A., & Friswell, M. (2004). Estimating unbalance and misalignment of a flexible rotating machine from a single run-down. *Journal of Sound and Vibration, 272*(3), 967-989.

Sinocera Piezotronics, I. (2011a). V/IEPE Input Data Acquisitions, from http://www.china-yec.com/en/products_details.asp?id=218

Sinocera Piezotronics, I. (2011b, 2011-9-29). YE7600 General Control & Analysis Software, from http://www.china-yec.com/en/products_details.asp?id=221

Smith, D. (1980). *Recognition of the causes of rotor vibration in turbomachinery.* Paper presented at the Proceedings of the Institution of Mechanical Engineers-Vibrations in Rotating Machinery.

Staebler, M. (2000). TMS320F240 DSP solution for obtaining resolver angular position and speed. *Texas Instrument Application Report SPRA605, February*.

Stephen, J., Hines, J. W., & Edmondson, A. (1999). *Motor Shaft Misalignment Bearing Load Analysis*. Paper presented at the Maintenance and Reliability Conference (MARCON 99).

Sudhakar, G. N. D. S., & Sekhar, A. S. (2011). Identification of unbalance in a rotor bearing system. *Journal of Sound and Vibration, 330*(10), 2299-2313. doi: http://dx.doi.org/10.1016/j.jsv.2010.11.028

Suphattana, C., & Surawatpunya, K. (2010). *Vibration Analaysis and Improvment for unbalance Electromagnetic Flux within Airgap of AC Induction Motor*. Paper presented at the CEPSI 2010 Taipei -Taiwan retrieved from

Sweeney, P. J., & Randall, R. B. (1996). Gear Transmission Error Measurement Using Phase Demodulation. *IMechE, 210*, 201-213.

Taylor, J. I. (1995). Back to the Basics of the Rotating Machinery Vibration Analysis. *Sound and Vibration, 29*(2), 12-16.

Tejas, H. P., & Ashish, K. D. (2009). Experimental investigations on vibration response of misaligned rotors. [doi: DOI: 10.1016/j.ymssp.2009.04.004]. *Mechanical Systems and Signal Processing, 23*(7), 2236-2252.

Tejas, H. P., & Ashish, K. D. (2009). Vibration response of misaligned rotors. [doi: 10.1016/j.jsv.2009.03.024]. *Journal of Sound and Vibration, 325*(3), 609-628.

Texas, & Instruments, I. (2000). Low Power Dual Operational Amplifiers (LM358 datasheet), 2009, from http://www.ti.com/lit/ds/slos068r/slos068r.pdf

Texas Instruments, I. (1999). Analysis of the Sallen-Key Architecture *Mixed Signal Products*.

Trevor, & Hunt, M. (1996). *Condition Monitoring of Mechanical and Hydraulic plant: a concise introduction and guide*. London, UK: Chapman and Hall.

Tsoumas, I., Mitronikas, E., Georgoulas, G., & Safacas, A. (2005, 7-9 Sept. 2005). *A comparative study of induction motor current signature analysis techniques for mechanical faults detection.* Paper presented at the Diagnostics for Electric Machines, Power Electronics and Drives, 2005. SDEMPED 2005. 5th IEEE International Symposium on.

Vakman, D. (1994). Computer measuring of frequency stability and the analytic signal. *Instrumentation and Measurement, IEEE Transactions on, 43*(4), 668-671.

Vakman, D. (2000). New high precision frequency measurement. *Measurement Science and Technology, 11*(10), 1493.

Vance, J. (1988). *Rotor dynamics of Turbomachinery*. New York: John Wiley & Sons.

Weinberg, H. (1999). Dual axis, low g, fully integrated accelerometers. *Analog Dialogue, 33*, 33-01.

Woodcock, J. S. (1977). The effects of couplings upon the vibrations of the rotating machinery. *In Proceedings of International Conference on Flexible Couplings, University of Sussex, Brighton*, 1-20

Xu, M., & Marangoni, R. D. (1994 a). Vibration analysis of a motor-flexible coupling-rotor system subjected to misalignment and unbalance Part I: Theoretical model and analysis. *Journal of Sound and Vibration* (176), 663–679.

Xu, M., & Marangoni, R. D. (1994 b). Vibration Analysis Of A Motor-flexible Coupling-Rotor System Subject To Misalignment And Unbalance, Part II: Experimental Validation. *Journal of Sound and Vibration, 176*(5), 681-691. doi: http://dx.doi.org/10.1006/jsvi.1994.1406

Yang, J., Pu, L., Wang, Z., Zhou, Y., & Yan, X. (2001). Fault Detection in a Diesel Engine by Analysing the Instantaneous Angular Speed. *Mechanical Systems and Signal Processing, 15*(3), 549-564. doi: http://dx.doi.org/10.1006/mssp.2000.1344

Yang, T., & Hsu, M.-W. (2009). *An efficient diagnosis technique for variations of shaft-bow and unbalance*.

Yesilyhurt, I. (1997). *Gearbox Fault Detection and Severity Assessment Using Vibration Analysis.* PhD Thesis, The University of Manchester, Manchester, UK.

Zhou, Q., Wang, D., Feng, C., & Du, Y. (2011, 16-18 April 2011). *The dynamical behaviors of a misalignment rotor-bearing system.* Paper presented at the Consumer Electronics, Communications and Networks (CECNet), 2011 International Conference on.

Zigbee Alliance, I. (2007). specification-document . 053474r17. from Zigbee Alliance: [Online]. http://www.zigbee.org

Zimmerman, R. (2002). Resolvers as Velocity and Position Encoding Devices Retrieved 01/02/2010, 2010, from http://controlsciences.com/resolver_application_data.php

Appendices

Appendix A: Mathematical equation manipulation

Nomenclature

j	Bolt reference index
J_1,J_2	Polar moments of inertia
N	Number of coupling bolts
Kb	Effective stiffness of each bolt
K_1,K_2	Component of stiffness matrix
δ (e_{12})	Horizontal misalignment at the coupling
e_c	Geometric mass centre from rotational centre
ε	Torsional displacement
φ	Total rotation of shaft 1
θ	Total rotation of shaft 2
Ω	Reference rotor speed
α_j	Angular position of bolt j on first shaft
φ_j	Angular position of bolt j on second shaft
r	Radius of coupling bolt positions on reference shaft
R_j	Radius position of bolt j on second shaft
X1,Y1	Vibration displacement levels of shaft 1
X2,Y2	Vibration displacement levels of shaft 2
X,Y	Vibration differentials
U	Total stored energy
$dmtorque1$	Torque generated by eccentric mass due to misalignment (shaft1)
$dmtorque2$	Torque generated by eccentric mass due to misalignment (shaft2)
$dmforcex1$	Forces generated by eccentric mass due to misalignment in the x-direction (shaft 1)
$dmforcey1$	Forces generated by eccentric mass due to misalignment in the y-direction (shaft 1)
$dmforcex2$	Forces generated by eccentric mass due to misalignment in the x-direction (shaft 2)
$dmforcey2$	Forces generated by eccentric mass due to misalignment in the y-direction (shaft 2)
Mg_{12}	Torque excitation of coupling due to misalignment
M_{x12}	Torque generated by coupling due to misalignment
Fx_{12}	Force excitations due to misalignment in the x-direction
Fy_{12}	Force excitations due to misalignment in the y-direction

Equation of motion derivation

On the flange of rotor 1, the coupling bolts will be arranged about the centre. Let the number of bolts be *N*, equally positioned around the circumference of the first rotor. Then at time zero, the position of bolt *j* is given by(Lees, A. W., 2007 (a))

$$x_j = r\cos\alpha_j \text{ and } \quad y_j = r\sin\alpha_j$$

Where $\alpha_j = (j-1)\alpha$
And $\alpha = \frac{2\pi}{N}$ A. 1

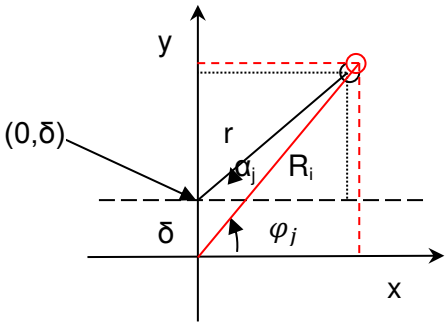

On the other rotor, the holes are not distributed around the centre of the first rotor, but offset. Simple geometry shows that the position of the j[th] bolt relative to the centre of this rotor is

$$x_j = r\cos\alpha_j \text{ , and } \quad y_j = \delta + r\sin\alpha_j$$
$$R_j{}^2 = \delta^2 + r^2 + 2\delta r\cos(90-\alpha_j) \quad \text{A. 2}$$

$$\varphi_j = \tan^{-1}\left(\frac{\delta + r\sin\alpha_j}{r\cos\alpha_j}\right) \quad \text{A. 3}$$

By rotating the point (0, δ) counter clockwise by an angle of φ_j around the new centre. The coordinates become as

$$\begin{bmatrix} X_j \\ Y_j \end{bmatrix} = R_j \begin{bmatrix} \cos\varphi_j \\ \sin\varphi_j \end{bmatrix} + \begin{bmatrix} \cos\varphi & \sin\varphi \\ -\sin\varphi & \cos\varphi \end{bmatrix} \begin{bmatrix} 0 \\ \delta \end{bmatrix}$$

To start with initial simple model, assume that the two rotors rotate at speeds Ω,$\dot{\phi}$ respectively, where Ω is treated as constant for simplifying the model. Then the kinetic energy is:

$$T = \frac{1}{2}J_1\Omega^2 + \frac{1}{2}J_2\dot{\phi}^2 + \frac{1}{2}m_1\dot{X}_1{}^2 + \frac{1}{2}m_1\dot{Y}_1{}^2 + \frac{1}{2}m_2\dot{X}_2{}^2 + \frac{1}{2}m_2\dot{Y}_2{}^2 \quad \text{A. 4}$$

Lagrange's equation: L=T-U

$$L = T - U$$

$$\frac{\mathrm{d}}{\mathrm{dt}}\left(\frac{\partial \mathrm{L}}{\partial \dot{\mathrm{q}}}\right)-\frac{\partial \mathrm{L}}{\partial \mathrm{q_i}}=0; \qquad \text{A. 5}$$

The locus of the coupling bolts on the driving rotor (1) follow a single circle of radius r whereas the driven (2) rotor each follow different circle diameter as shown in equation A. 2.

The analysis of the motion commences with the evaluation of the energy stored within the coupling bolts. The first shaft is rotating at constant speed Ω, whilst the second rotor can vary by ϕ. The potential energy of the bolts of the second rotor is given by

$$U=\frac{K_b}{2}\sum_{j=1}^{N}\left(R_j cos(\varphi_j+\theta)+X_2-r\cos(\alpha_j+\phi)-X_1\right)^2 + \frac{K_b}{2}\sum_{j=1}^{N}\left(R_j sin(\varphi_j+\theta)+Y_2-\delta-r\sin(\alpha_j+\phi)-Y_1\right)^2 \qquad \text{A. 6}$$

The 6 DOF variables involved namely, X1, X2, Y1, Y2, θ, Φ. As shown in equation A. 6 there are additional forces contributing on either side of the coupling.

Equation A. 6 can be re-written as

$$\frac{2U}{K_b}=\sum_{j=1}^{N}{R_j}^2cos^2(\varphi_j+\theta)+r^2cos^2(\alpha_j+\phi)+(X_2-X_1)^2+2(X_2-X_1)R_j cos(\varphi_j+\theta)-\sum_{j=1}^{N}2R_j rcos(\varphi_j+\theta)cos(\alpha_j+\phi)-\sum_{j=1}^{N}2(X_2-X_1)rcos(\alpha_j+\phi)+\sum_{j=1}^{N}{R_j}^2sin^2(\varphi_j+\theta)+r^2sin^2(\alpha_j+\phi)+(Y_2-Y_1-\delta)^2+2(Y_2-Y_1-\delta)R_j\,sin(\varphi_j+\theta)-\sum_{j=1}^{N}2R_j rsin(\varphi_j+\theta)sin(\alpha_j+\phi)-2(Y_2-Y_1-\delta)rsin(\alpha_j+\phi) \qquad \text{A. 7}$$

This can be simplified as

$$U=\frac{K_b}{2}\sum_{j=1}^{N}\left[{R_j}^2+r^2+X^2+(Y-\delta)^2\right]+\frac{K_b}{2}\sum_{j=1}^{N}2XR_j cos(\varphi_j+\theta)-\frac{K_b}{2}\sum_{j=1}^{N}2R_j rcos(\varphi_j+\theta-\alpha_j-\phi)-\frac{K_b}{2}\sum_{j=1}^{N}2Xrcos(\alpha_j+\phi)+\frac{K_b}{2}\sum_{j=1}^{N}2(Y-\delta)R_j sin(\varphi_j+\theta)-\frac{K_b}{2}\sum_{j=1}^{N}2(Y-\delta)rsin(\alpha_j+\phi) \qquad \text{A. 8}$$

Where X=X2-X1 and Y=Y2-Y1;

The angular displacement of the second rotor can be approximated by the reference angular displacement ∅ adding a small angular displacement ε due to the torsional motion of rotors:

$$\theta = \phi + \varepsilon = \Omega t + \varepsilon \qquad \text{A. 9}$$

By using this approximation and taking the first-order quantities, $\sin\theta$ can be expressed as

$$\sin\theta = \varepsilon\cos\Omega t + \sin\Omega t$$

Because $\varepsilon = \theta - \Omega t = \theta - \emptyset$,

$$\sin\theta = \theta\cos\Omega t - \emptyset\cos\Omega t + \sin\Omega t \qquad \text{A. 10}$$

Similarly, $\cos\theta$ can be expressed as

$$\cos\theta = \cos\Omega t - \varepsilon\sin\Omega t$$

$$\cos\theta = -\theta\sin\Omega t + \phi\sin\Omega t + \cos\Omega t \qquad \text{A. 11}$$

Since the bolt positioning error is on rotor 1, it is clear that

$$\sum_{j=1}^{N} R_j cos(\varphi_j) = 0 \quad , \sum_{j=1}^{N} R_j sin(\varphi_j) = \frac{N\delta}{2} \qquad \text{A. 12}$$

The equation A. 8 can be simplified as

$$U = \frac{K_b}{2}\sum_{j=1}^{N}\big[R_j^2 + X^2 + r^2 + (Y-\delta)^2 + 2XR_j cos\left(\varphi_j + \theta\right) + 2(Y-\delta)\,R_j\sin\left(\varphi_j + \theta\right) - 2R_j r\cos\left(\varphi_j - \alpha_j + \theta - \phi\right)\big] \qquad \text{A. 13}$$

Using these relationships, Lagrange differentiation can be applied:

For X1 differentiation

$$-\frac{\partial U}{\partial X1} = -\frac{\partial}{\partial X1}\left\{\frac{K_b}{2}\sum_{j=1}^{N}\left[X^2 + 2X\,R_j\cos\left(\varphi_j + \theta\right)\right]\right\} = -K_b\sum_{j=1}^{N}\left[-X - R_j\cos\left(\varphi_j + \theta\right)\right]$$

$$= NK_bX + K_b\sum_{j=1}^{N}R_j\cos\left(\varphi_j + \theta\right) = NK_bX + (K_b\sum_{j=1}^{N}R_j\cos\varphi_j\cos\theta - K_b\sum_{j=1}^{N}R_j\sin\varphi_j\sin\theta)$$

$$= NK_bX + K_b(0)\cos\theta - K_b\frac{N\delta}{2}\sin\theta = NK_bX - \frac{NK_b\delta}{2}(\theta\cos\Omega t - \emptyset\cos\Omega t + \sin\Omega t)$$

$$-\frac{\partial U}{\partial X1} = NK_bX2 - NK_bX1 - \frac{NK_b\delta}{2}\cos\Omega t\;\theta + \frac{NK_b\delta}{2}\cos\Omega t\,\emptyset - \frac{NK_b\delta}{2}\sin\Omega t$$

Applying differentiation to equation A. 14 with respect to $\dot{X}_1$, equation for X1 can be written as (Force term does not need change sign)

$$m_1\ddot{X}_1 = NK_bX1 - NK_bX2 + \frac{NK_b\delta}{2}\cos\Omega t\,\theta - \frac{NK_b\delta}{2}\cos\Omega t\,\emptyset + \frac{NK_b\delta}{2}\sin\Omega t \qquad \text{A. 15}$$

Similarly for X2 differentiation

$$-\frac{\partial U}{\partial X2} = -\frac{\partial}{\partial X2}\left\{\frac{K_b}{2}\sum_{j=1}^{N}\left[X^2 + 2X\,R_j\cos(\varphi_j+\theta)\right]\right\} = -K_b\sum_{j=1}^{N}\left[X + R_j\cos(\varphi_j+\theta)\right]$$

$$= -NK_bX - K_b\sum_{j=1}^{N}R_j\cos(\varphi_j+\theta) = -NK_bX - (K_b\sum_{j=1}^{N}R_j\cos\varphi_j\cos\theta - K_b\sum_{j=1}^{N}R_j\sin\varphi_j\sin\theta)$$

$$= -NK_bX - K_b(0)\cos\theta + K_b\frac{N\delta}{2}\sin\theta = -NK_bX + \frac{NK_b\delta}{2}(\theta\cos\Omega t - \phi\cos\Omega t + \sin\Omega t)$$

$$-\frac{\partial U}{\partial X2} = NK_bX1 - NK_bX2 + \frac{NK_b\delta}{2}\cos\Omega t\,\theta - \frac{NK_b\delta}{2}\cos\Omega t\,\phi + \frac{NK_b\delta}{2}\sin\Omega t$$

Equation for X2

$$m_2\ddot{X}_2 = -NK_bX1 + NK_bX2 - \frac{NK_b\delta}{2}\cos\Omega t\,\theta + \frac{NK_b\delta}{2}\cos\Omega t\,\emptyset - \frac{NK_b\delta}{2}\sin\Omega t \qquad \text{A. 16}$$

For Y1 differentiation

$$-\frac{\partial U}{\partial Y1} = -\frac{\partial}{\partial Y1}\left\{\frac{K_b}{2}\sum_{j=1}^{N}\left[(Y-\delta)^2 + 2(Y-\delta)\sin(\varphi_j+\theta)\right]\right\}$$

$$= -K_b\sum_{j=1}^{N}\left[-(Y-\delta) - \sin(\varphi_j+\theta)\right] = NK_b(Y-\delta) + K_b\sum_{j=1}^{N}\left[\sin(\varphi_j+\theta)\right]$$

$$= NK_b(Y-\delta) + K_b\sum_{j=1}^{N}\sin\varphi_j\cos\theta - K_b\sum_{j=1}^{N}\cos\varphi_j\sin\theta$$

$$= NK_b(Y-\delta) + \frac{NK_b\delta}{2}\cos\theta + K_b(0)\sin\theta = NK_b(Y-\delta) + \frac{NK_b\delta}{2}(-\theta\sin\Omega t + \phi\sin\Omega t + \cos\Omega t)$$

$$= -NK_bY1 + NK_bY2 - NK_b\,\delta + \frac{NK_b\delta}{2}\sin\Omega t\,\theta - \frac{NK_b\delta}{2}\sin\Omega t\,\phi - \frac{NK_b\delta}{2}\cos\Omega t$$

Equation for Y1

$$m_1\ddot{Y}_1 = NK_bY1 - NK_bY2 - \frac{NK_b\delta}{2}\sin\Omega t\,\theta + \frac{NK_b\delta}{2}\sin\Omega t\,\phi + \frac{NK_b\delta}{2}\cos\Omega t + NK_b\delta \qquad \text{A. 17}$$

For Y2 differentiation

$$-\frac{\partial U}{\partial Y2} = -\frac{\partial}{\partial Y2}\left\{\frac{K_b}{2}\sum_{j=1}^{N}\left[(Y-\delta)^2 + 2(Y-\delta)\sin(\varphi_j+\theta)\right]\right\}$$

$$= -K_b\sum_{j=1}^{N}\left[(Y-\delta) + \sin(\varphi_j+\theta)\right] = -NK_b(Y-\delta) - K_b\sum_{j=1}^{N}\left[\sin(\varphi_j+\theta)\right]$$

$$= -NK_b(Y-\delta) - K_b\sum_{j=1}^{N}\sin\varphi_j\cos\theta - K_b\sum_{j=1}^{N}\cos\varphi_j\sin\theta$$

$$= -NK_b(Y-\delta) - \frac{NK_b\delta}{2}\cos\theta - K_b\,(0)\sin\theta = -NK_b(Y-\delta) - \frac{NK_b\delta}{2}(-\theta\sin\Omega t + \phi\sin\Omega t + \cos\Omega t)$$

$$= -NK_b(Y2-Y1) + NK_b\,\delta + \frac{NK_b\delta}{2}\sin\Omega t\,(\theta-\phi) - \frac{NK_b\delta}{2}\cos\Omega t$$

Equation for Y2

$$m_2\ddot{Y}_2 = -NK_b(Y2-Y1) + \frac{NK_b\delta}{2}\sin\Omega t\,(\theta-\phi) - \frac{NK_b\delta}{2}\cos\Omega t) + NK_b\,\delta \qquad \text{A. 18}$$

For θ differentiation

$$-\frac{\partial U}{\partial\theta} = -\frac{\partial}{\partial\theta}\left\{\frac{K_b}{2}\sum_{j=1}^{N}\left[2XR_j cos\left(\varphi_j+\theta\right)+2(Y-\delta)R_j\sin\left(\varphi_j+\theta\right)-2R_j r\cos\left(\varphi_j-\alpha_j+\theta-\phi\right)\right]\right\}$$

$$-\frac{\partial U}{\partial\theta} = -\frac{K_b}{2}\frac{\partial}{\partial\theta}\sum_{j=1}^{N}2XR_j\cos\left(\varphi_j+\theta\right) - \frac{K_b}{2}\frac{\partial}{\partial\theta}\sum_{j=1}^{N}2(Y-\delta)\sin\left(\varphi_j+\theta\right) + \frac{K_b}{2}\frac{\partial}{\partial\theta}\sum_{j=1}^{N}2R_j r\cos\left(\varphi_j-\alpha_j+\theta-\phi\right)$$

Recall As $R_j \approx r \; and \; \varphi_j \approx \alpha_j$

$$\approx -\frac{K_b}{2}\frac{\partial}{\partial\theta}\sum_{j=1}^{N}2XR_j\left[\cos\varphi_j\cos\theta-\sin\varphi_j\sin\theta\right] + \frac{K_b}{2}\frac{\partial}{\partial\theta}\sum_{j=1}^{N}2(Y-\delta)\left[\sin\varphi_j\cos\theta+\cos\varphi_j\sin\theta\right]$$

$$+\frac{K_b}{2}\frac{\partial}{\partial\theta}\sum_{j=1}^{N}2rr\cos(0+\theta-\emptyset)$$

$$\approx -\frac{K_b}{2}\frac{\partial}{\partial\theta}\left\{\sum_{j=1}^{N}2XR_j\cos\varphi_j\cos\theta - \sum_{j=1}^{N}2XR_j\sin\varphi_j\sin\theta\right\}$$

$$+\frac{K_b}{2}\frac{\partial}{\partial\theta}\left\{\sum_{j=1}^{N}2(Y-\delta)\left[\sin\varphi_j\cos\theta\right]+\sum_{j=1}^{N}2(Y-\delta)\left[\cos\varphi_j\sin\theta\right]\right\} + \frac{K_b}{2}\frac{\partial}{\partial\theta}\sum_{j=1}^{N}2rr\cos(\theta-\phi)$$

$$= -\frac{K_b}{2}\frac{\partial}{\partial\theta}\left\{-\frac{N\delta 2X}{2}\sin\theta\right\} + \frac{\partial}{\partial\theta}\left\{\frac{K_b 2(Y-\delta)}{2}\frac{N\delta}{2}\cos\theta\right\} + \frac{K_b}{2}\frac{\partial}{\partial\theta}\sum_{j=1}^{N}2rr\cos(\theta-\phi)$$

$$\approx \frac{\partial}{\partial\theta}\left\{\frac{N\delta K_b X}{2}(\theta\cos\Omega t - \phi\cos\Omega t + \sin\Omega t)\right\} + \frac{\partial}{\partial\theta}\left\{\frac{N\delta K_b(Y-\delta)}{2}(-\theta\sin\Omega t + \phi\sin\Omega t + \cos\Omega t)\right\}$$

$$+\frac{K_b}{2}\frac{\partial}{\partial\theta}\sum_{j=1}^{N}2r^2\cos(\theta-\emptyset)$$

$$= \left\{\frac{N\delta K_b X}{2}\cos\Omega t\right\} - \left\{\frac{N\delta K_b(Y-\delta)}{2}\sin\Omega t\right\} - r^2\,NK_b\sin(\theta-\phi)$$

$$-\frac{\partial U}{\partial\theta} \approx -\frac{N\delta K_b}{2}\cos\Omega t\,X1 + \frac{N\delta K_b}{2}\cos\Omega t\,X2 + \frac{N\delta K_b}{2}\sin\Omega t\,Y1 - \frac{N\delta K_b}{2}\sin\Omega t\,Y2 - r^2NK_b\theta + r^2NK_b\phi$$

$$+\frac{N\delta K_b}{2}\delta\sin\Omega t$$

Equation for θ

$$J_1\ddot{\theta} = \frac{N\delta K_b}{2}\cos\Omega t\, X1 - \frac{N\delta K_b}{2}\sin\Omega t\, Y1 - \frac{N\delta K_b}{2}\cos\Omega t\, X2 + \frac{N\delta K_b}{2}\sin\Omega t\, Y2 - r^2 N K_b\phi + r^2 N K_b\theta - \frac{N\delta K_b}{2}\delta\sin\Omega t + Tm \quad \text{A. 19}$$

For ϕ differentiation

$$-\frac{\partial U}{\partial \emptyset} = -\frac{\partial}{\partial \phi}\left\{\frac{K_b}{2}\sum_{j=1}^{N}\left[2XR_j cos\left(\varphi_j+\theta\right)+2(Y-\delta)R_j\sin\left(\varphi_j+\theta\right)-2R_j r\cos\left(\varphi_j-\alpha_j+\theta-\phi\right)\right]\right\}$$

$$-\frac{\partial U}{\partial \emptyset} = -\frac{K_b}{2}\frac{\partial}{\partial\phi}\sum_{j=1}^{N}2XR_j\cos\left(\varphi_j+\theta\right)-\frac{K_b}{2}\frac{\partial}{\partial\phi}\sum_{j=1}^{N}2(Y-\delta)\sin\left(\varphi_j+\theta\right)+\frac{K_b}{2}\frac{\partial}{\partial\emptyset}\sum_{j=1}^{N}2R_j r\cos\left(\varphi_j-\alpha_j+\theta-\phi\right)$$

$$\approx -\frac{K_b}{2}\frac{\partial}{\partial\phi}\sum_{j=1}^{N}2XR_j\left[\cos\varphi_j\cos\theta-\sin\varphi_j\sin\theta\right]+\frac{K_b}{2}\frac{\partial}{\partial\emptyset}\sum_{j=1}^{N}2(Y-\delta)\left[\sin\varphi_j\cos\theta+\cos\varphi_j\sin\theta\right]$$
$$+\frac{K_b}{2}\frac{\partial}{\partial\emptyset}\sum_{j=1}^{N}2rr\cos(0+\theta-\phi)$$

$$\approx -\frac{K_b}{2}\frac{\partial}{\partial\phi}\left\{\sum_{j=1}^{N}2XR_j\cos\varphi_j\cos\theta-\sum_{j=1}^{N}2XR_j\sin\varphi_j\sin\theta\right\}$$
$$+\frac{K_b}{2}\frac{\partial}{\partial\phi}\left\{\sum_{j=1}^{N}2(Y-\delta)\left[\sin\varphi_j\cos\theta\right]+\sum_{j=1}^{N}2(Y-\delta)\left[\cos\varphi_j\sin\theta\right]\right\}+\frac{K_b}{2}\frac{\partial}{\partial\phi}\sum_{j=1}^{N}2rr\cos(\theta-\emptyset)$$

$$=-\frac{K_b}{2}\frac{\partial}{\partial\phi}\left\{-\frac{N\delta 2X}{2}\sin\theta\right\}+\frac{\partial}{\partial\phi}\left\{\frac{K_b 2(Y-\delta)}{2}\frac{N\delta}{2}\cos\theta\right\}+\frac{K_b}{2}\frac{\partial}{\partial\phi}\sum_{j=1}^{N}2rr\cos(\theta-\emptyset)$$

$$\approx \frac{N\delta K_b}{2}\frac{\partial}{\partial\phi}\{X[\theta\cos\Omega t-\emptyset\cos\Omega t+\sin\Omega t]\}+\frac{\partial}{\partial\phi}\left\{\frac{N\delta K_b}{2}(Y-\delta)(-\theta\sin\Omega t+\phi\sin\Omega t+\cos\Omega t)\right\}$$
$$+\frac{K_b}{2}\frac{\partial}{\partial\phi}\sum_{j=1}^{N}2rr\cos(\theta-\phi)$$

$$=\frac{N\delta K_b}{2}\{-X\cos\Omega t\}+\left\{\frac{N\delta K_b}{2}(Y-\delta)(\sin\Omega t)\right\}+NK_b\,r^2\sin(\theta-\emptyset)$$

$$\approx \frac{NK_b\delta}{2}\cos\Omega t\, X2-\frac{NK_b\delta}{2}\cos\Omega t\, X1-\frac{NK_b\delta}{2}\sin\Omega t\, Y2+\frac{NK_b\delta}{2}\sin\Omega t\, Y2+NK_b r^2\theta+NK_b r^2\phi-\frac{NK_b\delta}{2}\delta\sin\Omega t$$

$$-\frac{\partial U}{\partial\emptyset}\approx -\frac{NK_b\delta}{2}\cos\Omega t\, X1+\frac{NK_b\delta}{2}\cos\Omega t\, X2+\frac{NK_b\delta}{2}\sin\Omega t\, Y1-\frac{NK_b\delta}{2}\sin\Omega t\, Y2+NK_b r^2\theta-NK_b r^2\phi$$
$$-\frac{NK_b\delta}{2}\delta\sin\Omega t$$

Equation for ϕ

$$J_2\ddot{\phi} = \frac{NK_b\delta}{2}\cos\Omega t\, X1 - \frac{NK_b\delta}{2}\cos\Omega t\, X2 - \frac{NK_b\delta}{2}\sin\Omega t\, Y1 + \frac{NK_b\delta}{2}\sin\Omega t\, Y2 - NK_b r^2\theta + NK_b r^2\phi + \frac{NK_b\delta}{2}\delta\sin\Omega t + T_m \quad \text{A. 20}$$

Non-conservative forces due to variations

Shaft 1

$$\begin{aligned} Q_{X1} &= -K_1X_1 - C_1\dot{X}_1 \\ Q_{Y1} &= -K_1Y_1 - C_1\dot{Y}_1 \\ Q_\theta &= -C_r(\dot{\theta} - \dot{\phi}) \end{aligned} \quad \text{A. 21}$$

Shaft2

$$\begin{aligned} Q_{X2} &= -K_2X_2 - C_2\dot{X}_2 \\ Q_{Y2} &= -K_2Y_2 - C_2\dot{Y}_2 \\ Q_\phi &= -C_r(\dot{\phi} - \dot{\theta}) \end{aligned} \quad \text{A. 22}$$

Adding these forces to the corresponding equations A.15 to A.20, the equation of motion can be rewritten as:

Shaft1:

$$\begin{aligned} m_1\ddot{X}_1 &= -K_1X_1 + NK_bX_1 - NK_bX_2 + \frac{NK_b\delta}{2}\cos\Omega t\,\theta - \frac{NK_b\delta}{2}\cos\Omega t\,\phi + \frac{NK_b\delta}{2}\sin\Omega t - C_1\dot{X}_1 \\ m_1\ddot{Y}_1 &= -K_1Y_1 + NK_bY_1 - NK_bY_2 - \frac{NK_b\delta}{2}\sin\Omega t\,\theta + \frac{NK_b\delta}{2}\sin\Omega t\,\phi + \frac{NK_b\delta}{2}\cos\Omega t + NK_b\delta - C_1\dot{Y}_1 \\ J_1\ddot{\theta} &= -C_r(\dot{\theta} - \dot{\phi}) + \frac{N\delta K_b}{2}\cos\Omega t\, X_1 - \frac{N\delta K_b}{2}\sin\Omega t\, Y_1 - \frac{N\delta K_b}{2}\cos\Omega t\, X_2 + \frac{N\delta K_b}{2}\sin\Omega t\, Y_2 - r^2NK_b\phi \\ &\quad + r^2NK_b\theta - \frac{N\delta K_b}{2}\delta\sin\Omega t + T_m \end{aligned} \quad \text{A. 23}$$

Shaft2:

$$\begin{aligned} m_2\ddot{X}_2 &= -K_2X_2 + -NK_bX1 + NK_bX2 - \frac{NK_b\delta}{2}\cos\Omega t\,\theta + \frac{NK_b\delta}{2}\cos\Omega t\,\phi - \frac{NK_b\delta}{2}\sin\Omega t - C_2\dot{X}_2 \\ m_2\ddot{Y}_2 &= -K_2Y_2 - NK_b(Y_2 - Y_1) + \frac{NK_b\delta}{2}\sin\Omega t\,(\theta - \phi) - \frac{NK_b\delta}{2}\cos\Omega t + NK_b\,\delta - C_2\dot{Y}_2 \\ J_2\ddot{\emptyset} &= C_r\big(\dot{\phi} - \dot{\theta}\big) + \frac{NK_b\delta}{2}\cos\Omega t\, X_1 - \frac{NK_b\delta}{2}\cos\Omega t\, X_2 - \frac{NK_b\delta}{2}\sin\Omega t\, Y_1 + \frac{NK_b\delta}{2}\sin\Omega t\, Y_2 - NK_br^2\theta \\ &\quad + NK_br^2\phi + \frac{NK_b\delta}{2}\delta\sin\Omega t + T_l \end{aligned} \quad \text{A. 24}$$

Forces excitations, due to misalignment the forces acting in the x and y direction, are:

$$Fx_{12} = NK_b \frac{\delta}{2} sin\Omega t$$
$$Fy_{12} = NK_b \frac{\delta}{2} cos\Omega t - NK_b\delta \quad \text{A. 25}$$

Also, the torque excitation of coupling due to misalignment is

$$Mg_{12} = NK_b \frac{\delta^2}{2} sin\Omega t \quad \text{A. 26}$$

Oscillating torque generated by coupling due to misalignment is;

$$M_{x12} = NK_b \frac{\delta}{2}(x_1 \sin\Omega t + y_1 \cos\Omega t - x_2 \sin\Omega t - y_2 \cos\Omega t) \quad \text{A. 27}$$

For simplicity, the eccentricity mass from geometric centre for each rotor is e_c.

Hence, oscillating torque generated by eccentric mass due to geometric centre (dynamic unbalance)

$$dmtorque1 = 9.81 e_c m_{e1} \cos\Omega t$$
$$dmtorque2 = 9.81 e_c m_{e2} \cos\Omega t \quad \text{A. 28}$$

Oscillating forces generated by eccentric mass due to geometric centre (dynamic unbalance):

$$dmforcex1 = e_c\dot{\theta}^2 m_{e1} \cos\Omega t$$
$$dmforcey1 = e_c\dot{\theta}^2 m_{e1} \sin\Omega t$$
$$dmforcex2 = e_c\dot{\phi}^2 m_{e2} \cos\Omega t$$
$$dmforcey2 = e_c\dot{\phi}^2 m_{e2} \sin\Omega t \quad \text{A. 29}$$

Adding these forces to its corresponding equation in equations A.23 and A.24 the final equation of motions can be written as:

Shaft1:

$$m_1\ddot{X}_1 = -K_1X_1 + NK_bX_1 - NK_bX_2 + \frac{NK_b\delta}{2}\cos\Omega t\,\theta - \frac{NK_b\delta}{2}\cos\Omega t\,\phi + \frac{NK_b\delta}{2}\sin\Omega t + Fx_{12} - C_1\dot{X}_1 + dmforcex1$$
$$m_1\ddot{Y}_1 = -K_1Y_1 + NK_bY_1 - NK_bY_2 - \frac{NK_b\delta}{2}\sin\Omega t\,\theta + \frac{NK_b\delta}{2}\sin\Omega t\,\phi + \frac{NK_b\delta}{2}\cos\Omega t + NK_b\delta + Fy_{12} - C_1\dot{Y}_1 + dmforcey1 \quad \text{A. 30}$$
$$J_1\ddot{\theta} = -C_r(\dot{\theta} - \dot{\phi}) + \frac{N\delta K_b}{2}\cos\Omega t\,X_1 - \frac{N\delta K_b}{2}\sin\Omega t\,Y_1 - \frac{N\delta K_b}{2}\cos\Omega t\,X_2 + \frac{N\delta K_b}{2}\sin\Omega t\,Y_2 - r^2NK_b\phi + r^2NK_b\theta - \frac{N\delta K_b}{2}\delta\sin\Omega t + Mg_{12} + M_{x12} + T_m - dmtorque1$$

Shaft2:

$$m_2\ddot{X}_2 = -K_2X_2 \pm NK_bX1 + NK_bX2 - \frac{NK_b\delta}{2}\cos\Omega t\,\theta + \frac{NK_b\delta}{2}\cos\Omega t\,\phi - \frac{NK_b\delta}{2}\sin\Omega t + Fx_{12} - C_2\dot{X}_2 + dmforcex2$$

$$m_2\ddot{Y}_2 = -K_2Y_2 - NK_b(Y_2 - Y_1) + \frac{NK_b\delta}{2}\sin\Omega t\,(\theta - \phi) - \frac{NK_b\delta}{2}\cos\Omega t + NK_b\,\delta + Fy_{12} - C_2\dot{Y}_2 + dmforcey2 \quad \text{A. 31}$$

$$J_2\ddot{\phi} = C_r(\dot{\phi} - \dot{\theta}) + \frac{NK_b\delta}{2}\cos\Omega t\,X_1 - \frac{NK_b\delta}{2}\cos\Omega t\,X_2 - \frac{NK_b\delta}{2}\sin\Omega t\,Y_1 + \frac{NK_b\delta}{2}\sin\Omega t\,Y_2 - NK_br^2\theta + NK_br^2\phi + \frac{NK_b\delta}{2}\delta\sin\Omega t - Mg_{12} - M_{x12} + T_l - dmtorque2$$

Appendix B: Test Rig Parameter Calculation

1. Moment of inertia of shafts

The moment of inertia, usually denoted J, measures the extent to which an object resists rotational acceleration about an axis, and is the rotational analogue to mass. Mass moments of inertia have units of dimension mass × length2. The following moment of inertia assumes constant density throughout the object, and the axis of rotation is taken to be through the centre of mass:

$$J = m{r_g}^2$$

Where, r_g is the radius of gyration of solid cylinder. The r_g can be expressed by the following equation:

$${r_g}^2 = \frac{d^2}{8} = \frac{(2r)^2}{8} = \frac{r^2}{2}$$

$$r_g = \frac{r}{\sqrt{2}}$$

The steel density is given as

$$\sigma_{\text{steel}} = 7.8\ {}^{kg}/_{dm^3} = 7.8 \times 10^3\ {}^{kg}/_{m^3}$$

1- Shaft one (Motor shaft)

Total mass of shaft one (m_1) =10 kg (excluding half coupling mass=2.73 kg)

Radius of gyration of shaft one (r_{g1})

$$r_{g1} = \frac{1}{\sqrt{2}}\left(\frac{14 + 15 + 19 + 51.15 + 15 + 19 + 14}{7}\right)$$

$$r_{g1} = 14.8644mm = 0.0149m$$

Moment of inertia of shaft one:

$$J_1 = m_1 \times {r_{g1}}^2$$

$$J_1 = 10 \times (0.0149)^2 = 0.0022\ kg.m^2$$

With one flange of coupling on:

$$J_1 = 0.0022 + \frac{0.0078}{2} = 0.0061\ kg.m^2$$

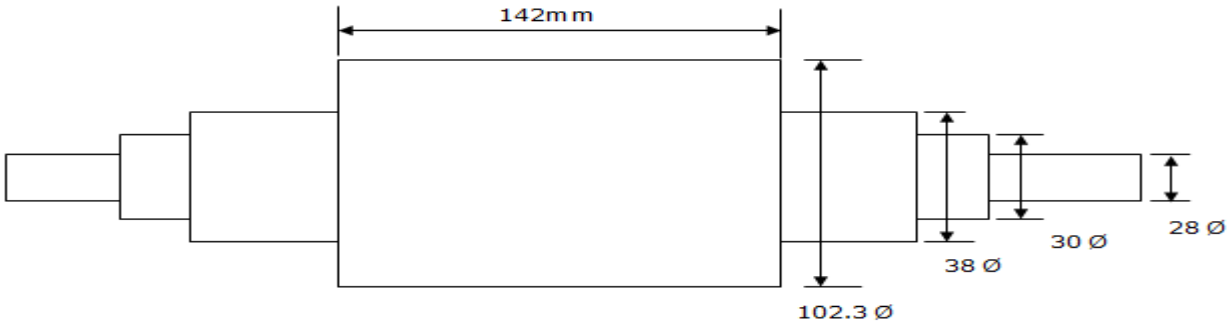

Figure E1. Motor shaft

2- Shaft two and three

Total mass of shaft two and three (m_2, m_3) =2.0 kg =2.0 kg (excluding 5.46 kg of coupling)

Radius of gyration of shaft two and three ($r_{g2,3}$)

$$r_{g2,3} = \frac{1}{\sqrt{2}}\left(\frac{15+20+25+20+15}{5}\right)$$

$$r_{g2,3} = 13.435mm = 0.0134m$$

Moment of inertia of shaft one:

$$J_{2,3} = m_2 \times {r_{g2}}^2$$

$$J_{2,3} = 2.0 \times (0.0134)^2 = 0.000356\ kg.m^2$$

With coupling on:

$$J_{2,3} = 0.000356 + 0.0078 = 0.0082\ kg.m^2$$

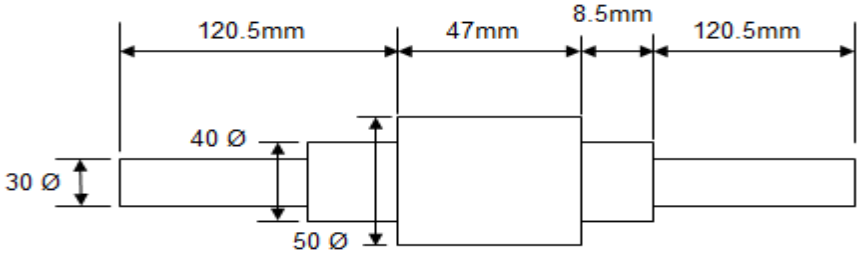

Figure E2. Shaft two and three dimensions

3- Shaft four (DC generator)

Total mass of shaft two and three (m_4) =32.23 kg (excluding half coupling mass=2.73 kg)

Radius of gyration of shaft two and three (r_{g4})

$$r_{g4} = \frac{1}{\sqrt{2}}\left(\frac{20+30+70+30+20+17.5}{6}\right)$$

$$r_{g4} = 22.0971mm = 0.0221m$$

Moment of inertia of shaft one:

$$J_4 = m_4 \times {r_{g4}}^2$$

$$J_4 = 32.23 \times (0.0221)^2 = 0.0157\ kg.m^2$$

With half coupling on:

$$J_4 = 0.0157 + 0.0078/2 = 0.0196\ kg.m^2$$

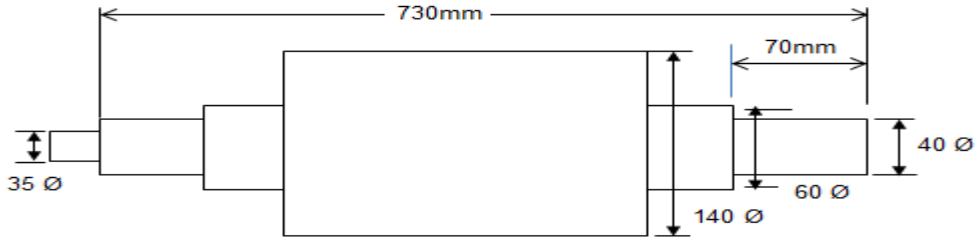

Figure E3. DC generator rotor dimensions (shaft four)

4- Moment of inertia of coupling

The total mass of coupling (see Table 5.1) = 5.46 kg

Moment of inertia of coupling (Maryland, 2008):

$$J_c = 0.0078\ kg.m^2$$

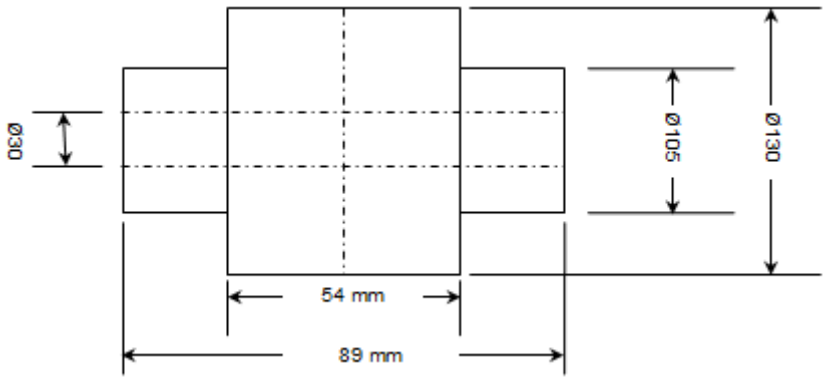

Figure E4. Coupling dimensions

Appendix C: Balance quality and permissable residual unbalance

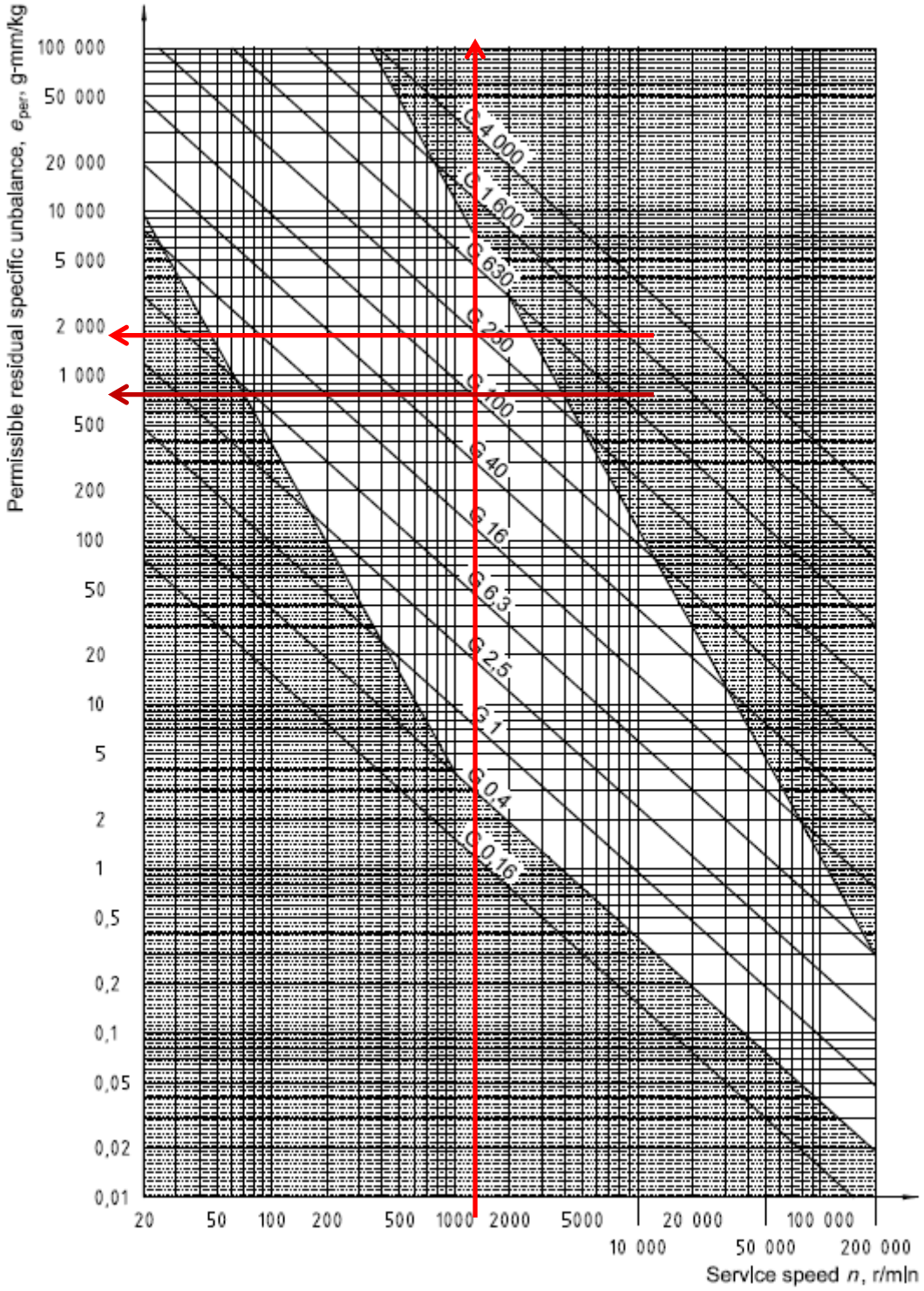

Figure C. 1 Permissible residual specific unbalance based on balance quality grade G and service speed n(Iso1940-1, 2003)

Machinery types: General examples	Balance quality grade G	Magnitude $e_{per} \cdot \Omega$ mm/s
Crankshaft drives for large slow marine diesel engines (piston speed below 9 m/s), inherently unbalanced	G 4000	4 000
Crankshaft drives for large slow marine diesel engines (piston speed below 9 m/s), inherently balanced	G 1600	1 600
Crankshaft drives, inherently unbalanced, elastically mounted	G 630	630
Crankshaft drives, inherently unbalanced, rigidly mounted	G 250	250
Complete reciprocating engines for cars, trucks and locomotives	G 100	100
Cars: wheels, wheel rims, wheel sets, drive shafts Crankshaft drives, inherently balanced, elastically mounted	G 40	40
Agricultural machinery Crankshaft drives, inherently balanced, rigidly mounted Crushing machines Drive shafts (cardan shafts, propeller shafts)	G 16	16
Aircraft gas turbines Centrifuges (separators, decanters) Electric motors and generators (of at least 80 mm shaft height), of maximum rated speeds up to 950 r/min Electric motors of shaft heights smaller than 80 mm Fans Gears Machinery, general Machine-tools Paper machines Process plant machines Pumps Turbo-chargers Water turbines	G 6,3	6,3
Compressors Computer drives Electric motors and generators (of at least 80 mm shaft height), of maximum rated speeds above 950 r/min Gas turbines and steam turbines Machine-tool drives Textile machines	G 2,5	2,5
Audio and video drives Grinding machine drives	G 1	1
Gyroscopes Spindles and drives of high-precision systems	G 0,4	0,4

NOTE 1 Typically completely assembled rotors are classified here. Depending on the particular application, the next higher or lower grade may be used instead. For components, see Clause 9.

NOTE 2 All items are rotating if not otherwise mentioned (reciprocating) or self-evident (e.g. crankshaft drives).

NOTE 3 For limitations due to set-up conditions (balancing machine, tooling), see Notes 4 and 5 in 5.2.

NOTE 4 For some additional information on the chosen balance quality grade, see Figure 2. It contains generally used areas (service speed and balance quality grade G), based on common experience.

NOTE 5 Crankshaft drives may include crankshaft, flywheel, clutch, vibration damper, rotating portion of connecting rod. Inherently unbalanced crankshaft drives theoretically cannot be balanced; inherently balanced crankshaft drives theoretically can be balanced.

NOTE 6 For some machines, specific International Standards stating balance tolerances may exist (see Bibliography).

Table C. 1Guidance for balance quality grades for rotors in a constant (rigid) state (Iso1940-1, 2003)